Slow-mode nanophotonics and cold atoms : towards a versatile Waveguide QED platform

Adrien Bouscal

SORBONNE UNIVERSITÉ

Laboratoire Kastler Brossel
Physique quantique et applications

THÈSE DE DOCTORAT DE SORBONNE UNIVERSITÉ

Spécialité : Physique

École doctorale n°564: Physique en Île-de-France

réalisée

au Laboratoire Kastler Brossel

sous la direction de Julien Laurat

présentée par

Adrien BOUSCAL

Pour obtenir le grade de :

DOCTEUR DE SORBONNE UNIVERSITÉ

Sujet de la thèse :

Slow-mode nanophotonics and cold atoms: Towards a versatile Waveguide QED platform

Soutenue publiquement le : 15 Décembre 2023

Devant le jury composé de :

M.	**Simon BERNON**, Maître de Conférences, Université de Bordeaux	Rapporteur
M.	**Alejandro GONZÁLEZ-TUDELA**, Research Scientist, CSIC	Rapporteur
M^{me}	**Juliette BILLY**, Maîtresse de Conférences, Université de Toulouse III	Examinatrice
M.	**Thomas KRAUSS**, Professor, University of York	Examinateur
M^{me}	**Agnès MAÎTRE**, Professeure, Sorbonne Université	Présidente du jury
M.	**Julien LAURAT**, Professeur, Sorbonne Université	Directeur de thèse
M.	**Alban URVOY**, Maître de Conférences, Sorbonne Université	Co-encadrant

REMERCIEMENTS

Mon premier projet au sein du laboratoire Kastler Brossel date du printemps 2018, déjà au sein de l'équipe de Julien Laurat. C'est dire le temps que j'ai passé dans le couloir 13-23 ! Je n'ai pourtant commencé ma thèse qu'à l'automne 2019, après une riche année de césure.

Tout d'abord, je tiens à remercier Julien Laurat, mon directeur de thèse, de m'avoir accepté dans son groupe Quantum Networks, d'abord en Master, à une époque où je n'avais que peu d'expérience de la recherche, puis en thèse, il y a plus de 4 ans. Merci de m'avoir fait confiance sur cet ambitieux projet alors que j'étais débutant complet en nanophotonique. Un grand merci pour les relectures, corrections et directions données tout au long de ces années, et avant ça, pour la clarté de tes cours qui ont confirmé mon attrait pour les atomes et la lumière. Bien sûr, je n'ai rien fait seul. Alban Urvoy mon co-encadrant, initialement post-doc, m'a constamment soutenu, assisté, orienté et grandement enrichi de son savoir technique pléthorique. Merci infiniment pour ces conseils ainsi que pour ton amitié. Je te souhaite tout le meilleur pour la suite de ta brillante carrière et j'espère pouvoir me mesurer à ton allemand à mon retour.

Je remercie également les rapporteurs de ma thèse Simon Bernon et Alejandro González-Tudela, qui ont pris le temps de lire mon manuscrit malgré leurs nombreux engagements. Un grand merci aux autres membres du jury : Juliette Billy, Thomas Krauss et Agnès Maître pour leur intérêt, questions et encouragements.

Ces longues années de thèse je ne les ai bien sûr pas passées seul avec mes directeurs, mais au sein d'un laboratoire plein de personnes fascinantes. Les premières qu'on rencontre quand on arrive, ce sont sûrement celles de l'administration. Merci Stéphanie, David, Laetitia et Céline pour votre bonne humeur, votre accueil et votre fiabilité, et pour toutes les fois où je suis venu vous voir sans la moindre idée de la marche à suivre (et pour les gossips). Je remercie également Antoine Heidmann, le directeur du laboratoire, pour son accueil chaleureux et son écoute sincère de nos suggestions et problèmes.

Bien que le travail expérimental puisse être solitaire, on le fait au sein d'une équipe, qui se transforme parfois en un groupe d'amis. Ce fut le cas avec la "team COVID" qui était là avant mon arrivée, Thomas, Jérémy, Tom, Tridib et Félix, qui m'ont tout de suite adopté. Une pensée toute particulière pour Jérémy, que je suis depuis le M2, pour m'avoir envoyé un template LateX de thèse cassé (et pour les heures à coder ensemble). Merci bien sûr à tous les "nouveaux", bien que certains soient très proches de la soutenance. Beate, Hadriel, merci pour votre bonne humeur

et votre bienveillance. Ambroise, Félix, Jean-Gabriel, Ioanna, bon courage pour la suite, restez solidaires comme vous l'êtes actuellement. Merci enfin à Anaïs pour ce que tu fais, tant au sein du labo qu'à l'extérieur (la recherche a besoin de toi) et avec qui j'ai partagé beaucoup de souvenirs en finalement peu de temps[1]. Le Waveguide (je compte sur toi pour lui trouver un surnom) est entre de bonnes mains.

Merci à tous les autres collègues en dehors du groupe qui rendent le laboratoire vivant et accueillant : le LKBar qui meurt et renaît à chaque édition, le groupe élargi d'Optique Quantique fan d'escape games et d'escalade, nos voisins d'optomécanique, le labo 218, le QICS, les soirées jeux, mes collègues représentants des doctorants et tous ceux qui sont devenus plus que des collègues. Merci à Pauline ma marraine avec qui on peut échanger simplement, autour d'un petit dej ou en manif.

Je tiens également à exprimer ma reconnaissance envers toutes les personnes avec lesquelles j'ai eu la chance de collaborer en dehors du laboratoire. Christophe, Nikos et Jean-Jacques, votre aide a été plus que précieuse pour permettre à un simple atomiste d'acquérir des notions de photonique. Kamel, Ariel, Malik et Sukanya, votre expertise est sans pareille et votre persévérance a rendu ce projet réalisable.

La thèse peut parfois occuper un espace mental excessif, et je remercie du fond du cœur tous les amis qui m'ont soutenu, voire supporté, durant ces quatre ans et demi. Que ce soit en partageant mon expérience de thèse avec mes colocataires Stéphane et Arthur[2], ou en changeant d'air avec mes amis de Chartres, toujours aussi fous et fidèles depuis plus de 10 ans, cela aide d'être entouré. Merci bien sûr à Juliette, Vass, Simon, Robin, Michael les physiciens originels[3] et à Pierre-Louis, Pierre, Maxence et Michael, bien que la distance nous sépare souvent. À vous tous, je vous attends à Munich.

Je veux bien sûr remercier ma famille, en particulier mes parents et mes frères, qui m'ont apporté un soutien sans faille à tous les niveaux et qui ont tout fait pour s'intéresser à ce que je faisais. J'espère que la soutenance vous aura donné un aperçu de mon monde.

Enfin, après les amis et la famille, il me faut remercier Cécile, qui est les deux à la fois. Si tu maintiens que j'aurais réussi à finir ma thèse même sans ta présence, j'aurais raté un monde de rires, de discussions et de tendresse (et toi des essais de vulgarisation plus ou moins concluants). Merci, pour ton soutien et le reste.

Paris, Janvier 2024

[1] Barcelone, Palerme, le derby et le rap waveguide, pour n'en citer que quelques uns.

[2] Pas toutes les discussions entre amis donnent lieu au lancement d'une collection de livres de vulgarisation.

[3] et Livio

CONTENTS

LIST OF FIGURES

PUBLICATIONS

The work carried out during this thesis has led to the following publications:

- Berroir, J.*, **Bouscal, A.***, Urvoy, A., Ray, T. and Laurat, J. (2022). "Nanotrappy: An open-source versatile package for cold-atom trapping close to nanostructures". *Phys. Rev. Res.* **4**, p. 013079.

  DOI: 10.1103/PhysRevResearch.4.013079

- Fayard, N., **Bouscal, A.**, Berroir, J., Urvoy, A., Ray, T., Mahapatra, S., Kemiche, M., Levenson, J.A., Greffet, J.-J., Bencheikh, K., Laurat, J. and Sauvan, C. (2022). "Asymmetric comb waveguide for strong interactions between atoms and light". *Opt. Express* **30**, pp. 45093–45109.

  DOI: 10.1364/oe.475162

- **Bouscal, A.**, Kemiche, M., Mahapatra, S., Fayard, N., Berroir, J., Ray, T., Greffet, J.-J., Raineri, F., Levenson, J.A., Bencheikh, K., Sauvan, C., Urvoy, A. and Laurat, J. (2024). "Systematic design of a robust half-W1 photonic crystal waveguide for interfacing slow light and trapped cold atoms". *New J. Phys.* **26**, p. 023026.

  DOI: 10.1088/1367-2630/ad23a4

INTRODUCTION

This thesis focuses on the interaction between light and atoms, and how to probe and enhance it on a very fundamental level. This light-matter interaction forms the cornerstone of many scientific and technological disciplines, from fundamental physics to diverse practical applications like laser cutting and quantum computing. This introduction presents in layman terms the concepts at hand.

Atoms and their energy ladder

Even before the first evidence of single atoms given by Jean Perrin in 1903, it was clear that matter was made of small neutral particles. J.J. Thompson first described the atom as a positively charged sphere embedded with negatively charged electrons, a model which became known as the "plum pudding". Then came Ernst Rutherford, whose "planetary model", proposed to explain the observed emptiness of matter[4], likened atoms to a miniature solar system, with electrons orbiting a central nucleus much like planets orbit the Sun. This analogy resonated due to its simplicity, perhaps explaining its enduring popularity in the depiction of atoms. However, this model failed to explain the stability of atomic structures and the quantization of their energy levels. It was known indeed that electron energies could only take some precise values, like the notes on a guitar, as opposed to the continuous range possible on a violin.

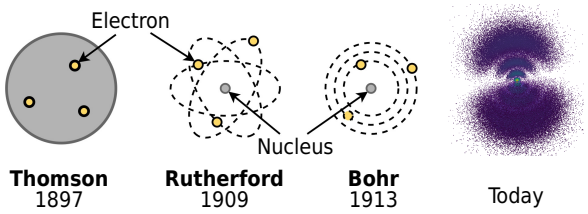

Figure 1: Some representations of the atomic structure. From [Bouscal and D'Ascoli 2022].

This question was solved with the advent of quantum mechanics which introduced groundbreaking concepts like wave-particle duality and quantum superposition. One of its founding fathers, Niels Bohr, proposed a quantized planetary model, where electrons can hop from one orbit to the next with discrete energy jumps. The last image of Fig. 1 proposes a more precise depiction of a single electron in an atom[5]: each point represents a position where the electron *might* be, we don't where until we measure exactly its position. This cloud of probabilities is called an orbital. When an electron gains energy, the cloud changes shape and gets further away from the nucleus.

[4] If a nucleus was the size of a marble, the electrons would be orbiting kilometers away from it.

[5] For an online, interactive visualizer see: https://asliceofcuriosity.fr/assets/atom/orbitalsApp-1M.html

Light to make the jump

What happens when an electron jumps from one orbital to another? It emits or absorbs light. But not any light, it has to be a single photon which has an energy exactly matching the jump. Indeed, photons are elementary particles of light carrying an energy proportional to their frequency. Isaac Newton was the first to think of light as a particle. Quickly contradicted by Christian Huygens and interference experiments, it seemed clear at the end of the 19th century, that light was not a particle but a wave, like sound or tides. Maxwell had even written wave equations describing it! But Einstein, working at that time as a patent officer in Bern, realized that this depiction was not sufficient to explain all experimental observations, and that light had to be made of particles.

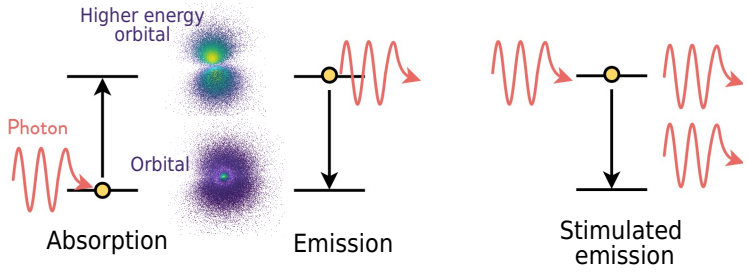

Figure 2: The three different processes of interaction between photons and atoms. Two electronic orbital of different energy are shown in blue.

This particle was eventually called *photon*. Einstein wrote three different processes under which atoms can climb up or down the orbital ladder, summarized in Fig. 2. An atom can absorb or emit a particle of light at the right energy, and its electron subsequently goes up or down one orbital. More subtle, stimulated emission happens when a photon of the right color is sent on an excited atom: this triggers the emission of an identical photon. Like sheep, photons have a gregarious instinct. This is the effect is harnessed in lasers, which emit pure light made of identical photons.

Combining light and matter for quantum information

Bohr eventually reconciled the dual nature of light, stating it was both a wave and a particle. Like a wave, it is subject to diffraction and cannot be focused to an infinitesimal point, which makes it a challenge to force light to interact with almost point-like atoms. The probability of an atom absorbing a photon is reduced when the light spans a region much larger than the atom itself. This is what we observe, as it is hard experimentally to make an atom absorb a single photon.

Pioneering experiments have tried to get rid of this limitation by putting a single atom in between two mirrors, so that the photon would travel back and forth until being absorbed, with great success. Another idea is to try to focus more the light, or to make it interact longer with the atom. The platform described in this thesis tries to do both at once. We use a nanoscale structure that guides the light, confining it a lot, making it more focused while slowing it down. We then want to approach atoms so that they can interact more efficiently.

Why design such complicated experiments, one might ask? The aim can be to observe the light-matter interaction at the most fundamental level and to master the manipulation of matter's individual components. The implications of such control are vast, with the potential to employ atoms as quantum bits for computation or to delve into the exploration of physical phenomena that defy intuition.

Goal of this work

Light-matter interaction is at the heart of new technologies from the so-called second quantum revolution. Quantum computers, simulators and, even more, networks all rely at some point on the transmission of information from static qubits (atoms, superconducting qubits, molecules, quantum dots..) to flying qubits. For the exchange of information to be efficient, the interaction between light and matter has to be as efficient as possible. This is usually limited by both the cross section of the emitter considered and diffraction. Methods have been pursued to increase this interaction rate, first with cavities and more recently with nanoscopic waveguides, establishing the field of Waveguide QED. While cavities ensure a unity interaction probability, waveguides have other interesting capabilities. They can allow many emitters to be in the same electromagnetic environment, making them suitable to explore collective effects, while being able to be directly integrated into a network. Pioneering experiments in waveguide QED with cold atoms were done with optical nanofibers. Because of their very small diameter, guided modes have a substantial part of their energy into the air as an evanescent tail. Atoms can be coupled with 1% efficiency to this mode. More recently, groundbreaking experimental attempts have started using slow-mode photonic-crystal waveguides to this end.

The experiment detailed in this PhD work pursues this quest of coupling efficiently atoms to slow-mode waveguides. It aims at bridging the gap between two communities: cold atoms and nanophotonics. On the one hand, atoms hate surfaces, as their proximity makes them fall in the realm of chemistry. On the other hand, nanophotonics are more studied for their light-guiding properties in the infrared range. This thesis deals with theoretical work to define clearly the figures of merit of the interaction in this regime, numerical simulations to design realistic photonic-crystal waveguides that can be suited to interface in a cold atom experiment, and experimental work in building such experiment and developing a toolbox to get the atoms to the waveguide surface.

Context

I started my PhD in the Quantum Networks Team in October 2019, under the supervision of Prof. Julien Laurat, with the task to build a cold atom experiment from scratch in order to welcome slow-mode waveguides whose guided modes would be interfaced with cold Rubidium atoms. Groundbreaking work by the group of Jeff Kimble had shown this was a possible [Goban et al. 2014; Yu et al. 2014; Hood et al. 2016; Burgers et al. 2019], yet extremely challenging task. There was an opportunity to join this adventure building from all the knowledge they had accumulated[6] and Julien's connection with their team. In addition, the Paris area had all necessary partners for this ambitious research. The ANR Nanostrong project was carried out in collaboration with a theory team at Institut d'Optique for the design of the waveguides (led by Christophe Sauvan and Jean-Jacques Greffet) and a team at Centre des Nanosciences et Nanotechnologies (C2N), led by Kamel Bencheikh and Ariel Levenson, expert at design and fabrication of nanophotonic structures for quantum optics, while LKB had to build the cold atom setup. Instead of Cesium, we chose Rubidium for its reduced reactivity and the existence of integrated lasers at 780 nm which can jumpstart the setting up of a cold atoms experiment.

Simultaneously, I joined after Alban Urvoy, who had arrived as a postdoc, and had the task to supervise this project. Building an experiment from scratch is a challenge,

[6] The Caltech work had stopped following the retirement of Jeff Kimble.

and starts very slowly. After some design and the delivery of the integrated laser we could start building it at the very start of 2020. Then, something happened.

I used the many lockdowns to switch gears and try my hand at more numerical work. Indeed, there was an idea of the kind of waveguide we wanted to use (a W1 waveguide) from the beginning of the project but it still needed to be designed. I delved into the simulations (choosing to focus on a half-W1 instead), from dispersion engineering of photonic crystals, to optical dipole trap simulations, to work on the Casimir-Polder interactions. The assembly of the vacuum system was delayed to the end of 2020, and a MOT was obtained by September 2021. Work carried in parallel concerned setting up of the experimental control, the interfacing of the SLM (thanks to Anaïs Chochon who joined for a M1 internship in the spring), while continuing the work on simulations. This latter work led to the release of a Python package with Jérémy Berroir [Berroir et al. 2022], and later, the proposal for the half-W1 and comb waveguides [Fayard et al. 2022; Bouscal et al. 2024].

In October 2022, Anaïs Chochon joined as a PhD student to eventually take the lead on the experiment. She worked very hard to achieve a more stable and optimized platform, ready to welcome our first tweezers.

Outline of the thesis

This thesis is organized into seven chapters.

- **Chapter 1** provides an introduction to the emerging field of Waveguide QED, highlighting the recent proposals and reviewing the existing experimental implementations combining emitters and guided waveguide modes.
- In **Chapter 2** presents a theoretical study of the coupling between emitters and resonant 1D guided modes with a Green's function approach. An expression of the Purcell factor adapted to realistic multilevel atoms (like Rubidium) is derived.
- **Chapter 3** still focuses on atom-light interaction but far-off resonance, used for optical dipole trapping. We focus on the challenges of trapping atoms close to structures and introduce a user-friendly Python package `nanotrappy`, that we test on different existing evanescent traps.
- **Chapter 4** introduces photonic crystals and explain how they can be used as waveguides. Numerical methods for simulating and designing band structures are presented, alongside criteria that photonic-crystals waveguides need to verify to be interfaced with cold atoms.
- **Chapter 5** provides the main results obtained in the design of three nanoscopic waveguides made in GaInP, suitable for our platform and optimized for robustness against fabrication imperfections. Fabrication methods and characterization of the obtained samples is detailed.
- **Chapter 6** describes the building of the cold atom experimental platform. It delves into the design of an experiment suited to interface both cold atoms and photonic-crystal waveguides and shows first results on the obtention of a cold atomic cloud.
- Finally, **Chapter 7** presents an ongoing improvement of the setup to be able to deliver single atoms to the sample with structured optical tweezers relying on higher-order Laguerre-Gaussian modes.

Part I:

Atom-light interaction and Waveguide QED

Theory will only take you so far.
Oppenheimer (2023)

CHAPTER 1

WAVEGUIDE QED: A NOVEL APPROACH FOR ENGINEERING LIGHT-MATTER INTERACTION

Contents

This first chapter aims at introducing the recent field of Waveguide QED, providing context and motivation for the experimental work described throughout this dissertation. We first highlight that coupling single emitters to the guided mode of a waveguide can be a way of enhancing the interaction between light and matter while suppressing the need for a cavity. More importantly, we introduce unique collective effects that can be probed and quantum optics protocols that can be implemented with a chain of emitters coupled to waveguides. A short review on the existing experimental platforms closes the chapter.

1.1 The quest for stronger atom-light interaction

Decades of outstanding research in atomic physics and quantum optics have allowed to manipulate and control light and atom-like systems (i.e. atoms and other systems with discrete transitions) to unprecedented levels. The main challenge to implement quantum information processing protocols is that most require interfacing these two. The goal is worth pursuing as exciting features can arise from realizing such atom-light interfaces.

From a quite fundamental perspective, these interfaces are captivating because they can induce non-linear interactions between photons — interactions that do not

exists naturally [Chang et al. 2014b]. This feature may allow for the implementation of photon-photon gates, single-photon switches and transistors, and the formation of exotic states of light. On a more applicative side, the interfaces between atoms and light are critical components for constructing quantum networks. Such networks are envisioned to facilitate the distribution and manipulation of quantum information at continental scales, for quantum computing, cryptography and more. As anticipated by Jeff Kimble [Kimble 2008], quantum networks are expected to be built around the exchange of quantum states between static nodes (atoms, ions, solid state systems...) and travelling ones (photons). Atoms are great candidates as a static interface as they can sometimes be approximated by perfect non-linear two-level systems (TLS) which *naturally* produce quantum Fock states of light when decaying from their excited level.

Unfortunately, promoting an atom into an excited state, i.e. implementing coherent atom-photon interaction is fundamentally inefficient. Indeed, the probability of interaction between an atom and resonant light is given by:

$$P = \frac{\sigma_{\text{sc}}}{A_{\text{eff}}} \tag{1.1}$$

where σ_{sc} is the resonant scattering cross section of the atom and A_{eff} the effective mode area of the incoming light. For an ideal two-level atom with energy gap $\Delta E = hc/\lambda$, $\sigma_{\text{sc}} = 3\lambda^2/2\pi$. More generally, the following relation applies:

$$P \propto \frac{\lambda^2}{A_{\text{eff}}}. \tag{1.2}$$

Even at the focus of a lens with high numerical aperture, the relevant size of the beam cannot be lower than the wavelength because of diffraction[1], which imposes a strong limit on the maximum probability achievable. A few strategies have been developed over the years to try to increase this interaction as much as possible.

Strong focusing. The mode area of a laser in free space can be strongly decreased by using high numerical aperture optics. Using such optics to focus a resonant laser on a single trapped atom has shown promising results in pioneering experiments [Darquié et al. 2005; Tey et al. 2008]. With this approach, it was shown that a single atom could attenuate the transmission of the light by up to $P \simeq 10\%$, without the need for a cavity. More recently, a probability of 36% has been demonstrated [Chin et al. 2017] by using two opposing lenses with coinciding focal points illuminated by two counter-propagating parts of the field simultaneously. In this configuration, inspired from 4Pi microscopy, the solid angle covered by the input mode is doubled, increasing the interaction strength by as much. The main limitation of this method is scaling up, as only the single atom in the focal spot can have his local density of states increased.

Atomic ensembles. Another approach in free space is to increase the number of scatterers the light can interact with [Hammerer et al. 2010]. It is possible to completely attenuate an incident beam impinging on a cold atomic ensemble. Indeed, by modelling the cloud as a vapour of atoms with a density n, each one acting as

[1] Sending a plane wave through a lens gives a Airy spot of diameter $d = 1.22\lambda/\text{NA}$, where the numerical aperture of the lens $\text{NA} = n \times \sin\theta$, is at maximum of the order of 1. The prefactor 1.22 comes from the first zero of the first order Bessel function J_1 which appears when taking the Fourier transform of a circular aperture (here the lens) [Born and Wolf 1999]. This gives an upper limit on the effective mode area $A_{\text{eff}} \leq 1.17\lambda^2/\text{NA}^2$ and so $P \propto 1.17\,\text{NA}^2$.

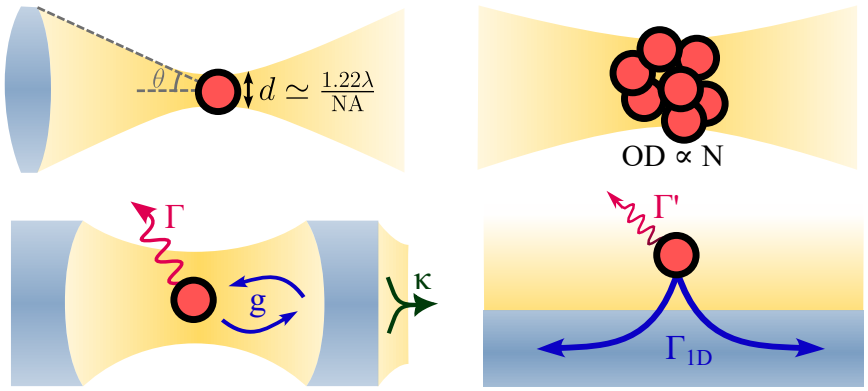

Figure 1.1: Four ways of enhancing the light-matter interaction probability. (a) Strong focusing of a laser on an atom with a high numerical aperture lens. d is the typical diameter of the focused beam. (b) Using multiple emitters. For an atomic ensemble, the relevant figure of merit is the optical depth, proportional to the number of atoms interacting with the field. Loss a priori of the non-linear behaviour of the interaction. (c) Cavity QED system with a single atom. The important parameters needed to define the cooperativity C are represented (g coherent coupling to the cavity mode, Γ atom decay outside of the cavity, κ loss of the mode by the mirror). (d) Waveguide QED system: emission in (Γ_{1D}) and out (Γ') of the waveguide mode. The mode transverse size can be very small.

a independent particle with an absorption cross section σ_{sc}, the Beer-Lambert law states that the transmitted light exponentially decays with the optical depth (OD), which is proportional to the atomic density n and σ_{sc}. A drawback of using atomic ensembles is that the addition of many atoms tends to blur the intrinsic non-linearity of the absorption process. Atomic ensembles are used in our team to achieve a high-efficiency quantum memory and for single-photon generation using the non-linear Duan-Lukin-Cirac-Zoller (DLCZ) protocol [Vernaz-Gris et al. 2018; Cao et al. 2020]. In clouds with higher density, collective effects can further increase the coupling to the field. In the multiple excitation regime, reached by inverting a substantial number of atoms, superradiance can be observed in dense atomic clouds, smaller than the transition wavelength [Ferioli et al. 2021, 2023]. For a dilute cloud, the collective mode decays at the rate of a single atom as they are independent. But in the dense case, the decay is enhanced by the number of atoms. This is due to interference processes, as the scattered field by one atom will act on the neighboring ones [Dicke 1954]. In such scenarios, the atomic density that can be reached by cold atoms experiments is the main limitation.

Cavity QED. The most common approach to enhance the atom-light interaction consists in placing an atom into a high-finesse optical cavity. The mode area of the cavity field is given by the cavity design, but the interaction probability is enhanced by the finesse, proportional to the number of round trips the photon makes before being lost. In such a configuration, the interaction probability P is not relevant anymore as it goes to unity. The cooperativity C becomes the new relevant figure of merit, defined as:

$$C = \frac{2g}{\kappa\Gamma} \tag{1.3}$$

where g is the coupling to the cavity mode, κ its loss rate and Γ the spontaneous decay rate of the atom (see Figure 1.1(c)). C is related to the number of exchange

processes between the cavity field and the atom before loss of the photon or atom decoherence. A high cooperativity is then given by a lossless cavity with a very small mode area. The regime of strong coupling (for $C \gg 1$) can be achieved, a hallmark of which is the observation of vacuum Rabi splitting [Thompson et al. 1992]. Of course, these ideas are not platform-dependent and cavity QED (cQED) systems are not restricted to single atoms in optical cavity, but include Rydberg atoms in microwave cavities [Gleyzes et al. 2007], Rydberg ensembles in optical cavities [Vaneecloo et al. 2022], trapped ions in optical cavities [Stute et al. 2012], superconducting qubits coupled to microwave resonators [Wallraff et al. 2004], atoms coupled to photonic-crystal cavities [Thompson et al. 2013] or microresonators [Aoki et al. 2006a] and even optomechanical systems [Aspelmeyer et al. 2014]. From a fundamental goal to control single quantum systems, cavity QED systems now offers strong promises in the field of quantum networks [Reiserer and Rempe 2015; Welte et al. 2018; Krutyanskiy et al. 2023], as potential quantum nodes, allowing to convert information encoded on flying qubits into static, material ones, over a large scale network. However these systems naturally offer limited bandwidth, suffer from insertion losses and scaling up is a daunting task.

Waveguide QED. An emerging idea for interaction enhancement is to couple the emitters to the guided mode of a nanoscale waveguide, instead of a cavity. Because of the sub-wavelength size of the waveguides involved, mode areas close to the diffraction limit can be achieved. At resonance, the probability of interaction can now be expressed as:

$$\frac{\Gamma_{1D}}{\Gamma_{tot}} \propto n_g \frac{\lambda^2}{A_{eff}} \tag{1.4}$$

where Γ_{1D} is the decay rate of the atoms in the guided mode, and Γ_{tot} the total spontaneous decay rate of the atoms in the same environment. n_g is the group index of the guided mode the emitters are coupled to. Both A_{eff} and n_g can be tuned by playing on the waveguide geometrical parameters. This ratio known as the β factor will be introduced in Chapter 2. Usual Waveguide QED systems do not allow for a coupling as strong as with cavities, as the photons interact with the emitters only once. A fundamental difference with cQED is that Waveguide QED systems are intrinsically open systems. The propagating photons lost at the output of the fiber are not counted as a loss term (as κ in cQED), but as an open photonic reservoir the atoms can couple to. Furthermore, we note that this coupling is broadband, as it arises purely from geometrical considerations as opposed to any resonant features of the guided modes (unlike for cQED). The main advantage of these systems are that many emitters can easily be coupled to the same propagating mode [Chang et al. 2018; Türschmann et al. 2019; Sheremet et al. 2023], easing the scaling up process as they will all experience the same coupling to this mode (i.e. same β factor). This feature, combined with a high β, allows for engineering of collective modes. This thesis focuses on this last strategy and we introduce its promises and applications in the following.

1.2 The emergence of Waveguide QED for quantum nonlinear optics

1.2.1 An emerging field of research

While cavity QED systems have shown atom-light interaction enhancement since the early 1980s [Goy et al. 1983], first theoretical proposals to interface emitters and waveguide modes were only published in the 1990s. [Ol'Shanii et al. 1993] proposed for example to couple atoms to the mode of a hollow-core optical fiber by guiding the atoms inside it with a red-detuned mode. While groups successfully managed to transport cold atoms through photonic-crystal fibers in 2010 [Vorrath et al. 2010; Bajcsy et al. 2011], the first experimental observation of the coupling of emitters to a waveguide was achieved in the late 2000s [Sagué et al. 2007] with cold atoms coupled to optical nanofibers (ONF) [Nieddu et al. 2016]. Indeed ONFs had become over the years a more popular and realistic platform since a protocol to get atoms trapped around ONFs was proposed in 2004 [Balykin et al. 2004]. Since then, many experimental platforms have demonstrated successfully coupling of emitters to guided modes of a waveguide as discussed in the following. Apart from the promised enhancement of light-matter interaction through low mode areas or high group indices, Waveguide QED systems offer some specific advantages.

A first interest of Waveguide QED systems in the optical domain using nanophotonics waveguides is their integrability. After interaction with the atoms, the desired state of light can be collected at the output of a fiber. This state can directly be brought to anywhere it is useful through the fiber (like to a quantum computer) for subsequent processing.

A second interesting feature of these systems is that waveguides can have non trivial dispersion diagrams. Photonic band gaps might exists, impeding the light propagation in the waveguide in some frequency ranges (as we will see in Chapter 4). This behaviour can be harnessed in order to create exotic states of light. As such, since the early 2000s an important number of theoretical proposals as well as pioneering experiments have emerged in order to take advantage of this promising avenue of Waveguide QED.

In the following we distinguish three regimes for the Waveguide QED proposals and experimental setups (see Figure 1.3):

- **Single-atom coupling enhancement:** Only one emitter is coupled to the waveguide mode, with an interaction probability much larger than in free space.
- **Physics in the band:** An array of emitters is coupled to a guided mode for the waveguide at their resonant frequency.
- **Physics in the band gap:** The resonant frequency of the emitters lies within the band gap of the waveguide.

1.2.2 Single atom coupling enhancement: a single atom in an open system

We detail in the following the coupling of a single emitter to a guided mode. We then show how an enhancement of this coupling can be of significant interest in quantum optics and quantum information by presenting some theoretical proposals.

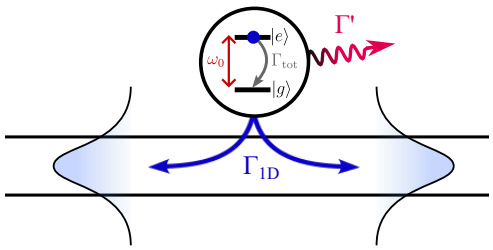

Figure 1.2: Coupling of a single atom to a guided mode. The atom is modeled as a TLS with a ground $|g\rangle$ and excited state $|e\rangle$ separated by ω_0. Of the total decay rate Γ_{tot} from $|e\rangle$, some part is emitted into the guided mode $\Gamma_{1\text{D}}$, the rest into a continuum of radiative modes Γ'.

The Hamiltonian of a TLS with states $|g\rangle$ and $|e\rangle$ separated by ω_0 and strongly coupled to a set of travelling waveguide modes is given by [Chang et al. 2007]:

$$\mathcal{H} = \hbar(\omega_0 - i\Gamma'/2)\sigma_{ee} + \int_{-\infty}^{+\infty} dk\omega_k a_k^\dagger a_k - \hbar\int_{-\infty}^{+\infty} dk g_k \left(\sigma_{eg}\hat{a}_k e^{-ikx} + h.c.\right) \quad (1.5)$$

where $\sigma_{ij}^j = |i\rangle\langle j|$ is the atomic coherence operator between the states $|i\rangle$ and $|j\rangle$, $\hat{a}_k$ is the annihilation operator for the mode with wave vector k and x is the emitter position along the waveguide. This Hamiltonian differs from the Cavity QED one in the sense that each atom can couple to a continuum of modes. This system can be described by a master equation with a Lindblad operator accounting for the loss of the photons in the environment. Here, the quantum jump due to the decay of state $|e\rangle$ at a rate Γ' into the other channels is included as the non-Hermitian term in $\mathcal{H}$. The last two terms describe the photonic field energy and the coherent exchange between the atom and the field (summed over the continuum of modes).

For $\Gamma_{1\text{D}}/\Gamma_{\text{tot}} \approx 1$, a TLS in its ground state coupled to such a mode at resonance will behave as a nearly perfect mirror for a single photon. But as absorption is a highly non-linear process, the atom will saturate right above the single photon regime. This effect can be harnessed in order to realize a single-photon transistor [Chang et al. 2007]. If two photons impinge on the atom at the same time, this will generate time-frequency entanglement between the scattered two-photon component [Le Jeannic et al. 2022]. As such, a single atom coupled to a waveguide can strongly modify the statistics of incoming light and create non classical states of light. As an example, in the case of an atom coupled to a low intensity mode, the reflected light will show strong antibunching, while the transmitted one will be bunched. Other theoretical proposals propose to use this non-linear interaction for stimulating emission [Rephaeli and Fan 2012], generating squeezed states [Kusmierek et al. 2023], Fock states photon sorting [Yang et al. 2022] or creating photonic bound states [Shen and Fan 2007].

Interestingly, most of these results hold even for weak coupling, and high dissipation, as long as a sufficient number of atoms is involved [Mahmoodian et al. 2018]. Nanofiber-based platforms fall into this regime as they can trap many atoms but with a $\beta < 1\%$. They can be interesting platforms for observing such low-power non-linear effects even at limited Purcell factor.

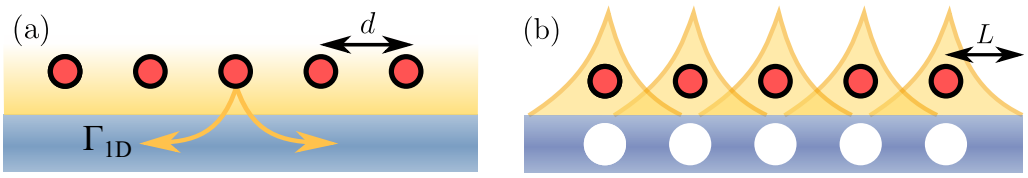

Figure 1.3: Two regimes of interaction of a 1D atomic array coupled to a waveguide. (a) Array of atoms coupled to a guided mode (with evanescent part in yellow) with individual decay rate Γ_{1D} into this mode. An all-to-all infinite-range interaction between the trapped atoms is mediated by the light. (b) Array of atoms in the case where their transition frequency falls within the band gap of a 1D photonic crystal. Atom-photon bound states form, leading a coupled cavity system with a finite interaction length L with can be tuned with the detuning to the band edge.

1.2.3 Physics in the band: Harnessing collective effects for quantum information processing

As emphasized by Philip W. Anderson, "More is different". This also applies for a few particles trapped in a 1D array close to a waveguide. Increasing the number of particles does not only compensates the relatively low coupling achievable in most platforms with higher atom number but also leads to new, interesting physics of collective effects.

We review in the following the theoretical proposals set in the situation of array of atoms coupled to a guided mode of a nanoscale waveguide (Fig. 1.3(a)). We adapt Hamiltonian (1.5) for the case of a linear chain of ideal TLS coupled to a waveguide by summing the first and third terms over the atom number N. This Hamiltonian can be heavily simplified by tracing out the photonic modes and only keeping the dynamics of the atomic degrees of freedom. This reduces to the so-called spin model [Asenjo-Garcia et al. 2017b] where the dynamics of the atomic spins are given by:

$$\mathcal{H} = \hbar\omega_0 \sum_i^N \sigma_{ee}^i + \mathcal{H}_{\text{eff}} \quad \text{with} \quad \mathcal{H}_{\text{eff}} = \sum_{j,l} f(\mathbf{r},\omega)\sigma_{eg}^j \sigma_{ge}^l \tag{1.6}$$

$\mathcal{H}_{\text{eff}}$ is the spin-flip interaction Hamiltonian between the atoms mediated by the guided mode. As we will see in the next chapter, this function $f(\mathbf{r},\omega)$ is directly related to the Green's function of the environment. For a non-absorptive waveguide, this function is usually constant or periodic in the atom positions and does not decay with the distance between the atoms. In this case, as the sum in Eq.(1.6) runs over all atoms, there is then an **all-to-all** interaction between the spins mediated by the photonic mode they couple to. We are left with a spin-flip Hamiltonian between the atoms with infinite range. This interaction can be harnessed for multiple applications.

Theoretical proposals have been put forward in the last 10 years to exploit this rich all-to-all Hamiltonian, from spin squeezing of the coupled atoms for quantum non demolition [Qi et al. 2018] to obervation of directional superradiance [Cardenas-Lopez et al. 2023].

Instead of harnessing this photon-mediated interaction, some older theoretical proposals suggest to exploit the fact that each coupled atom behaves as an independent scatterer that will reflect some part of the light. By tuning their distance, all the reflected light can interfere constructively, making the chain behave as a perfect mirror [Artoni et al. 2005].

1.2.4 Physics in the band gap: Towards quantum simulation and computing

If the guided mode falls into a band gap, the atoms cannot couple to a propagative mode and instead act as localized cavity modes (see Fig. 1.3(b)). We can derive the band gap Hamiltonian from the Jaynes Cummings one [Douglas et al. 2015]:

$$\mathcal{H}_{\text{eff}} \propto \sum_{j,l}^{N} \sigma_{eg}^{j} \sigma_{ge}^{l} e^{(|z_j - z_l|/L)} \tag{1.7}$$

where the distance $L \propto \sqrt{1/\Delta}$, where Δ is the detuning of the atomic transition frequency ω_0 from the band edge. The closer the frequency is from the band edge, the closer it is to the propagating regime, hence giving a longer range of interaction. L can be tuned by changing this detuning. This could be done dynamically through local modification of the dispersion of the waveguide via heating or electronic tuning [Panuski et al. 2022].

The main difference with the former case is the exponential decay with the distance of the interaction between the atoms and its tunability. This makes this Hamiltonian fall into a whole new class of nearest-neighbors-like, as the atom dressed with this localized field can be seen as a cavity system. The whole chain can then be mapped to a coupled cavities system valued by theoreticians. Theoretically predicted since the 1990s [Kurizki 1990], it is only recently that the interest of these atom-photon bound states in quantum technologies have been highlighted. They could indeed be used for quantum simulation of such Hamiltonians [Douglas et al. 2015] or to engineering topological states of the atomic excitation [Bello et al. 2019]. A more recent proposal shows that using such atom-photon bound states as a variational ansatz could provide some computational advantage in variational quantum computing over conventional methods [Tabares et al. 2023].

1.2.5 A zoology of pioneering experiments

While many theoretical proposals exist to harness the capabilities of Waveguide QED, a polyvalent platform combining arrays of quantum emitters and guided modes in the strong coupling regime has yet to be demonstrated. Nevertheless, some pioneering experiments are pursuing these goals, in a wide range of physical systems. We briefly describe the most notable efforts in the following.

Cold atoms coupled to nanofibers. The first experimental realization of Waveguide QED platforms dates back to the early 2010s in tapered fibers with interfaced cold atoms. Pioneer experiments created MOTs around such suspended nanofibers, before being able to trap them in 1D arrays [Vetsch et al. 2010; Goban et al. 2012], giving more striking results. As the oldest Waveguide QED platform with atoms, many different collective phenomena have been explored experimentally like Bragg reflection switched by a few photons [Berroir 2022], collective excitations delocalized over the whole array [Corzo et al. 2019], directional superradiance [Liedl et al. 2023], quantum memory protocols [Gouraud et al. 2015] or dissipation-assisted photon bunching [Prasad et al. 2020]. The main limitation of this platform is its relatively low β factor usually just below 1%. Equation (1.4) tells us this quantity is given by the group index of the guided mode, close to 1 in a nanofiber, and the mode area, determined by the diameter of the ONF [Gouraud 2016; Berroir 2022], leaving no tunable parameter left to increase β in this setup.

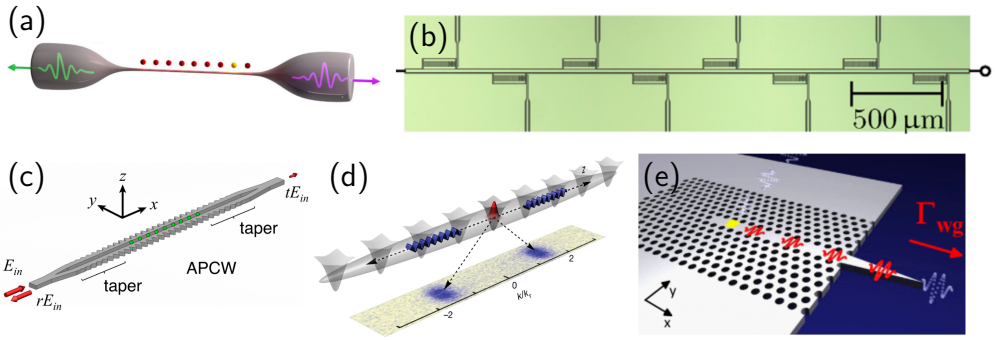

Figure 1.4: Existing experimental Waveguide QED platforms. (a) 1D array of cold atoms trapped along a nanofiber [Corzo et al. 2019]. (b) Superconducting qubits coupled to a transmission line [Brehm et al. 2022]. (c) Cold atoms coupled to the "Alligator photonic crystal waveguide" (APCW) [Goban et al. 2015]. (d) Rubidium atoms as a matter-wave emitter trapped in a 1D optical lattice working as a structured waveguide for atoms [Krinner et al. 2018]. (e) Quantum dot embedded in a W1 photonic-crystal waveguide [Arcari et al. 2014].

Superconducting qubits coupled to transmission lines. Waveguide QED systems have been implemented in solid state physics systems early on as it is usually possible to embed an emitter exactly at the maximum of the field, which can allow for almost unity β factor. In the field of superconducting (SC) qubits, the superradiant and subradiant decays of two emitters have been observed [van Loo et al. 2013], and slow microwave light has been highlighted in a chain of superconducting qubits coupled to a transmission line, exhibiting the non trivial structure of the waveguide dispersion relation [Brehm et al. 2022]. The main constraint is here nanofabrication which limits the indistinguishability between the emitters.

Quantum dots coupled to photonic-crystal waveguides. Almost the same advantages and limitations apply for quantum dots (QD) systems in optical waveguides. Near unity coupling as been reported in this system years ago [Arcari et al. 2014], making it possible to observe two-photon non-linear dynamics like photon-sorting [Le Jeannic et al. 2022]. It has however been extremely challenging to observe collective effects between the quantum dots as they are usually quite different and dephase really fast. Coherent exchange has been observed recently in this platform with states exhibiting sub- and superradiant behaviors [Tiranov et al. 2023].

Matter waves coupled to a 1D optical lattice. Some experiments have reversed the paradigm of coupling emitters of light to photonic modes. Instead, in [Krinner et al. 2018] atomic waves emit atoms in a given k vector. The emitted atoms are constrained in a 1D optical lattice. This periodic potential changes the dispersion relation of the atoms (from the quadratic $\omega = \hbar k/2m$) and opens a band gap. For a specific set of parameters, the matter wave will emit atoms in the band gap of the optical lattice, giving analogues of the atom-photon bound states described in Sec. 1.2.4. These bound states, characteristic of a emitter-waveguide coupling in the band gap have been observed for the first time in this matter-wave system.

Cold atoms coupled to photonic-crystal waveguides (PCW). Finally, the platform developed in this thesis has had only one previous experimental trial in the group of Prof. Jeff Kimble at Caltech, and took the form of cold cesium atoms coupled to a quasi-1D photonic-crystal waveguide nicknamed the Alligator PCW (APCW). Superradiant decay was observed for atoms in a surrounding MOT [Goban et al. 2014; Yu et al. 2014] or trapped at the vicinity of the crystal by external light fields [Goban et al. 2015]. They also observed signs of cooperative-only interactions between atoms just inside the band gap [Hood et al. 2016]. This pioneering work is the main inspiration of the experiment described throughout this thesis.

Other, even more exotic experiments fall in the range of Waveguide QED. We can think of a 2D atom array used as a mirror to be coupled to a single propagating mode that can go either forward (transmission) or backward (reflection) [Rui et al. 2020]. Similarly, cascaded Rydberg superatoms in an optical dipole trap can be described as emitters strongly coupled to a perfectly chiral waveguide [Stiesdal et al. 2021]. The Waveguide QED framework can help encovering interesting physics in such cases.

All the experimental platforms detailed previously are shown in Figure 1.4 and the observed collective effects summarized in Table 1.1.

Platform		Experimental results		
Emitters	Waveguide	β	Collective effect	Reference
Cold atoms	Nanofibers	0.01	EIT memory Delocalized excitation Superradiance Few-photon switching	[Gouraud et al. 2015] [Corzo et al. 2019] [Liedl et al. 2023] [Berroir 2022]
QD	W1 PCW	0.98	Superradiance	[Tiranov et al. 2023]
SC qubits	Transmission line	~ 1	Slow light Superradiance	[Brehm et al. 2022] [van Loo et al. 2013]
Matter waves	Optical lattice	~ 0.5	Atom-photon bound state	[Krinner et al. 2018]
Cold atoms	APCW	0.24 - 0.5	Superradiance Cooperative interactions in the band gap	[Goban et al. 2015] [Hood et al. 2016]

Table 1.1: Summary of the different experimental realizations of 1D array of quantum emitters coupled to the guided mode of a waveguide.

Conclusion

In conclusion, this chapter has provided a comprehensive overview of the emerging field of Waveguide QED, illustrating its fundamental principles and the possible applications it promises. The scope of Waveguide QED extends across the entire spectrum of quantum optics, with exciting uses in non-linear quantum optics, quantum simulation and quantum computing. Whatever the platform chosen, experiments are challenging and many technical barriers must be overcome in order to achieve a robust experimental platform interfacing array of emitters and guided modes. This is being pursued by many pioneering efforts, with already significant achievements.

More capabilities are unlocked when working with waveguides with a non-trivial dispersion relation. This, with a potential enhanced coupling, motivates the will to work with photonic-crystal waveguides in our experiment. We will in the following of this thesis only focus on the particular Waveguide QED platform that involves atoms interacting with such PCWs.

CHAPTER 2

ATOM-LIGHT INTERACTION CLOSE TO DIELECTRIC STRUCTURES

Contents

Whether it is for exciting atoms through the guided mode of a waveguide (see Chapters 5) or for optical trapping (see Chapters 3 and 7), this thesis main focus is on the interaction between light and matter.

In this chapter we introduce the formalism for describing this interaction **at resonance**, with an emphasis on the case where atoms are close to 1D waveguides, interacting with a guided mode. We first introduce the textbook atom-field interaction Hamiltonian between a classical field and a two-level system (TLS) alongside the concept of Purcell factor. The Green's function formalism is then presented in order to express the 1D Purcell factor, which quantifies the coupling of emitters to the guided mode of a waveguide, with mostly classical waveguide optics arguments. Finally, we extend our results to the more realistic case of a multilevel atom (Rubidium 87) in order to have expressions of the 1D Purcell factor that we can use in our experiment.

The aim is not to derive from scratch expressions that can be found in any textbook about light-matter interaction but to introduce notations and concepts relevant in this 1D geometry that we will use throughout the whole manuscript, while giving some intuition on the concepts.

2.1 Interaction between an electromagnetic field and a two-level system

2.1.1 The interaction Hamiltonian

Since this work deals mostly with the interaction of atoms with a radiation field either in or out of resonance, we start by introducing an usual model for the atom-light interaction, which can be found in many textbooks. We will follow the derivation from [Haroche and Raimond 2006]. We use a semi-classical approach, treating the field here as classical, and the atom as a perfect quantum two-level system.

The Hamiltonian of a free atom with a single valence electron is given by:

$$\mathcal{H}_0 = \frac{\mathbf{P}^2}{2m} + qU(\mathbf{R}) \tag{2.1}$$

where $\mathbf{P}$ and $\mathbf{R}$ are the momentum and position operators of the electron, and U the electrostatic potential binding the electron to the nucleus. We now place the atom in an electromagnetic field defined by its electric and magnetic fields $\mathbf{E}$ and $\mathbf{B}$, but more conveniently by its vector and scalar potentials $\mathbf{A}(\mathbf{r},t)$ and $V(\mathbf{r},t)$. By analogy to the classical Hamiltonian of a charged particle in an electromagnetic field we get:

$$\mathcal{H}_{\text{tot}} = \frac{1}{2m}(\mathbf{P} - q\mathbf{A}(\mathbf{R},t))^2 + qU(\mathbf{R}) + qV(\mathbf{R}). \tag{2.2}$$

By performing the dipole approximation ($A(\mathbf{R},t) \simeq A(0,t)$) and expanding the static potential to the first order in $\mathbf{R}$, the total Hamiltonian reduces to:

$$\mathcal{H}_{\text{tot}} = \mathcal{H}_0 - \frac{q}{m}\mathbf{P}\cdot\mathbf{A}(0,t) + \mathbf{D}\cdot\nabla V \tag{2.3}$$

where $\mathbf{D}$ is the dipole operator $\mathbf{D} = q\mathbf{R}$.

As only the fields $\mathbf{E}$ and $\mathbf{B}$ are physical quantities, we can add extra conditions on the potentials $\mathbf{A}$ and V if they don't modify the former. A clever gauge choice[1] reduces the total Hamiltonian to

$$\boxed{\mathcal{H}_{\text{tot}} = \mathcal{H}_0 - \mathbf{D}\cdot\mathbf{E}(0,t)} \tag{2.4}$$

Written like that, the interaction Hamiltonian between an atom and an electromagnetic field has the same form as the one between a classical dipole and an electric field, which aligns with the concept of an atom being a "quantum dipole".

2.1.2 The Purcell factor, a tool to quantify the interaction strength

During the first half of the 20th century, the spontaneous decay rate of an atom Γ, given by the Einstein's coefficient, was considered to be an intrinsic property of an atomic species. Edward M. Purcell established in 1946 that the emission of a magnetic dipole placed into a resonant cavity could be strongly enhanced [Purcell et al. 1946]. Similarly, it was demonstrated afterwards that this phenomenon also applied to quantum dipoles, e.g. atomic transitions, first by putting them very close to a mirror [Drexhage et al. 1968] or in an optical cavity [Kleppner 1981; Goy et al.

[1] i.e. the Goeppert-Mayer gauge, with $\chi(\mathbf{r},t) = -\mathbf{r}\cdot\mathbf{A}(0,t)$

$$\begin{cases} A' = A + \nabla\chi(\mathbf{r},t) \\ V' = V - \dfrac{\partial\chi(\mathbf{r},t)}{\partial t} \end{cases}$$

1983]. It is now well understood that the spontaneous decay rate of quantum emitters can be enhanced or suppressed [Asenjo-Garcia et al. 2017a] by engineering the electromagnetic environment surrounding these systems, on scales of the order of the wavelength.

With the advent of sophisticated nanofabrication techniques, it is now feasible to strategically position atoms or other quantum emitters within more complex structured environments such as photonic-crystal waveguides [Arcari et al. 2014; Goban et al. 2015] or plasmonic nanostructures [Su et al. 2019] in order to increase their emission or at the contrary obtain long-lived excited states.

The Purcell factor (PF) quantifies the change of the spontaneous decay rate of an emitter in the given environment compared to the one in free space:

$$\mathrm{PF} = \frac{\Gamma}{\Gamma_0} \tag{2.5}$$

In the following we will establish a general expression of the Purcell factor in terms of the impulsional response of a given electromagnetic environment (i.e. the Green's function) and then apply it to our specific case: a Rubidium atom coupled to a waveguide.

2.2 The Green's function formalism

2.2.1 The Green's function, or the environment response

The Purcell factor depends on the environment of the dipole. We introduce in this section the Green's tensor as it is a very convenient object to describe it. The Green's tensor $\overleftrightarrow{\mathbf{G}}(\mathbf{r}, \mathbf{r}')$ is essentially defined as the electric field $\mathbf{E}$ at the field point $\mathbf{r}$ generated by a radiating electric dipole $\mathbf{p}$ located at the source point $\mathbf{r}'$ (see Fig. 2.1). We will only consider classical dipoles unless specified otherwise. Most derivations come from Lukas Novotny's seminal book "Principles of Nano-Optics" [Novotny 2006].

To introduce the Green's function that describes the electromagnetic environment, we first need Maxwell's equations for an isotropic dielectric material. They are written as:

$$\begin{cases} \nabla \cdot \mathbf{D}(\mathbf{r}, t) = \rho_f(\mathbf{r}, t) \\ \nabla \cdot \mathbf{B}(\mathbf{r}, t) = 0 \\ \nabla \times \mathbf{E}(\mathbf{r}, t) = -\dfrac{\partial \mathbf{B}}{\partial t}(\mathbf{r}, t) \\ \nabla \times \mathbf{H}(\mathbf{r}, t) = \dfrac{\partial \mathbf{D}}{\partial t}(\mathbf{r}, t) + \mathbf{J}_f(\mathbf{r}, t) \end{cases} \tag{2.6}$$

where $\mathbf{D}$ is the electric displacement field, $\mathbf{B}$ the magnetic induction field, $\mathbf{E}$ the electric field, $\mathbf{H}$ the magnetic field, ρ_f the free charge density and $\mathbf{J}_f$ the free current density.

Going to frequency space (but staying in the real position space), we can derive the following wave equation, by considering propagation in a dielectric medium with a frequency- and space- dependent dielectric function $\epsilon(\mathbf{r}, \omega) = \epsilon_0 \epsilon_r(\mathbf{r}, \omega)$, with ϵ_0 the vacuum permittivity:

$$\nabla \times \nabla \times \mathbf{E}(\mathbf{r}, \omega) - \frac{\omega^2}{c^2} \epsilon(\mathbf{r}, \omega) \mathbf{E}(\mathbf{r}, \omega) = \mu_0 \omega^2 \mathbf{P}(\mathbf{r}, \omega) \tag{2.7}$$

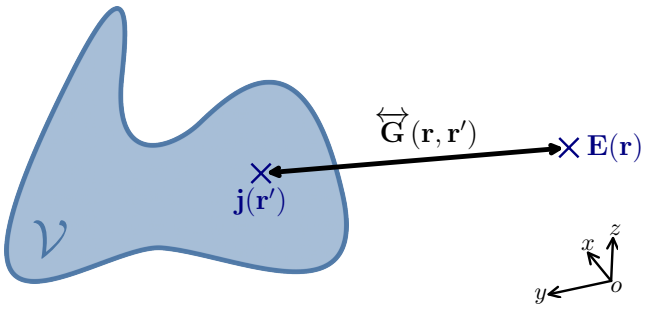

Figure 2.1: The Green's function gives the electric field at position r (in the coordinate system represented) created by a single point source j at position r′. Since both $\mathbf{E}$ and $\mathbf{j}$ are vectors, $\overleftrightarrow{\mathbf{G}}$ must be a second order tensor. To get the full electric field at $\mathbf{r}$, one needs to know $\overleftrightarrow{\mathbf{G}}$ for all $\mathbf{r}'$ in $\mathcal{V}$, the whole volume where the source density is non-zero.

where the polarization of the medium $\mathbf{P}(\mathbf{r},\omega)$ is defined as the primitive of the current density, hence $\mathbf{J}_f(\mathbf{r},\omega) = -i\omega\mathbf{P}(\mathbf{r},\omega)$ in frequency space. If we define the operator $\mathcal{L}_E := \nabla\times\nabla\times - \frac{\omega^2}{c^2}\epsilon(\mathbf{r},\omega)$, Eq. (2.7) reduces to finding the response of a linear differential operator $\mathcal{L}_E$:

$$\mathcal{L}_E\mathbf{E}(\mathbf{r},\omega) = \mu_0\omega^2\mathbf{P}(\mathbf{r},\omega). \tag{2.8}$$

Mathematically, the Green's function is defined as the impulse response of any linear differential operator. More precisely, it is the solution of this operator for a Dirac inhomogeneity $\delta(\mathbf{r}-\mathbf{r}')$, equal to 0 everywhere except for $\mathbf{r}=\mathbf{r}'$. As the polarization is a vector field, the impulse Dirac source has to be oriented in a direction. We have in fact a set of 3 linear independent equations to solve for each independent direction:

$$\mathcal{L}_E\mathbf{G}_i(\mathbf{r},\mathbf{r}',\omega) = \hat{\mathbf{e}}_i\delta(\mathbf{r}-\mathbf{r}') \tag{2.9}$$

where $\hat{\mathbf{e}}_i$ is a unit vector in a given basis. $\mathbf{G}_i(\mathbf{r},\mathbf{r}',\omega)$ is the electric field (vector of 3 components) generated by a Dirac excitation along $\hat{\mathbf{e}}_i$, at position $\mathbf{r}'$. We can summarize all three equations by introducing the Green's tensor $\overleftrightarrow{\mathbf{G}}(\mathbf{r},\mathbf{r}',\omega)$

$$\boxed{\mathcal{L}_E\overleftrightarrow{\mathbf{G}}(\mathbf{r},\mathbf{r}';\omega) = \mathbb{1}\delta(\mathbf{r}-\mathbf{r}')} \tag{2.10}$$

where $\mathbb{1}$ is the identity tensor. For each couple of positions $(\mathbf{r},\mathbf{r}')$, a 3×3 symmetric tensor is associated. The matrix element G_{ij} corresponds to the field component along $\hat{\mathbf{e}}_i$ at $\mathbf{r}$ created by a dipole source in $\mathbf{r}'$ oriented along $\hat{\mathbf{e}}_j$.

The main interest of this formalism is that knowing the response to an impulse is sufficient to reconstruct the response of the system to any source term in Eq. (2.8), i.e. to any density of polarization (see Fig 2.1). Indeed the solution of Eq. (2.7) for any $\mathbf{P}(\mathbf{r},\omega)$ can be written, thanks to linearity, as:

$$\mathbf{E}(\mathbf{r},\omega) = \mathbf{E}_0(\mathbf{r},\omega) + \mu_0\omega^2\int_{\mathcal{V}} d^3\mathbf{r}'\overleftrightarrow{\mathbf{G}}(\mathbf{r},\mathbf{r}';\omega)\cdot\mathbf{P}(\mathbf{r}',\omega) \tag{2.11}$$

with $\mathbf{E}_0(\mathbf{r},\omega)$ a solution to the homogeneous equation, that we will neglect in the following.

Let us consider a dipole at position $\mathbf{r}'$, with dipole moment $\mathbf{p}_0$. Taking the derivative of the dipole moment we find the current density $\frac{\partial \mathbf{p_0}}{\partial t} = \mathbf{j}dV$. For a homogeneous vacuum except for this dipole, the polarization density is given by $\mathbf{P}(\mathbf{r},\omega) = \mathbf{p}_0\delta(\mathbf{r}-\mathbf{r}')$. In this case, Eq. (2.11) reduces to:

$$\mathbf{E}(\mathbf{r},\omega) = \mu_0\omega^2 \overleftrightarrow{\mathbf{G}}(\mathbf{r},\mathbf{r}';\omega)\cdot\mathbf{p}_0. \tag{2.12}$$

Knowing the Green's function, it is trivial to compute the electric field created by any dipole. The two former expressions have the benefit of offering a practical way of computing fields numerically for any polarization density. As we will see in Chapter 4, dipole simulations are usually carried out to compute the Green's function. With a single simulation with a dipole at position $\mathbf{r}'$ along $\hat{\mathbf{e}}_j$, we can record the total electric field produced and compute three components of the Green's tensor at once:

$$G_{ij}(\mathbf{r},\mathbf{r}') = \frac{E_i(\mathbf{r},\omega)}{\mu_0\omega^2 p_j}, \quad i\in\{x,y,z\}. \tag{2.13}$$

2.2.2 Expressing the Purcell factor in terms of the Green's function

The Purcell factor is strongly dependent on the electromagnetic environment. In the following, we derive an expression for the Purcell factor involving $\overleftrightarrow{\mathbf{G}}(\mathbf{r},\mathbf{r}';\omega)$.

Power emitted by a classical dipole in a given environment

We consider an oscillating dipole $\mathbf{p}$ in an arbitrary electromagnetic environment. A standard result in classical electrodynamics states that in a given volume $\mathcal{V}$ (enclosed by a surface $\mathcal{S}$), the change of the total electromagnetic energy density $\mathbf{W}$ of the system is only caused by the interaction between the electric field and the "matter" (represented by the current density $\mathbf{j}$). It is also equal to the integrated flux of the time-averaged Poynting vector $\langle\mathbf{\Pi}\rangle = \frac{1}{2}\mathrm{Re}\{\mathbf{E}\times\mathbf{H}^*\}$ out of this volume, i.e. the radiated flux by the sources:

$$\frac{dW}{dt} = P_{\mathrm{rad}} = -\frac{1}{2}\int_{\mathcal{V}}\mathrm{Re}\{\mathbf{j}^*\cdot\mathbf{E}\}d\mathcal{V} \tag{2.14}$$

$$= \int_{\mathcal{S}}\langle\mathbf{\Pi}\rangle\cdot\mathbf{d}\mathcal{S}. \tag{2.15}$$

Recalling $\mathbf{j}(\mathbf{r},t) = \frac{\partial\mathbf{p}(t)}{\partial t}\delta(\mathbf{r}-\mathbf{r}')$ for our simple case with a single emitting dipole, Eq. (2.14) gives the following important expression linking the radiated power and the field at the position of the dipole:

$$P_{\mathrm{rad}} = \frac{\omega}{2}\mathrm{Im}\{\mathbf{p}^*\cdot\mathbf{E}(\mathbf{r}')\}. \tag{2.16}$$

When replacing $\mathbf{E}$ with its expression in terms of the Green's tensor from Eq. (2.12), we obtain:

$$\boxed{P_{\mathrm{rad}} = \frac{\mu_0\omega^3|\mathbf{p}|^2}{2}\,\mathrm{Im}\left[\hat{\mathbf{e}}_q^*\cdot\overleftrightarrow{\mathbf{G}}(\mathbf{r}',\mathbf{r}',\omega)\cdot\hat{\mathbf{e}}_q\right]} \tag{2.17}$$

where $\mathbf{p} = |\mathbf{p}|\hat{\mathbf{e}}_i$, $\hat{\mathbf{e}}_i$ is the unit vector along the dipole axis. Note that we need here the expression of the Green's tensor at the position of the dipole, also known as the self Green's tensor.

Spontaneous decay rate of a quantum emitter

We now want to derive an expression of the spontaneous decay rate Γ of a quantum emitter with the Green's tensor. All the former equations are valid for a classical dipole. An atom is a quantum system, so we would have to derive this expression from a pure quantum theory. We will not carry out the full derivation here as it is done in many seminal papers and textbooks [Wylie and Sipe 1984] but we will give heuristic arguments on why we can adapt Eq. (2.17) in a simple way to get the Purcell factor in the quantum case [Carminati et al. 2015].

Let us switch from a purely classical dipole, defined by its dipole moment $\mathbf{p}$, to a perfect two-level system comprised of a ground and excited states $|g\rangle$ and $|e\rangle$, with a transition frequency ω_{eg}. This transition is characterized by a dipole element $\mathbf{p}_{eg} = \langle g|\mathbf{D}|e\rangle$, where $\mathbf{D}$ is the electric dipole operator defined in Sec. 2.1.1. The dipole element direction gives the polarization of the transition, while its magnitude gives the strength of the interaction due to the distribution of charge within the system.

We can adapt Eq. (2.17) to our quantum dipole by noticing that the total radiated power in this new scenario is quantized by the energy of the emitted photon $\hbar\omega_{eg}$. We can then determine the spontaneous decay rate of such dipole by dividing P_{rad} by this energy, and obtain the mean number of transitions over time. We also substitute ω by ω_{eg} and $\mathbf{p}$ by $\mathbf{p}_{eg}$. This change from $\mathbf{p}$ to $\mathbf{p}_{eg}$ comes with a factor of two, as we only consider positive frequencies for emission in quantum mechanics [Carminati et al. 2015]. This contrasts with classical mechanics, where both positive and negative frequencies are taken into account. These adjustements lead to:

$$\boxed{\Gamma = \frac{2\mu_0\omega_{eg}^2}{\hbar}|\mathbf{p}_{eg}|^2 \,\mathrm{Im}\left[\hat{\mathbf{e}}_q^* \cdot \overleftrightarrow{\mathbf{G}}(\mathbf{r},\mathbf{r},\omega)\cdot\hat{\mathbf{e}}_q\right]} \tag{2.18}$$

It can be shown that we find the same expression by doing the full quantum derivation. It is usually computed starting from Fermi's Golden rule (see for example an uncommon approach in [Steck 2019] Section 11.6.1.), as the atom in a given electromagnetic field will couple to a continuum of modes.

Equation (2.18) shows that the total decay rate of the atom is proportional to the imaginary part of the Green's function, hence is completely determined by the electromagnetic environment. By shaping this environment we might engineer the value of this decay rate. This is the main motivation of this work. In order to get the Purcell factor, we just need to divide Eq. (2.18) by Γ_0. This quantity is derived in the following.

Spontaneous decay rate of an atom in free space

We will derive the spontaneous decay rate of an atom in free space Γ_0 with classical arguments. Let us start with the electric field radiated by an oscillating classical dipole oriented along $\hat{\mathbf{e}}_y$:

$$E_\theta = \mu_0\omega^2|\mathbf{p}|\sin\theta\frac{\omega}{4\pi c}\left[e^{ikr}\left(\frac{1}{k^3r^3} - \frac{i}{k^2r^2} - \frac{1}{kr}\right)\right] \tag{2.19}$$

$$E_r = \mu_0\omega^2|\mathbf{p}|\cos\theta\frac{\omega}{4\pi c}\left[e^{ikr}\left(\frac{2}{k^3r^3} - \frac{2i}{k^2r^2}\right)\right]. \tag{2.20}$$

Figure 2.2(a) shows the intensity distribution and polarization for such a dipole in free space ($\epsilon(\mathbf{r},\omega) = 1$). As we can see, even though the dipole oscillates along y, strong components along both x and y axes exist.

The power transferred to the environment is the one radiated to the far-field. Keeping only the far-field terms in Eq. (2.20), and computing the magnetic field from the electric one, we can get the total power radiated by an oscillating dipole in free space using Eq. (2.15):

$$P_{\text{rad}} = \frac{1}{2}\int_{\mathcal{S}} \text{Re}\{\mathbf{E}(\mathbf{r}) \times \mathbf{H}^*(\mathbf{r})\} \cdot \mathbf{d}\mathcal{S} \tag{2.21}$$

$$= |\mathbf{p}|^2 \frac{\mu_0 \omega^4}{12\pi c} \tag{2.22}$$

where we have left out the mathematical details, as it is a very standard calculation. Using the same heuristic argument as before we can write:

$$\Gamma_0 = |\mathbf{p}_{eg}|^2 \frac{\mu_0 \omega_{eg}^3}{3\hbar\pi c}. \tag{2.23}$$

A full derivation involving the computation of the free-space Green's function and plugging it into Eq. (2.18) gives the same result as $\text{Im}\left[\overleftrightarrow{\mathbf{G}}_0(\mathbf{r}_0, \mathbf{r}_0, \omega)\right] = \frac{\omega}{6\pi c}\mathbb{1}$.

Purcell factor and effect of the environment

With Eq. (2.18) and Eq. (2.23), we can get the expression for the Purcell factor Γ/Γ_0. It reduces to:

$$\boxed{\frac{\Gamma}{\Gamma_0} = \frac{6\pi c}{\omega_{eg}} \text{Im}\left[\hat{\mathbf{e}}_q^* \cdot \overleftrightarrow{\mathbf{G}}(\mathbf{r}, \mathbf{r}, \omega) \cdot \hat{\mathbf{e}}_q\right]} \tag{2.24}$$

This expression is now independent of the dipole moment as it compares the spontaneous decay rate of the same dipole in two different settings. We notice that $\frac{\Gamma}{\Gamma_0} = \frac{P}{P_0}$ even though the first ratio comes from a quantum theory calculation while the second one is purely classical electrodynamics. This is an important result: if classical electrodynamics cannot predict the absolute value of the decay rate of a quantum emitter, they can be used to predict its enhancement in a given electromagnetic environment.

Figure 2.2 shows a first simple example of this decay engineering. Following the idea by Karl-Heinz Drexhage [Drexhage et al. 1968], we place a classical dipole in front of a mirror. In this simple setup the self Green's function at the position of the dipole can be obtained from the free-space one: $\overleftrightarrow{\mathbf{G}}_{\text{mirror}}(\mathbf{r}', \mathbf{r}') = \overleftrightarrow{\mathbf{G}}_0^{\text{2D}}(\mathbf{r}', \mathbf{r}') - \overleftrightarrow{\mathbf{G}}_0^{\text{2D}}(\mathbf{r}' + 2h\,\hat{\mathbf{e}}_x, \mathbf{r}')$, where $\overleftrightarrow{\mathbf{G}}_0^{\text{2D}}$ is the free-space Green's function in 2D [Frisch 1968]. It is the sum of the Green's function from the dipole itself and its image dipole by the mirror. The minus sign comes from the π shift picked up by the beam at the mirror reflection. The quantities in Fig. 2.2(b-d) are computed from $\overleftrightarrow{\mathbf{G}}_{\text{mirror}}$. At distances on the order of a few wavelengths, we see that the total emitted power oscillates with the distance (Fig. 2.2(d)) and that the emission pattern is strongly position-dependent (Fig. 2.2(b-c)). This can be thought as the dipole interacting with its own image, producing a well known interference pattern on the overlap zone. If this effect can explain the shape of the emission pattern, even more interesting is the oscillation of the radiated power (that can be linked to the decay rate) with distance from the surface. We then see that in such a simple setup, it is possible to either enhance or suppress the total decay rate of a dipole just by tuning its position. This perturbation in the electromagnetic environment can be harnessed to already modify

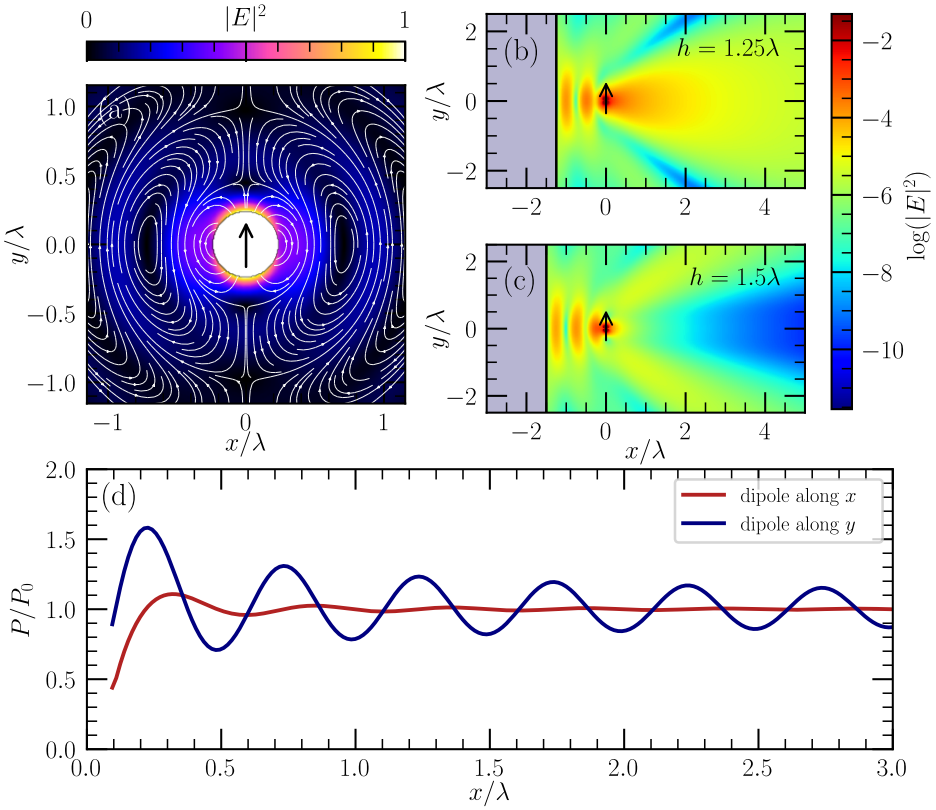

Figure 2.2: Classical dipole spontaneous decay and emitted power modulation in front of a mirror. (a) Normalized electric field produced by an oscillating electric dipole. The colors show the field intensity while the lines and arrows reveal the polarization direction. We see that even though the dipole is polarized along y, it creates important components of E along both x and y. (b-c) Electric field magnitude of a classical dipole along y in front of a perfect mirror at distances (b) $h = 1.25\lambda$ and (c) $h = 1.5\lambda$. We see the emission pattern is modified at different distances due to interferences with the reflected field. The electric field has been computed from the free-space Green's function in 2D $\propto H_0^{(1)}(r)$[2]. (d) Total power radiated by a dipole in front of a mirror as a function of the distance. At the mirror interface, the field picks up a π phase shift, causing destructive interference at distances which are multiples of $\lambda/2$. Interestingly, the total emitted power depends on the distance from the mirror, revealing it is possible to enhance the decay of an atom even in such a simple setup.

the Purcell factor to some extent. We understand why it took years to observe such an effect as it becomes proeminent only for distances on the order of the wavelength of the radiated light [Goy et al. 1983; Bennett et al. 2016].

The Purcell factor introduced up to now measures the enhancement or inhibition of the total decay rate of the atoms. As our goal is to couple atoms to a single guided mode of a waveguide, we are more interested in comparing the decay rate of the atoms inside this guided mode to the free space one. We define in the following the so-called 1D Purcell factor which measures exactly that and show it can be conveniently written in term of the spatial profile of such guided mode.

[2] $H_0^{(1)}$ is a Hankel function of the first kind defined as $H_0^{(1)}(x) = J_0(x) + Y_0(x)$, with J_0 and Y_0 the Bessel functions of first and second kind respectively

2.2.3 Expressing the 1D Purcell factor of emitters coupled to a waveguide

Derivation of the 1D Green's tensor through mode expansion

As we want to look at the decay of atoms into the guided mode of a waveguide, we will distinguish between the contributions of the Green's function coming from said mode and all the other other radiative modes the atoms can couple to. Let us assume we have a non-magnetic ($\mu = 1$) and lossless ($\mathrm{Im}[\epsilon] = 0$) environment. It can be shown that it is possible to decompose the Green's tensor on a basis of optical modes of the system [Hood 2017]:

$$\boxed{\overleftrightarrow{\mathbf{G}}(\mathbf{r},\mathbf{r}',\omega) = \frac{c^2}{\omega^2}\sum_l \left(\frac{\omega_l^2}{\omega_l^2-\omega^2}\right)\mathbf{E}_l(\mathbf{r})\otimes\mathbf{E}_l^*(\mathbf{r}')} \tag{2.25}$$

where the sum is over all possible modes l, and ω_l is the frequency of said mode[3].

A waveguide can only support a finite number of spatial modes [Snyder and Love 2012], but we suppose that the atoms couple to only one of them that we will write as $\mathbf{E}_k^g(\mathbf{r})$, where k is the wave vector of the mode and the g superscript stands for *guided*. We suppose that the waveguide has a propagation axis along x and is periodic with period a. Even if it is uniform we can assume this and choose an arbitrary period. This assumption will ease the calculations. Because of this periodicity we can write the guided mode as Bloch waves (see Chapter 4) defined as $\mathbf{E}_k^g(\mathbf{r}) = \mathbf{u}_k^g(\mathbf{r})\mathrm{e}^{ikx}$, $\mathbf{u}_k^g(\mathbf{r})$ periodic in x with period a.

Equation (2.25) allows to separate the Green's tensor into a component related to the guided mode contribution and all the other ones as $\overleftrightarrow{\mathbf{G}} = \overleftrightarrow{\mathbf{G}}_{1\mathrm{D}} + \overleftrightarrow{\mathbf{G}}'$. As the Purcell factor in Eq. (2.24) is linear in $\overleftrightarrow{\mathbf{G}}$, it can also be decomposed as $\mathrm{PF} = \Gamma_{1\mathrm{D}}/\Gamma_0 + \Gamma'/\Gamma_0$. In the rest of this work the **1D Purcell factor** will refer to the first term of this expression, i.e. the enhancement of the coupling of the atoms to the specified guided mode of the waveguide.

We derive in the following an analytical expression for $\Gamma_{1\mathrm{D}}/\Gamma_0$, by expressing $\overleftrightarrow{\mathbf{G}}_{1\mathrm{D}}$ from Eq. (2.25):

$$\overleftrightarrow{\mathbf{G}}_{1\mathrm{D}}(\mathbf{r},\mathbf{r}',\omega) = \frac{c^2}{\omega^2}\sum_k \left(\frac{\omega_k^2}{\omega_k^2-(\omega+i\delta)^2}\right)\mathbf{E}_k^g(\mathbf{r})\otimes\mathbf{E}_k^{g*}(\mathbf{r}') \tag{2.27}$$

where the sum is now over the possible wave vectors of the guided mode, and δ is an infinitesimal positive quantity added to ensure to have a causal Green's function[4]. We

[3] The set of solutions of Eq. (2.7) for the electric field is both orthogonal and complete (by taking $\mathbf{P} = 0$). The completeness condition [Snyder and Love 2012] states:

$$\delta(\mathbf{r}-\mathbf{r}')\hat{\mathbb{1}} = \epsilon(\mathbf{r})\left[\sum_l \mathbf{E}_l(\mathbf{r})\otimes\mathbf{E}_l^*(\mathbf{r}') + \sum_l \mathbf{E}_l^{(L)}(\mathbf{r})\otimes\mathbf{E}_l^{(L)*}(\mathbf{r}')\right] \tag{2.26}$$

where the $\mathbf{E}_l^{(L)}$ are the longitudinal modes. We obtain the Green's function decomposition by plugging this completeness relation into Eq. (2.10) and neglecting the longitudinal terms that can have an effect only on the real part of the Green's function.

[4] Maxwell's equations connect quantities that are simultaneous in time, but the Green's function in time domain connects a source to a point in space and as such, has to respect causality. Causality has then to be enforced mathematically which is what is done here.

replace the sum over the k by an integral by setting $\sum_k \to \frac{a}{2\pi}\int dk$, and decompose the fraction into two terms:

$$\overleftrightarrow{\mathbf{G}}_{1\mathrm{D}}(\mathbf{r},\mathbf{r}',\omega) = \frac{c^2}{\omega^2}\frac{a}{4\pi}\int_{-\infty}^{+\infty} dk \left(\frac{\omega(k)}{\omega(k)+\omega+i\delta} + \frac{\omega(k)}{\omega(k)-\omega-i\delta}\right) \mathbf{u}_k^g(\mathbf{r})\otimes\mathbf{u}_k^{g*}(\mathbf{r}')\mathrm{e}^{ik(x-x')} \tag{2.28}$$

The two terms in the sum have poles in the complex plane and following [Patterson 2009] we can perform the complex integration for the two terms independently.

The first term, with a residue at the pole (k_0,ω) $2\pi i\,\mathrm{Res}|_{k_0} = 2\pi i\,\omega\,(\partial\omega/\partial k)^{-1}$, leads to a solution with $x \geq x'$:

$$\overleftrightarrow{\mathbf{G}}_{1\mathrm{D}}(x>x',\omega) = i\frac{ac^2}{2\omega v_\mathrm{g}}\mathbf{u}_{k_0}^g(\mathbf{r})\otimes\mathbf{u}_{k_0}^{g*}(\mathbf{r}')\mathrm{e}^{ik_0(x-x')} \tag{2.29}$$

where v_g is the group velocity at the position of the pole.

A similar solution is found for $x \leq x'$. Combining the two solutions together we find:

$$\begin{aligned}\overleftrightarrow{\mathbf{G}}_{1\mathrm{D}}(\mathbf{r},\mathbf{r}',\omega) = i\frac{c}{2\omega}\frac{c}{v_\mathrm{g}}a\Big[&\mathbf{u}_{k_0}(\mathbf{r})\otimes\mathbf{u}_{k_0}^*(\mathbf{r}')e^{ik_0(x-x')}\Theta(x-x')\\ &+\mathbf{u}_{k_0}^*(\mathbf{r})\otimes\mathbf{u}_{k_0}(\mathbf{r}')e^{-ik_0(x-x')}\Theta(x'-x)\Big]\end{aligned} \tag{2.30}$$

where $\Theta(x)$ is the Heaviside function, which is discontinuous at $x=0$.

Equation (2.30) expresses that if you have a dipole at position $\mathbf{r}'$ exciting a waveguide mode $\mathbf{u}_k$, and that you look at what field you have at position $\mathbf{r}$ you have to compare x and x' to know what you will get. If $x > x'$, the only field contributing is the forward propagating mode and if $x < x'$, the only field you will pick up at $\mathbf{r}$ is the backward propagating field. In either case, only one mode remains from the initial infinite sum in Eq. (2.27).

However, in order to compute the 1D Purcell factor we need the self Green's function, evaluated at the position of the exciting dipole. What happens then if $x = x'$?

If $x > x'$, and we take the limit $x \to x'^{+}$, then:

$$\lim_{x\to x'^{+}} \overleftrightarrow{\mathbf{G}}_{1\mathrm{D}}(\mathbf{r},\mathbf{r}',\omega) \propto \mathbf{u}_k(\mathbf{r}')\otimes\mathbf{u}_k^*(\mathbf{r}') \tag{2.31}$$

while for $x < x'$:

$$\lim_{x\to x'^{-}} \overleftrightarrow{\mathbf{G}}_{1\mathrm{D}}(\mathbf{r},\mathbf{r}',\omega) \propto \mathbf{u}_k^*(\mathbf{r}')\otimes\mathbf{u}_k(\mathbf{r}'). \tag{2.32}$$

As the tensor product is non commutative here, we have:

$$\lim_{x\to x'^{+}} \overleftrightarrow{\mathbf{G}}_{1\mathrm{D}} \neq \lim_{x\to x'^{-}} \overleftrightarrow{\mathbf{G}}_{1\mathrm{D}}, \tag{2.33}$$

hence the limit is not defined. It is not obvious to express the self 1D Green's function $\overleftrightarrow{\mathbf{G}}_{1\mathrm{D}}(\mathbf{r}',\mathbf{r}',\omega)$ from Eq. (2.30) for any ω. This is at odds to what is usually done (for example in [Hood 2017]).

This result is not so dramatic as we can see in Eq. (2.24) that only the imaginary

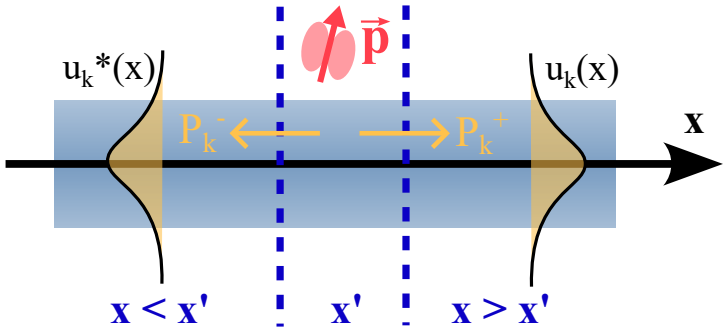

Figure 2.3: Diagram of a dipole p at position x' oscillating at a frequency ω, exciting a waveguide mode $\mathbf{E}_j$ in either forward or backward propagation. P_j^+ and P_j^- are the powers (surface integral of the flux of the Poynting vector) carried by mode j along the positive and negative axis respectively, as defined in the text.

part of the projection of the Green's function is sufficient to compute it. Fortunately, the quantity $\mathrm{Im}\left[\mathbf{e}_q^* \cdot \mathbf{G}_{1\mathrm{D}}(\mathbf{r},\mathbf{r},\omega)\cdot\mathbf{e}_q\right]$ is defined (this limit exists) and can be estimated through classical electrodynamics and energy conservation.

Spontaneous decay rate of a dipole coupled to a waveguide through energy conservation

We consider the case depicted in Fig. 2.3, where we have a single dipole at position $\mathbf{r}'$, which emits into a given uniform waveguide mode. In general, the total electric field in a waveguide can be written as a sum of forward and backward propagating modes, travelling in positive x and negative x directions respectively [Snyder and Love 2012]:

$$\mathbf{E}(\mathbf{r}) = \sum_j a_{+j}\mathbf{E}_j^+(\mathbf{r}) + \sum_j a_{-j}\mathbf{E}_j^-(\mathbf{r}) \tag{2.34}$$

The constants a_{+j} and a_{-j} are the modal amplitudes. An optical waveguide can only support a finite number of guided modes, hence the sum is finite. The same expansion can be made for the magnetic field $\mathbf{H}$, with the same modal amplitudes.

Each of these modes will carry power through the waveguide, and parallel to the waveguide axis x. We can define the power carried by a given mode in a given direction by the integral of the flux of the Poynting vector across an infinite surface $\mathcal{A}$ perpendicular to the waveguide axis (see Fig. 2.3):

$$P_j^\pm = \pm\int_{\mathcal{A}} \frac{1}{2}|a_{\pm j}|^2\,\mathrm{Re}\left\{\mathbf{E}_j\times\mathbf{H}_j^*\right\}d\mathcal{A} \tag{2.35}$$

$$= \pm|a_{\pm j}|^2\phi_j \tag{2.36}$$

where $\phi_j = \int_{\mathcal{A}}\frac{1}{2}\,\mathrm{Re}\left\{\mathbf{E}_j\times\mathbf{H}_j^*\right\}d\mathcal{A}$. We define the power as positive when going from left to right. From [Snyder and Love 2012], we get the expression of the modal amplitude for a given excitation density at a position x', which is the overlap between the mode shape and the current density of the source over the whole 3D space:

$$a_{\pm j} = -\frac{1}{4\phi_j}\int_{\mathcal{V}}\mathbf{E}_j^{\pm *}\cdot\mathbf{J}(\mathbf{r})\,d\mathcal{V}. \tag{2.37}$$

In our case, the current density is a single dipole at $\mathbf{r}'$, oriented along $\hat{\mathbf{e}}_q$, hence $\mathbf{J}(\mathbf{r}) = -i\omega|\mathbf{p}|\delta(\mathbf{r}-\mathbf{r}')\hat{\mathbf{e}}_q$. The modal amplitudes reduces to:

$$a_{\pm j} = \frac{i\omega}{4\phi_j}\mathbf{E}_j^{\mp}(\mathbf{r}')\cdot\mathbf{p} \tag{2.38}$$

as $\mathbf{E}_j^{+*} = \mathbf{E}_j^{-}$. Hence, using Eq. (2.36), the power carried by mode j in either forward or backward direction is:

$$P_j^{\pm} = \frac{\omega^2}{16\phi_j}|\mathbf{p}|^2|\hat{\mathbf{e}}_q\cdot\mathbf{E}_j^{\mp}(\mathbf{r}')|^2 \tag{2.39}$$

The total power carried by mode j in the waveguide is the sum of the two propagation directions:

$$P_{\text{tot}} = P_j^{+} + P_j^{-} = \frac{\omega^2}{16\phi_j}|\mathbf{p}|^2|\hat{\mathbf{e}}_q\cdot\mathbf{E}_j^{-}(\mathbf{r}')|^2 + \frac{\omega^2}{16\phi_j}|\mathbf{p}|^2|\hat{\mathbf{e}}_q\cdot\mathbf{E}_j^{+}(\mathbf{r}')|^2. \tag{2.40}$$

This value must be equal to the power radiated by the dipole P_{rad} as we assume that the mode j constitutes the whole electromagnetic environment accessible and all of its light couples to the waveguide. Hence $P_{\text{tot}} = P_{\text{rad}}$ where the total power radiated by this dipole into the waveguide, is given as before by Eq. (2.17):

$$P_{\text{rad}} = \frac{\mu_0\omega^3}{2}|\mathbf{p}|^2\,\text{Im}\left[\hat{\mathbf{e}}_q^*\cdot\mathbf{G}_{1\text{D}}(\mathbf{r}',\mathbf{r}',\omega)\cdot\hat{\mathbf{e}}_q\right]. \tag{2.41}$$

We finally have an expression for $\text{Im}\left[\hat{\mathbf{e}}_q^*\cdot\mathbf{G}_{1\text{D}}(\mathbf{r}',\mathbf{r}',\omega)\cdot\hat{\mathbf{e}}_q\right]$ by combining Eqs. (2.41) and (2.40):

$$\text{Im}\left[\hat{\mathbf{e}}_q^*\cdot\mathbf{G}_{1\text{D}}(\mathbf{r}',\mathbf{r}',\omega)\cdot\hat{\mathbf{e}}_q\right] = \frac{2}{\mu_0\omega^3}\frac{1}{|\mathbf{p}|^2}(P_j^{+}+P_j^{-}) \tag{2.42}$$

$$= \frac{1}{8\mu_0\omega\phi_j}\left[|\hat{\mathbf{e}}_q\cdot\mathbf{E}_j^{+}(\mathbf{r}')|^2 + |\hat{\mathbf{e}}_q\cdot\mathbf{E}_j^{-}(\mathbf{r}')|^2\right]. \tag{2.43}$$

Thanks to these classical waveguide optics considerations we get a practical expression for $\text{Im}\left[\hat{\mathbf{e}}_q^*\cdot\mathbf{G}_{1\text{D}}(\mathbf{r},\mathbf{r},\omega)\cdot\hat{\mathbf{e}}_q\right]$. Plugging Eq. (2.43) into Eq. (2.24), we get the Purcell factor for an atom at position $\mathbf{r}$, with a transition dipole element along $\hat{\mathbf{e}}_q$, coupled to a single waveguide mode:

$$\boxed{\frac{\Gamma_{1\text{D}}}{\Gamma_0} = \frac{3\pi c^2}{2\omega_{eg}^2}\frac{c}{v_{\text{g}}}\left[\frac{|\hat{\mathbf{e}}_q\cdot\mathbf{E}^{+}(\mathbf{r})|^2}{\int_{\mathcal{A}}d\mathbf{r}'\epsilon(\mathbf{r}')|\mathbf{E}^{+}(\mathbf{r}')|^2} + \frac{|\hat{\mathbf{e}}_q\cdot\mathbf{E}^{-}(\mathbf{r})|^2}{\int_{\mathcal{A}}d\mathbf{r}'\epsilon(\mathbf{r}')|\mathbf{E}^{+}(\mathbf{r}')|^2}\right]} \tag{2.44}$$

considering that the flux $\phi = \frac{1}{2}v_{\text{g}}\int_{\mathcal{A}}\epsilon(\mathbf{r}')|\mathbf{E}^{+}(\mathbf{r}')|^2 d\mathbf{r}'$, where v_{g} is the group velocity and we dropped the j index as we consider a single coupling mode[5].

This expression depends only on the transverse spatial profile of the guided mode and the group velocity of said mode. It is very convenient when computing spontaneous decay rates as you only need a classical calculation of the transverse modes of the waveguide which can be achieved numerically in various ways (see Chapter 4). This derivation also holds for a periodic waveguide along x of period a, by replacing the integration over the transverse plane $\mathcal{A}$ by an average over a cell volume $\mathcal{V}_{\text{cell}}$ of

[5] This expression comes from [Snyder and Love 2012] Eq. (11.33).

length a:

$$\int_{\mathcal{A}} d\mathbf{r}'\epsilon(\mathbf{r}')|\mathbf{E}^+(\mathbf{r}')|^2 \rightarrow \frac{1}{a}\int_{\mathcal{V}_{\text{cell}}} d\mathbf{r}'\epsilon(\mathbf{r}')|\mathbf{E}^+(\mathbf{r}')|^2.$$

A more accurate measure of probability than the Purcell factor would be comparing this decay to the total emission of the atom in the same configuration Γ_{tot}. This is the β factor defined as $\beta = \Gamma_{1\text{D}}/\Gamma_{\text{tot}}$. We usually prefer the Purcell factor as Γ_{tot} can be very hard to estimate in many cases. We will address this issue in specific scenarios in Chapter 5.

2.3 The case of a multilevel atom

Until now, we have considered our emitters coupled to waveguide modes as perfect two-level systems. However, in the experiment described in this thesis we work with ^{87}Rb which has many states and transitions.

2.3.1 Waveguide QED with Rubidium 87

Real life atoms are multilevel

Rubidium is an **alkali atom** with 37 electrons and a nuclear spin $\mathbf{I} = 3/2$. Alkali atoms are widely used in quantum optics experiments for many reasons. Even though they have multiple electrons, all of their electronic shells are filled except the last which only has one electron (e.g for Rb, [Kr]5s^1). As such, they all have an electronic spin $\mathbf{S} = 1/2$. Their electronic structure is hence quite similar to the one of Hydrogen. Even if they share similarities with it, they are heavier and less reactive, which are both advantages when it comes to cooling and trapping. Last but not least, they often offer accessible electronic transitions at near-infrared or visible wavelengths, which is the range where lasers are the most widely available.

As alkali atoms are hence very convenient to cool, it is no coincidence if Rubidium 87 was the first atom to be cooled down to degeneracy by Eric Cornell and Carl Wieman to form the first Bose-Einstein Condensate in Boulder [Anderson et al. 1995].

Electronic fine and hyperfine structures of Rubidium

The spin $\mathbf{S}$ of the single valence electron of Rb can couple to its orbital angular momentum $\mathbf{L}$. This interaction gives rise to the **fine structure**. The total angular momentum of the atom is then $\mathbf{J} = \mathbf{L} + \mathbf{S}$ and by following the rules of addition of angular momentum, J can take the values $|L - S| \leq J \leq L + S$. For the ground state of Rubidium we have $L = 0$ and $S = 1/2$ hence $J = 1/2$ and there is only a single fine level $5S_{1/2}$. For the first excited state, $L = 1, S = 1/2$ hence $J = 1/2$ ($5P_{1/2}$ state) or $3/2$ ($5P_{3/2}$ state). The transitions between the ground state and these two excited levels correspond to clearly defined optical transitions called respectively the D_1 (795 nm) and D_2 lines (780 nm), see Fig. 2.4(a). These transitions are quite fast with linewidths of 5.75 and 6.07 MHz respectively, which makes them ideal candidates for cooling procedures [Steck 2001]. Moreover, very reliable lasers exist today at these wavelengths, making them even more appealing. These MHz-range D-lines is a common feature of alkali atoms.

A **hyperfine splitting** of these states exists as Rubidium 87 has a non zero nuclear spin. Indeed, the total angular momentum $\mathbf{J}$ can couple to the nuclear spin $\mathbf{I}$. As previously, the total atomic angular momentum $\mathbf{F} = \mathbf{I} + \mathbf{J}$ can take values

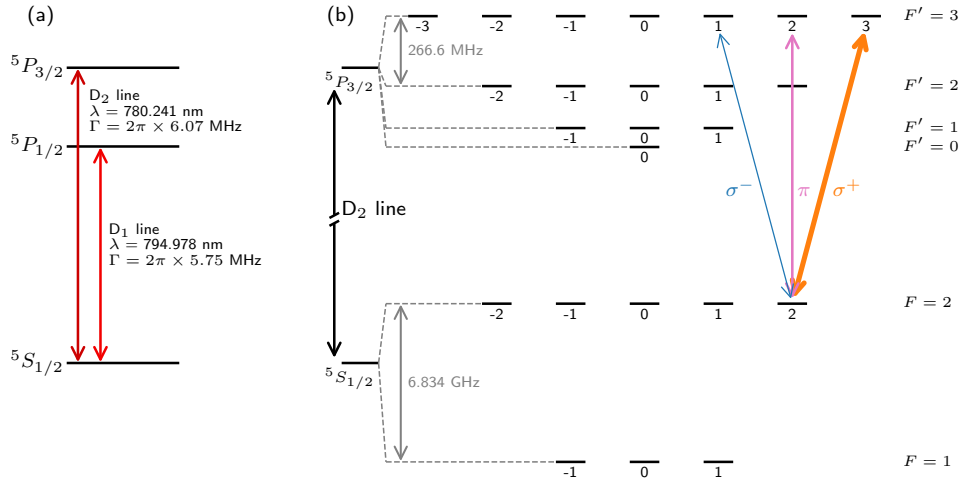

Figure 2.4: Fine and hyperfine structure of Rubidium 87. (a) Main transitions used in Rubidium 87 experiments. (b) Detail of the hyperfine structure of the D_2 line (used for cooling and interaction with the guided mode) [Steck 2001]. We draw as an example the allowed transitions for an atom in the state $|F = 2, m_F = 2\rangle$. The σ^+ transition is favoured because of the Clebsch-Gordan coefficients (see main text).

$|I - J| \leq F \leq I + J$. While the hyperfine sublevels are shown as degenerate in Fig. 2.4(b), a magnetic field can split them, with a Zeeman splitting proportional to m_F and $|\mathbf{B}|$.

2.3.2 A polarization-dependent Purcell factor

In the following we adapt Eq. (2.18) of the spontaneous decay rate of a TLS in the guided mode of a waveguide to the case of a multilevel atom. The main difference is that in the absence of a magnetic field, an atom in a given state can now couple to 3 different excited levels with the same frequencies. For example an atom in the ground state sublevel $|F = 2, m_F = 2\rangle$ is coupled to the levels $|F' = 3, m_F = 2 + q\rangle$ with $q \in \{-1, 0, 1\}$. Depending on the value of q, the transitions are called σ^+, π and σ^- respectively (see Fig. 2.4).

As in Eq. (2.18), we need to compute the dipole element of the transition to get the spontaneous decay rate. Most of the complexity introduced by considering multilevel atoms is in this dipole element. As we have many ground states, the dipole element of a given transition is now defined by $\langle F m_F | D_q | F' m_{F'} \rangle$. We want to write this dipole element in a way that would make explicit its dependence on the polarization of the transition.

According to the Wigner-Eckart theorem, the dependence of the matrix elements of tensor component operators D_q on m_F, $m_{F'}$ and q is entirely included in the Wigner 3-j symbol [Steck 2019]:

$$\langle F m_F | D_q | F' m_{F'} \rangle = |\langle F || \mathbf{D} || F' \rangle|^2 C_{m_F, q} \tag{2.45}$$

where the $C_{m_F,q}$ are the Clebsch-Gordan coefficients associated with the transition from $|F, m_F\rangle$ to $|F', m_F + q\rangle$ and are given by[6]:

$$C_{m_F,q} = (-1)^{F'-1+m_F}\sqrt{2F+1}\begin{pmatrix} F' & 1 & F \\ m_F - q & q & -m_F \end{pmatrix} \tag{2.47}$$

and $\langle F||\mathbf{D}||F'\rangle$ is the reduced dipole matrix element for the set of tensor component operators D_q, with the normalization convention[7]:

$$|\langle F||\mathbf{D}||F'\rangle|^2 = \sum_{m_F,m_{F'},q} |\langle F m_F|D_q|F' m_{F'}\rangle|^2 \tag{2.48}$$

Replacing Eq. (2.45) into Eq. (2.18), we obtain a state- and polarization-dependent spontaneous decay rate $\Gamma_{1\mathrm{D},F,F',m_F,q}$, from state $|F', m_F + q\rangle$ to $|F, m_F\rangle$[8]:

$$\Gamma_{1\mathrm{D},F,F',m_F,q} = \frac{2\mu_0\omega^2}{\hbar}|\langle F||\mathbf{D}||F'\rangle|^2|C_{m_F,q}|^2\,\mathrm{Im}\left[\hat{\mathbf{e}}_q^* \cdot \overleftrightarrow{\mathbf{G}}_{1\mathrm{D}}(\mathbf{r},\mathbf{r},\omega)\cdot\hat{\mathbf{e}}_q\right] \tag{2.49}$$

$$\boxed{\Gamma_{1\mathrm{D},F,F',m_F,q} = \frac{\pi a c}{\hbar}\frac{|\langle F||\mathbf{D}||F'\rangle|^2}{\lambda_0 v_\mathrm{g}}|C_{m_F,q}|^2\left[\frac{|\hat{\mathbf{e}}_q\cdot\mathbf{E}^+(\mathbf{r})|^2}{\int_{\mathcal{V}_\mathrm{cell}} d\mathbf{r}'\epsilon(\mathbf{r}')|\mathbf{E}^+(\mathbf{r}')|^2} + \frac{|\hat{\mathbf{e}}_q\cdot\mathbf{E}^-(\mathbf{r})|^2}{\int_{\mathcal{V}_\mathrm{cell}} d\mathbf{r}'\epsilon(\mathbf{r}')|\mathbf{E}^+(\mathbf{r}')|^2}\right]} \tag{2.50}$$

Equation (2.50) shows that the coupling to the guided mode is transition dependent for two reasons:

- The term in brackets is evaluated by taking the component of the forward and backward propagating fields in the $\{\pi, \sigma^+, \sigma^-\}$ basis. Depending on the chosen quantization axis and the waveguide design, the electric field can have very different polarization profiles near the surface. A careful study of polarization has then to be carried out to understand which transition will be favored for a given waveguide mode.
- The Clebsch Gordan coefficients intrinsically give weights to the different transitions between hyperfine sublevels and can favor one or another. For example values of $C_{m_F,q}$ are given in Table 2.1 for the $|F, m_F = 2\rangle$ to $|F', m_F + q\rangle$ transition. The σ^+ transition is 15 times stronger than the σ^- one.

$m_{F'}$	1	2	3
$C_{m_F,q}$	$\sqrt{\frac{1}{21}}$	$-\sqrt{\frac{5}{21}}$	$\sqrt{\frac{5}{7}}$

Table 2.1: Clebsch-Gordan coefficients for the transition $|F = 2, m_F = 2\rangle$ to $|F' = 3, m_{F'}\rangle$.

[6] This comes directly from the definition of the Wigner 3-j symbols:

$$\begin{pmatrix} j_1 & j_2 & j_3 \\ m_1 & m_2 & m_3 \end{pmatrix} := \frac{(-1)^{j_1-j_2-m_3}}{\sqrt{2j_3+1}}\langle j_1, m_1; j_2, m_2|j_3, -m_3\rangle \tag{2.46}$$

[7] We follow the normalization of the dipole elements from [Steck 2019] p. 335, which differs from the one used in [Le Kien et al. 2013a] or in the Alkali-Rydberg-Calculator package (ARC) [Šibalić et al. 2017] by a factor $\sqrt{2F+1}$.

[8] Note that we can also define an excitation rate $\gamma^{\pm}_{\mathrm{exc},F,F',m_F,q}$ of an atom initially in $|F, m_F\rangle$ and promoted to $|F', m_F - q\rangle$ when sending an input guided mode. Since the excitation comes from a single direction ($+x$ or $-x$), only one term from Eq. 2.50 is kept. This figure of merit makes sense experimentally as we usually start with atoms in the ground state.

When considering a π transition, the dipole vector is real and since $\mathbf{E}^+(\mathbf{r})^* = \mathbf{E}^-(\mathbf{r})$, the two terms of the sum in Eq. (2.50) are equal.

Even though the structure of Rubidium differs a lot from a TLS, this approximation can still be made in some situations as closed transitions exist. We can see in Fig. 2.4(b) that driving the $|F = 2\rangle \rightarrow |F' = 3\rangle$ transition with a σ^+ or σ^- polarization will eventually pump the atoms into one of the extremal m_F states. Then only one transition will be addressed, with no parasitic decay channel. In this situation, the Purcell factor obtained from Eq. (2.50) reduces to Eq. (2.44). As we will see in Chapter 5, polarization of nanoscale waveguides modes usually have an important circular component that can be used to address these closed σ transitions (by choosing an appropriate quantization axis) and can lead to a strong chiral behaviour [Pucher et al. 2022; Bouscal et al. 2024].

Conclusion

In this chapter we have introduced all the necessary framework for describing atom-light interactions at the vicinity of 1D or quasi-1D waveguides. This formalism was established thanks to the Green's function approach which is a crucial object for describing electromagnetic environments. We have found a practical expression for the 1D Purcell factor in terms of the guided modes transverse shapes, deriving it from first principles of optical waveguide theory. This expression is very useful as mode shapes are usually what you get from numerical waveguide simulations. With further derivations, we obtained a formula better suited to realistic case of multilevel atoms, which are manipulated experimentally. That way we are able to make predictions on the coupling of the atoms to a given mode, depending on the transition considered. The methods developed in this chapter apply to other emitters embedded in 1D waveguides as quantum dots or superconducting qubits.

While this chapter focused on description and quantification of the atom-light interaction at resonance, the next will look at the physics of optical trapping that happen out of resonance.

CHAPTER 3

TRAPPING ATOMS CLOSE TO NANOSTRUCTURES

Contents

There are two independent approaches to achieve strong atom-photon interaction between a waveguide guided mode and an atom, as can be seen in the expression of the Purcell factor derived in Chapter 2 (see Eq. (2.44)). One can increase the group index of the guided mode by designing slow-light waveguides or maximize the right component of the electric field at the position of the atoms (depending on the transition that should be addressed). In any scenario, a key ingredient is to be able to trap the atoms very close to the nanophotonic waveguides, as the guided modes used for coupling decay exponentially out of the structure. Keeping the atoms at fixed positions is a requirement in order to create ordered 1D arrays that are the main resources of many Waveguide QED theoretical proposals [Chin et al. 2017; Tabares et al. 2023].

The most fruitful idea has been to use out-of-resonance evanescent modes of the structure in order to trap the atoms with the dipole force. This is a challenging task. In a nanofiber-based platform, thanks to a featureless dispersion relation, a two-color evanescent trap [Le Kien et al. 2004; Vetsch et al. 2010; Goban et al. 2012; Lacroûte et al. 2012] is commonly used (see Fig. 3.1). For more complex structures, e.g., microtoroids or photonic-crystal waveguides, atom trapping via guided modes

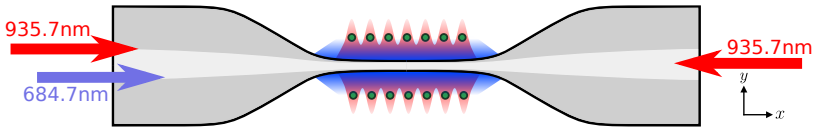

Figure 3.1: Diagram of evanescent trapping around a nanofiber. Experimental configuration from [Corzo et al. 2019]. In the nanofiber region, a substantial fraction of the fields is into the air, as shown by the shadings. Trapped Cesium atoms are shown in green. A red-detuned beam from the D_2 transition is sent through both ports, creating a standing wave. A blue-detuned mode creates a uniform repulsive potential. The sum of the two potentials can allow to create a stable trap in all directions.

has been proposed but has remained a roadblock and side illumination was mostly used heretofore [Thompson et al. 2013; Goban et al. 2014; Will et al. 2021]. A specific added complexity of such optical microtraps is the strong gradients of electric fields and polarization, which can introduce spatially varying shift to the atomic energy levels, leading to inhomogeneous shift and fictitious magnetic fields [Albrecht et al. 2016]. Hence, finding an adequate trapping scheme can require a long optimization process for each structure. It will thus be convenient to have a versatile tool to optimize and characterize optical dipole traps near nanophotonic devices.

This chapter presents theory, tools and a state of the art on evanescent optical trapping close to nanostructures. For this purpose, we first introduce the theoretical basis of **out-of-resonance** light-matter interaction, main resource for optical trapping. We compute the optical potentials for multilevel alkali atoms, including all the scalar, vector and tensor light shifts. We then introduce the most common scheme for trapping atoms close to nanoscopic waveguide: the two-color dipole trap. Finally we present `nanotrappy`[1], an open-source Python package developed as a way to optimize the development workflow of dipole traps around various nanostructures. The versatility of the package is demonstrated for three examples of nanophotonic structures. This chapter is mostly based on the work published in [Berroir, Bouscal, et al. 2022].

3.1 Theory of optical trapping: atom-light interaction out of resonance

Optical trapping of atoms relies on the conservative potential created by the intensity distribution of detuned laser beams [Grimm et al. 2000], a technique now widely used for trapping cold atoms in free space. For trapping atoms optically at subwavelength distance from a dielectric surface, two specificities arise. First, the evanescent field leaking out of the dielectric material should be able to provide a stable trapping potential close to the surfaces [Ovchinnikov et al. 1991; Le Kien et al. 2004; Vetsch et al. 2010; Goban et al. 2012]. Second, the Casimir-Polder interaction becomes sizeable at such distances and has to be taken into account [Boustimi et al. 2002; Le Kien et al. 2004].

In this section, we introduce the atom-light interaction concepts at the heart of the dipole trapping potential, with an emphasis on the influence of the Zeeman hyperfine levels. We recall the origin of scalar, vector and tensor shifts on the hyperfine manifold

[1] Website of the project at `https://LKB-QuantumNetworks.github.io/nanotrappy`.

and their contributions to the polarizability tensor. Then we discuss the Casimir-Polder interaction at subwavelength distance from the surface. Finally, all these contributions are included to compute the total trapping potential.

Note that despite the emphasis on trapping in the evanescent field of modes guided by dielectric waveguide, the following presentation remains general and valid for any electric field distribution of the trapping light.

3.1.1 Atom-light interaction: light shifts

We will consider here the case of a multilevel alkali atom interacting with a monochromatic optical field. To simplify the notation and describe easily the internal state of the atoms, we will adopt convenient notations, following the works presented in [Steck 2019], [Le Kien et al. 2013a] and [Gouraud 2016]. We denote by $|s\rangle = |N, J, F, m_F\rangle$ the state of interest with energy E_s and $|e_i\rangle = |N'_i, J'_i, F'_i, m'_{F,i}\rangle$ all the states to which it is coupled with energies E_{e_i}. As before, J stands for the total electronic angular momenta, F for the total atomic angular momenta and m_F for the magnetic quantum number. Here we choose z as the quantization axis.

Interaction Hamiltonian far from resonance

We have seen in Section 2.1.1 how to write the Hamiltonian of such an atom-field interaction $\mathcal{H}_{\mathrm{AF}} = -\mathbf{D}\cdot\mathbf{E}$. All the trapping fields are again assumed to be classical fields, which is well justified experimentally considering the powers that are typically used.

In order to study the frequency response of an electric dipole interacting with an optical electric field, we define a polarizability tensor $\alpha_{\mu\nu}$ such that the mean induced dipole moment vector becomes:

$$\langle D_\mu^{(+)}(\omega)\rangle = \alpha_{\mu\nu}(F, m_F; \omega) E_\nu^{(+)}, \tag{3.1}$$

where $E^{(+)}$ ($E^{(-)}$) denotes the positive (negative) frequency terms of the electric field. We have used the Einstein summation convention.

Using time-dependent perturbation theory, one can derive the Kramers-Heisenberg polarizability tensor for a given state $|s\rangle$ and a given angular frequency ω for the electric field[2]:

$$\alpha_{\mu\nu}(s;\omega) = \sum_i \left(\frac{\langle s|D_\nu|e_i\rangle\langle e_i|D_\mu|s\rangle}{\hbar(\omega_{e_i s} - \omega)} + \frac{\langle e_i|D_\nu|s\rangle\langle s|D_\mu|e_i\rangle}{\hbar(\omega_{e_i s} + \omega)} \right). \tag{3.2}$$

Here D_q represents the tensor component of the dipole operator $\mathbf{D}$ and $\omega_{e_i s} = (E_{e_i} - E_s)/\hbar$.

Once this polarizability tensor has been defined, we can then express the Stark shift induced by the electric field $\mathbf{E}$ written in the $\{\pi, \sigma^+, \sigma^-\}$ basis as:

$$\begin{aligned} \Delta E(F, m_F; \omega) &= -\frac{1}{2}\langle \mathbf{D}(\omega)\rangle \cdot \mathbf{E} \\ &= -\frac{1}{2}\langle \mathbf{D}^{(+)} + \mathbf{D}^{(-)}\rangle \cdot (\mathbf{E}^{(+)} + \mathbf{E}^{(-)}) \\ &= -Re(\alpha_{\mu\nu}) E_\mu^{(-)} E_\nu^{(+)}. \end{aligned} \tag{3.3}$$

[2]Note the difference here in the expression of $\alpha_{\mu\nu}$ from [Steck 2019]. The two terms allow for a rank-dependent frequency dependence when reducing the tensor, which seems to correct the error signaled in p. 373.

Irreducible parts decomposition

In order to study the effects of each component of the electric field, a usual method is to split the polarizability tensor into its irreducible parts, which will give us respectively the scalar, vector and tensor polarizabilities. Such decomposition is detailed in [Steck 2019]. For a rank-2 tensor $\alpha_{\mu\nu}$, the decomposition gives:

$$\alpha_{\mu\nu} = \frac{1}{3}\alpha^{(0)}\delta_{\mu\nu} + \frac{1}{4}\alpha^{(1)}_{\sigma}\epsilon_{\sigma\mu\nu} + \alpha^{(2)}_{\mu\nu}$$

where:

$$\begin{cases} \alpha^{(0)} = \alpha_{\mu\mu} \\ \alpha^{(1)}_{\sigma} = \epsilon_{\sigma\mu\nu}(\alpha_{\mu\nu} - \alpha_{\nu\mu}) \\ \alpha^{(2)}_{\mu\nu} = \alpha_{(\mu\nu)} - \frac{1}{3}\alpha_{\sigma\sigma}\delta_{\mu\nu}. \end{cases} \tag{3.4}$$

After adding all three contributions in Eq. 3.3, we get:

$$\begin{aligned} \Delta E(F, m_F; \omega) = &-\alpha^{(0)}(F;\omega)|\mathbf{E}^{(+)}|^2 - \alpha^{(1)}(i\mathbf{E}^{(-)} \times \mathbf{E}^{(+)})_0 \frac{m_F}{F} \\ &- \alpha^{(2)}(F;\omega)\frac{(3|E_0^{(+)}|^2 - |\mathbf{E}^{(+)}|^2)}{2}\left(\frac{3m_F^2 - F(F+1)}{F(2F-1)}\right) \end{aligned} \tag{3.5}$$

with:

$$\begin{cases} \alpha^{(0)}(F;\omega) = \sum_{F'} \dfrac{2\omega_{FF'}\langle F||\mathbf{D}||F'\rangle^2}{3\hbar(\omega_{FF'}^2 - \omega^2)} \\ \alpha^{(1)}(F;\omega) = \sum_{F'}(-1)^{(F+F')}\sqrt{\dfrac{3F(2F+1)}{2(F+1)}}\begin{Bmatrix} 1 & 1 & 1 \\ F & F & F' \end{Bmatrix}\dfrac{\omega\langle F||\mathbf{D}||F'\rangle^2}{\hbar(\omega_{FF'}^2 - \omega^2)} \\ \alpha^{(2)}(F;\omega) = \sum_{F'}(-1)^{(F+F')}\sqrt{\dfrac{40F(2F+1)(2F-1)}{3(F+1)(2F+3)}}\begin{Bmatrix} 1 & 1 & 1 \\ F & F & F' \end{Bmatrix}\dfrac{\omega_{FF'}\langle F||\mathbf{D}||F'\rangle^2}{\hbar(\omega_{FF'}^2 - \omega^2)}. \end{cases} \tag{3.6}$$

$\alpha^{(0)}$, $\alpha^{(1)}$ and $\alpha^{(2)}$ stand for the scalar, vector and tensor polarizabilities respectively.

The hyperfine reduced dipole elements $\langle F||\mathbf{D}||F'\rangle$ can be written in terms of the fine ones $\langle J||\mathbf{D}||J'\rangle$, whose values can be found in [Steck 2001]:

$$\begin{aligned} \langle F||\mathbf{D}||F'\rangle = &\langle J||\mathbf{D}||J'\rangle \times (-1)^{1+F'+J+I} \\ &\times \sqrt{2F'+1}\begin{Bmatrix} J & J' & 1 \\ F' & F & I \end{Bmatrix}. \end{aligned} \tag{3.7}$$

Analysis of the different light shift contributions

We now focus on the effects of the different contributions, as shown in Fig. 3.2.

Fig. 3.2(a) shows the unperturbed structure of the $|F = 4\rangle$ and $|F' = 5\rangle$ manifolds of Cesium. We can see in Fig. 3.2(b) that the scalar shift amounts to an offset of the hyperfine manifold which depends only on the wavelength and the intensity of the light. This offset is state-dependent (between ground and excited state manifolds)

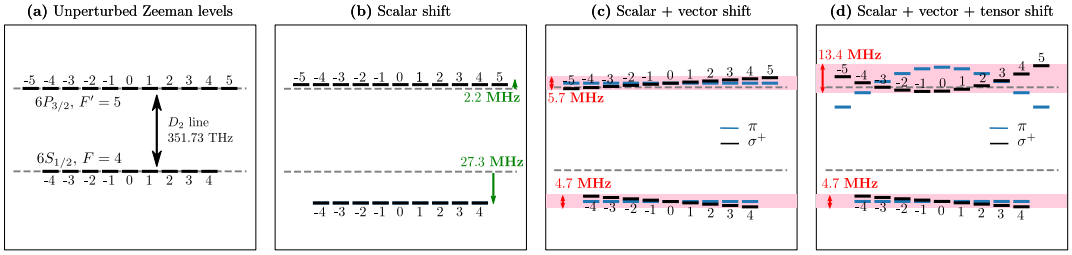

Figure 3.2: Effect of the different shift contributions induced by a π and σ^+ polarized light on the $|F = 4\rangle$ and $|F' = 5\rangle$ manifolds of Cesium. As an example, numerical values for the shifts and broadenings are given for an intensity of 10 mW/μm^2 at a wavelength of 1064 nm. Vertical axis not to scale. (a) Unperturbed hyperfine structure. (b) Effect of the scalar light shift: each hyperfine manifold is offset depending on its F number but irrespective of the m_F number. This amounts to a change of the resonant transition frequency. This can be compensated using magic wavelengths, for which the shift becomes independent of F: the levels are still perturbed but the transition frequency remains the same. (c) Effect of the scalar and vector light shifts. The linear dependence on m_F of the vector shift is clearly visible, hence the parallel made with a fictitious magnetic field. This shift causes a broadening of the hyperfine manifold when performing spectroscopic measurements, and can be cancelled by using only linearly polarized light fields. (d) Total shift. The tensor shift has a quadratic dependence on m_F. In most cases, the unperturbed Zeemaan states $|m_F\rangle$ are not eigenstates of the complete hamiltonian. Reproduced from [Berroir, Bouscal, et al. 2022].

and thus leads to a shift of the resonant transition. From an experimental point of view, this shift can in some cases be suppressed by making use of the so-called magic wavelengths [McKeever et al. 2003; Ye et al. 2008], which are available for some alkali atoms like Cesium (but not Rubidium). When the trapping light is at a magic wavelength, the shift becomes state independent and thus the resonant transition remains unchanged.

The form of the second term of Eq. (3.5) highlights the different dependencies of the vector part. The main parameter is the ellipticity of the incident light, and the effect is a state-dependent shift proportional to the magnetic quantum number, which is shown in Fig. 3.2(c). This can be seen as the action of a fictitious magnetic field given by [Le Kien et al. 2013b; Albrecht et al. 2016]:

$$\mathbf{B}_{\text{fict}} = \frac{\alpha^{(1)}}{\mu_B g_{nJF} F}(i[\mathbf{E}^{(-)} \times \mathbf{E}^{(+)}]).$$

This shift can be canceled by using linearly polarized light, for which the cross product vanishes and thus the fictitious magnetic field as well. In practice around nanophotonic waveguides, or in the tight-focusing regime, this is non trivial because of the strong longitudinal component of the electric field that typically introduces ellipticity [Van Mechelen and Jacob 2016]. In such settings counterpropagating beams have been used [Le Kien et al. 2005; Goban et al. 2012; Lacroûte et al. 2012; Corzo et al. 2019] to cancel out this longitudinal component.

The tensor part indicated by the third term is the most difficult to cancel in practice. We will not detail the mathematical description of this contribution and only make practical statements. Most noticeably, it vanishes for $J = 0$ and $J = 1/2$ states due to the dependence on J of the tensor polarizability. However, it is not the case for excited $J = 3/2$ states, which will then experience a significant tensor shift. Regarding the electric field dependence, for pure π or $\sigma^{\pm}$ polarizations, the tensor

shift part of the Hamiltonian is diagonal in the unperturbed hyperfine basis. It leaves the eigenvectors unchanged while adding a m_F-dependent shift proportional to m_F^2, as seen in Fig. 3.2(d). For arbitrary polarizations however, the tensor shift part of the Hamiltonian is non-diagonal and thus introduces coupling terms between hyperfine states. This situation is more complex and best solved numerically.

3.1.2 Casimir-Polder interactions

The interaction of the atom with a close surface can lead to an additional light shift, which can be critical when computing traps close to nanostructures. Indeed, a neutral atom can have a dipole induced by vacuum fluctuations of the electromagnetic field. If this atom is at a very short distance from a perfect conductor surface, the radiation pattern of this induced dipole will be modified by the time-lagged reflected field from the surface: the dipole interferes with its mirror image. Dispersive QED calculations show this usually leads to a short-range attractive potential. For a dielectric structure, its dielectric function over all possible frequencies enters into the game. This so-called Casimir-Polder (CP) potential [Casimir and Polder 1948] has to be taken into account in order to have a full description of the potential seen by the atoms. The CP potential, which is a vacuum-induced force, is usually complex to calculate as it depends on the atoms, the material and the precise geometry of the structure (see Appendix A.2), all these factors influencing the exact response of the system to a vacuum-induced fluctuating dipole.

For simplicity, only the first order of the potential for an infinite plane is usually considered $U_{\mathrm{CP}} = C_3/d^3$ [Johnson et al. 2004], where d is the distance to the surface. For an optical nanofiber (ONF), it is a sufficiently good approximation especially at very short distances. Even if the curvature of the surface can lead to a 40% error at the position of the trap minimum, the effect remains negligible compared to the light-induced potentials [Le Kien et al. 2004]. For more complex structures like dielectric slabs that we will encounter in Chapter 5, we use a more detailed approximation based on pairwise summation that takes into account the overall shape of the structure (see Appendix A.3).

3.1.3 Total optical trap around a nanostructure

After introducing the formalisms needed to describe both atom-light and atom-surface interactions, we can combine them to compute the full trapping potential created by arbitrary optical fields close to a surface. In order to compute this trapping potential as well as the level mixing induced by the interactions, it is convenient to define an effective Hamiltonian for the system, which can be eventually diagonalized. For the Stark shift defined in Eq. (3.5) this effective Hamiltonian is given by:

$$\begin{aligned}\mathcal{H}_{\mathrm{Stark}} = &- \alpha^{(0)}(F;\omega)|\mathbf{E}^{(+)}|^2 \\ &- \alpha^{(1)}(F;\omega)(i\mathbf{E}^{(-)}\times\mathbf{E}^{(+)})_0\frac{F_0}{F} \\ &- \alpha^{(2)}(F;\omega)\frac{(3|E_0^{(+)}|^2-|\mathbf{E}^{(+)}|^2)}{2}\left(\frac{3F_0^2-\mathbf{F}^2}{F(2F-1)}\right).\end{aligned} \tag{3.8}$$

As the CP interactions do not mix m_F sublevels, we can write the CP Hamiltonian as $H_{\mathrm{CP}} = U_{\mathrm{CP}}\hat{\mathbb{1}}$. Using perturbation theory, the total shift for a level $|N, J, F, m_F\rangle$ is then given by:

$$\Delta E_{|N,J,F,m_F\rangle}(\omega) = \\ \langle N, J, F, m_F | \mathcal{H}_{\text{Stark}}(F;\omega) + \mathcal{H}_{\text{CP}} | N, J, F, m_F \rangle. \tag{3.9}$$

It is important to notice that, in general, the Hamiltonian is not diagonal in the $|N, J, F, m_F\rangle$ basis, because of the vector and tensor terms. Therefore it is necessary to diagonalize it in order to obtain both the correct eigenvalues and eigenvectors. Even though for low power, F is still a good quantum number, it is not the case anymore for m_F and the interaction gives rise to level mixing inside the magnetic Zeeman manifold.

3.2 Trapping atoms around waveguides: the two-color evanescent trap scheme

In the field of cold atoms, optical trapping with far-off resonance light has a long history [Chu et al. 1986]. Whether it is for creating optical lattices in order to study atom hopping [Wintersperger et al. 2020], or for optical tweezers to trap single atoms [Schlosser et al. 2001], harnessing optical dipole trapping has had prolific applications. All of these traps are usually done in free space, far from any dielectric material.

Trapping atoms close to nanostructures, with trap sites at less than λ away from the surface, has been a withholding challenge for many years. While it is possible to retro-reflect a trap beam on the surface [Thompson et al. 2013], it became clear that using guided modes of the structures, with evanescent behaviour in vacuum was a promising idea.

The first trap around nanoscale waveguides exploiting guided modes to have been proposed concerned ONFs. It was first suggested to use a red-detuned guided mode to attract the atoms to the fiber, and repulse them with the centrifugal force that appears when the fiber diameter is about half the wavelength of the trapping light [Balykin et al. 2004]. [Le Kien et al. 2004] proposed instead to use a second guided beam, blue-detuned this time, as a repulsive potential in order to overcome the attractive red light at short distances.

As the two beams have a different decay length away from the structure, by tuning the relative powers, it is possible to engineer a stable trap at around 200 nm from the fiber surface. The main condition for stable trapping is that the decay length of the red is slower than of the blue, so that a repulsive barrier can exist at short distances. The first experimental realization of such a trap was achieved in 2010 in [Vetsch et al. 2010] and then in [Goban et al. 2012] in a state-independent, compensated configuration. Since then, this two-color trap has been proposed in other nanoscopic waveguides that we will encounter throughout this manuscript [Yu et al. 2014; Fayard et al. 2022; Bouscal et al. 2024].

After introducing the theoretical framework enabling to calculate trapping potentials and state dependent light shifts as well as the most common trapping scheme, we will now present its implementation in `nanotrappy`.

3.3 `nanotrappy`, a package to compute dipole traps around nanostructures

`nanotrappy` is a Python package that computes the trapping potentials induced by laser beams, with an emphasis on modes guided inside nanostructures. It has been

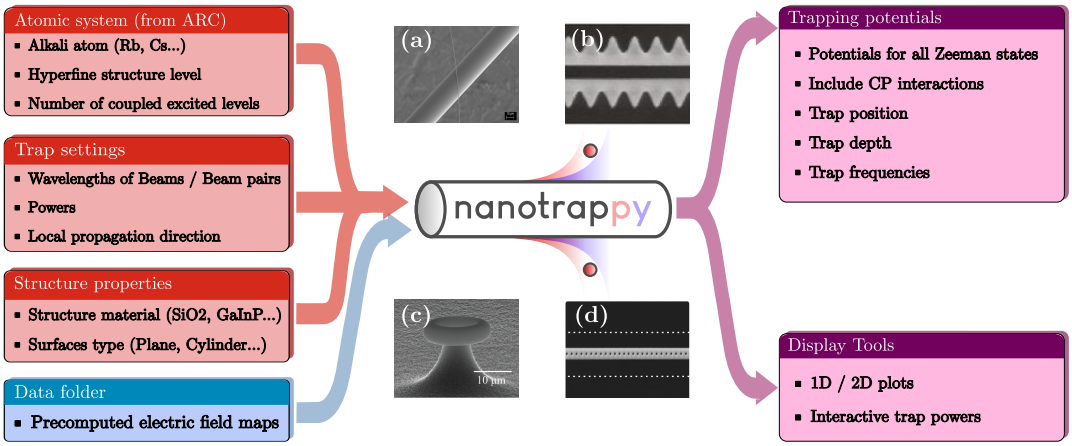

Figure 3.3: Workflow of the `nanotrappy` package for calculating optical trap potentials. The Python package takes multiple physical parameters as inputs (atom, trap configuration, material) as well as pre-computed electric field maps, and returns the trap and its properties. A user-friendly graphical interface enables also to tune the powers of the trapping beams, making it easy to integrate the simulation in a structure optimization workflow. Some examples of nanostructures for which optical trapping of atoms can be simulated in `nanotrappy`: (a) Optical nanofiber [Gouraud 2016], (b) Alligator photonic-crystal waveguide [Hood et al. 2016], (c) Microtoroid [Alton 2013], (d) Nanoscale optical cavity [Thompson et al. 2013].

tested on Python 3.7-3.11 distributions. `nanotrappy` is programmed for being efficiently included in the optimization workflow of nanophotonic structure design. We take advantage of the object-oriented programming style of Python in order to provide the user with a simple and accessible API, and present the simulation results in a user-friendly manner (see Fig. 3.4). Note that the package is not a field solver. Instead, based on a pre-computed electric field (done using any third-party solver), `nanotrappy` interfaces this electric field distribution with an atomic system given physical parameters. Figure 3.3 summarizes the capabilities of the package. Performance-wise, even if the limiting factor of such optimization workflows is often the actual computation of the fields, an effort has been made to make this package efficient, and to provide a parallelizable option that allows to split the computation on multiple CPU cores if needed. In the following, we introduce the structure of the code through the base classes provided.

Atomic system

The first class defined is the `atomicsystem` class. It is based on the Alkali-Rydberg-Calculator (ARC) package [Šibalić et al. 2017]. ARC was created for Rydberg physics, i.e. computation of Rydberg levels, transitions and interaction potentials for any alkali atom. Conveniently, it was also populated with the up-to-date spectroscopic data such as transition frequencies or dipole matrix elements for non Rydberg transitions. It is very useful to use as a basis but has to be adapted as it natively handles J states but does not have as much capabilities regarding hyperfine F states. Building an `atomicsystem` amounts to selecting an alkali species, as well as a state defined by the N, L, J, F quantum numbers.

As `nanotrappy` is closely linked with current experiments, it incorporates features that have proven to be crucial for the development of such systems. Among those, the issues linked with inhomogeneous broadening of an optical transition due to the

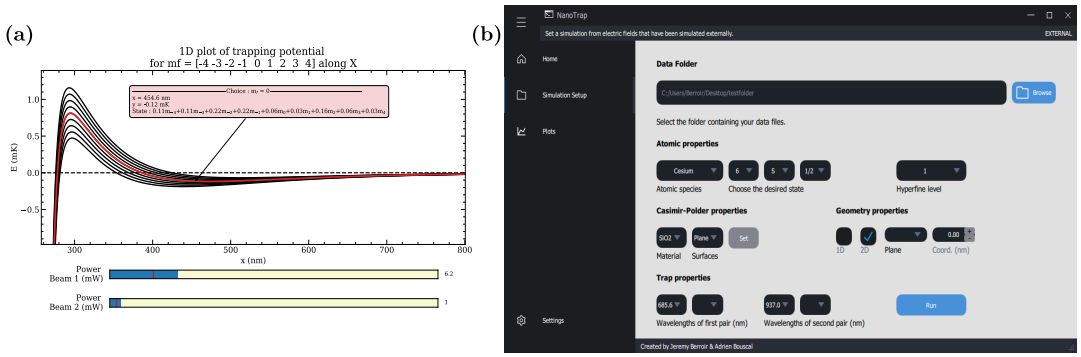

Figure 3.4: Screenshots illustrating the interactivity of `nanotrappy`. (a) Interactive 1D plot with sliders to control the powers of the red-detuned and blue-detuned trapping lights. The levels can also be selected to see their decomposition on the unperturbed basis. The same controls are given for 2D plots. (b) Screenshot of the Graphical User Interface (GUI) provided as an .exe file with the package. It offers the same functionalities through dropdown menus and allows to optimize the trapping scheme without having to interact with Python code.

Zeeman dependent nature of the light shifts call for calculations of such light shifts down to the hyperfine structure level. The polarizability of any given hyperfine state is thus computed by `nanotrappy`, as well as C_3 coefficient of the Casimir-Polder atom-surface interaction.

Beams and Trap

Specific classes are used to describe the trapping light. For each trapping light, a `Beam` instance is created, based on a wavelength, a power and a folder containing formatted pre-computed electric fields[3]. The package will then check if the electric fields are available at that wavelength in the specified folder and select the relevant data. Counterprogating beams geometries can also be created with the `BeamPair` class, as well as more complex trapping schemes with more that two beams with `BeamSum`. Once the beams are created, they are bundled into the `TrapBeam` class together with a local propagation axis.

Materials and Surfaces

To handle CP interactions, a `Surface` class is available, as well as three main subclasses `Plane`, `Cylinder` and `Slab`. The first two use the first order approximation $U_{\mathrm{CP}} = C_3/d^3$ which allows to handle most practical cases. The latter uses an expression derived with the pairwise summation approximation introduced in Appendix A.3.

The `Material` class comes with pre-implemented subclasses of materials (air, SiO_2, SiN, GaInP...). The C_3 coefficient is computed on the fly for the atom-material combination. This class can be easily extended to add other materials.

Running the simulation

Once all these physical parameters have been defined in the respective classes, they are bundled together in a `Simulation` class that realizes the actual computation. Along the way, the parameters are saved as JSON files and the results as .npy numeric tables. Conveniently, a check is performed before any simulation whether these particular

[3]Formatting of the fields should follow a predefined convention, see website of the project at https://LKB-QuantumNetworks.github.io/nanotrappy.

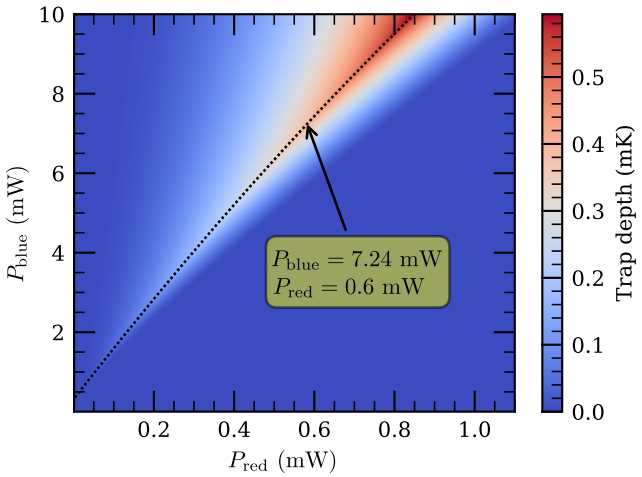

Figure 3.5: Automatic optimization of the trap depth with nanotrappy. The powers of the two beams (P_1 and P_2) are varied and the trap depth is calculated to generate a 2D map. The dotted line follows the local trap depth maximum. A value of 0 means that the configuration chosen does not allow atom trapping.

parameters have already been used, in which case the previously computed data is used, avoiding thereby unnecessary computation.

Interactivity and optimization

The `Vizualizer` class is a core class that allows for easy optimization of the structure. Once the simulation has run, the vizualizer will display the results along with interactive sliders that allow to control the power of each individual beam, as seen on Fig. 3.4(a). As mentioned in Section 3.3, it is possible to display the trapping potential for all Zeeman sublevels inside a given hyperfine state. An interactive tool allows to select a chosen Zeeman state and display additional information such as the decomposition of this new eigenstate on the basis of the unperturbed ones. If a stable trap (i.e. a potential local minimum in all 3 directions) exists, the trapping position and frequencies are also displayed. This enables to quickly and conveniently scan the powers of the beams in order to check whether the desired value for these parameters are accessible or if the structure design needs to be improved. Moreover, automatic optimization is available: the powers of the red- and blue-detuned beams can be scanned to optimize a chosen parameter (either the trap depth, trap frequency or the trap position) given electric field distributions, as displayed in Fig. 3.5.

A standalone GUI application is also made available with the same functionalities, and shown in Fig. 3.4(b).

3.4 Use of nanotrappy for existing structures

In this section we now show the versatility of `nanotrappy` by computing the trapping potentials for atoms around three well-known nanotructures that have been used by the community. We benchmark `nanotrappy`'s results against published literature to demonstrate the accuracy of the package. We also use `nanotrappy` to introduce a novel nanofiber trap configuration allowing to trap atoms at distances below 100 nm from the fiber surface.

3.4.1 Nanofibers and uniform waveguides

Optical nanofibers have been largely used for atom-nanophotonics interfaces. Relatively simple fabrication technique of subwavelength diameter, low-loss silica nanofibers [Tong et al. 2003] and their easy integrability with cold atoms makes them a popular choice. Early works involved an optical nanofiber embedded in an ensemble of atoms in a magneto-optical trap (MOT) [Nayak et al. 2007, 2009]. Nanofibers were the platforms where the two-color trap was proposed, but it took a few more years to have a state insensitive (same light shift for the ground and excited states) and compensated trap proposed to suppress the inhomogeneous light shifts and later demonstrated for Cesium atoms [Le Kien et al. 2005; Goban et al. 2012; Lacroûte et al. 2012].

In `nanotrappy`, both electric and magnetic fields of the guided modes of a nanofiber can be analytically computed thanks to the fiber eigenvalue equation [Snyder and Love 2012], given a radius and a refractive index for the dielectric. This calculation is implemented in `nanotrappy`, so that for this simple structure the package can be used for computing both the electric field distributions and the trapping potentials.

We use `nanotrappy` to compute the trapping potentials for an uncompensated trap and a compensated one, and compare them to published literature [Vetsch et al. 2010; Lacroûte et al. 2012]. The results are shown in Fig. 3.6. In both cases the goal is to compute the characteristics of the traps for ground and excited state of Cesium atoms around a SiO_2 nanofiber with 250 nm radius. The differences between the schemes come from the wavelengths, powers, polarization and number of beams used.

Figure 3.6(a) shows the configuration of the uncompensated trap. The parameters are chosen as per [Vetsch et al. 2010]. A pair of red-detuned, counterpropagating beams at 1064 nm and a single, blue-detuned beam at 780 nm are used to create the trapping potential. The red- and blue-detuned beams have orthogonal linear polarization. The total powers used are $P_{\text{red}} = 2 \times 2.2$ mW and $P_{\text{blue}} = 25$ mW respectively. The obtained results are shown in Fig. 3.6(b-d). A 1D array of evenly spaced traps along the nanofiber with depth 0.4 mK is achieved at around 195 nm from the surface. The corresponding trap frequencies are 355 kHz, 71 kHz, 355 kHz along r, θ and z respectively. We note that, in such a trap only the ground state Cesium atoms are trapped, the excited $6P_{3/2}$ states experience a repulsive potential as shown in 3.6(d). The results are in excellent agreement with [Vetsch et al. 2010; Vetsch 2010].

For the compensated trap, as shown in Fig. 3.6(e), the scheme and parameters are chosen as per [Lacroûte et al. 2012]. In this configuration, a second, counterpropagating blue beam is used in order to reduce the vector shift as much as possible. The powers are $P_{\text{blue}} = 2 \times 16$ mW and $P_{\text{red}} = 2 \times 0.95$mW. The results are shown in Fig. 3.6(e-h). Stable traps are obtained for both the ground and excited levels. The computation yields a trap at 190 nm from the surface with depth ~ 0.5 mK for the ground state and 0.3 to 0.6 mK for the excited state. The results are also in excellent agreement with [Lacroûte et al. 2012; Goban 2015].

We now use this well-known example of a trap around a nanofiber to illustrate step-by-step how to compute dipole traps with `nanotrappy`. This sample code, only a few lines long, can be easily adapted to any structure and alkali atom of interest.

1. First, an atomic system has to be specified. This part is built on the ARC package [Robertson et al. 2021], hence all alkali atoms can be used. The

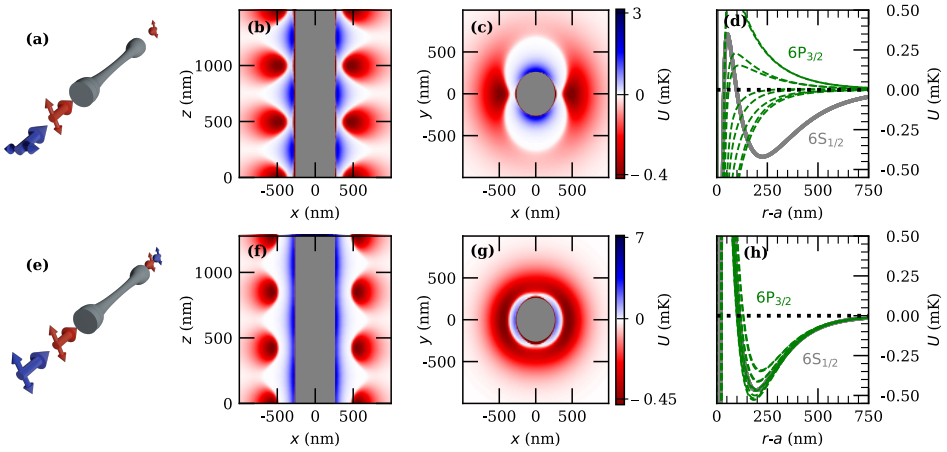

Figure 3.6: Two configurations of optical trapping around a nanofiber. (a) Non-compensated nanofiber trap configuration with only one blue-detuned beam, and crossed polarizations. (b) 2D potential in the (x,z) plane, with same parameters as in [Vetsch et al. 2010]. Trapping sites are periodically placed with distance $\lambda_{\mathrm{red}}/2$ because of the red standing wave. Stable traps with depth of around 0.4 mK are achieved. (c) 2D potential in the (x,y) plane at the z-position of a trap. (d) Radial dependence of the trapping potential of the ground ($6S_{1/2}$) and excited ($6P_{3/2}$) states along the x axis. The splitting of the m_F states in the ground state is not visible at this scale. The trap minimum is located at around 195 nm from the surface but the atoms in the excited state are not trapped. (e-h) Same plots for the state-insensitive, compensated configuration (see text) with parameters from [Lacroûte et al. 2012]. (g) Azimuthal trapping is less efficient in this configuration but (h) a stable trap for excited atoms, with low inhomogeneous broadening is obtained.

other parameters of the `atomicsystem` define the hyperfine level of the ground state considered for trapping, here ground state $6S_{1/2}$ Cesium with $F = 4$.

```
import nanotrappy as nt
#Definition of the atomic system
syst = nt.atomicsystem(Caesium(), "6S1/2",f = 4)
```

2. The trapping scheme has then to be defined: Number of beams, wavelengths, counterpropagating or not... The wavelength is of the utmost importance as the package will look for the spatial mode corresponding to this wavelength in the data folder.

```
#Defining the beams used for trapping
blue_beam = nt.Beam(780e-9,"f",25*mW)
red_standing_wave = nt.BeamPair(1064e-9, 2.2*mW, 1064e-9,
    ↪2.2*mW)
trap = nt.Trap_beams(blue_beam, red_standing_wave,
    ↪propagation_axis="Z")
```

3. (Optional) The structure around which the atoms are trapped can also be defined. This is necessary for including the CP potential U_{CP} (see Sec. 3.1.2). Infinite planes and cylinders are already implemented in the package using $U_{\mathrm{CP}} = C_3/d^3$, as well as slabs with tunable thickness. Many materials are also included. If not specified, no surface is added.

```
#Adding a surface for CP interactions
surface = nt.Cylinder((0,0,0),250e-9,"Z")
```

4. The `simulation` object that will store the results of the calculations is created, taking as arguments all the previous objects, plus the data folder and the structure material.

```
#Create the simulation object that will store the results
Simul = nt.Simulation(syst,Nm.SiO2(),
    ↪trap,datafolder,surface)
```

5. The geometry (Axis or Plane) on which we want to compute the trap is defined. Running the simulation then boils down to one line of code.

```
Simul.geometry = nt.PlaneXZ(y=0)
Simul.compute()
trap2D = Simul.total_potential()
```

   For the 500x500 grid of Fig. 3.6 this evaluation takes only a few seconds on a standard office computer.

6. A `vizualizer` object has then to be created to display the results and manipulate the optical powers.

```
viz = nt.Vizualizer(Simul,"Y")
fig, ax, slider_ax = viz.plot_trap()
```

3.4.2 Photonic-crystal waveguides: the APCW

We now consider a second example involving trapping atoms around a slow-mode photonic-crystal waveguide. Such a platform with atoms trapped by evanescent modes is still to be experimentally demonstrated, but several theoretical proposals for trapping have recently emerged. A one-color dipole trap for trapping Cesium atoms was first proposed around structured nanobeams or slot waveguides [Hung et al. 2013; Yu et al. 2014], using only a single laser blue-detuned from the D_2 transition. But this schemes lead to small trap depths of a few tens of microkelvins.

To overcome this difficulty without increasing the powers of the trapping beams, generally limited by the power handling of such devices, a two-color dipole trap was also proposed for the Caltech alligator photonic crystal waveguide (APCW), following the ideas implemented with nanofibers. As many designs were proposed over the years for the APCW, we choose the last one that comes with a computation of the optical trap [Burgers et al. 2019]. We compute the trapping potential for this APCW with `nanotrappy` and compare them to [Luan 2020]. The results are presented in Fig. 3.7.

Figure 3.7(a) shows the aforementioned waveguide and Fig. 3.7(b) its band structure. The parameters of the device are the same as in [Burgers et al. 2019]: the period is 370 nm, the gap is 240 nm wide, the edge modulation is 140 nm and the refractive index is 2 (for SiN). With these numbers the air and dielectric bands are aligned to the D_2 and D_1 lines of Cesium, respectively.

Figure 3.7(c) shows a trapping potential in two dimensions. The parameters for the trap are chosen as in [Luan 2020]. A beam red-detuned from the D_1 line of Cs at 895 nm ($\delta = 2\pi \times 1700$ GHz) and a beam blue-detuned from the D_2 line at 848.1 nm ($\delta = 2\pi \times -130$ GHz) are used to create the trapping potential. The total powers are $P_{\text{blue}} = 230\,\mu\text{W}$ and $P_{\text{red}} = 3\,\mu\text{W}$.

As shown in Fig. 3.7(d-e), a stable trap in the x and y directions is obtained. There is also trapping in the z direction, although with less strength. The trapping sites are positioned in the center of the gap, with a trap depth of 3 mK. The trapping

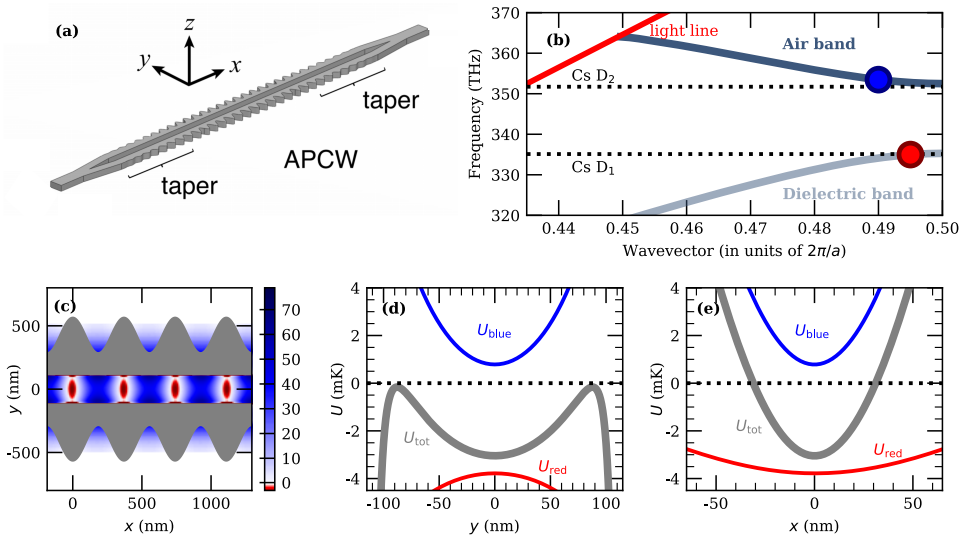

Figure 3.7: Stable trapping of atoms inside the slot of the Caltech alligator photonic-crystal waveguide (APCW). (a) Schematic of the full APCW, with taper regions, extracted from [Goban et al. 2015]. (b) Optimized band structure of the APCW with band edges aligned to D_1 and D_2 lines. Blue- and red-detuned modes used for trapping are shown with the corresponding color circles. The light line for a suspended waveguide in vacuum is shown in red. (c) 2D total trapping potential with superimposed structure. Periodic stable traps with depth of more than 3 mK are achievable with powers of 230 µW for the blue beam and 3 µW for the red one. (d) Calculated trapping potential along the y axis. The grey curve corresponds to the total potential $\mathrm{U_{tot}} = \mathrm{U_{red}} + \mathrm{U_{blue}} + \mathrm{U_{CP}}$. Blue- and red-detuned beam contributions are plotted separately for comparison. (e) Trap along the x axis. The trapping frequency in this direction is large, with $\omega_x = 2\pi \times 3$ MHz.

frequencies are $\omega_y = 2\pi \times 1.1$ MHz, $\omega_x = 2\pi \times 3$ MHz and $\omega_z = 2\pi \times 570$ kHz. Confinement on the propagation direction is therefore very strong. The values computed with `nanotrappy` are in very good agreement with [Luan 2020]. The slight differences come mostly from electric field simulations which were performed independently here.

In Chapter 5, we will introduce two other photonic-crystal waveguides (the comb waveguide [Fayard et al. 2022] and the half-W1 waveguide [Bouscal et al. 2024]) for which we have also found stable trapping schemes thanks to `nanotrappy`.

3.4.3 Microtoroid resonators

`nanotrappy` is a versatile package as it can also be used for structures that are not waveguides. We demonstrate this here by studying the trapping of atoms near a microtoroid resonator.

One of the earliest proposal of trapping atoms with the evanescent field of a microstructure was to use the whispering gallery mode (WGM) of a microsphere [Mabuchi and Kimble 1994]. High Q factor and small mode volume of such resonator [Vernooy et al. 1998b] can achieve single-atom strong coupling on average [Vernooy et al. 1998a], even with hot vapor. Later, a toroidal microcavity was proposed as ultrahigh-Q microresonator for cavity QED [Spillane et al. 2005]. It shows an even smaller mode volume and increased tunability arising from the added degree of freedom associated with the principal and minor diameters of the microtoroid. Experimentally, strong interaction with a WGM of a microtoroid was demonstrated with

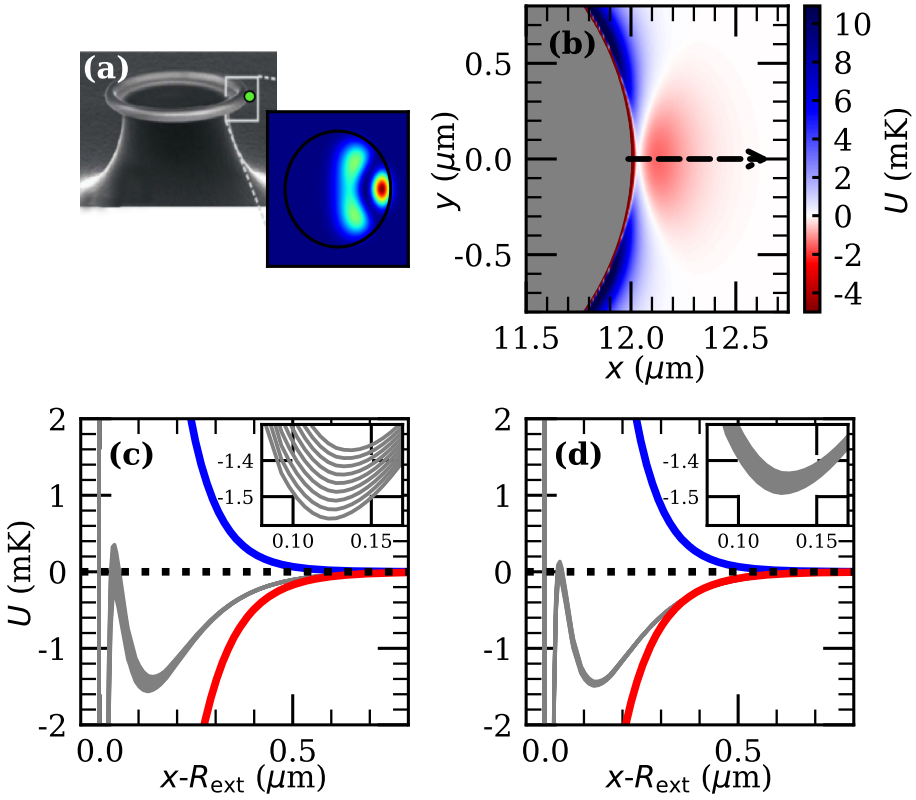

Figure 3.8: Two-color scheme for trapping atoms on the symmetry plane of a microtoroid resonator. (a) SEM image of a fabricated SiO_2 microtoroid extracted from [Spillane et al. 2005]. Inset: 2D intensity profile of the red-detuned higher-order mode used for trapping at 898 nm. (b) 2D potential on the outer edge of the structure. The line cuts (c) and (d) are taken along the dashed arrrow. (c) Trapping potential along y, at $z = 0$ and with CP potential included. The inset shows a zoom at the position of the minimum to highlight the splitting of the m_f states due mostly to the vector shift. (d) Trapping potential along x with a counterpropagating red-detuned beam. The inset shows a reduced splitting than on the former case due to cancellation of the vector shift thanks to the red-detuned beam (from 0.19 to 0.05 mK). Residual splitting is caused by the blue beam.

free-falling Cesium atoms [Aoki et al. 2006b; Dayan et al. 2008]. Following these first demonstrations, schemes for trapping Cesium atoms in the evanescent field of such microresonators were proposed [Alton et al. 2011; Stern et al. 2011; Alton 2013].

Following [Alton et al. 2011; Stern et al. 2011] we compute with `nanotrappy` the trapping potential for Cesium atoms near a SiO_2 microtoroid with a 12 µm outer major radius R_{ext}, and a 1.5 µm minor radius r. Figure 3.8(a) shows the above mentioned waveguide and the transverse shape of the red-detuned mode used for trapping. The blue one is composed of only one lobe in this plane. Modes of the electric field in a microtoroid can be described by their azimuthal number m, corresponding to the number of cancellations of the field in one turn, and their number p, counting the number of lobes in the transverse plane. We choose $m = 119$ and $p = 0$ for the blue mode and $m = 106$ and $p = 1$ for the red-detuned beam (same modes as in [Alton 2013]). The latter has a faster decay in the vertical direction than the blue one, preventing the atoms from approaching the surface out of the symmetry plane

[Vernooy and Kimble 1997; Alton 2013].

Figure 3.8(b) shows the simulation of a two-color dipole trap in a section of the microtoroid with beams red- and blue-detuned from the Cs D_2 line at 852 nm. Lasers with powers ~ 50 mW give a trap depth of about 1.5 mK. Field profiles were computed with COMSOL Wave Optics module[2]. Using only one beam of each color produces a strong vector shift at the position of the atoms, manifested by a inhomogeneous broadening of around 0.2 mK at the trap minimum. Adding a counterpropagating red beam reduces this effect by a factor 4. This reduction is shown on Figs. 3.8(c) and (d). As for the previous examples, the numbers are in very good agreement with the litterature. This validates the accuracy of the package and makes it an efficient tool to study optical trapping near nanostructures. `nanotrappy` has proven to be valuable as it has been used by our partners in a FET-Open European project (DAALI) and other research groups [Fayard et al. 2022].

3.4.4 Development of a nanofiber near-field trap

We come back to the nanofiber and use `nanotrappy` this time not to confirm existing trapping schemes, but to propose a new one that could achieve trapping sites just 50 nm away from the nanofiber surface.

To make faster and more efficient quantum operations with trapped atoms, it is necessary to have them as close as possible from a given structure or to be able to have lattice sites closer than the wavelength [González-Tudela et al. 2015]. As today most of the dipole traps are based on optical lattices or on evanescent waves, the characteristic lengths in such traps are given by the laser wavelength, even if some tunability can be achieved (by varying the angles in the lattices [Wintersperger et al. 2020], or tuning the powers of the guided modes [Goban et al. 2012]). Some theoretical proposals which use the CP interactions as a resource are pushing the limits down to few tens of nanometers [Chang et al. 2014a; Bellouvet 2018; Bellouvet et al. 2018], but were limited to plasmonic structures. We show that using `nanotrappy` to carry out the calculations, we can propose a novel, near-field trapping scheme for Cesium atoms close to a dielectric ONF.

This trap differs from the usual two-color dipole trap used in all former examples. In this scheme, the attractive potential is solely caused by the vacuum forces, i.e the Casimir-Polder potential. This potential is only significant at close distances and has a power law decay ($\propto r^{-3}$ at close distances) and not exponential like the evanescent guided modes used in the two-color dipole traps [Engelen et al. 2009].

We achieve a metastable trap by dressing the electronic transition $6P_{3/2} \rightarrow 7S_{1/2}$ between two excited states with a guided evanescent mode ("Shift beam" in Fig. 3.9(a), slightly blue-detuned). This spatially modulates the light shift of state $6P_{3/2}$ while leaving the ground state unaffected (except by the CP). A second guided beam is sent through the fiber at at frequency ω_L, slightly blue-detuned from the $6S_{1/2} \rightarrow 6P_{3/2}$ bare transition ω_0 ("Dressing beam"). Because of the state $6P_{3/2}$ energy, ω_L becomes resonant at a single tunable point $y = y_b$. An atom that slowly approaches the surface will only follow the Casimir-Polder ground state attractive potential U_{CP}. But moving closer to y_b, its $6S_{1/2} \rightarrow 6P_{3/2}$ transition will become resonant with ω_L, as the energy of the dressed $6P_{3/2}$ increases close to the surface. This creates an atomic-dressed state, with a small excited-state component when the atom is close to

[2] 2019 COMSOL Multiphysics simulation software https://www.comsol.fr/wave-optics-module. The simulation was done in 2D, considering axis symmetry of the system.

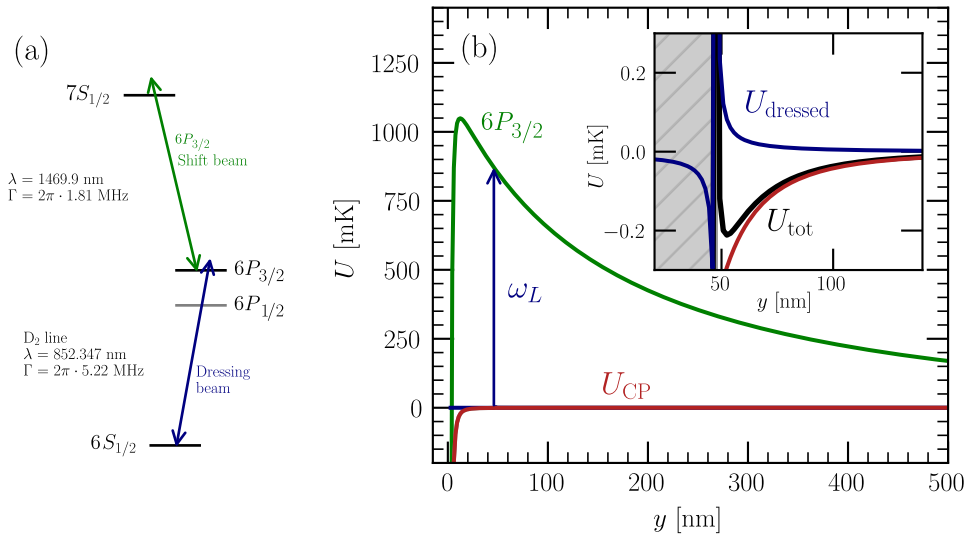

Figure 3.9: A double dressed subwalength trap for Cesium around a nanofiber. (a) Relevant energy levels used for the doubly-dressed subwavelength trapping scheme. (b) A guided blue-detuned beam from the $6P_{3/2} \rightarrow 7S_{1/2}$ transition creates a repulsive spatially dependent shift for the $6P_{3/2}$ state. A second weak guided beam at frequency ω_L, slightly blue-detuned beam from the $6S_{1/2} \rightarrow 6P_{3/2}$ bare transition, is sent through the fiber. It becomes at resonance at a few tens of nanometers from the fiber surface (at the position of the blue arrow) creating a very sharp repulsive potential $U_{\rm dressed}$ (see text) for the ground state atoms. The sum with the CP potential $U_{\rm CP}$ creates a metastable trapping potential $U_{\rm tot}$. The grey hatched area corresponds to a region where the potential prediction of our steady-state simulation are not physical.

y_b. This excited component follows the $6P_{3/2}$ potential (in green in Fig. 3.9(b)) which is strongly repulsive. This leads to an average net repulsive force which is represented by the steady-state potential $U_{\rm dressed}$ for $y > y_b$. The sum with $U_{\rm CP}$ yields $U_{\rm tot}$ with a trapping position at $y_t = 52\text{nm} > y_b$ and a depth of 200 µK. At this distance, the β factor is around 0.2 (compared to < 0.04 in actual ONF experiments).

The shift beam is at a wavelength 1469 nm and 25 mW of power. It is detuned from the transition by 125 GHz. Only 9 nW of dressing beam is needed, it is detuned by 18 GHz from the $6S_{1/2} \rightarrow 6P_{3/2}$ bare transition.

The detuning $\Delta = \omega_L - \omega_0$ varies spatially and is very small at the position of the trap minimum. It is then important to consider the heating of the atoms via photon scattering, even for such small powers. The scattering rate of a two-level system in a far-off detuned trap of depth $U_{\rm dip}$ is given by [Steck 2019]:

$$\Gamma_{\rm sc} = \frac{\Gamma U_{\rm dip}}{\hbar \Delta} \tag{3.10}$$

In our simulation, $\Delta \simeq 1\text{GHz}$ at the trap minimum and $U_{\rm dip} = 0.2\text{mK}$. This gives $\Gamma_{\rm sc} \simeq 1\text{MHz}$ which converts to a heating rate of around 0.05 K.s^{-1}. With these parameters, it seems unlikely to observe atoms trapped in this near-field trap as they would be kicked out in a few milliseconds because of strong scattering. We might however play with the different powers and detunings to limit this effect.

To our knowledge, this is the first theoretical proposal of a near-field trap using guided modes. Indeed, this scheme has been introduced with plasmons as they also

permit an evanescent decay that can be used to dress the excited state [Bellouvet et al. 2018][3]. In this case, the in-trap atom heating is less important as the plasmonic resonance intensity, which modulates the $6P_{3/2}$ energy, decays faster than the "Shift beam" in the nanofiber case These traps can be critical tools to go to regimes of even stronger interactions, as we will see in the proposal in Chapter 5, going closer to the waveguide surface enables a very strong enhancement of the Purcell factor.

Conclusion

In this chapter we have introduced thoroughly the theory of interaction of atoms with a light field out of resonance. We have shown the importance of taking into account the complex light-shift structure for our realistic traps in experiments and have introduced a Python package that efficiently simulates these traps for alkali atoms close to nanostructures. Its main strengths is that it is fast and can give the trapping potentials and all relevant parameters for all the Zeeman sublevels for the specified ground and excited states. We provided three example of atom trapping near nanophotonic structures and demonstrated thereby the accuracy of the calculation by comparing our results with published literature. We also introduced a realistic near-field trap with guided evanescent modes of an ONF. `nanotrappy` has also been critical for the design of the photonic-crystal waveguides proposed for the hybrid atom-nanophotonics platform studied throughout this thesis, making the search for stable traps around these complex structures more efficient.

The application of the package `nanotrappy` is not limited to the simulation of dipole trap around nanophotonic structure or in evanescent fields. It can also be used to simulate optical dipole trap for any given intensity distribution of the trapping field. It will be used in Chapter 7 for computing optical tweezer traps. This makes the package appealing to a larger atomic physics community. In addition, the capability of calculating the shifts of the Zeeman levels in a given light field, can be used for estimating dephasing and fidelity of a quantum operation and is therefore useful to the large atom-based quantum information community.

We will now switch gears and introduce the field of photonic crystals to get a better idea of the waveguides we want to fabricate and around which we want to trap atoms via evanescent dipole trapping.

[3] This decay is faster than for the intensity of a nanofiber-guided mode, allowing to have a larger detuning at the trap minimum therefore reducing the heating rate of the atoms inside the trap.

Part II:

Realistic platforms based on photonic-crystal waveguides

- Prepare ship for light speed.
- No, no, no, light speed is too slow.
- Light speed, too slow?
- Yes, we're gonna have to go right to... ludicrous speed. [*Gasps*]

Space Balls (1987)

CHAPTER 4

THE ROAD TO COMBINE PHOTONIC-CRYSTAL WAVEGUIDES AND COLD ATOMS

Contents

This chapter is an introduction to photonic-crystal waveguides and how they can be designed in order to be interfaced with atoms. As photonic crystals are a wide field of research, this chapter only aims at introducing some important concepts in order to understand the dispersion engineering which is one of the main emphasis of this work. After a general introduction on the theory of bands in photonic crystals, we look at how a structure guiding light in one direction at a reduced velocity can be engineered from them. We introduce some relevant methods for the simulation of these structures and techniques for the optimization of their dispersion curves. We finally list the design constraints our waveguides must meet in order to be able to interface them with Rubidium atoms. Some constraints common to all the designed waveguides are discussed.

4.1 The promising case of photonic crystals

What is the similarity between the skin of chameleons, peacock feathers and distributed Bragg reflector lasers? All exhibit a nanoscopic periodic arrangement of transparent materials that modify the propagation behaviour of the light. The properties of these arrangements explain the change of color of the mentioned reptiles [Teyssier et al. 2015], the iridescence of the bird feathers [Yoshioka and Kinoshita 2001; Saranathan et al. 2021] and the light confinement in some diode lasers. Moreover, chameleons can tune the periodicity of these structures depending on whether they are stressed or relaxed, modifying dynamically those properties. These periodic arrangements of materials with different refractive indices are common in nature, and are called **photonic crystals**.

4.1.1 Photonic crystals and their band gaps

Electrical properties of materials have been studied since the mid-19$^{\text{th}}$ century. Semiconductors, displaying more exotic behaviors than simple conducting or insulating materials, were discovered and a theory explaining them was proposed shortly after that. This theory states that all the non-trivial features in electron transport, characteristic of semiconductors, arise from the periodicity of the potential seen by the free electrons as they travel through a static lattice of cations.

Photonic crystals (PC) can be seen as an optical equivalent to these semiconductors. Light propagates through a periodic environment created by the dielectric function of the material $\epsilon(\mathbf{r})$. Their most striking feature is the existence of photonic band gaps at some frequencies, which forbid the propagation of light (as in their electrical counterparts). This feature was predicted by Eli Yablonovitch [Yablonovitch 1987] and Sajeev John [John 1987] in the 1980s. Their theoretical analysis sparked enthusiasm in the community to fabricate structures showing a complete photonic band gap.

In the optical regime, the first demonstration of a PC with a photonic band gap (in 2 dimensions) was made at the University of Glasgow by [Krauss et al. 1996]. Photonic crystals were soon used to control the light in high-index semiconductor structures, combining light confinement via photonic bandgaps and non-linear electronic processes. This lead to many optical applications such as efficient four-wave mixing devices [Chopin et al. 2022], electrically pumped lasers [Crosnier et al. 2017] or autocorrelators for picosecond pulses [Monat et al. 2014]. More exotic applications of photonic crystals in the optical regime include gaz spectroscopy with waveguides [Vlk et al. 2021; Peng et al. 2023] and weighing of living bacteria thanks to hollow cavities [Therisod et al. 2022]. In all following discussions, we will consider photonic crystals in the optical regime.

Periodicity in optical materials: a simple example

Works on the propagation of light in periodic materials go back well before the seminal papers of Yablonovitch and John. As such, Lord Rayleigh was already interested in multilayer structures as early as 1887 [Rayleigh 1887]. We will in the next paragraph try to give some intuition on the phenomena causing the appearance of a band gap in periodic structures by taking the example of a one-dimensional multilayer mirror.

Figure 4.1 shows the most simple case of a 1D photonic crystal, i.e. a stack of layers of two materials with different dielectric constants. This structure, known

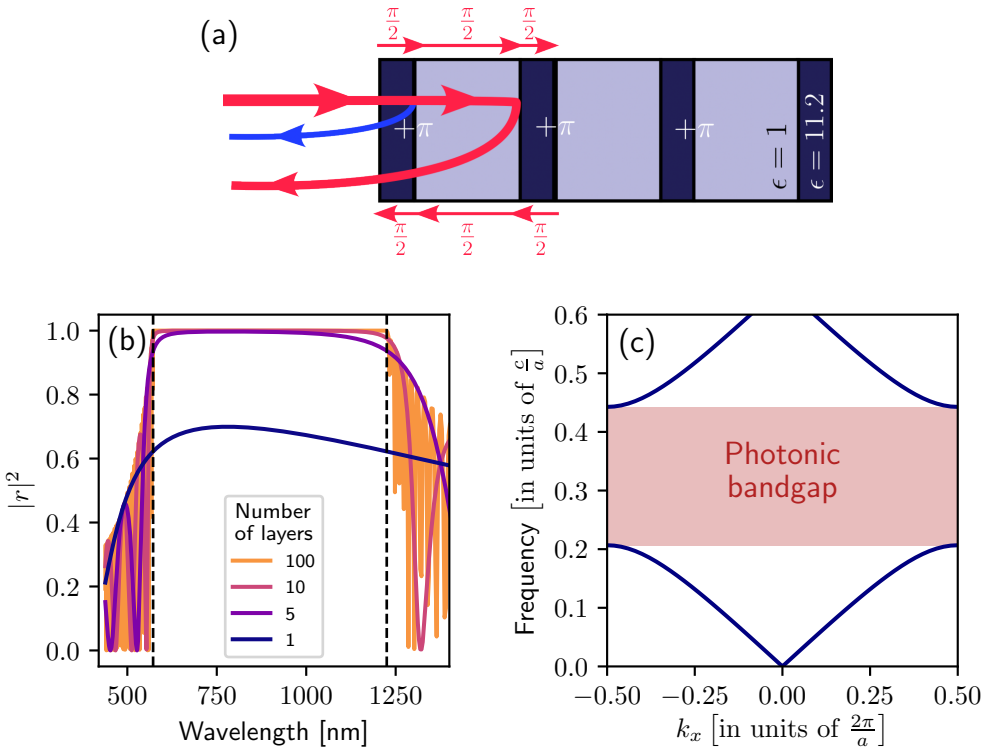

Figure 4.1: Photonic band gap opening in a 1D photonic crystal. (a) Sketch of a 1D Bragg mirror, with layers of different dielectric constants and widths. The arrows show the splitting of the light at each interface. The π phase shifts are displayed at the relevant interfaces. (b) Reflectivity as a function of the number of layers constituting the mirror. A photonic band gap, manifested by high reflectivity, appears progressively when increasing the number of layers. We note that only a few layers are enough to see some reflection. Dotted lines show the extent of the theoretical band gap computed via Plane wave expansion (PWE). As PWE assumes periodic boundary conditions, it amounts to simulating an infinite number of layers. (c) Dispersion relation of the infinite 1D Bragg mirror in reduced units. $a = d_1 + d_2$ is a period of the Bragg grating. The reflection spectrum of (b) was obtained through transfer matrix formalism and the band diagram in (c) via PWE (see Appendix B).

as a Bragg mirror[1], exhibits most of the interesting properties of PCs. At each interface, some of the light is reflected while some is transmitted. This structure can be made to work as a mirror. To this end, we want all the reflected waves to interfere constructively (and the transmitted ones destructively). We recall that a wave going from a medium with index n_1 to a medium with index $n_2 > n_1$ acquires a phase of π upon reflection on the interface, while it is not the case on the opposite case. We can design the structure so that each reflected beam has a phase that is a multiple of 2π on the input plane of the Bragg mirror by ensuring the waves pick up a phase $\pi/2$ while propagating in any given layer (as highlighted in Fig. 4.1(a)). This can be simply written as a condition on the width of the layers:

$$d_i = \frac{\lambda}{4n_i} \tag{4.1}$$

where λ is the wavelength of interest and n_i the refractive index of layer i.

[1]Main component of the distributed Bragg reflector (DBR) lasers mentioned in the introduction.

Figure 4.1(b) shows that even for a single layer we already get 70% reflection at the design wavelength λ. This approaches 100% after only a few layers. We note that the reflection is high for a wide range of wavelengths around λ. We conclude that light cannot propagate inside the structure in this range (from about 590 nm to 980 nm). Figure 4.1(b) hence shows the gradual appearance of a photonic band gap caused by the periodicity of ϵ. Figure 4.1(c) provides the dispersion relation of light in a Bragg mirror with infinite layers. The resulting band gap matches the finite layers predictions.

Even if condition (4.1) is not strictly met, a photonic band gap usually exists. Any scattering off the interfaces couples the modes travelling in opposite directions (i.e. separated by $2\pi/a$ in k space) which gives rises to an anti-crossing between optical modes, creating forbidden bands for the light. It can be shown that the gap is the largest for the Bragg condition. As the band gap opens through an interference effect, we can anticipate that the electric field enters quite far into the Bragg mirror. This is in strong contrast with the common process of total reflection at an interface which creates an evanescent field on the opposite side. Note that these effects will hold for all the more complex PCs encountered in the following.

From Bloch waves to band gaps

The exotic behaviors of PCs hence come from coherent scattering of the light on the periodic structure. We here derive a more general framework to study them. We partially follow the approach described in [Joannopoulos et al. 2008]. We are mostly interested in photonic crystals periodic in two dimensions but the following also applies to 3D. To study the propagation of light, one can solve the Maxwell's equations with a periodic dielectric function, already encountered in Chapter 2. It is usually written for the macroscopic magnetic field[2] $\mathbf{H}$ as:

$$\nabla \times \left(\frac{1}{\epsilon(\mathbf{r})} \nabla \times \mathbf{H}(\mathbf{r}) \right) = \left(\frac{\omega}{c} \right)^2 \mathbf{H}(\mathbf{r}). \tag{4.2}$$

Note that we already removed the temporal dependence of the field assumed to be of the form $e^{i\omega t}$. This expression is known as the master eigenvalue equation as it is an eigenvalue equation of the linear operator $\mathcal{L}_\epsilon = \nabla \times \frac{1}{\epsilon(\mathbf{r})} \nabla \times$, with eigenvectors $\mathbf{H}$ and eigenvalues $(\frac{\omega}{c})^2$.

If the structure is not periodic, but defined by a uniform dielectric function $\epsilon(\mathbf{r}) = \epsilon_0 \epsilon_r$, the solutions of Eq. (4.2) are plane waves with wave vector $\mathbf{k}$, such that $\mathbf{H}_\mathbf{k}(\mathbf{r}) = \mathbf{H}_0 e^{i\mathbf{k}\cdot\mathbf{r}}$, where the eigenvectors are now indexed by their wave vector. Injecting these solutions back into Eq. (4.2) gives a relation between $\mathbf{k}$ and ω:

$$\|\mathbf{k}\|^2 = \epsilon_r \left(\frac{\omega}{c} \right). \tag{4.3}$$

This expression is known as the dispersion relation of the structure, and gives crucial information about the propagation of light in this material. We notice that for any given ω, we can find a solution $\mathbf{H}_\mathbf{k}(\mathbf{r})$ such that the dispersion relation is satisfied. The eigenvalue spectrum of Eq. (4.2) is hence continuous in this uniform case.

Let us now assume we have a more general 1D photonic crystal, defined by a periodic dielectric function of period a, $\epsilon(\mathbf{r}) = \epsilon(\mathbf{r} + na\,\hat{\mathbf{e}}_x), n \in \mathbb{Z}$. Can we find a

[2] Expressing the problem in terms of the magnetic field is a convention from the PC community because of mathematical convenience. Indeed, we could find an equation like Eq. (4.2) on the electric field $\mathbf{E}$ but the obtained operator is no longer Hermitian and many mathematical derivations become more involved. $\mathbf{E}$ can anyway be easily derived from $\mathbf{H}$ from the structure relation.

similar relation between $\mathbf{k}$ and ω? Because of the discrete symmetries that exist in the system, it can be shown that all modes with wave vector along x of the form $k'_x + m(2\pi/a)$ are degenerate in frequency [Joannopoulos et al. 2008]. By linearity, a solution of the Maxwell's equations can be written as an infinite sum of plane waves with $k_x = k'_x + m(2\pi/a), m \in \mathbb{Z}$. By factorizing by $\mathrm{e}^{ik'_x x}$, and seeing the infinite sum as a Fourier series, we can write the solutions as:

$$\mathbf{E}_\mathbf{k}(\mathbf{r}) = \mathrm{e}^{ik'_x x}\mathbf{E}_p(\mathbf{r}) \quad \text{and} \quad \mathbf{H}_\mathbf{k}(\mathbf{r}) = \mathrm{e}^{ik'_x x}\mathbf{H}_p(\mathbf{r}), \tag{4.4}$$

where $\mathbf{k} = (k_x, k_y, k_z)$ and $\mathbf{E}_p(\mathbf{r})$ and $\mathbf{H}_p(\mathbf{r})$ are periodic functions in x:

$$\mathbf{E}_p(\mathbf{r} + na\,\hat{\mathbf{e}}_x) = \mathbf{E}_p(\mathbf{r}) \quad \text{and} \quad \mathbf{H}_p(\mathbf{r} + na\,\hat{\mathbf{e}}_x) = \mathbf{H}_p(\mathbf{r}) \quad \text{for } n \in \mathbb{Z}. \tag{4.5}$$

This is known as the **Bloch's theorem**. It means that any mode of the periodic crystal can be written as a plane wave modulated by a periodic function. Because this function is an infinite sum of all modes differing in k_x by $2\pi/a$, two solutions $\mathbf{H}_{\mathbf{k}_1}$ and $\mathbf{H}_{\mathbf{k}_2}$ with $\mathbf{k}_1 - \mathbf{k}_2 = m\frac{2\pi}{a}\hat{\mathbf{e}}_x$, with m an integer, actually represent the same physical modes. It means they will have the same frequency, and the dispersion diagram of the crystal is hence periodic of period $2\pi/a$. This allows to restrict k_x to the range $[-\pi/a, \pi/a]$. This range is known as the first Brillouin zone (1BZ).

Physically, this theorem has crucial implications. It means that for a wave propagating in a periodic structure, its wave vector is not unique anymore, but defined up to a multiple of $\frac{2\pi}{a}$. One could think that adding discrete scatterers in a structure could just impede the propagation as light would randomly scatter off of them. Bloch's theorem shows it is not the case as all the scattering processes are coherent, forming a periodic Bloch enveloppe $\mathbf{u}_\mathbf{k}$.

Because of this periodic enveloppe, the Bloch modes are bounded spatially. This imposes that the spectrum of Eq. (4.2) cannot be continuous anymore[3]. This means that instead of having a continuous spectrum of frequencies ω, we have a discrete ensemble $\omega_n(\mathbf{k})$ associated to the solution $\mathbf{H}_{\mathbf{k},n}$. $\omega_n(\mathbf{k})$ is the dispersion relation of the structure, also referred to as the band structure, as it is composed of a given number of bands. Knowing $\omega_n(\mathbf{k})$ is crucial as it gives enormous amounts of information on the light propagation. The most important aspect for us in the following is the group velocity of the light. It is defined as the velocity of a wavepacket inside the structure. For a given band n, it is given by:

$$v_{\mathrm{g},n}(\mathbf{k}) = \nabla_\mathbf{k}\omega_n(\mathbf{k}). \tag{4.6}$$

We see in Fig. 4.1(c) that the band becomes flat at the edge of the 1BZ. This means that the group velocity goes to 0 for this mode. This feature is common to all photonic crystals. Light can propagate very slowly in a PC, and this is exactly what we will try to harness in our platform.

[3] While this property is very general, [Joannopoulos et al. 2008] give an intuitive explanation by using the orthogonality of guided modes. If the spectrum was continuous, two modes of frequency ω and $\omega + \delta\omega$ should not be too different and could be written as $\mathbf{H}_\mathbf{k}$ and $\mathbf{H}_\mathbf{k} + \delta\mathbf{H}_\mathbf{k}$. Taking their dot product gives $(\mathbf{H}_\mathbf{k}, \mathbf{H}_\mathbf{k}) + (\mathbf{H}_\mathbf{k}, \delta\mathbf{H}_\mathbf{k})$ which cannot be zero as the two terms are not of the same order of magnitude. Hence the spectrum has to be discrete, allowing for important changes of the spatial mode structure from one band to another, preserving the orthogonality.

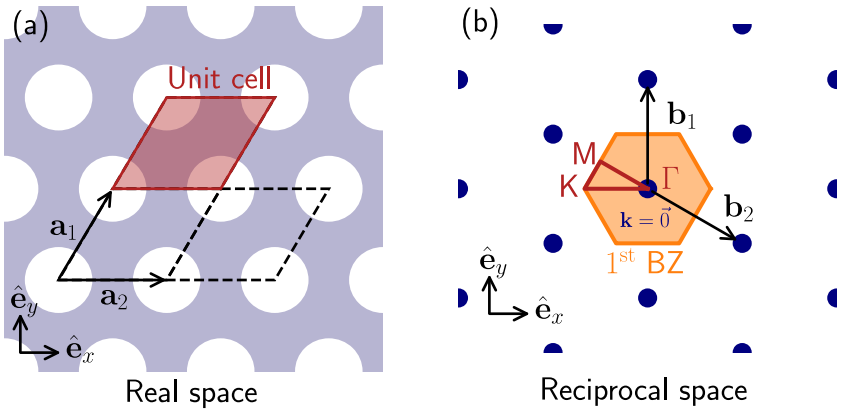

Figure 4.2: Real and reciprocal lattice for a 2D hexagonal photonic crystal. (a) Lattice in real space with the unit vectors that leave the lattice unchanged. $\mathbf{a}_1 = \frac{a}{2}\hat{\mathbf{e}}_x + \frac{a\sqrt{3}}{2}\hat{\mathbf{e}}_y$ and $\mathbf{a}_2 = a\,\hat{\mathbf{e}}_x$. A few unit cells are represented. (b) Reciprocal lattice in k space. $\mathbf{b}_1 = \frac{4\pi}{\sqrt{3}a}\hat{\mathbf{e}}_y$ and $\mathbf{b}_2 = \frac{2\pi}{a}\hat{\mathbf{e}}_x - \frac{2\pi}{a\sqrt{3}}\hat{\mathbf{e}}_y$. The dots are spaced by $\frac{4\pi}{a\sqrt{3}}$ and have no extension. The orange shaded area is the 1st Brillouin zone around $\mathbf{k} = 0$. The red triangle is the irreducible part of the 1BZ with the high symmetry points (Γ, M, K). As the dots are separated by a linear combination of the $\mathbf{b}_i$, they all represent the same physical mode.

4.1.2 How to make waveguides out of photonic crystals

In this section, we show how to guide light with a structure based on a 2D photonic crystal. We analyze the band structure of a common waveguide made with a linear defect introduced in a 2D structure.

Photonic crystals in two dimensions

Figure 4.2 generalizes the concept of Brillouin zone in two dimensions. For a 2D lattice, there is a periodicity along 2 unit vectors ($\mathbf{a}_1$ and $\mathbf{a}_2$) represented in Figure 4.2(a). Any solution of the eigenvalue equation is hence written:

$$\mathbf{H}_\mathbf{k} = \mathrm{e}^{i\mathbf{k}\cdot\mathbf{r}}\mathbf{u}(\mathbf{r}), \tag{4.7}$$

with $\mathbf{k} = k_1\mathbf{b}_1 + k_2\mathbf{b}_2$ where the reciprocal lattice vectors $\mathbf{b}_i$ are given by $\mathbf{a}_i \cdot \mathbf{b}_j = 2\pi\delta_{ij}$. Figure 4.2(b) shows the corresponding reciprocal lattice and the 1st Brillouin zone in orange. The 1BZ is hence two-dimensional and each band is a surface immersed in a 3D space. Such a full band structure in 3D would be very hard to read. To simplify the vizualization, we exploit the rotational symmetries of the structure. The full 1BZ can be reconstructed by rotations and mirror symmetries from the red triangle shown in Fig. 4.2(b), known as the irreducible 1BZ. Γ, K and M are referred to as high-symmetry points, and the band structure is usually plotted along the lines joining them.

A final symmetry has to be noted. Indeed, as it is invariant along z, the 2D PC is unchanged by a mirror reflection by the (x, y) plane (changing z into $-z$ while leaving x and y invariant). This property allows Eq. (4.2) to be separated into two independent equations, depending on the parity of the mode by this mirror reflection. If the mode is symmetric, it means the normal component of the electric field has to be zero. $\mathbf{E}_\mathbf{k}$ will be tangential to the symmetry plane. Conversely, as $\mathbf{H}_\mathbf{k}$ is a pseudovector, its

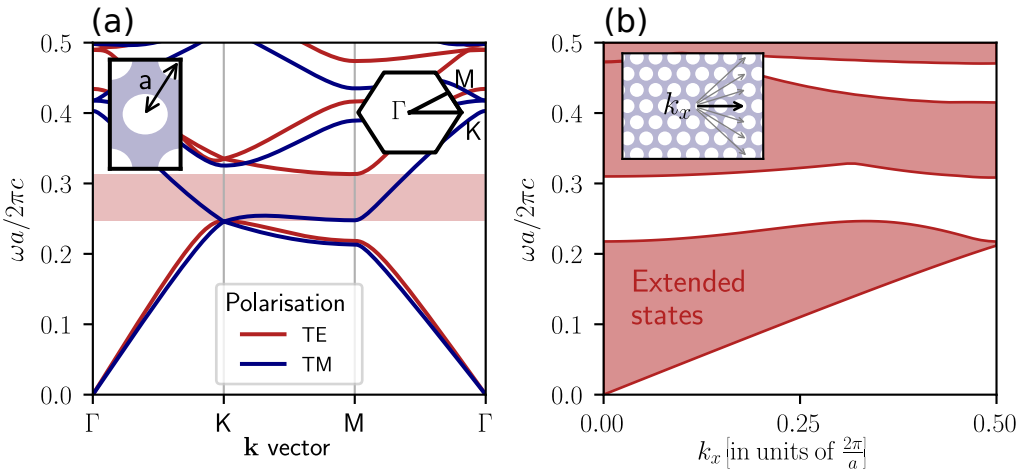

Figure 4.3: Band diagram of a 2D PC with hexagonal lattice and its projection in 1D. The parameters are the same as in Figure 4.2(a). (a) Band structure for both TE and TM polarizations. A band gap, shaded in red, exists only for the TE polarization. Insets recall the real and reciprocal lattices. (b) Projection of the TE-polarization diagram onto the x direction. The discrete modes become bands as for a given k_x we consider all possible extended modes with any k_y as depicted in the inset. The TE band gap is conserved as the highest and lowest frequencies are usually at the high symmetry points. Both diagrams are computed with a Guided Mode Expansion (GME) algorithm (see Appendix B).

tangent component will vanish, and only H_z will be non zero. This mode, which can be described completely by its (E_x, E_y, H_z) components is called *transverse-electric* (TE). If the mode is anti-symmetric, the same reasoning gives a mode described only by its (H_x, H_y, E_z) components, and referred to as *transverse-magnetic* (TM). These two polarizations have different behaviors and dispersion relations, so we have to consider them independently.

Plotting the cut of the band structure of the two polarizations along the edges of the irreducible 1BZ gives rise to the diagram shown in 4.3(a). A band gap exists for the TE symmetry, but not for the TM one [Johnson et al. 1999]. It can be shown that the extrema of a band are usually reached on the edges of the 1BZ[4], which makes the restriction to the irreducible BZ reasonable. Note that the band diagram is given in terms of the reduced frequency $\omega a/2\pi c$.

Instead of following the edges of the irreducible BZ, we can choose to represent the band structure by projecting it along a given axis, for example along x. For every point $\mathbf{k}$ in the 1BZ, we compute its frequency, and display it at the corresponding position k_x, with k_x the projection of $\mathbf{k}$ along x. Figure 4.3(b) shows such a projection for the TE modes. We see that the band structure is no longer a set of lines, but is composed of a discrete set of continuous bands. Indeed, for a given k_x, we have the contribution of an infinite number of modes, spanning a perpendicular line at position k_x (as represented in real space in the inset of Fig. 4.3(b)). The slight variation of ω_n for neighboring $\mathbf{k}$ gives rise to wide, continuous bands. We notice, as expected, that the TE gap is conserved by this projection.

[4]Consider a 1D photonic crystal (for example the one in Fig. 4.1(c)). The frequency is the lowest at $k = 0$ and increases with k. A band gap opens at $k = \frac{\pi}{a}$ and the upper band energy keeps increasing for higher values of k widening the band gap. The band gap is hence the smallest at the edge of the 1BZ.

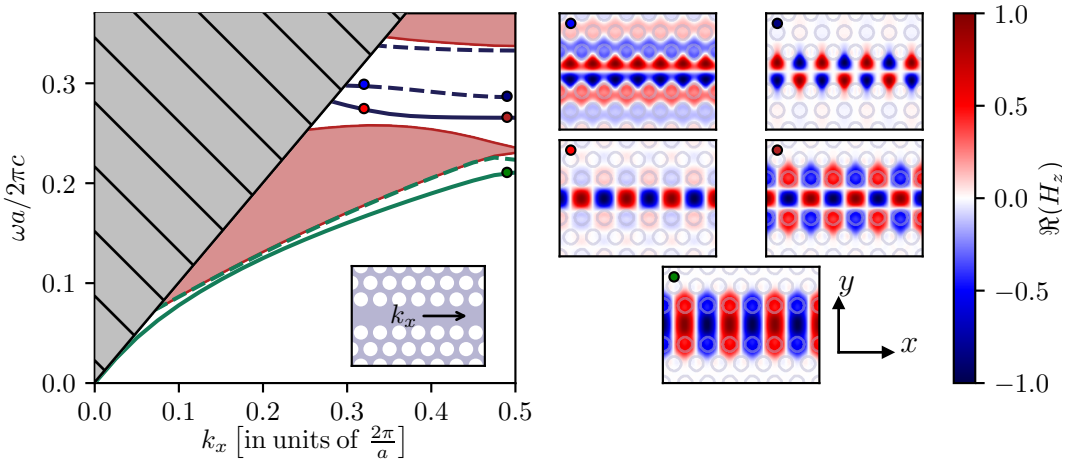

Figure 4.4: Band structure of a W1 waveguide with a thickness of 150 nm, and mode profiles of some H_z modes. Left: Band structure of a W1 waveguide. Blue bands are index guided along y, while purple bands are gap guided. Dashed bands are y-even while continuous ones are y-odd. Right: 5 maps of the real part of H_z as indicated by the dots in the band structure. Because the real part of the magnetic field (pseudovector) is displayed, the even and odd modes are reversed.

Optical waveguiding in the band gap of a 2D PC

In order to create a waveguide out of this photonic-crystal structure, we would want modes to propagate inside the crystal along a given direction. A common way of making photonic-crystal waveguides (PCW) consists in adding a defect along a line into the periodic structure which makes a mode appear inside the band gap of the 2D PC. For the 2D hexagonal PC considered before, this can be done by removing a line of holes along the x direction. This so-called linear defect creates an effective 1D waveguide, called a **W1 waveguide**, out of a 2D structure and adds a few modes on the projected band structure, as can be seen in Fig. 4.4. These added modes are guided along the linear defect. Two mechanisms explain this guiding:

- Total internal reflection: the average index of refraction of the 2D PC is smaller than the one of the linear defect because of the presence of the holes. Hence the light sees a core of high refractive index, surrounded by an effective cladding. The guiding happens by total internal reflection as in optical fibers. This mechanism explains the two lowest bands in Figure 4.4. These modes are very similar to uniform ridge waveguide modes of adequate width and index contrast (as we will see in Figure 4.6).

- Photonic band gap guiding: For frequencies inside the photonic band gap of the 2D PC, the PC behaves as a perfect mirror and as the light cannot enter this regions, it remains guided into the defect. This is the dominant effect explaining the bands located inside the band gap in Figure 4.4. Their field maps show a lot of diversity not achievable with the index guided bands.

W1 waveguides have attracted a lot of interest since the late 1990s [Krauss et al. 1996]. They have been used already for the creation of correlated photon pairs through four-wave mixing [Xiong et al. 2011], for gas spectroscopy [Vlk et al. 2021] or as single-photon sources via integration of quantum dots [Arcari et al. 2014]. They will serve as a basis to introduce important concepts in the following. The

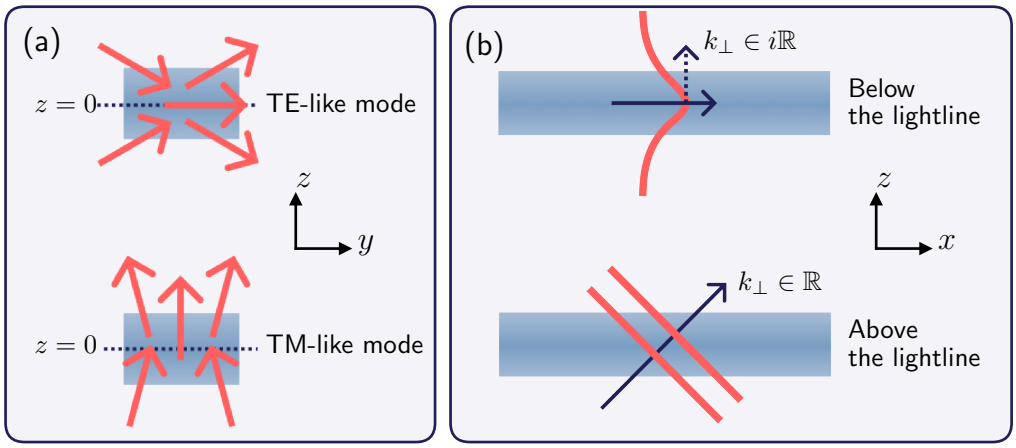

Figure 4.5: Symmetries and confinements along z. (a) Difference of symmetries of the electric field for a TE-like and TM-like modes in the transverse plane. (b) The guiding in the slab depends on the projection of the total wave vector $\mathbf{k}$ along the z axis. Radiative modes (down) have an intrinsic loss mechanism due to out-of plane diffraction.

main waveguide studied in this work [Bouscal et al. 2024] is derived from the W1 design.

Photonic-crystal waveguide slabs

Realistic structures do not have translational invariance along the z axis. They have a limited transverse size, which can be on the order of the wavelength. We call slabs these structures that are close to a 2D geometry. This limited size along z can be wanted as it allows for confinement of the light in the third direction. We obtain waveguides with confinement along y because of the 2D PC and along z by total internal reflection.

However, this breaking of z-invariance adds constraints on the existence of guided modes within the slab. We neglected earlier the component of the k vector along z which cannot be the case here anymore. For a mode to stay guided inside the structure, one needs to ensure the conditions for total internal reflection guiding on the top and bottom interfaces are respected. It is the case if k_z is an imaginary number, as this will translate as an evanescent wave in this direction. This can be written as:

$$k_z^2 = \|k\|^2 - k_\|^2 < 0 \Leftrightarrow \omega < \frac{c}{n} k_\| \tag{4.8}$$

with $k_\|$ the component of the wave vector within the slab. If this condition is not fulfilled, k_z is real[5] the modes cannot be constrained between the two faces of the slab and they will just propagate through. We call them *radiative modes* (see Figure 4.5(b)). In a band diagram this manifests as a zone that we call the light cone. It is represented by the hatched area in Fig. 4.4(a).

Another modification from the 2D regime concerns the polarization of the modes. Indeed, the mirror symmetry now only exists only on the plane $z = 0$. TE and TM

[5] k_z is either real or imaginary and cannot be any complex number. Indeed, as light propagates in the PCW, $k_\|$ must be real, hence k_z^2 is a real number, which means $k_z \in \mathbb{R}$ or $k_z \in i\mathbb{R}$.

modes cannot be defined as before as z invariance is broken. It is still possible to define TE-like and TM-like modes, depending on their symmetry upon reflection by the remaining symmetry plane (x, y) at $z = 0$. Figure 4.5(a) shows schematically how these new modes behave.

4.1.3 Slow light in 2D photonic-crystal waveguide slabs

We showed in the previous section that we can use linear defects in 2D PC to create gap-guided bands inside such defects. We note from Fig. 4.4 that the gap-guided bands are much flatter than the index-guided ones, meaning light propagates at a much lower group velocity. This can be interesting for enhancing the interaction with trapped atoms as we will see later.

Why PCWs have such flat bands?

We try to develop here an intuitive understanding on the origin of these flat bands. We start by looking at the simplest possible 1D waveguide, a nanobeam of constant refractive index (taken here to be $n = 3.35$). Its band diagram is shown in Fig. 4.6(a). The dispersion has been artificially folded as the waveguide is not periodic. We then add periodicity, for example by introducing air holes in the center of the structure with a period a. The diagram is folded at the edge of the 1BZ, and gaps appear at these positions. Moreover, light scatters coherently on the holes, coupling the modes travelling in opposite directions. The blue and green bands couple even though they have opposite group velocities giving rise to an additional avoided crossing in the band structure (i.e. a band gap of width Δ) and a mixing of the spatial mode profiles along the band, represented by the green-to-blue shading.

Depending on the strength of the coupling and the position of the crossing in k_x, this can give rise to rather flat bands. Changing the strength of the coupling to tune the curvature of the slow mode is the main idea of the dispersion engineering that will be the heart of next section.

We showed that we can have waveguiding and slow light in one-dimensional PCWs. The 1D strategy has attracted a lot of attention in the quest to enhance light-matter interactions with PCWs. Indeed, the proposed Alligator [Goban et al. 2014], comb [Fayard et al. 2022] and sawfish [Bopp et al. 2022] waveguides are all one-dimensional. They can be realized with structures with less tunable geometrical parameters (hence easier to design) and provide strong confinement in the transverse directions via total internal reflection. We focus on this work on using linear defects in 2D PC slabs instead. What are the advantages of such 2D waveguides with respect to their 1D counterparts?

1D vs 2D photonic-crystal waveguides

2D PCWs offer many advantages regarding fabrication, tunability and available bandwidth of guided modes. Indeed, we show in the following that 2D PCWs allow to use guided modes that are further away from the light line, opening more space for red- and blue- detuned modes which will be critical to our platform. 2D PCWs also have some interesting advantages when it comes to dispersion engineering.

As seen before, there are two different kinds of processes to guide the light inside a waveguide, internal reflection and band gap guiding. The lowest bands in the W1 band diagram are index-guided bands. At these frequencies, the light "sees" a central uniform slab of dielectric constant 11.2, and external regions on each side of a lower refractive index. Figure 4.6(b) shows some equivalent uniform waveguide that gives

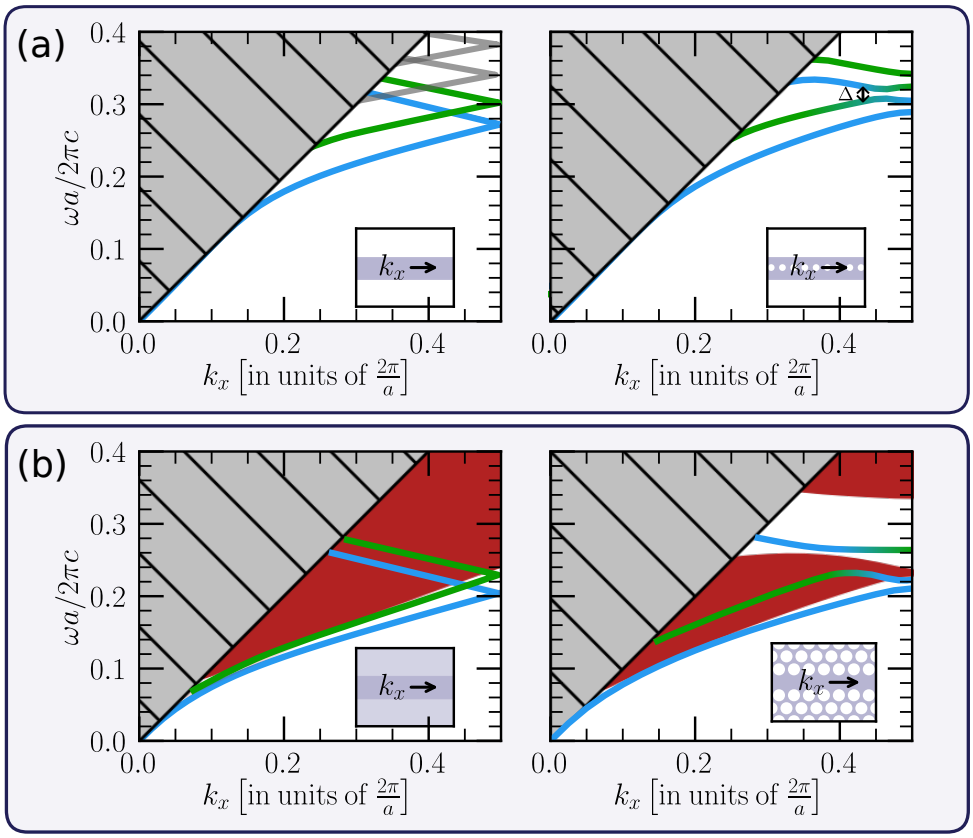

Figure 4.6: Scheme of the effect of the periodicity on 1D and 2D PCWs. (a) Left: Artificially folded band diagram of a 1D uniform slab waveguide of thickness 150 nm, width 450 nm and dielectric constant $\epsilon = n^2_{\text{GaInP}}$ suspended in air. Inset shows the structure in the (x, y) plane. The blue and green lines are the first two guided modes (higher orders in grey). Right: Adding the periodicity (via air holes of radius 70 nm separated by $a = 230$ nm) opens band gaps at the edges, and enables coupling between bands which manifests as an avoided crossing (gap of width Δ) and mixing of the bands as shown by the green to blue shadings. This creates relatively flat bands. (b) Left: Uniform waveguide of the same refractive index as (a) but with claddings on each side with $\epsilon = \bar{\epsilon}$, the average dielectric constant over the 2D PC. The lower index contrast drags the modes lower in frequency, represented by the red continuum of guided modes. Right: When introducing periodicity, a band gap opens in the continuum, the same as in Fig. 4.3(b), allowing to access the slow mixed guided mode of Fig. 4.4. The lowest band is not mixed, hence is only index-guided.

index-guided bands similar to the W1 ones. The dielectric constant in the brighter regions is given by the average ϵ over a 2D PC with hexagonal lattice ($\bar{\epsilon} = 7.88$). The first two modes with the lowest energy are highlighted. They are below the continuum[6] and do not interact, as the folding of the Brillouin zone is again artificial. Compared to the same nanobeam into the air, we notice that reducing the index constrast Δn has shifted the available guided modes down, way further from the light line.

We turn on the periodicity, this time by replacing the external regions by a periodic array of holes. The dispersion relation becomes the one of the already encountered W1 waveguide. The blue and green bands couple, giving rise to the slow-mode gap-guided band of W1 which will populate the band gap, which just opened in the continuum (see Fig. 4.4). As before the shading represents the mode mixing. This interpretation is supported by the variation of the modes profiles along a given band. On the insets showing the gap-guided band profiles of Fig. 4.4, we see that the modes in a band are drastically different at low k or close to the edge of the 1BZ, which makes sense as they originate from different bands before coupling through the periodicity.

Figure 4.6(b) shows the main advantage of 2D PCWs over 1D ones. We have access, with the same materials as in Fig. 4.6(a), to guided modes over a wider range of frequencies. Most importantly, as these bands have globally lower frequencies, they are available over a wider range of k vectors, being further away from the light line.

Finally, 2D PCWs are very much suited for dispersion engineering as we can independently modify the shape of the gap-guided bands by tuning the geometry of the first rows of holes as we will see later, without affecting much the bulk modes nor the index-guided bands[7], which is not at all the case for 1D PCW where everything shifts together. This is a very convenient feature as designing such a 2D PCW can hence be broken down into independent steps.

4.1.4 PCWs for increased interaction with quantum emitters

PCWs provide low effective area and high group index

Equation (2.50) from Chapter 2 tells us there are two main knobs to increase the interaction of an emitter to a waveguide mode: reducing the effective mode area A_{eff}[8], and reducing the group velocity v_{g} of the light in the waveguide.

PCWs can guide light in a slab even for small transverse dimensions. This leads to a mode that extends into the air (vertically for a W1 waveguide), leading to lower effective areas, as the intensity is integrated against the dielectric constant in the expression of A_{eff}. To have a more quantitative understading we take the example of a nanowire with square section of width d (also known as nanobeam). We see in Figure 4.7(a) that, starting from a wide waveguide, A_{eff} decreases until a minimum value, reached at around λ/n [Tong et al. 2004], before increasing fast for lower sizes. In this latter regime the mode field resembles a plane wave, strongly deconfined into the air. For emitters embedded in a PCW, one has hence to find this minimum, which still supports guided modes. For atoms trapped outside the structure, we want both the effective mode area to be small and the field at the atom position to be important. As shown in Fig. 4.7(b), a trade-off has to be found to have a significant

[6] The edge of the continuum is linear as it can be though of as a light line in the y direction where the condition (4.8) $\omega < c/n_{\text{clad}}\, k_x$ has to be verified, with $n_{\text{clad}} = \sqrt{\bar{\epsilon}} = 2.8$ the refractive index of the cladding. $n_{\text{clad}} > n_{\text{air}}$, which explains why it is a stricter constraint than the z light line.

[7] See for example in Fig. 5.5(b).

[8] Defined as $A_{\text{eff}} = \frac{\int_{\mathcal{A}} d\mathbf{r}\epsilon(\mathbf{r})|\mathbf{E}(\mathbf{r})|^2}{\max\left[\epsilon(\mathbf{r})|\mathbf{E}(\mathbf{r})|^2\right]}$

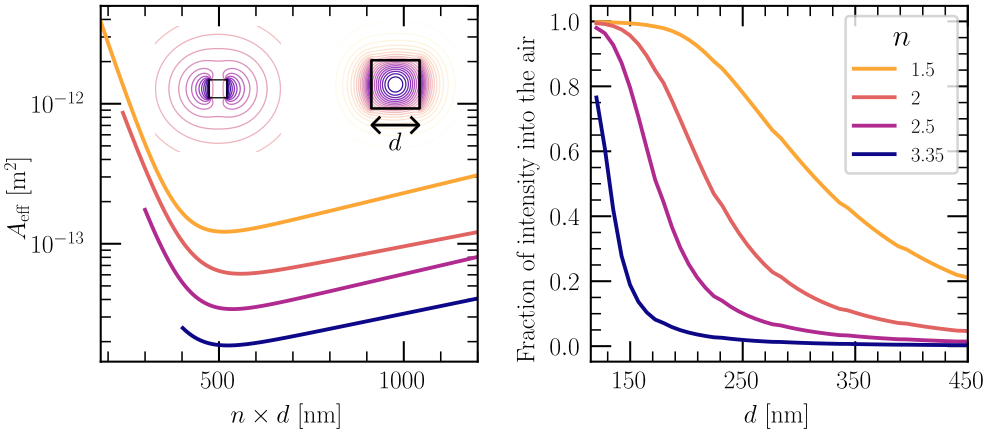

Figure 4.7: Variation of A_{eff} and the fraction of intensity in the air with the waveguide transverse size. (a) Variation of the effective mode area of a guided mode at $\lambda = 780$ nm in a nanobeam suspended in air at varying width d. The insets show the shape of the intensity of the electric field at each end of the x axis, revealing the extension of the field into the air for small sizes. The x-axis is d multiplied by the refractive index of the waveguide. With that normalization we see the position of the minimum of A_{eff} is almost constant. (b) Fraction of intensity of the electric field out of the waveguide. For the high refractive indices that offer the lowest mode areas, this decays very fast.

fraction of the field into the air, while not increasing A_{eff} too much when reducing the transverse size.

We saw before that PCWs usually have slow bands, whose shape can be tuned by changing the parameters of the waveguide, allowing to design the value of the group index at which we want to operate. Figure 4.8 shows the difference of the achievable 1D Purcell factors when taking modes at two very different group indices. The highest coupling factors are obtained inside the structure, accessible for solid-state emitters.

PCWs hence allow to play on both knobs identified earlier thanks to their strong transverse confinement and tunable slow guided modes.

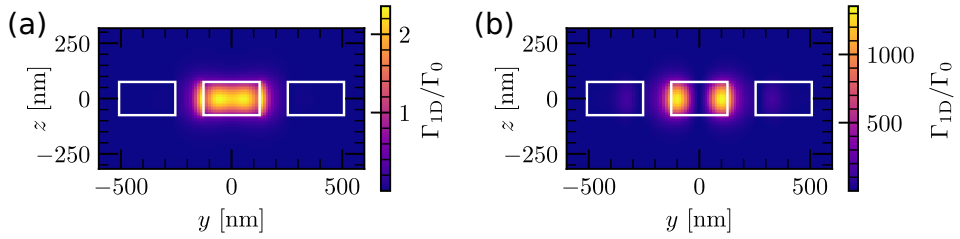

Figure 4.8: Comparison of the estimated 1D Purcell factor in the W1 (a) 1D Purcell factor for the mode at $k = 0.3$ on the W1 slow band (pale red in Fig. 4.4) (b) 1D Purcell factor for the mode at $k = 0.5$ on the W1 slow band (dark red in Fig. 4.4). Edges of the waveguide are highlighted in white. The huge differences in the values of the Purcell factor are due to the extreme differences in group indexes in the two cases (5.8 vs > 100) and the effective mode areas. The highest 1D Purcell is inside the slabs, but significant values can also be reached outside.

Experiments with emitters and PCWs

Pioneering experiments have already harnessed these strengths and shown near unity coupling of a solid state emitter in a W1 waveguide, either with quantum dots [Arcari et al. 2014] or with dopants (Erbium ions) [Weiss et al. 2021]. The embedded quantum dots have even been successfully exploited for quantum operations [Tiranov et al. 2023]. As solid state emitters have some limitations, especially regarding scaling up in numbers, some groups have demonstrated this increased interaction for either hot [Peng et al. 2023] or cold atoms in the vicinity of slow-mode PCWs [Goban et al. 2014]. The latter have shown an interaction probability on the order of $30 - 50$ % which is remarkable. These experimental achievements have asserted the interest of such platforms, but a fully integrated platforms with trapped cold atoms is still to be realized. We will propose some other PCWs in the following in order to achieve it.

4.2 Methods for simulating photonic crystals

The photonic eigenvalue equation (4.2) has very few analytic solutions (except in free space or in uniform waveguides). In most cases, numerical methods have to be used in order to solve it. Different methods exist, each having their own advantages and drawbacks. Some methods are very versatile, but at the cost of long computation time, while faster PCW-specific techniques can be tailored, usually with some approximations.

This section gives a very short overview of the main numerical techniques used throughout this thesis (Plane Wave Expansion, Guided Mode Expansion and Finite Difference Time Domain). A more in-depth explanation of each method, of the simulation parameters used and some considerations on convergence are provided in Appendix B[9].

4.2.1 Plane wave expansion and Guided mode expansion

As the eigenvalue equation (4.2) is linear, it is possible to solve for $\mathbf{H}$ by expanding it on a basis of orthonormal modes. This basis can be chosen to be the set of plane waves or the set of guided modes of a uniform slab.

Plane Wave Expansion

If we choose the basis of plane waves, we realize the Plane Wave Expansion method (PWE), introduced in [Johnson and Joannopoulos 2001]. The idea is the following: as solutions of the eigenvalue equation (4.2) are Bloch modes, we can write the Bloch envelope as a Fourier series, i.e. an infinite sum of plane waves. Finding the Bloch mode boils down to finding the coefficients of the Fourier decomposition. The dielectric constant can also be expanded as a Fourier series and then inverted. The coefficients of the Fourier series can be derived through diagonalization of the obtained matrix. While the series is theoretically infinite, one has to specify a truncation level in order to have a finite matrix to diagonalize. This parameter limits the accuracy of the method and gives rise to the Gibbs phenomenon[10] as it means ignoring high

[9] Other techniques are also introduced, used for design of the comb waveguide [Fayard et al. 2022].

[10] The dielectric function and the fields are computed as truncated Fourier series. Gibbs phenomenon is a consequence of the fact that you need an extremely high number of harmonics to approximate a step function. In our case, such a function representing a sharp interface will then represented as an oscillating function which overshoots the step.

frequency components of the field. PWE can only be used for 2D PC and not slabs and cannot be used for dispersive materials.

Guided Mode Expansion

If instead, we choose the basis of guided modes of a uniform slab, we perform the Guided Mode Expansion (GME), introduced in [Andreani and Gerace 2006]. This method is by essence approximate: the guided modes of a slab are orthogonal [Snyder and Love 2012], but do not form a complete basis. GME also suffers from the Gibbs phenomenon and is hence not suited for computing fields close to interfaces. GME is well suited for PC slabs, giving usually more accurate results that PWE, but is a bit slower. As its PWE counterpart it is limited to non-dispersive materials.

In the following we use the *legume* Python package[11] for performing both PWE and GME simulations.

4.2.2 Finite Difference Time Domain method

The Finite Difference Time Domain (FDTD) method is the most versatile one. FDTD simulations are based on the direct resolution of Maxwell's equations in time domain and allows to get the full evolution of $\mathbf{E}$ and $\mathbf{H}$ in time and space. The equations are solved on a discrete grid in both space and time. Derivatives are approximated by taking the difference between neighbouring sites on the grid. The mesh is necessarily rectangular.

Unfortunately, these simulations can be very extensive in terms of computation time, especially in 3D where the simulation time scale as $\frac{1}{(\Delta x)^4}$ where Δx is the grid discretization (see Appendix B). For this reason, we usually prefer the expansion methods (PWE, GME) to carry out systematic optimizations of the PCs over a wide parameter space, and we then validate the results and perform a finer optimization with the more time-consuming 3D FDTD software.

In the following, the FDTD simulations are performed with *Lumerical*[12].

4.3 Designing photonic-crystal waveguides to work with cold atoms

We have seen that photonic-crystal waveguides are interesting devices as they allow to have guided modes with evanescent decay in vacuum, offering enhanced interaction with neighboring emitters, while enabling to tune this mode dispersion by structure engineering. This can be interesting for coupling cold atoms in a Waveguide QED platform as it amounts to being able to shape their electromagnetic environment i.e their 1D Purcell factor. But PCWs have historically been developed for telecom applications and have rarely been interfaced with cold atoms.

As the number of atomic species that can be easily cooled is limited (and share many similarities), bridging the gap between nanophotonics and atomic physics sets some strong constraints on the nanophotonics part. This section explores such requirements and how they can be met.

[11] le GUided Mode Expansion (*legume*) available freely at https://legume.readthedocs.io/en/latest/.

[12] 2022 Ansys Lumerical simulation software based on the finite-difference time-domain (FDTD) method. https://www.lumerical.com/

4.3.1 A stringent bill of specifications

The design of a periodic waveguide aimed at increasing the coupling with cold atoms should maximize the emission rate into the waveguide mode Γ_{1D}, expressed by Eq. (2.50). Since the group index diverges at a band edge, a naive approach could be to align the transition frequency of the atom with any band edge of the photonic dispersion diagram. Unfortunately, slow light is very sensitive to fabrication imperfections. In a practical situation, fabrication imperfections set an upper bound to the group index n_g that can be reached with low uncertainty. This effect is discussed in the following subsection.

A second issue that emerges in such a design process concerns the value of the effective mode area at the position of the atom A_{eff}. Indeed, the design is a trade-off between two opposite trends. On the one hand, we need a mode whose field extends far into the air cladding so that atoms can interact with it, implying that it weakly interacts with the periodic pattern. On the other hand, we need to be able to control carefully the group velocity and the curvature of the dispersion relation, meaning that we need a mode that strongly interacts with the periodic pattern.

Finally, a third important challenge is to generate a stable optical trap for the atoms at subwavelength distances of the waveguide and to be able to bring the atoms inside this trap. A fully integrated trapping scheme can be achieved by using guided modes at frequencies detuned from the atomic transition. For instance, red- and blue-detuned modes can be used to create a two-color trap as discussed in Sec. 3.2 with other waveguides. The design of the periodic waveguide should thus ensure the presence of additional modes with adequate field profiles, which spatially overlap with each other and with the slow mode.

As a whole, the design of a periodic waveguide with increased atom-photon interactions is a complex task that should meet the following criteria:

1. Slow and single-mode operation at the transition frequency of the atom (large n_g),
2. Large fraction of the electric field in air outside the structure (while keeping a small A_{eff}),
3. Robustness to fabrication imperfections,
4. Material with high n that is transparent at the alkali wavelengths,
5. Existence of additional modes at frequencies detuned from the atomic transition for trapping the atoms optically with low powers (few mW),
6. Clear access around the structure to ease the transport of the atoms to the trapping sites,
7. Efficient coupling of free-space light into and out of the waveguide.

Some general ideas can be put forward for most of these conditions, in the case of an optical waveguide coupled to Rubidium atoms. They will be discussed in the following. A case by case design of three PCW-atom hybrid platforms will be the main focus of Chapter 5.

4.3.2 Dispersion engineering for robustness against fabrication imperfections

Fabrication of any nanoscale structure can introduce deviations with regard to the simulated one because of unavoidable fabrication inaccuracies. As we want these

deviations to have the smallest possible impact, we have to study how they affect dispersion of the guided modes and how to tune the waveguide properties to make it robust to these effects.

The double curse of fabrication imperfections

Two kinds of imperfections can appear when fabricating a structure. The fabrication can introduce random errors (low precision), for example by having a random distribution of hole sizes and positions along the structure, or systematic errors (low accuracy) by having all parameters offset by some value with respect to the settings. Even if state-of-the-art techniques can limit errors down to a 2 nm accuracy [Asano et al. 2006], their effect on the dispersion properties of the crystal has to be considered.

Random errors in fabrication are disorder. It is critical as it breaks the translational symmetry of the crystal and makes Bloch's theorem not applicable. Simulating disorder in PCW has to be done by solving Maxwell's equations over a full waveguide with many periods, for many realizations of the disorder [García et al. 2017]. This comes at a prohibitive computational cost. The effect of disorder on the dispersion can instead to be quantified thanks to proxys or first principles, introducing various levels of approximations. Even small amounts of disorder will introduce Anderson-localized states with finite localization length at frequencies close to the guided band. As this effect is stronger for slow group velocities, e.g. at the band edge, this will smear out the sharp density of states at $k = 0.5$ [Huisman et al. 2012; Faggiani et al. 2016]. This is shown as a blur of the guided band at the edge of the 1BZ in Fig. 4.9. Finally, disorder can couple guided modes to radiative ones (over the light line) and introduce losses [Savona 2011].

Systematic errors in the fabrication (for example a period $a + \delta a$) introduce a shift in the guided bands without deformation, to the first order [Soljačić and Joannopoulos 2004]. This situation is shown in Fig. 4.9 by red lines, shifted up or down. This shift can cause the atoms to couple to a mode with a very different group index than expected or even to fall into the band gap and not propagate at all. This effect can also be computationally costly to estimate as many parameters can differ from their nominal value, spanning a multidimensional space to explore. The parameter space can be reduced via machine learning methods (as Gaussian Processes in [Bopp et al. 2022]), but, as for disorder, finding adequate proxys can be more convenient. This effect can also be mitigated by fabricating various samples with different parameters and selecting the good ones after characterization, but it is also very time consuming.

Proxys and methods for making the structure robust

We saw that getting a quantitative understanding of these effects comes at the cost of high computational power. Over the years, proxys have been introduced in order to describe the behaviour of a given dispersion band against imperfections.

For example, [Faggiani et al. 2016] points out the importance of the effective mass at the band edge $m_{\text{eff}} = \left(\frac{\partial^2 \omega}{\partial k^2}\right)^{-1}$ to characterize the minimal size of the localized modes. The higher the mass, the smaller number of periods is needed to observe a localized mode at the band edge. Even for state-of-the-art fabrication, we expect some localized modes due to randomness, in the high m_{eff} PCWs we consider in this work. At the same time, [Zang et al. 2016] shows that a large effective photon mass is still interesting as it improves the tolerance of a slow mode to systematic errors.

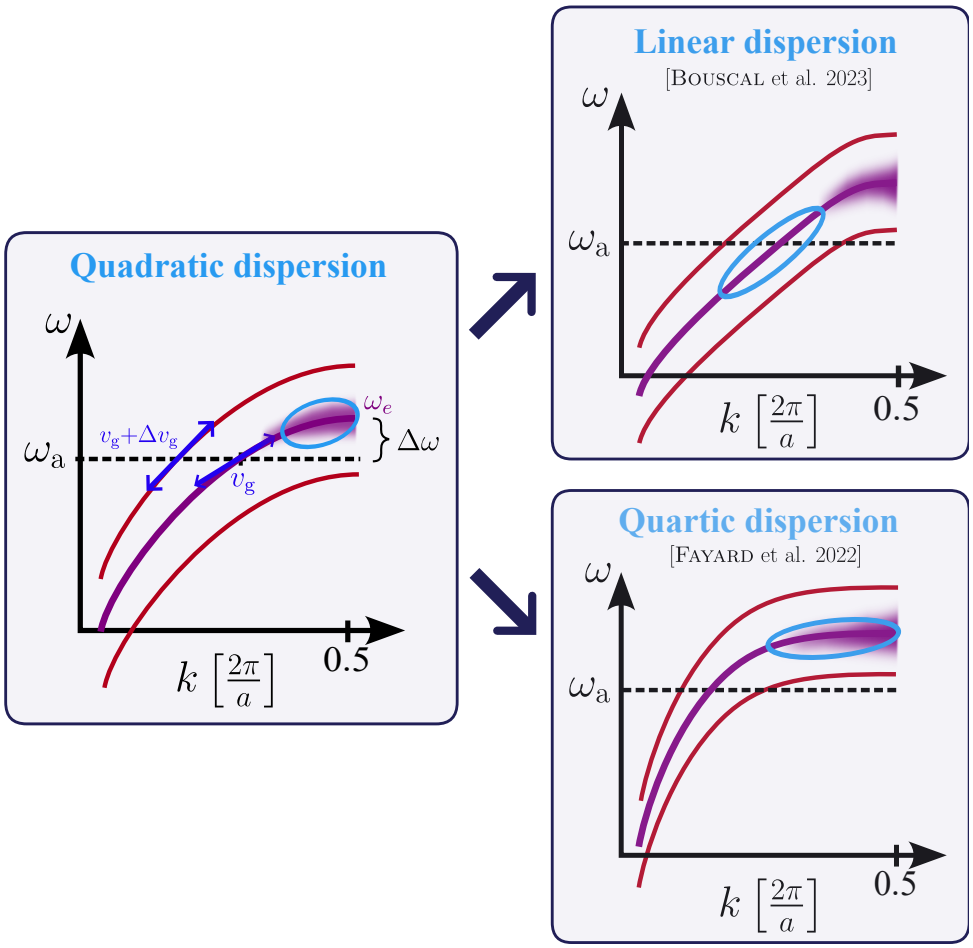

Figure 4.9: Effect of fabrication imperfections and two scenarios to mitigate them. Left: Imperfections lead to both disorder (broadening of the band at the edge) and shifts (in red). The shift can cause the guided mode to have a very different group velocity than the one predicted or even to fall into the band gap of the 2D PC. Right: Two mitigation techniques discussed in the manuscript: dispersion engineering to have a linear band and cancel the group velocity dispersion, or designing quartic bands that automatically push $\Delta\omega$ up for a given value of n_g

Two strategies emerge to mitigate the effect of fabrication imperfections:

- Against disorder: As randomness smears out the sharpness of the band edge and introduces modes that undergo Anderson localization in its vicinity, the simplest idea to reduce its effect is to choose a mode as far as possible from the band edge. We introduce $\Delta\omega = \omega_e - \omega_a$, where ω_e and ω_a denote the frequency of the band edge and the atomic transition respectively. Choosing a mode far from the band edge amounts to maximizing $\Delta\omega$.
- Against systematic errors: As these errors introduce a shift in frequency (without deformation to 1st order), one has to make sure that such a shift does not put ω_a into the 2D PC band gap and has limited impact on the dispersion properties at this frequency. The idea can be the same as for disorder: maximize $\Delta\omega$.

If both errors seem to be mitigated by setting the working frequency as far as possible to the band edge, a trade-off has to be found as going away from ω_e usually leads to lower group indices as the bands become steeper, reducing the maximum 1D

Purcell factor achievable. Some ideas, developed in the following can help to get the best of both worlds.

One can engineer the slow mode to make it as close as possible to a **linear band**, minimizing the group velocity dispersion (GVD)[13] over a given range, see (Fig. 4.9, up). This amounts to obtaining a constant group index over a broad wavelength range. If this feature allows for the propagation of broadband pulses without distorsion, it is also a crucial feature when it comes to dealing with fabrication imperfections. Indeed, a mode at ω_a will propagate at the same group velocity, even if the imperfections introduce a substantial frequency shift of the slow mode band (see Fig. 4.9(b). This strategy has been applied in-depth to W1 waveguides, by varying locally the geometrical parameters, either by tuning the position of the first rows of holes [Li et al. 2008; Wu et al. 2010; Liang et al. 2011; Colman et al. 2012; Vyas et al. 2022], by chirping the refractive index over the length [Mori and Baba 2005], by changing the width of the line defect [Petrov and Eich 2004] or the size of the holes [Frandsen et al. 2006; Schulz et al. 2010]. A relevant figure of merit to maximize in this situation is the group index - bandwidth product (GBP), defined as GBP $= n_g \frac{\Delta\omega_{BW}}{\omega_c}$, where ω_{BW} is the frequency range for which the group index is constant around the center value ω_c. It has been increased up to 0.32 with these techniques (leading for example to a 14 nm bandwidth at $n_g = 32$ [Li et al. 2008]). In Sec. 5.2, we introduce an asymmetric, halved-W1 waveguide and show it can support a slow linear band over 10 nm [Bouscal et al. 2024].

Another fruitful approach to dispersion engineering for having modes far detuned from the band edge but still with high n_g, is to look for **quartic dispersion** curves of the form $\omega - \omega_e \propto -(k - \pi/a)^4$. Coupled modes theory shows from first principles that at the edge of a band gap, the dispersion is usually of quadratic form. Some waveguides can allow more complex interactions which make the quartic dispersion possible [Nguyen et al. 2018]. We will see in Sec. 4.3.4 that this is particularly the case for asymetric waveguides. A band with a quartic dispersion broadens the useful bandwidth of the slow mode, i.e., the bandwidth over which n_g is larger than a target value. Indeed, a quartic dispersion produces a group index that scales as $\Delta\omega^{-3/4}$ while the group index of a quadratic dispersion scales as $\Delta\omega^{-1/2}$ [Fayard et al. 2022]. Therefore, if one wants to work at a given group index, the quartic dispersion allows an operation at a larger $\Delta\omega$, i.e. at a frequency further from the band edge. This is the optimization realized for the comb waveguide introduced in Sec. 5.3 [Fayard et al. 2022].

Inverse-design photonics for unlocking the full possible phase space

The methods presented before to achieve any of the two kinds of dispersions, rely on intuition-based approaches. They are very efficient in many cases, but usually do not apply directly to other setups. Intuition is also less reliable when the complexity of the system increases.

The inverse-design approach in nanophotonics, pioneered by Cox and Dobson [Cox and Dobson 1999], gained momentum in the early 2000s. To implement these methods, a target value of some parameter has to be set (transmission, Q factor, emitting wavelength...). Then, an evolutionary or a gradient-based algorithm (both in the realm of machine learning) updates iteratively the allowed parameters in order to reach the target. If these parameters can be global geometrical parameters of the structure, a more drastic approach is to discretize the whole simulation space into

[13] Defined as the second order derivative of the dispersion curve $\omega(k_x)$ by k_x.

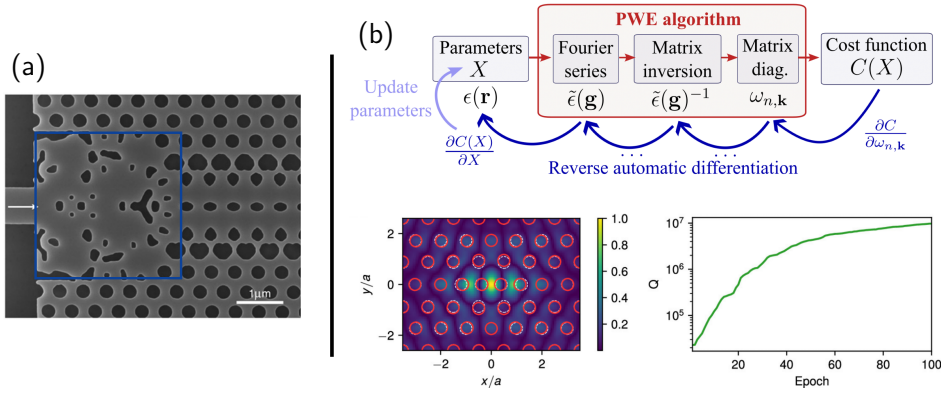

Figure 4.10: Two inverse design methods in nanophotonics. (a) 3D voxel optimization of a nanobeam-to-PCW converter for the y-odd mode, pioneered in the group of Jelena Vučković. The blue rectangle indicates the design region. Figure reproduced from [Vercruysse et al. 2021]. (b) Up: Schematic diagram of the automatic differentiation optimization algorithm used with PWE. Derivatives of the cost function are computed with the chain rule, starting by the last one. The parameters are updated thanks to the gradient. Down: Example of optimization of a photonic crystal cavity, by setting the position of the holes as parameters. The Q factor reaches 10^7 after 100 epochs. The optimized positions are displayed in red. At odds with the former method, only a small number of structural parameters is optimized. Picture reproduced from [Minkov et al. 2020].

3D voxels for which the refractive index can be tuned independently by the algorithm. This results in optimized designs with interesting shapes, that could not have been found with intuition-based approaches (see Fig. 4.10(a)). The latter method is however computationally extensive and hard to implement.

Applications of these techniques are wide-ranging: from metasurface design for chiral light emission [Mou et al. 2023], to optimization of solid-state cavities for SHG efficiency [Molesky et al. 2018], to many types of optimizations on photonic-crystals waveguides, regarding the shape of their dispersion curves or the direction of light emission [Vercruysse et al. 2021].

In the case of photonic crystals, [Minkov et al. 2020] have developed a gradient-descent-based approach for the GME and PWE method, sketched in Fig. 4.10(b). A set of structural parameters X is given as an input. The PC is simulated and the cost function evaluated. The gradient of the cost function $C(X)$ is computed by reverse automatic differentiation. If N steps are needed to evaluate the cost function, the derivative will be evaluated by differentiating by the last expression available and then applying the chain rule N times until arriving at the quantity $\frac{\partial C}{\partial X}$. The direction of the gradient sets the next set of parameters to be tried. A simple optimization example is shown in Figure 4.10(b) to show its strength and speed. Their framework is easy to use and is suited for optimization of Q factors in PC cavities or for matching a specific band shape. It will be used in the following for linear band optimization.

4.3.3 Use of a high-index material for higher interaction

Another criterion from Sec. 4.3.1 is the fact that we need to use a transparent, high-index material to fabricate the waveguides. Indeed, we saw in Fig. 4.7(a), that for a given index contrast, reducing the dimensions up to some value reduces the effective mode area. It also shows that we can reach lower mode areas for higher group indices

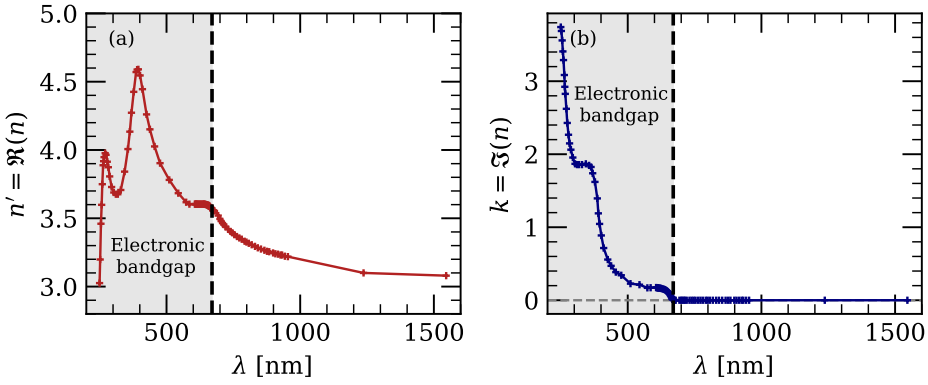

Figure 4.11: Real and imaginary part of the complex refractive index of GaInP with the wavelength. (a) Refractive index of GaInP. At 780 nm, $n' = 3.35$. (b) Imaginary part of n, i.e. absorption coefficient. The sharp increase in absorption at 670 nm corresponds to the electronic band gap of the material (1.85 eV). The data is experimental and taken from [Schubert et al. 1995].

at dimensions which are realistic, while maintaining an important fraction of the field into the air. For these reasons we choose a high-index material for our waveguides.

Common materials for fabricating waveguides are SiO_2 (glass, for nanofibers) or Silicon Nitride (SiN). They have a refractive index of respectively 1.5 and 2.0 at 780 nm. As we are looking for high-index materials, a promising candidate is Silicon ($n = 3.6$) but it has an electronic band gap at an energy lower than the D_2 transition of Rubidium, and is hence absorptive at 780 nm.

The chosen material, GaInP, has been selected for its advantageous optical and electronic properties. GaInP has a wide electronic band gap below 1.85 eV (see Fig. 4.11), and as such is transparent for a wide range of wavelengths (from 670 nm up), meaning it could be used with several alkali. At 780 nm, its refractive index is $n = 3.35$, reaching 3.55 at the electronic band edge [Schubert et al. 1995]. This large index contrast $\Delta n = 2.35$ with the surrounding vacuum gives rise to wide band gaps, allowing for more flexibility in the design of the trapping modes. This material has attracted some attention in recent years due its advantageously low two-photon absorption in the telecom band [Combrié et al. 2009], and growth and fabrication processes have therefore been developed and well mastered.

Finally, our partner C2N has a solid expertise in working with GaInP. For example, it has been used recently to fabricate photonic-crystal cavities for time-entangled photon generation through four-wave mixing [Chopin et al. 2022]. Working with such high-index materials is also interesting for the longer term prospect of device integration. Indeed, the high index contrast allows to reduce the size of the integrated components, which could be an advantage for integration of many such Waveguide QED systems on a single chip of small scale.

4.3.4 Asymmetry: on the benefits of a hybrid-clad design

Having covered material and dispersion engineering criteria, we now focus on a common striking characteristic of the two PCW slabs introduced in the next chapter: they are both asymmetric in their transverse direction. We argue that this feature allows for complying with a few of the specifications from Sec. 4.3.1 at the same time.

Asymmetry for finer tuning of the dispersion

The introduction of symmetry breaking in the transverse direction allows for a more precise control on the dispersion properties of the waveguide since it offers extra degrees of freedom [Lü et al. 2010]. Transverse asymmetry has been harnessed in [Nguyen et al. 2018] to create exotic dispersion bands such as Dirac cones, multivalleys, or flat bands. In a transverse symmetric PCW slab, even for a given TE-like/TM-like polarization, the modes can be classified according to their symmetry about the $y = 0$ plane. These y-odd and y-even modes were distinguished in Fig. 4.4(a) by full and dashed lines.

By introducing asymmetry in the transverse direction, these y-odd/y-even modes are not solutions anymore, but they do not disappear[14]. Their overlap integral starts to differ from zero and they couple, leading to an avoided crossing and the opening of another band gap. The stronger the asymmetry, the stronger the interaction.

We recall that the opening of a band gap at the band edge is caused by the coupling of forward and backward propagating modes, coupled by the coherent scattering off of the periodicity. This usually leads to a quadratic dispersion. Here, asymmetry and periodicity can lead to the coupling of four different waves instead of two (y-even forward propagating, y-even backward, y-odd forward, y-odd backward), leading to a more complex behavior which can result in quartic dispersion curves [Dubois 2018; Fayard et al. 2022]. We have two coupling processes which produce each a band gap with a quadratic band edge either going up or down. Quartic bands are achieved when two band edges of opposite curvature are close enough with a strong enough coupling to cancel each other out. The increased control over the dispersion of asymmetric waveguides comes from the tunable interaction between the TE and TM band diagrams which were completely separated in symmetric ones.

Asymmetry for increased optical access

Another advantage of asymmetric waveguides for coupling to cold atoms is the increased optical access they offer. Indeed, with a symmetric PCW slab, the evanescent guided mode is usually in the center, and the atoms have to be brought there from the top or the bottom. In an asymmetric waveguide, the atoms can be approached from much more directions, offering a full 2π optical access. The possibility of approaching the atoms from the side is not only interesting for technical reasons, but also provides a more feasible route for optical trapping with guided modes.

In a W1 waveguide, the only accessible region to trap the atoms is a line over the structure. We show in Fig. 4.12(a) the intensity distribution over the waveguide, at 100 nm from the surface. We observe an intricate intensity profile with 3 anti-nodes on the transverse y direction. We expect this feature to make the search for a stable trap in y challenging. Moreover, when moving away from the structure, the spatial mode profile changes quite rapidly.

In the asymmetric half-W1 waveguide introduced in the following, we have now the option to place the atom chain on the edge of the PCW (as shown in the inset of Fig. 4.12(b)). The corresponding mode in the (x, z) plane is displayed in Fig. 4.12(b) and we can see a simpler structure, with, this time a fundamental mode profile along the transverse z direction. We can also show that this mode has a simpler evolution when going away from the edge. The two modes are slow bands at similar frequencies.

[14] Asymmetry can be introduced gradually, hence we expect a mode of the slightly perturbed asymmetric waveguide to be of the form $\mathbf{H}_{\mathbf{k}}^{\text{asym}} = \mathbf{H}_{\mathbf{k}}^{\text{sym}} + \delta\mathbf{H}_{\mathbf{k}}$. A small difference in the fields corresponds to a similar value of the electromagnetic energy functional and hence of the frequency. Hence the dispersion will change continuously with the asymmetrization.

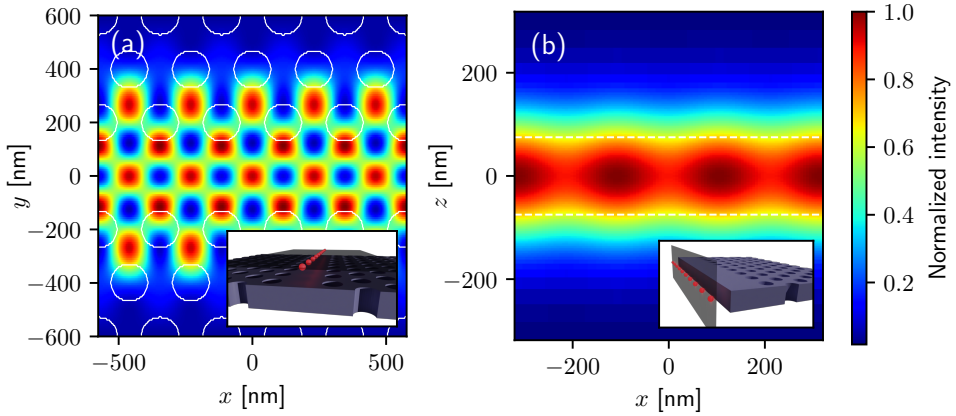

Figure 4.12: Field maps at 100 nm from the surface of either W1 or half-W1. 2D intensity of the electric field at 100 nm from (a) the surface of the W1 waveguide and (b) the edge of a W1 waveguide cut in half. Insets show the 3D structures, the theoretical position of the trapped atoms in red and the black planes on which the intensities are recorded. Field in (a) is computed with GME, field in (b) with 3D FDTD.

These are all hand-waiving arguments but that seem to indicate that halved waveguides are more suitable for trapping that their symmetric counterparts, as we can make use of the fact that the guided modes are fundamental modes of the slab.

4.3.5 Power handling: Coupling efficiently light in and out

All the different beams (probing, trapping) will be coupled into the waveguide from free space. It is then crucial to have an efficient coupler, that can transmit light at the relevant frequencies with a good efficiency. If out-of-plane grating couplers are usually a good method to couple broadband light into such structures, this technique is not adapted in our situation as everything is suspended into vacuum. For suspended platforms, simple tip couplers can be sufficient but can offer limited efficiency. [Luan et al. 2020] introduced a Y-shaped coupler that allows a better power handling, a notable limitation of their structure. We have fewer constraints in that regard as our waveguides will be thermally at equilibrium with 2D slabs that act as a heat sink. Following a design from [Almeida et al. 2003] (see Fig. 4.13(a)), we optimize this coupler for 780 nm light. We want high efficiency at this wavelength and over a few tens of nanometers around this value for dipole trapping. The result is displayed in Fig. 4.13(b), showing a transmission around 95 % at 780 nm. These transmission simulations are done with 3D FDTD.

Conclusion

We introduced the basic concepts of photonic crystals, and especially how to construct waveguides out of such periodic structures. As we are bridging the gap between two different fields, the constraints on the designs are many. If an asymetric, suspended, high-index waveguide seems to bridge many of the challenges to interface atoms and PCWs, we understand that it is not enough. The most critical constraints are the robustness of the structure to fabrication imperfections as this can destroy all the properties of the designed crystal, and the possibility to find a stable trap. Unfortunately, responses to these constraints are device-dependent and will be explored in

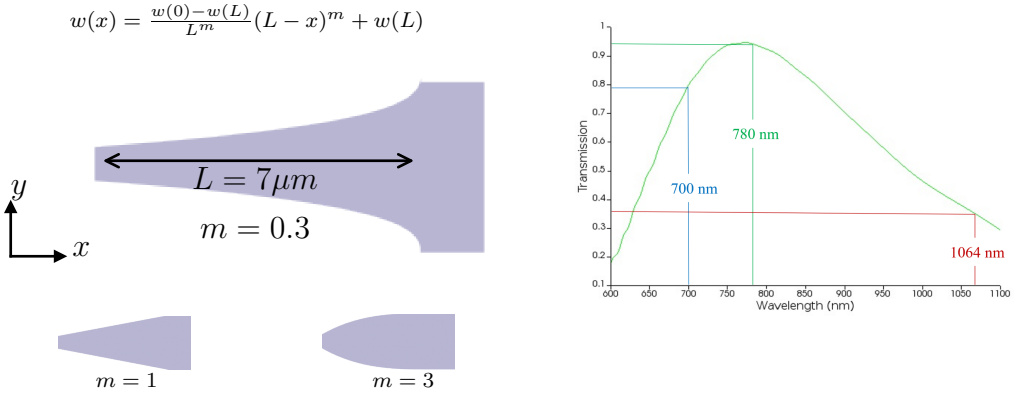

Figure 4.13: Tapered coupler for free space input and output coupling. (a) Scheme of the coupler and parameters (b) 3D FDTD computed transmission spectrum. The relevant wavelengths are displayed as vertical dashed lines

the following for a few different designs. For the robustness, mitigation solutions exist, relying on precise dispersion engineering of the selected platform. The numerical methods for doing so have been introduced, one has to find in the toolbox the right method for the right simulation.

In the following chapter we will present optimizations of three different waveguides. The goal is to optimize them such that atoms can be trapped around the edge, with the highest possible 1D Purcell factor and with the most robust design possible. A halved-W1 waveguide [Bouscal et al. 2024] and a so-called comb waveguide [Fayard et al. 2022] are precisely designed and shown to be a suitable platforms for trapping cold atoms in their surrounding. While the fabrication of such samples is still ongoing, all these important experimental constraints have been extensively studied in the designs.

CHAPTER 5

DESIGN AND FABRICATION OF WAVEGUIDES FOR HYBRID PLATFORMS

Contents

In this chapter, we explore the design and fabrication of nanophotonic devices to interface guided light and trapped cold atoms in the high 1D Purcell factor regime. We start with the simplest possible waveguide: a uniform slab with a rectangular transverse profile. We show that this so-called nanobeam offers an order of magnitude improvement in the achievable interaction compared to nanofibers, because of the higher confinement provided by the high refractive index. Trapping atoms around such structures with sharp edges is a challenge, common to all platforms studied in the following. Using the strategies developed in Chapter 4, which aim at engineering bands with a high group index far from the band edge, we introduce two designs of photonic-crystal waveguides (PCW) robust to fabrication imperfections and supporting stable dipole traps: a "comb" waveguide with quartic bands, and a "half-W1" waveguide with linear bands. These PCWs are promising as the predicted atom-photon interaction enhancement is similar to solid-state platforms, the half-W1 even showing chiral coupling. We finally report on the work carried out by our partners at Centre de Nanosciences et de Nanotechnologies (C2N) on the fabrication of these structures and show some first encouraging characterization results. This work was published in [Fayard et al. 2022] and [Bouscal et al. 2024].

5.1 Optimization of a uniform waveguide: the nanobeam

We showed in Chapter 4 that a high-index waveguide with small transverse dimensions can provide a very low mode area, increasing the 1D Purcell factor. We look here at a straightforward design, a uniform 1D slab of high-index material. What is the maximum coupling we can achieve in this simple case?

As we are considering semiconductor materials, guides with rectangular transverse geometries are more easily fabricated than circular ones. Figure 5.1(a) illustrates such a GaInP waveguide, of thickness t and width w, suspended in air. A typical intensity distribution of the fundamental mode is depicted with the red contour lines. A similar mode exists in the vertical direction. Because of fabrication constraints, we fix the thickness to 150 nm. We are left with a single parameter w to optimize to get the highest 1D Purcell factor possible for trapped atoms. The simplicity of uniform waveguides makes them interesting platforms for experiments with atoms [Ritter et al. 2015; Stern et al. 2017] and theoretical works have shown their strengths, for example for spin-squeezing of atom chains [Qi et al. 2018].

5.1.1 Optimization of the atom-light interaction

Figure 5.1(b) shows the average 1D Purcell factor for a Rubidium atom at the vicinity of the waveguide. We recall that the 1D Purcell factor is defined as Γ_{1D}/Γ_0, where Γ_{1D} is the decay rate of a single atom in the waveguide mode and Γ_0 the decay rate in vacuum. For simplicity, it is computed from Eq. (2.44) as an average over the three linear atomic dipole orientations.

We see that higher values are obtained for widths between 120 and 160 nm. This matches the intuition developed by Fig. 4.7: reducing the width of the nanobeam pushes the electric field into the air, reducing the mode area A_{eff} (as it is an integral of $\epsilon \times |\mathbf{E}|^2$) until a threshold value where the field is so delocalized that A_{eff} increases again. The optimal value for the nanobeam width depends on the distance d of the trapped atoms to the surface. But as the fields used for trapping are guided modes, a

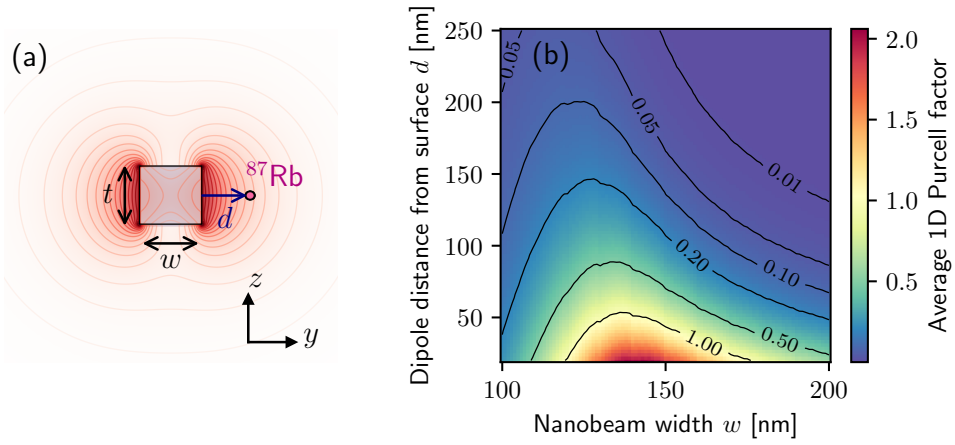

Figure 5.1: Optimization of the width of a suspended nanobeam. (a) Scheme of the transverse plane of a nanobeam, defined by its width w and thickness t. The contour plot shows the transverse intensity profile of a propagating TE-like mode. The nanobeam is made of GaInP (n = 3.35) (b) Average 1D Purcell factor Γ_{1D}/Γ_0 depending on the width of the nanobeam and the distance of the atom. Γ_{1D}/Γ_0 around $0.1 - 0.2$ are expected for nanobeams with $w = 140$ nm and realistic atom trap distances (see main text). The thickness t is fixed to $t = 150$ nm.

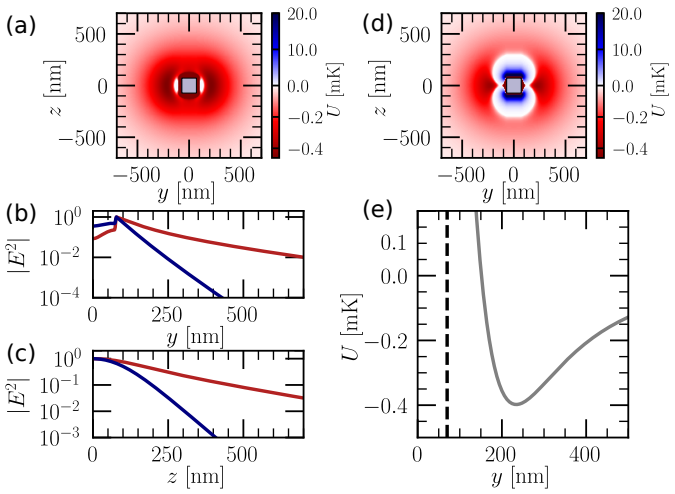

Figure 5.2: Trapping atoms around a nanobeam with two polarization configurations. Left: Same polarization (along y) for the blue- and red- detuned beams. (a) A stable trap is possible in the 2D (y,z) plane. (b-c) The decay of the red and blue intensities along (b) y (at z=0) and (c) z (at $y = w/2 + d_{\text{trap}}$). The slow decay of the red in both directions causes the weak trapping in the azimuthal direction. Right: Crossed polarization configuration. (d) The 2D potential shows a tighter azimuthal trap. (e) Trap along y. Dashed line shows the position of the nanobeam surface. Both simulations include the Casimir-Polder potential as seen by the strong attractive potential close to the surface (see Appendix A).

change in the width modifies their shape. There is then a co-dependent optimization to be realized, which is what we want to emphasize here. For a nanobeam there is only one optimization parameter and a systematic study can be carried out.

5.1.2 The challenge of trapping atoms around sharp edges

Finding a stable trap around a nanobeam presents similarities with the nanofiber case as both have a featureless dispersion relation and as such, can guide a fundamental mode for a very wide range of wavelengths. In theory, the two-color trap can be implemented with any pair of red- and blue- detuned wavelengths that the nanobeam can support. As Rubidium has no magic wavelengths, we choose $\lambda_{\text{red}} = 1064\,\text{nm}$ and $\lambda_{\text{blue}} = 750\,\text{nm}$, corresponding to easily available lasers. We show a stable trap in Fig. 5.2(a) with a few milliwatts in each beam, with the trap minimum at a distance $d_{\text{trap}} = 240\,\text{nm}$ from the edge[1]. Because of the shape of the fields, the azimuthal trapping of the atoms is weak. This is reminiscent to the two-color compensated trap for the nanofiber from Figs. 3.6(a-d) which also has a weak trap in that direction, albeit usable.

The low trapping in this direction comes from balancing opposing requirements needed for trapping. Indeed, a stable trap position with a repulsive barrier in the y direction, requires the blue evanescent mode to decay faster than the red one, as discussed in Sec. 3.2. This criterion, once met, also manifests itself in the azimuthal direction which leads to a predominant attractive trapping almost up to the surface, and the formation of a relatively flat valley in this direction. Figures 5.2(b-c) show the intensity decay of the red and blue beams along y and z (at $y = y_{\text{trap}}$) respectively. The red beam decays faster in both directions which is a liability in the z direction.

[1] All the trapping potentials from this chapter are computed with `nanotrappy` [Berroir et al. 2022], the Python package developed by our group presented in Chapter 3.

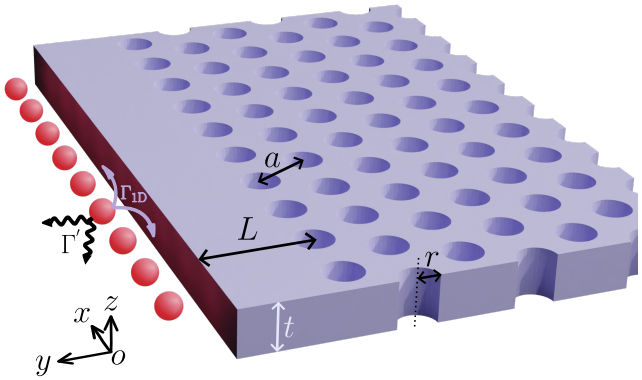

Figure 5.3: A half-W1 slow-mode photonic-crystal waveguide coupled to cold atoms. Sketch of the waveguide with an array of ^{87}Rb atoms trapped along its edge. Γ_{1D} and Γ' correspond to the decay rates into the guided mode and into the radiation continuum, respectively. The structure is etched in a GaInP membrane (refractive index $n = 3.35$) suspended in air, with a slab thickness t of 150 nm. a and r are the parameters of the 2D hexagonal PC, and L the width of the defect.

This low trapping valley is flatter here than in the nanofiber case because of the proximity of the surface (stronger CP interactions) and the presence of sharp edges.

A crossed-polarization trap can help, using the vertical blue-detuned lobes to reduce the extent of the trapping region in the azimuthal direction, as shown in Fig 5.2(b). A typical trap, 0.4 mK deep, at $d_{\text{trap}} = 160\,\text{nm}$ from the surface can be obtained. At this distance, we get from Fig. 5.1(b) that we can achieve a Γ_{1D}/Γ_0 on the order of 0.1 for $w = 140\,\text{nm}$. The trap position can be brought down to 120 nm, while lowering the depth, which increases Γ_{1D}/Γ_0 to 0.2.

We showed in this section that the nanobeam platform already enhances the interaction by a factor $\gtrsim 10$ compared to a nanofiber-based one [Corzo et al. 2016]. Studying this simple waveguide is interesting as it introduces some concepts we encounter in more involved designs: the co-dependence between the 1D Purcell factor enhancement and its impact on the trapping modes and the challenge of trapping around sharp edges. All this study was done with a mode having a near unity group index. We present in the following two asymmetric PCWs which allow higher group indices and whose slow bands have been engineered to have linear and quartic dispersions respectively.

5.2 Linear bands: Optimization of a half-W1 waveguide

We saw in Chapter 4 necessary criteria that have to be met to combine photonic-crystal waveguides (PCW) with cold atoms. In the following, we design a novel platform for interfacing trapped cold atoms and a slow-mode asymmetric PCW that satisfies all these criteria. Building on the promises of W1 waveguides and initial work from [Zang et al. 2016], we propose a tailored platform for trapping arrays of Rubidium atoms in its proximity.

The platform, sketched in Fig. 5.3, can be seen as a halved W1 waveguide, with the horizontal guidance mechanism relying on both photonic band gap and total internal reflection. As its W1 counterpart, this half-W1 waveguide[2] enables dispersion engineering (cf. Sec. 4.3.2) and offers a 2π solid-angle optical access to the edge of the structure, allowing for simpler transport of atoms close to it [Zang et al. 2016].

[2] Also known as the *cheese grater* waveguide

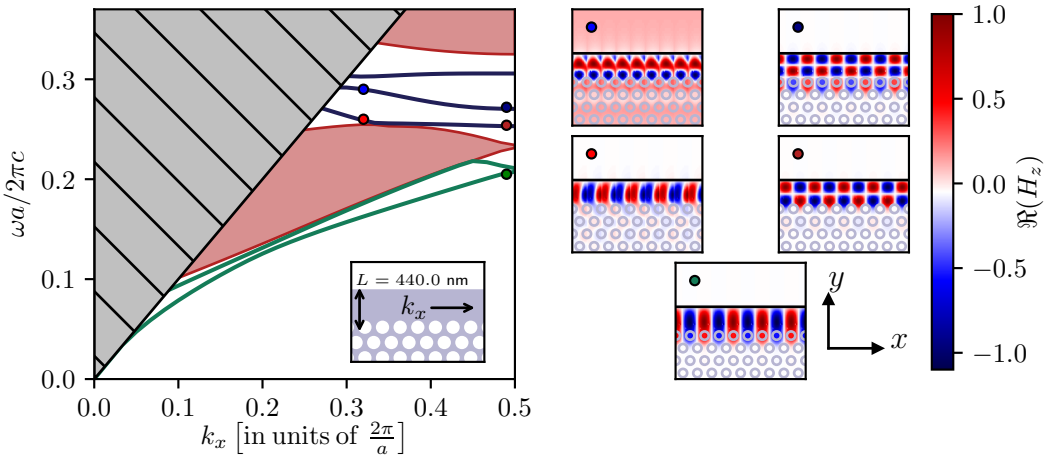

Figure 5.4: Band structure of a half-W1 waveguide with a thickness of 150 nm, and mode profiles of some H_z modes. Left: Band structure of a half-W1 waveguide. The inset recalls the structure of the waveguide. Values of the geometrical parameters have been set to match as closely as possible the band diagram of the W1 waveguide from Fig. 4.4. The slow mode band defined in the text is the lowest one inside the band gap. Right: 5 maps of the real part of H_z as indicated by the dots in the band structure. Spatial profiles are obtained via 3D FDTD simulations.

We use a large refractive index GaInP slab that facilitates the design by offering more flexibility in the engineering of guided modes and band gaps. As emphasized in Chapter 4, our effort focuses at each step on making the design robust to imperfections and on assessing the experimental feasibility of the full platform. In the following we detail the optimization of the slow-mode dispersion curve to achieve a robust **linear band**. We quantify the 1D Purcell factor achievable. Finally, using core concepts from Chapter 3 we show that guided modes can be used to trap atoms in the proximity of the waveguide via a two-color evanescent dipole trap. Stable traps down to 116 nm from the surface are obtained with low powers compatible with nanophotonic systems.

5.2.1 Introduction of the half-W1 structure

The structure is reminiscent of a W1 waveguide, but the holes etched in the GaInP slab do not go up to the edge, leaving a few hundreds of nanometers of unperturbed slab where the light can propagate [Zang et al. 2016]. The band diagram of this structure, as displayed in Fig. 5.4, is quite similar to the W1 one. The main difference is that the asymmetry now forbids to distinguish between y-odd and y-even modes, which are now coupled. Some spatial features are similar to the W1 ones, see for example the mode profile of the index guided bands (Fig. 5.4, green). We are interested here in the lowest gap-guided band (denoted with red dots in Fig 5.4), as the others have a higher order mode profile which might make coupling into these modes inefficient.

Being based on a 2D slab rather than a 1D structure, this geometry should be quite rigid and prevent detrimental effects from low frequency mechanical modes, as the ones pointed out in [Béguin et al. 2020b].

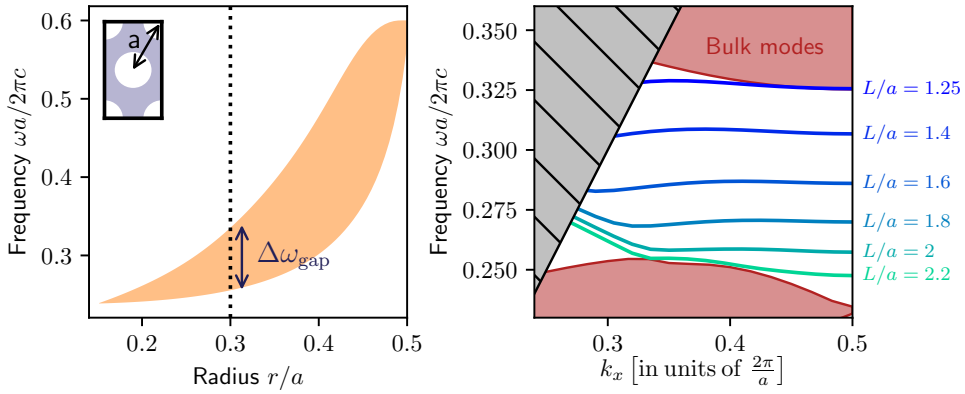

Figure 5.5: Effect of some critical parameters on the position of the band gap and slow mode for the half-W1. (a) TE gap map for a 2D triangular lattice of air columns in a slab with $n = 3.35$ as a function of r/a. (b) Influence of the width L of the defect on the position of the slow mode band of the half-W1 in the projected band diagram. Calculations are made with the GME method for a half-W1 of thickness 150 nm.

5.2.2 Manual alignment for operation at the target wavelength

For a given thickness t, chosen here to be $t = 150\,\text{nm}$, the first designing step consists in finding the lattice period a and hole radius r of the bulk 2D photonic crystal that allow for a band gap around the ^{87}Rb D_2 transition. Indeed, the width and position of the band gap is entirely determined by those values [Joannopoulos et al. 2008]. The variation of the width of the TE band gap with the ratio r/a is shown in Fig. 5.5(a). The band gap has to be wide enough to allow for at least two guided modes, one that supports a mode at 780 nm, and a blue-detuned one for trapping. We settle on $r/a = 0.3$. While this setting does not offer the widest gap, larger radii can be hard to fabricate as they reduce the rigidity of the structure[3]. We set the value of a so that we can have a band gap around 780 nm while not being too limited by the light line. For $a = 220\,\text{nm}$, the gap has a width $\Delta\omega_{\text{gap}}$ of around 110 THz ($\Delta\lambda_{\text{gap}} \approx 190\,\text{nm}$) which is more than enough for fitting two guided bands.

As these bands appear when introducing the defect at the edge, we can align the band of interest with respect to the D_2 line by adjusting the width L, with no effect of the bulk modes. This is highlighted in Fig. 5.5(b), showing how we bring a guided mode down from the upper bulk region by increasing the width L of the defect. Indeed, by increasing the width L, the mode becomes more concentrated in a region of larger refractive index, lowering the energy of the mode (hence its frequency). The rate of shifting of the slow-band frequency can be estimated as $\frac{\partial f}{\partial L} \approx -570\,\text{GHz}\,\text{nm}^{-1}$. We choose a ratio L/a around 1.6 to leave space for a higher frequency blue-detuned band. All these first coarse design steps are done with GME simulations.

Given these constraints, the geometrical parameters of the waveguide are found to be: $a = 220\,\text{nm}$, $r = 66\,\text{nm} = 0.3\,a$ and $L = 350\,\text{nm}$ for a fixed $t = 150\,\text{nm}$. With these settings, GME simulations find three guided bands inside the band gap of the photonic crystal slab between 365 and 435 THz.

[3] As in later design steps, we chose here a very conservative approach, leaving room for future improvements.

5.2.3 Systematic optimization to achieve a linear band

We showed in Sec. 4.3.2 that **linear bands** are a way to mitigate the effect of fabrication imperfections on the dispersion properties of the real waveguide. In this section we present the optimizations performed to achieve such bands, which facilitate the experimental realization of the proposed platform. Inspired by previous strategies from the research on W1 waveguides [Frandsen et al. 2006; Li et al. 2008; Schulz et al. 2010; Wu et al. 2010], we optimize the shape of the slow-mode band by tuning the geometry of the holes close to the line defect.

Optimization via Automatic Differentiation

These seminal papers played on either the radius or the position of the first row of holes, but this approach did not give as good results for our half-W1 waveguide. Instead, and because we are not limited by computational power, we decide to optimize both the radius and position of the first three rows of holes via a gradient-descent algorithm, the automatic differentiation algorithm (AD) introduced in Sec. **??**. The AD algorithm is given 6 independent parameters to optimize, depicted in Fig. 5.6(a). We denote the radius of the first three rows of holes as well as their position along the y axis by $(\delta r_i,\, \delta y_i)$, $i \in \{1, 2, 3\}$. As full 3D FDTD simulations are computationally intensive, we use the approximate method of Guided Mode Expansion (GME) [Andreani and Gerace 2006] thanks to the `legume` solver [Minkov et al. 2020] which integrates Autograd, a Python package for AD. Automatic differentiation computes the gradient of a given cost function with respect to the input parameters thanks to the chain rule and then follows this gradient to minimize the cost, updating the input parameters at each iteration (see Fig. 4.10(b)).

Definition of the cost functions and convergence

The most critical step to implement this gradient-descent algorithm is the definition of a suitable cost function to be minimized. We want the slow band to be as linear as possible, but on which range of wave vector and for what group index? We define a target linear band f_{target}, defined by a target constant index n_{target} over a given range Δk, sampled on N values of k. The value of the target on the k_i is written as f^i_{target}. We define the following 3-part cost function whose minimization makes the optimized band match both f_{target} and its derivative, while keeping the group velocity dispersion (GVD) to vanishing values. The cost function reads as follows:

$$C(X) = \underbrace{\alpha_0 \sum_i^N \left(f^i_{\text{opt}} - f^i_{\text{target}}\right)^2}_{\text{enforces position}} + \underbrace{\alpha_1 \sum_i^N \left(\frac{\partial f^i_{\text{opt}}}{\partial k} - \frac{c}{2\pi n_{\text{target}}}\right)^2}_{\text{enforces } n_{\text{target}}} + \underbrace{\alpha_2 \sum_i^N \left(\frac{\partial^2 f^i_{\text{opt}}}{\partial k^2}\right)^2}_{\text{enforces linearity}} \tag{5.1}$$

where f^i_{opt} is the value of the band being optimized on the sampled range Δk, and the α_i are coefficients to be determined empirically.

The most naive approach would be to use only the first part as cost function, as f_{target} is linear. We realized this approach led to oscillating solutions with values close to the target band with a strongly varying group index and a high GVD. The second and third terms were then added as regularization terms. We set the values of the α_i via trial and error to increase the convergence speed ($\alpha_1 = 100$, $\alpha_2 = 10^{-16}$, $\alpha_3 = 1$). Figure 5.6(b) shows the slow mode at different steps of the optimization for $n_{\text{target}} = 35$ and $\Delta k = 0.10\, \frac{2\pi}{a}$. The cost decreases first by setting the right slope to the band and then shifting it to the right position. After 40 iterations of the

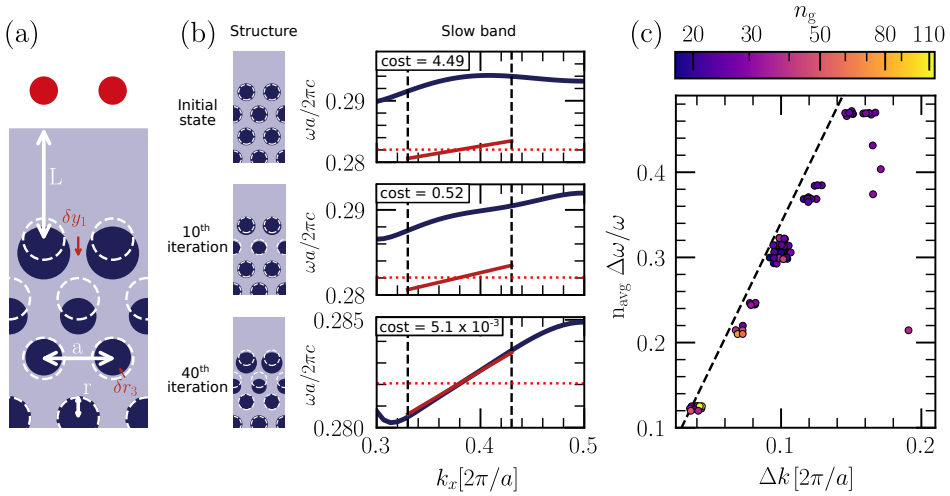

Figure 5.6: Optimization parameters and convergence of the automatic differentiation algorithm. (a) 2D photonic crystal geometry. The initial unshifted holes are shown as white dashed lines. For the first three rows of holes their position can be shifted along y and their radius tuned, amounting to 6 parameters (δy_i,δr_i), $i \in \{1, 2, 3\}$. For clarity, only two parameters are displayed. (b) Structure geometry and resulting band (in blue) at different steps of the algorithm. The red solid line is the target band and the dotted line is the Rubidium D_2 frequency. The optimization is done between the black dashed lines, i.e. for a given Δk, at some distance from the edge of the 1st Brillouin zone (1BZ). (c) GBP for many optimizations over different (n_{target}, Δk). Whatever the obtained n_g (marker color), all the values at a given Δk collapse at the same GBP, except for $\Delta k > 0.13\,\frac{2\pi}{a}$ where the algorithm does not converge anymore, whatever n_{target}. The maximum theoretical GBP for a given Δk is represented by the dashed line.

optimization algorithm the slow band matches the target very well. We conducted this optimization over a variety of parameters (n_{target}, Δk). The resulting group index - bandwidth product (GBP) of these many optimizations is displayed in Fig. 5.6(c). We note that we can achieve in theory a GBP higher than for previous optimizations in W1 waveguides (0.32 in [Li et al. 2008], 0.36 in [Frandsen et al. 2006]). Interestingly, the GBP is constant for a given Δk, whatever the target group index. This means the algorithm has converged to a satisfying fit. Indeed, if the band is linear over the whole target Δk the GBP is independent of n_g with GBP $= n_g \frac{\Delta\omega_{BW}}{\omega_c} = \Delta k \frac{\lambda}{a}$. The algorithm stays close to this line (dashed in Fig. 5.6(c)) when increasing Δk, until it cannot find a satisfying solution anymore, for $\Delta k > 0.13$. When increasing too much Δk, the upper end of the interval approaches $k = \pi/a$ where the group velocity

Row	Position δy [nm]	Radius δr [nm]
1	+42.7	+14.2
2	+53.8	−11.2
3	−3.7	−10.8

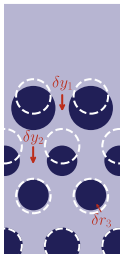

Figure 5.7: Optimal changes in row positions and holes radii via automatic differentiation optimization. All the rows after the third one are unperturbed.

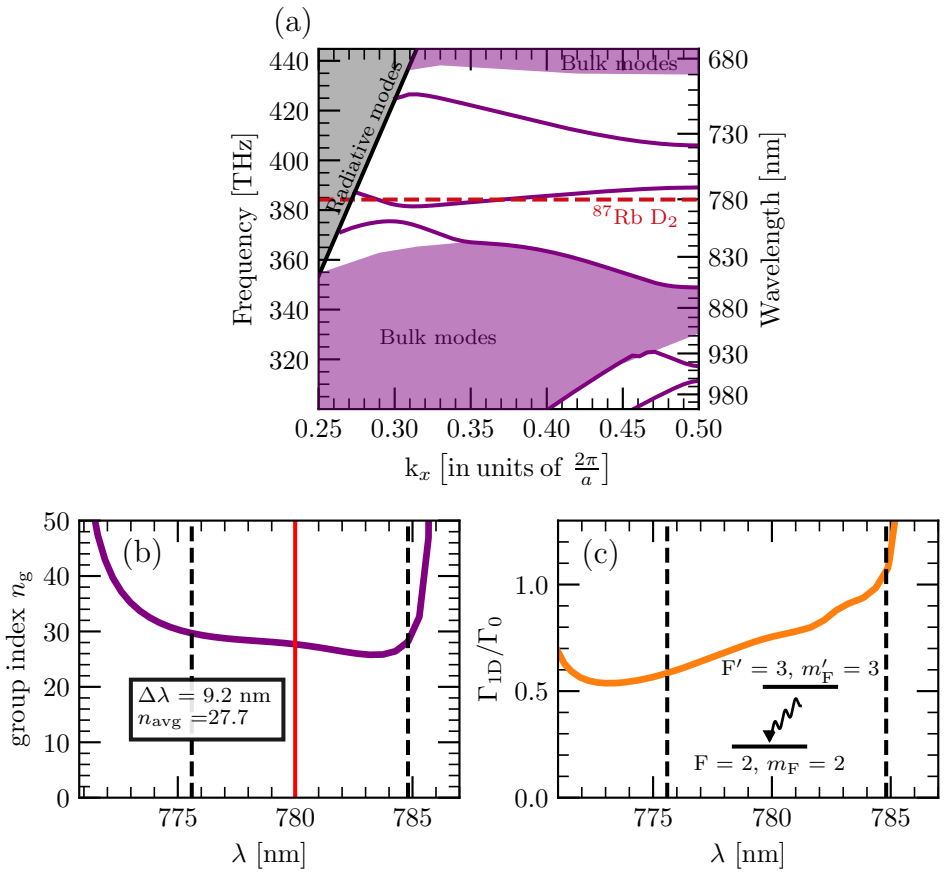

Figure 5.8: Optimized half-W1 photonic-crystal waveguide supporting a large-bandwidth linear slow band. (a) Band structure of the optimized structure calculated via 3D FDTD simulation. The band gap for the TE-like polarization sits between 365 and 435 THz. The ^{87}Rb D_2 line transition frequency is aligned with the linear part of the slow band. (b) Calculated n_g for the slow band. The dotted lines delimit the linear region where the group index value is constant up to 15%. (b) Calculated 1D Purcell factor Γ_{1D}/Γ_0 over the same range of wavelengths, for atoms trapped at 116 nm from the structure on the cyclic transition of the D_2 line. n_g is not the only parameter affecting this ratio (the field structure is also changing), but it is still critical as Γ_{1D}/Γ_0 diverges just outside the plateau of n_g.

vanishes, making it impossible to fit a linear dispersion.

An optimized structure with similar performances to its W1 counterpart

We choose an optimized design with a realistic group index and a wide enough bandwidth. Only group indices below 50 are considered as experiments have shown that it is challenging to reach higher values [Mazoyer et al. 2010]. The most concluding optimization results are obtained for a target around $n_g = 35$. The optimized structure is simulated in full 3D FDTD to validate the results from the approximate GME method (see Appendix B). The results given by both methods are usually quite similar (except when looking at spatial profiles) but FDTD leads to a shift in frequency and to a slight decrease in the group index. The discrepancy between the methods increases with n_g, reinforcing our strategy to work at moderate n_g. In the case of the optimization selected GBP = 0.33 for the GME calculation while 3D FDTD simulations led to a GBP of 0.32. The frequency shift can be compensated by playing on a and L and rescaling all the parameters (dy_i and dr_i included), without affecting much

the shape of the curves. Some deformation still occurs as we cannot rescale the value of the thickness which is a fixed experimental parameter. After compensation of the shift, we have $a_{\mathrm{FDTD}} = 212\,\mathrm{nm}$ $r_{\mathrm{FDTD}} = 63.6\,\mathrm{nm} = 0.3\,a$ and $L_{\mathrm{FDTD}} = 337.7\,\mathrm{nm}$. The shifts in position and radius after optimization and rescaling are given in the Table in Fig. 5.7 and the corresponding 3D FDTD band structure is presented in Fig. 5.8(a). Figure 5.8(b) shows that we engineered a band with a constant group index $n_{\mathrm{g}} \simeq 28$ over a 9.2 nm range, and hence reach similar performance than previous optimizations of W1 waveguides [Li et al. 2008]. This feature offers a two-fold advantage: in addition to making it robust to shifts caused by fabrication imperfections, the optimization enables to use the half-W1 waveguide in a large bandwidth regime (≥ 4 THz) with very little dispersion.

Finally, since the 1D Purcell factor is proportional to the group index n_{g} (see Eq. (2.44)), we obtain with our optimization strategy an almost constant coupling in this frequency range as seen in Fig. 5.8(c). The residual variation arises from small changes in the spatial structure of the electric field when moving along the guided band.

5.2.4 Strong chiral coupling to the guided slow mode

Given the optimized waveguide, we now look at the interaction between the slow mode and the ^{87}Rb atoms in its vicinity. Even with the conservative optimization carried out above, we show that the expected coupling (expressed in term of the 1D Purcell factor $\Gamma_{1\mathrm{D}}/\Gamma_0$) is significant.

Taking into account the multilevel character of Rubidium, we defined a transition-dependent 1D Purcell factor in Eq. (2.50) from Chapter 2. The group velocity v_{g} is evaluated from the simulated band structure, while the other terms are computed from the field map of the guided mode. Figures 5.9(a-b) show that in order to have the maximum coupling, the atoms should be trapped where the guided mode intensity

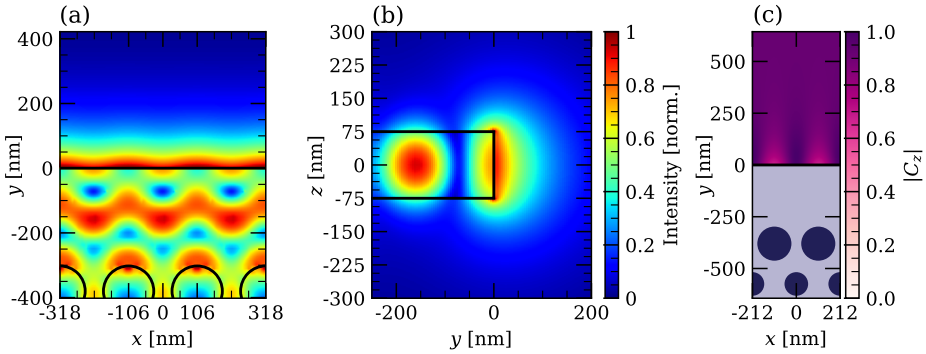

Figure 5.9: Structure of the forward-propagating slow mode at the ^{87}Rb D_2 line frequency. (a) Normalized intensity, in the (x, y)-plane at $z = 0$, shows maxima aligned with the first row of holes. (b) Same in the (y, z)-plane at $x = -a/2$, i.e., crossing the hole nearest to the slab edge. The mode is strongly expelled into the vacuum around the edge of the waveguide. (c) Polarization ellipticity z-component C_z in the (x,y) plane at $z = 0$. The other components of the ellipticity vector are 0. $|C_z| = 0$ indicates a linear polarization, while we have $|C_z| = 1$ for a circularly polarized light. Close to the edge, the polarization has a large circular component due to the strong longitudinal component that appears when light is confined at the nanoscale. By taking z as the quantification axis, the polarization will be close to σ^+ for atoms trapped in the proximity (92 to 99% fraction at 116 nm from the surface).

is largest, i.e. close to waveguide edge, aligned to the holes of the first row. Trapping will be detailed in the next section.

Figure 5.9(c) highlights the strong circular polarization of the slow mode along the whole structure, quantified by the ellipticity vector $\mathbf{C} = \mathrm{Im}\left[(\mathbf{E}\times\mathbf{E}^*)/|\mathbf{E}|^2\right]$[4]. This is reminiscent of the polarization of the light around nanofibers and comes from the longitudinal component of the electric field that appears when light is strongly confined. By choosing a quantization axis perpendicular to our waveguide (along z), the polarization of the forward propagating mode seen by the atoms is predominantly σ^+. The selectivity is further enhanced by the Clebsch-Gordan coefficients which favor transitions at larger m_F. We introduce the excitation rate γ^+_{exc} of an atom in the state $|F=2,m_F=+2\rangle$ with a resonant guided mode propagating along increasing x. Decay and excitation rates are distinct as atoms can be excited with a mode propagating in either direction while decay happens in both. The first (second) term in Eq. (2.50) corresponds to the emission of the atom into the guided mode in the forward (backward) direction. By reciprocity, we can define the excitation rates $\gamma^{\pm}_{\mathrm{exc},F,F',m_F,q}$ of an atom initially in $|F,m_F\rangle$ and promoted to $|F',m_F-q\rangle$ when coupled to an input propagating mode $\mathbf{E}^{\pm}$ at the resonance frequency:

$$\gamma^{\pm}_{\mathrm{exc},F,F',m_\mathrm{F},q} = \frac{\pi a c}{\hbar}\frac{|\langle F||\hat{\mathrm{d}}||F\rangle|^2}{\lambda_0 v_\mathrm{g}}|C_{m_F,q}|^2\frac{|\hat{\mathbf{e}}_q\cdot\mathbf{E}^{\pm}(\mathbf{r})|^2}{\int_{\mathcal{V}_\mathrm{cell}} d\mathbf{r}'\epsilon(\mathbf{r}')|\mathbf{E}^{+}(\mathbf{r}')|^2}. \tag{5.2}$$

This quantity is visualized in Fig. 5.10(a) for an incoming beam in the $+\hat{\mathbf{e}}_x$ direction. This figure confirms the important dependence of the excitation rate on the polarization. The σ^+ transition is stronger than the σ^- transition by two orders of magnitude, while the π transition is completely suppressed around $z=0$ as the TE-like slow mode does not have any E_z component in the symmetry plane. The excitation of an atom by a guided mode is thus highly chiral. Once promoted to $|F'=3,m_{F'}=+3\rangle$, guided mode emission will occur preferably in forward propagation, with a probability given by the polarization fraction of $\mathbf{E}^+$ in σ^+[5], $P_+=92\%$ at the position of the atoms.

The hybrid half-W1 platform hence exhibits high chiral coupling. This feature is crucial, as introducing chirality in 1D chains of emitters can modify their properties and give rise to new physics [Fedorovich et al. 2022]. From a technical point of view, chirality makes some theoretical models, such as the MPS formalism, more tractable. This allows for simulating larger systems more accurately, bridging the gap for better agreements between simulations and experimental data [Mahmoodian et al. 2020]. Finally, chiral coupling can be a tool for generating non-Gaussian states of light [Kleinbeck et al. 2023], highly entangled atomic states [Buonaiuto et al. 2019] and to implement original quantum information protocols [Lodahl et al. 2017; Li et al. 2018].

Besides, Fig. 5.10(a) shows that for atoms in state $|F=2,m_F=+2\rangle$ and trapped at 116 nm from the edge, the Purcell factor reaches a value of 0.71. As shown in Figs 5.10(b-c), a small modulation in the x direction exists and the value of the Purcell factor decays rapidly as a function of the distance to the surface. To quantify the response of the atoms to the guided mode we can also use the β factor, $\beta=\Gamma_{1\mathrm{D}}/\Gamma_{\mathrm{tot}}$ with $\Gamma_{\mathrm{tot}}=\Gamma_{1\mathrm{D}}+\Gamma'$, and Γ' the decay rate in all radiation modes other than the guided slow mode.

[4]The direction of $\mathbf{C}$ indicates that the field has some circular component in the normal plane. A norm of 1 means the field is perfectly circular. Its sign gives the direction of rotation.

[5]If we write the field polarization as the sum of left and right circular polarizations $\mathbf{E}\propto a_L\hat{\mathbf{e}}_L + a_R\hat{\mathbf{e}}_R$, $P_+=|a_L|^2$. $\mathbf{C}\cdot\hat{\mathbf{e}}_z=|a_R|^2-|a_L|^2$ so the polarization fraction becomes $P_+=(1-\mathbf{C}\cdot\hat{\mathbf{e}}_z)/2$.

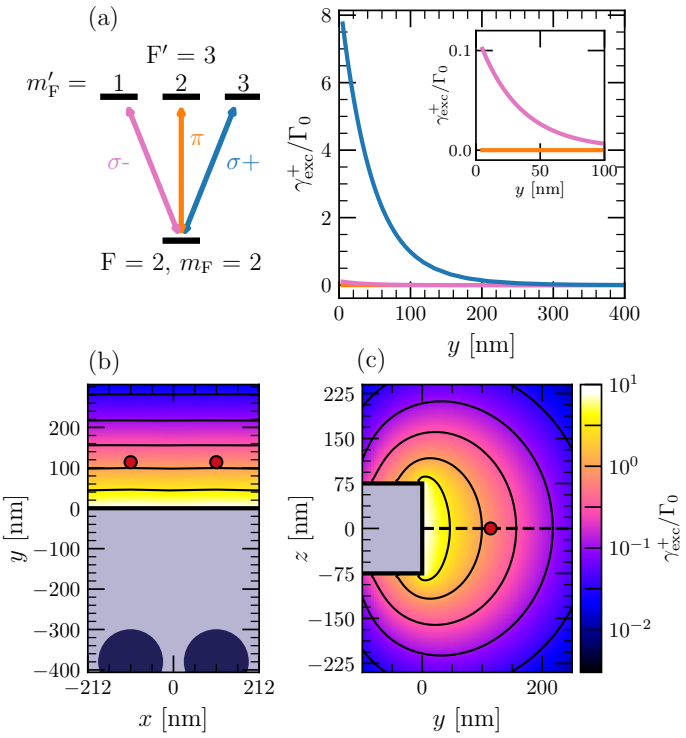

Figure 5.10: Excitation rates γ^+_{exc}/Γ_0 for ^{87}Rb atoms in the waveguide proximity. (a) Allowed transitions on the D_2 line for an atom in $|F = 2, m_F = +2\rangle$. Because of the large σ^+ component ($\sim 92\%$ at the position of the atoms) and the values of the Clebsch-Gordan coefficients, the excitation probability to the $|F' = 3, m_{F'} = +3\rangle$ is more than 100 times higher than the σ^- channel. The inset provides a zoom. (b) Purcell factor in the (x, y) plane, at $z = 0$. (c) Purcell factor in the (y, z) plane, at $x = -a/2$. The red dots indicate the position of the atoms at 116 nm from the surface, as detailed later.

Equation (2.18) tells us that Γ_{tot} is proportional to the total self Green's tensor $\overleftrightarrow{\mathbf{G}}(\mathbf{r}_0, \mathbf{r}_0; \omega_0)$ at the position $\mathbf{r}_0$ of the emitter. The calculation of $\overleftrightarrow{\mathbf{G}}$ for an atom close to an infinitely long periodic waveguide is not trivial and requires an accurate calculation of the emission into radiation modes. An approach often used is to assume that the emission rate into radiation modes is approximately equal to the one in vacuum, $\Gamma' \approx \Gamma_0$, see for instance [Zang et al. 2016][6]. Here, we calculate rigorously the Green's tensor of the periodic waveguide by using a modal method that relies on an exact Bloch-mode expansion [Lecamp et al. 2007; Fayard et al. 2022]. We find that $\Gamma' \simeq 0.8\,\Gamma_0$, at the position of the trap minimum, i.e at 116 nm from the surface.

We thus obtain $\beta = 0.47$, very close to the spatially averaged value $\tilde{\beta} = 0.46$ for a thermal distribution (at a temperature of one half of the trap depth). This is at least 50 times better than the current systems involving nanofibers ($\beta = 10^{-2}$) [Corzo et al. 2019] and in the same range of current PCW-based platforms ($\beta = 0.45$, with cavity enhancement) [Goban et al. 2015]. To the best of our knowledge, our proposed platform is the only one combining chirality and large individual light-matter coupling.

[6] Another approach consists in considering a long but finite structure with N cells and recording the response of a dipole placed at the position where we want to compute Γ_{tot}. This can be done through FDTD simulations but strong oscillations (with a period $\propto 1/N$) appear on the $\Gamma_{tot}(\omega)$ spectrum, making the estimation difficult [Hung et al. 2013].

5.2.5 Trapping Rubidium atoms near a half-W1 waveguide

In the previous section, simulations were performed for atoms at 116 nm from the edge of the waveguide. Indeed, in the following we show a stable trapping scheme based on an evanescent two-color dipole trap formed by fast guided modes, allowing the atoms to be trapped at this distance. As before, this trap has been designed following the ideas implemented in optical nanofibers [Le Kien et al. 2004; Vetsch et al. 2010]. Apart from the periodicity of the trapping modes, critical differences with the ONFs include the presence of sharp edges which can be detrimental for trapping and call for a more precise estimation of the CP potential.

Two-color dipole trap structure

In contrast with optical nanofibers and nanobeams, the guided modes in the half-W1 waveguide are structured along the propagation direction due to the Bloch wave structure of the light field. The intensity of the modes, which is an important quantity when looking at dipole trapping, is periodic with period a, as shown in Fig. 5.9(a) for the slow mode. This feature constrains the position of the trapped atoms to the maxima of intensity of the red-detuned mode. It makes the search for a blue detuned mode more challenging as this one will also be structured, while a uniform one would work perfectly well to repel the atoms from the surface [Goban et al. 2012]. A blue-detuned beam with an intensity pattern out of phase with the red-detuned one is needed. Fortunately, modes separated by a band gap usually have intensity maxima shifted by $a/2$ [Johnson et al. 2004]. For the blue-detuned beam, we use the available guided band above the slow mode between 400 and 420 THz (see Fig. 5.8(a)).

In order to have a full description of the potential seen by the atoms, we take into account the Casimir-Polder (CP) interaction [Casimir and Polder 1948] between the atoms and the surface, introduced in Chapter 3. Vacuum fluctuations can polarize the atoms, even if they are not charged. When put in proximity to structures, the vacuum-induced dipole moment creates a mirror charge that acts on the original dipole, leading to an additional light shift. The CP potential U_{CP} is only significant at very close distances (≤ 150 nm) but is crucial as it acts as an attractive potential close to the surface. For these systems, the approximation of an atom in the proximity of an infinite dielectric half space is often used $U_{\mathrm{CP}}^{\mathrm{plane}} = -C_3/d^3$ [Johnson et al. 2004], where d is the distance to the surface. However, as a slab, our structure deviates significantly from a half space. Hence, we computed a more realistic, space-dependent CP potential, based on the pairwise summation technique (PWS) [Bitbol et al. 2013], as described in Appendix A. This form of potential was already used in the previous Sec. 5.1 to compute the trapping potential around a nanobeam.

Trapping potential simulation

Figure 5.11 shows the total trapping potential U_{tot} in 3 directions for an atom in the $|F = 2, m_F = +2\rangle$ hyperfine level. U_{tot} is the sum of the contributions of the blue potential U_{blue}, the red potential U_{red} and the CP potential U_{CP}. Figures 5.11(a-c) show the trap along the x and y axis, in the symmetry plane of the waveguide. As shown in Fig. 5.11(d), trapping out of the (x, y) plane is less obvious as the confinement of the atom is low in the azimuthal direction. The curvilinear coordinate is computed as the total distance the atom can travel in the valley of minimal potential shown in the inset with the origin corresponding to $z = 0$. The real depth of the trap is given by the potential barriers that appear in Fig. 5.11(d), and are physically around $y = 0$. The trap in this direction is about 100 µK deep. The limited trapping

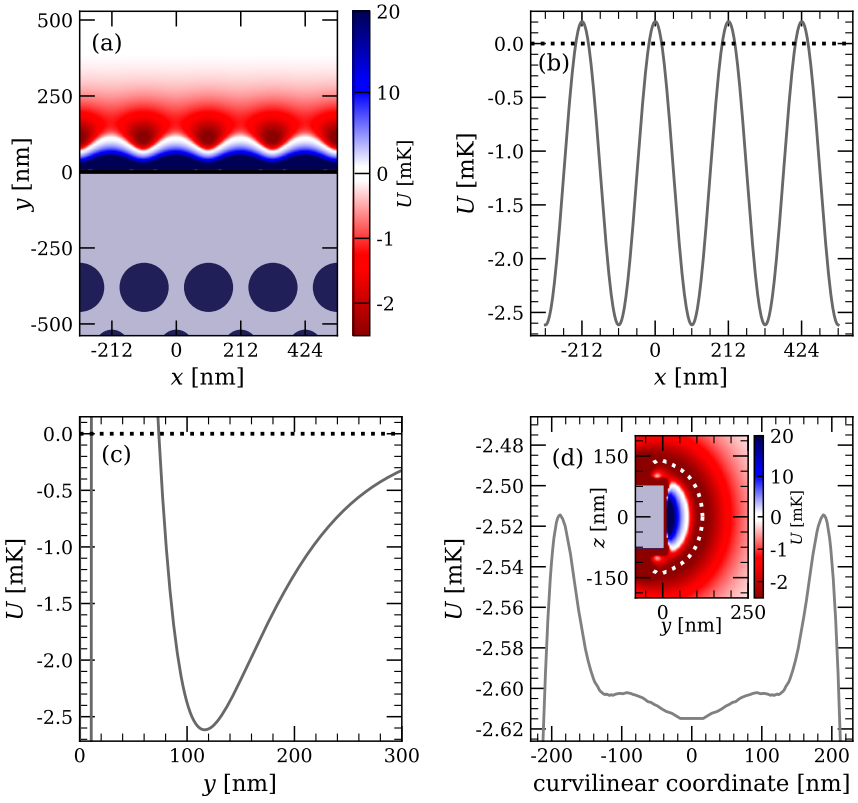

Figure 5.11: Calculated potential of the two-color dipole trap for $m_F = 0$. (a) 2D total trapping potential U_{tot} in the proximity of the waveguide, in the (x,y) plane. The trapping potential is given along (b) x, (c) y and (d) the azimuthal direction out of the symmetry axis. The inset shows the curved trap in the (y,z) plane. The trap is taken along the dotted white line. A periodic stable trap with depth of about 2.6 mK is obtained with powers of 3.1 mW for each blue beam and 93 µW for each red one. The simulations are performed with the `nanotrappy` package and can easily be done for the other m_F sublevels.

depth in this direction has the same origin as in the nanobeam case (see Sec. 5.1), the red beam decaying too slowly in the vertical direction. In the case of the half-W1 this effect can often lead to atoms that are not trapped at all and can crash onto the upper surface of the waveguide. While the atoms can be spread over this valley, the averaged beta factor $\tilde{\beta}$ for a thermal cloud in this trap typically remains close to the peak value, as the slow mode shares similar spatial distribution (see Fig 5.10(c)).

For this trap, a beam red-detuned from the D_2 line of ^{87}Rb at $\lambda_{\text{red}} = 784.45\,\text{nm}$ and a beam blue-detuned at $\lambda_{\text{blue}} = 735.86\,\text{nm}$ are used. For each color, another beam detuned by respectively 280 and 385 GHz at the same power is counterpropagated for vector shift cancellation (see Sec. 3.1.1). An absolute trap depth (relative to the atoms being infinitely far away) of 2.6 mK is obtained with a minimum at 116 nm from the surface. The total powers are $P_{\text{blue}} = 2 \times 3.1\,\text{mW}$ and $P_{\text{red}} = 2 \times 93\,\mu\text{W}$, but a stable trap can be obtained over a wide range of powers, with trapping positions ranging typically from 115 to a few hundreds of nanometers. The trapping frequencies are large in the x and y directions, with $\omega_x = 2\pi \times 1.75\,\text{MHz}$ and $\omega_y = 2\pi \times 2.00\,\text{MHz}$. Out of the symmetry plane however, there is an important anharmonicity of the trap in the azimuthal direction. The trap is less constrained in that direction and we extract $\omega_z = 2\pi \times 83$ kHz.

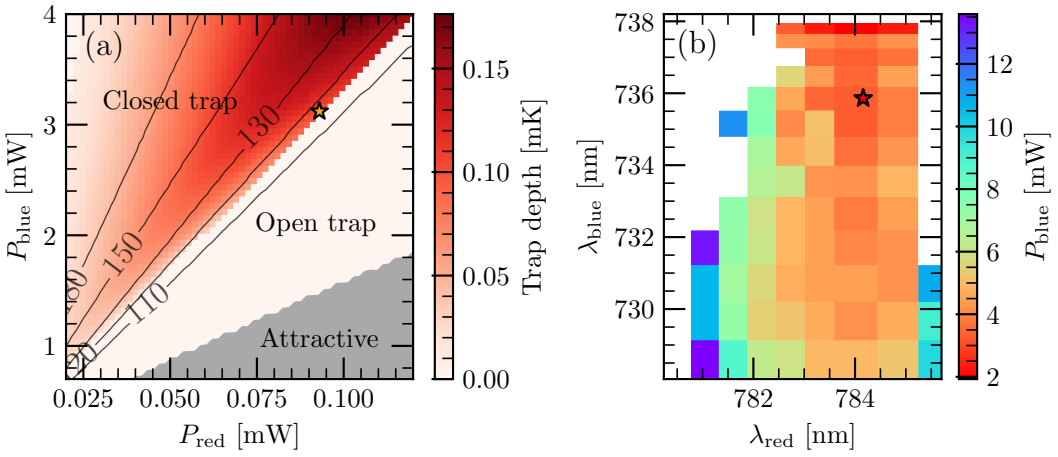

Figure 5.12: Trapping around the half-W1 for a wide range of powers and wavelengths. (a) Trap depth (measured as the depth along the curvilinear coordinate) as a function of the trapping powers for $\lambda_{\mathrm{blue}} = 735.86\,\mathrm{nm}$ and $\lambda_{\mathrm{red}} = 784.45\,\mathrm{nm}$. "Open trap" means a minimum of potential exists in the y direction but not along the curvilinear coordinate. "Attractive" that no local minimum exists in the y direction. The orange star is the setting in Fig. 5.11. (b) Minimum blue power P_{blue} needed to achieve a closed trap 100 µK deep at 116 nm from the surface for a wide range of blue and red of wavelengths (Only P_{blue} shown as $P_{\mathrm{blue}} \gg P_{\mathrm{red}}$ for these ranges). The red star is the set of wavelengths used in (a) and in the main text.

Figure 5.12(a) shows the depth of the two-color dipole trap along the curvilinear coordinate for a wide range of P_{blue} and P_{red}, with the same λ_{blue} and λ_{red}. Three regions are identified in the plot. There is an "attractive" region where the blue light shift cannot compensate the sum of the red light shift and the CP potential, leading to a monotonous attractive potential along the y direction down to the waveguide surface. The "open trap" region refers to the case where a trap exists in both the y and x axis, but the atoms can find their way up to the structure surface via the azimuthal direction, because the blue beam in this direction cannot compensate the longer decaying tail of the red-detuned mode. The "closed trap" is the case we are interested in as it means a barrier exists in this azimuthal direction. The height of the barrier is represented with the red shading, and the position of the minimum along y by the black contour lines. The trap presented in Fig. 5.11 is located by the orange star. It corresponds to a compromise between having a trap position close enough while not having a trap too deep. Indeed, having a large trap minimum can cause heating due to any residual vector shift or anti-trapping of the excited state atoms (no magic wavelengths exist for Rubidium).

As the structure can only handle a given maximum power P_{max} before being damaged by heating, we anticipate the existence of a forbidden region for $P_{\mathrm{blue}} + P_{\mathrm{red}} > P_{\mathrm{max}}$. P_{max} still has to be determined experimentally, but in [Combrié et al. 2009], power densities up to 1 GW/cm^2 were coupled to similar GaInP PCWs with group index 8.8. For our structure which has a cross section 10 times smaller and a group index 3 times bigger, this would be equivalent to coupling $\simeq 100\,\mathrm{mW}$ into our waveguide. The proposed powers for the trap fall well below this bound.

Importantly, we also verified that we can achieve a stable trap in the three directions for a wide range of wavelengths, which is a valuable feature for finding the right trade-off between heating the atoms with off-resonant scattering and power handling of the waveguide. Figure 5.12(b) shows the minimum blue power P_{blue} required to

achieve a closed trap 100 µK deep, at 116 nm from the surface along y, for a range of λ_{blue} and λ_{red}. The white region means no trap satisfying those constraints was found (it might exist for larger distances). We show here that for powers below 5 mW, we can find such a trap for blue wavelengths ranging from 728 nm to 738 nm. By allowing more power we can extend this to the full available blue-detuned air band, i.e. $\Delta\lambda_{\text{blue}} \approx 21$ nm. The wavelength of the red beam is more constrained, but still offers an available range from from 781.0 nm up to 785.5 nm. Laser diodes are easily available at these wavelengths (as they are between the D_1 and D_2 lines of Rubidium), reinforcing the feasibility of our platform.

Finally, as briefly noted before, we used counterpropagating beams here instead of simple ones, albeit standing waves are not needed for periodic intensity modulation. The strong ellipticity of the guided modes, shown in Fig. 5.9(c), acts as a fictitious magnetic field on the atoms, splitting the Zeeman levels [Cohen-Tannoudji and Dupont-Roc 1972]. If we start from atoms evenly distributed in all the m_F states, this effect would lead to a large inhomogeneous broadening up to a few GHz. This effect can be mitigated by using counterpropagating trapping beams slightly detuned from each other, as done for the blue-detuned beams in some compensated nanofiber traps [Goban et al. 2012], see Fig. 3.6(e). Via `nanotrappy`, we estimated that adding a red-detuned laser at 280 GHz from the first one and a blue detuned at 385 GHz from the other reduces this broadening by 90%. Counterpropagation creates a running wave at a velocity given by $\delta\omega/k$. This pattern propagates but at a speed so large the atoms only see the average of the potential.

Other possible trapping schemes

The former trapping scheme used blue- and red-detuned beams in the same TE-like polarization. This is interesting as it creates a stable trap for atoms at the position of the maximum of 1D Purcell factor in the x direction but leads to low trapping depths in the azimuthal direction. Figure 5.13 presents alternative trapping schemes which might be as promising as the former one. The top row of Fig. 5.13 shows a similar trapping scheme but using different bands of the band structure. The upper part of the slow band is now used for the blue-detuned beam and the lowest gap-guided band for the red ($\lambda_{\text{blue}} = 770.0$ nm, $\lambda_{\text{red}} = 800.0$ nm). This shifts the trapping position by $a/2$ in the x direction but as seen in Fig. 5.10(b) this is not critical as the 1D Purcell factor is almost constant along x. A stable trap at $d = 114$ nm from the surface with a depth of 2.2 mK is achieved, leading to a comparable 1D Purcell factor of 0.72. This trap is achieved for low powers ($P_{\text{blue}} = 135$ µW, $P_{\text{red}} = 55$ µW) as the detunings of the trapping beam with respect to the D_2 line are way smaller than in the previous case. The barrier along the azimuthal direction can be made higher than in the previous scheme, 250 µK in this case.

The bottom row of Fig. 5.13 shows another alternative trapping technique which further increases the azimuthal confinement. As for the nanobeam, one can use crossed polarizations. The blue beam will have an intensity maximum in the vertical direction, repelling the atoms from the upper surface. The TM-like band structure of the half-W1 does not have a band gap, but exposes index-guided bands at frequencies inside the TE band gap. Figure 5.13(e) shows explicitly the trapping scheme: the red-detuned mode is the same as in Sec. 5.2.5, while the blue-detuned one is taken around $k = 0.42$, just before the TM mode crosses the Rb D_2 line ($\lambda_{\text{blue}} = 771.46$ nm, $\lambda_{\text{red}} = 784.45$ nm). A stable trap is achieved at $x = 0$, $d = 107$ nm from the surface with at a depth of 0.82 mK with $P_{\text{blue}} = 5$ mW, $P_{\text{red}} = 114$ µW, leading to a 1D Purcell factor of 0.83. In this case the trap minimum is the real barrier the atoms

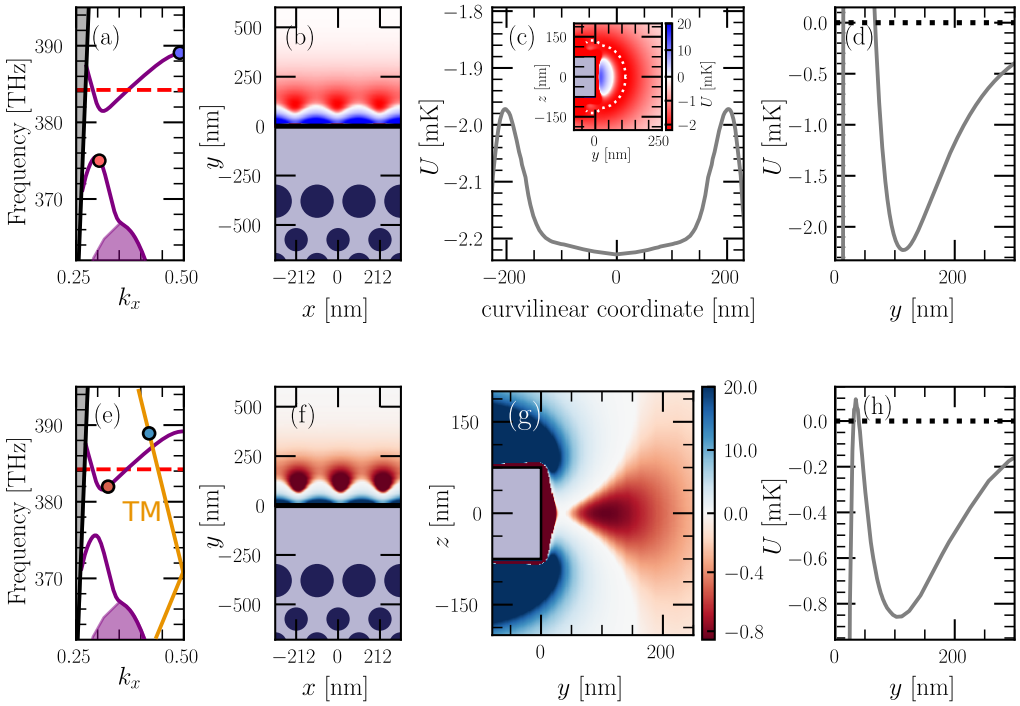

Figure 5.13: Alternative trapping schemes with the same waveguide: lower bands and TM modes. Top row: (a) We use the lower band as the red-detuned mode ($\lambda_{\text{red}} = 800.0\,\text{nm}$) and the slow one as the blue ($\lambda_{\text{blue}} = 770.0\,\text{nm}$). (b) 2D trapping with $P_{\text{blue}} = 135\,\mu\text{W}$ and $P_{\text{red}} = 55\,\mu\text{W}$. Notice the traps are shifted by $a/2$ with respect to the former scheme. (c) Trap in the azimuthal direction out of the symmetry axis, taken along the dotted line in the inset. (d) Trap along y. Bottom row: (e) We use the same red mode as the first scheme ($\lambda_{\text{red}} = 784.45\,\text{nm}$) and the blue comes from the lowest TM index-guided band, displayed in orange ($\lambda_{\text{blue}} = 771.46\,\text{nm}$). (f-h) Trapping potential for $P_{\text{blue}} = 5\,\text{mW}$ and $P_{\text{red}} = 114\,\mu\text{W}$ in the (x, y), (y, z) planes and along y. Because of the crossed polarizations, the blue beam repels the atoms from the upper surface.

are trapped into; as seen in Fig. 5.13(g), there is no weak trapping valley anymore. The relatively high power in the blue beam comes from the fact that most of the blue intensity is in the vertical direction, and power is needed to actually get the modulation in the x axis made by the blue repulsion.

In conclusion, the half-W1 waveguide with linear bands is very promising for the realization of a hybrid cold atom-PCW platform. Atoms can be trapped between ≈ 110 and a few hundreds of nanometers from the surface with trapping powers compatible with the nanophotonic device. As some of the trapping schemes use trapping wavelengths close to the resonant transition, future analysis will have to quantify the heating of the atoms via scattering. The slow mode couples to the atoms with $\beta = 0.47 - 0.51$ for the trapping schemes considered, with a group index around 28. This index can realistically be increased to give even stronger couplings. As such, this platform meets all requirements from Sec. 4.3.1. This study also shows that high GBP (at least as good as for W1 waveguides) can be achieved in such an asymmetric structure via careful dispersion engineering techniques, and we believe this systematic optimization can be applied to other structures for improving their robustness to imperfections.

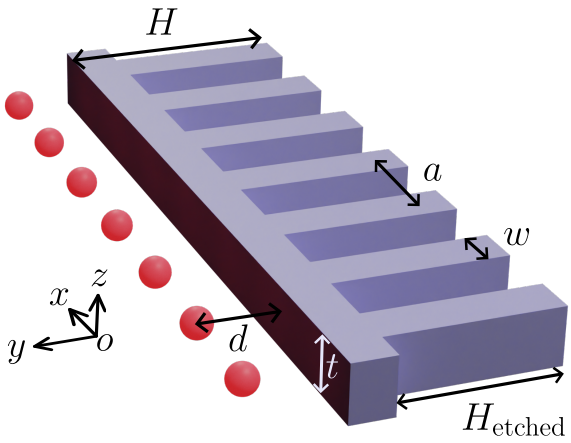

Figure 5.14: 3D scheme of the asymmetric comb waveguide with a chain of atoms on its edge. Like the half-W1, the waveguide is etched in a GaInP membrane suspended in air. It has a total width H along y and a thickness t in the vertical z direction. The comb pattern along the propagation direction x is made of teeth with a width w and a height H_{etched}, periodically spaced with a period a. The width of the guiding region is thus $H - H_{\text{etched}}$.

5.3 Quartic bands: the comb waveguide

We now study the feasability of another cold atom-PCW platform based on a one-dimensional asymmetric comb waveguide, exhibiting quartic dispersion in its slow-mode guided band. This waveguide has been introduced in [Nguyen et al. 2018] for its exotic dispersion engineering capabilites. The structure studied here is depicted in Fig. 5.14. It consists of a suspended bridge waveguide of width H and thickness t that has been periodically corrugated with an asymmetric rectangular pattern. Atoms are interfaced at the flat edge of the waveguide, where they can be trapped. Most of this section is adapted from [Fayard et al. 2022], and the simulations were realized in collaboration with our partners from Institut d'Optique, Nikos Fayard and Christophe Sauvan.

We exploit symmetry breaking to design precisely this comb platform and show that (i) it supports a slow mode with a **quartic dispersion**, (ii) it offers the possibility to trap atoms optically at subwavelength distances, and (iii) it provides very large β factors for such trapped atoms. As already hinted in Chapter 4, we discuss how the quartic dispersion makes the slow mode more tolerant to fabrication imperfections than previous proposals.

5.3.1 An asymmetric waveguide with quartic dispersion

Emergence of the quartic dispersion

We first look at how a quartic dispersion curve can emerge at the band edge of such an asymmetric waveguide from a quadratic one. We compare in Fig. 5.15(a-c) the band diagrams of different periodic waveguides with period a. Figure 5.15(a) displays the case of a comb waveguide whose corrugation is symmetric in the transverse direction[7]. As already discussed in Sec. 4.1.3, the corrugation couples forward and backward propagating modes of the uncorrugated waveguide, resulting in the opening of photonic band gaps at the edge of the 1BZ. Using a standard coupled-mode

[7]The band diagrams in this section are computed with the algorithm `reticolo` developed at Institut d'Optique based on rigorously coupled wave analysis (see Appendix B).

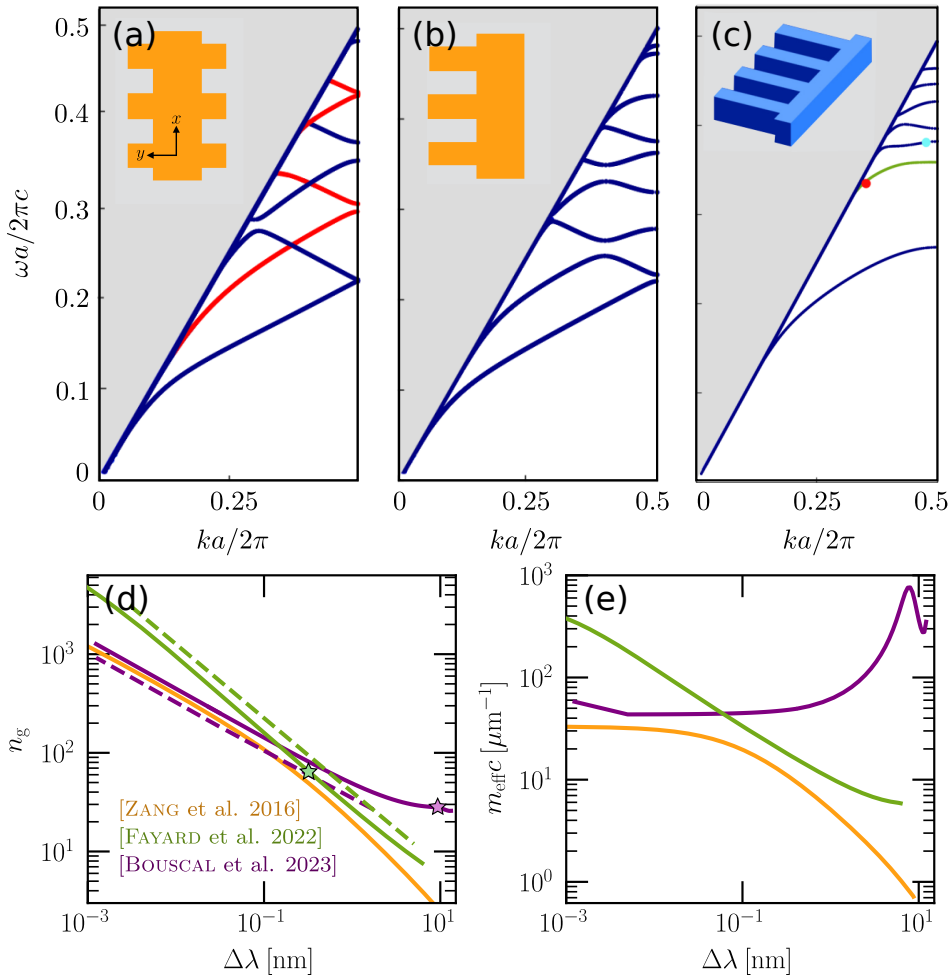

Figure 5.15: Impact of transverse symmetry breaking and increased robustness of quartic dispersions. (a) TE-like band diagram of a symmetric comb waveguide. The width of the teeth on both sides is $w = 0.5a$ and their depth is $H_{\text{etched}} = 0.25H$. (b) Asymmetric comb waveguide with $H_{\text{etched}} = 0.5H$ only on one side. We note the resemblance with (a), with the opening of band gaps at $k \neq 0.5$ because of the coupling between the former symmetric and antisymmetric modes. (c) Optimized 3D comb structure supporting a band with a quartic dispersion (in green). (d) Group index n_g and (e) effective photon mass $m_{\text{eff}}c$ as a function of the distance to the band edge, $\Delta\lambda$ (log scales). The green curves correspond to the slow mode of the 3D comb waveguide, the orange curves to the original half-W1 waveguide in [Zang et al. 2016] and the purple one to the linear band of the optimized half-W1 from Fig. 5.8 and [Bouscal et al. 2024]. Stars show the operating point chosen for the mode at 780 nm in both optimized waveguides. The dashed curves indicate the $\Delta\lambda^{-3/4}$ (green) and $\Delta\lambda^{-1/2}$ (purple) scaling laws.

approach with two waves having linear dispersions, one can show that the dispersion relation of the Bloch modes varies quadratically in the vicinity of these points: $\omega - \omega_e = \pm\alpha_2(k - \pi/a)^2$ [Dubois 2018], where ω_e is the frequency of the band edge and α_2 some proportionality factor. The symmetry of the corrugation forbids coupling between modes of different symmetry with respect to the (x, z) plane. The Bloch modes are either symmetric (blue curves) or antisymmetric (red curves) with vanishing overlap integrals at crossing points.

The situation is fundamentally different in the asymmetric waveguide presented in Fig. 5.15(b). Since the corrugation has no particular y-symmetry, all possible couplings between modes are allowed. As a result, gaps now open inside the Brillouin zone ($k \neq \pi/a$) around the points of intersection between the dispersion curves of the symmetric and antisymmetric modes of the uncorrugated waveguide. The coupling strengths depend on the size of the teeth, fixed by the width w and the depth H_{etched} defined in Fig. 5.14. Stronger corrugations result in larger coupling strengths and wider band gaps. If the coupling is strong enough, a band gap opening at $k \neq \pi/a$ can have an influence on the curvature of the band edge at $k = \pi/a$. Intuitively, we can change the dispersion at the edge of the 1BZ by playing on the strength of such couplings. Quantitatively, it can be shown in a mode coupling approach, that we can cancel the curvature at the band edge to first order at a given value of the coupling, leading to a quartic dispersion. The process now involves four waves (y-even forward propagating, y-even backward, y-odd forward, y-odd backward) instead of two [Nguyen et al. 2018]. The resulting dispersion can be written as $\omega - \omega_e = \pm\alpha_4(k - \pi/a)^4$.

An optimized waveguide with a quartic band

Figure 5.15(c) shows the band diagram of a comb waveguide with such a quartic band (highlighted in green). To achieve this, critical geometrical parameters of the PCW have been optimized to control the strength of the coupling, namely the width of the corrugation H_{etched} and the widths of the teeth w. The resulting structure parameters are $a = 283$ nm, $H = 2a$, $H_{\text{etched}} = 0.8H$, and $w = 0.422a$. As for all the previous PCWs, we considered a GaInP membrane with a thickness $t = 150$ nm.

This gives a band edge which is aligned to the Rubidium D_2 line and a group index of $n_g = 50$ at 780 nm. This value of the group index is compatible with current fabrication processes [Mazoyer et al. 2010].

The increased robustness of quartic bands

We explore more precisely why such quartic bands are significant. Sec. 4.3.2 presented the dependence of the group index n_g with $\Delta\omega$, the distance to the band edge, for both quadratic ($n_g \propto \Delta\omega^{-1/2}$) and quartic dispersions ($n_g \propto \Delta\omega^{-3/4}$). Indeed, the group index is given in each case by:

$$n_g = \frac{c}{v_g} = \frac{c}{\partial\omega/\partial k} = \begin{cases} \dfrac{c}{2\alpha_2\Delta k} = \dfrac{c}{2}(\alpha_2\Delta\omega)^{-1/2}, & \text{(quadratic dispersion)} \\ \dfrac{c}{4\alpha_4\Delta k^3} = \dfrac{c}{4}\alpha_4^{-1/4}\Delta\omega^{-3/4}, & \text{(quartic dispersion)} \end{cases} \tag{5.3}$$

where $\Delta k = k - \pi/a$. The relation between frequency and wavelength gives $\Delta\omega = -2\pi c\frac{\Delta\lambda}{\lambda_0}$. From Eq. 5.3, we obtain that a quartic dispersion produces a group index

that scales as $\Delta\lambda^{-3/4}$ while the group index of a quadratic dispersion scales as $\Delta\lambda^{-1/2}$. This effectively broadens the useful bandwidth of the slow mode.

Indeed, if one wants to work at a given group index, the quartic dispersion allows operation at a larger $\Delta\lambda$, i.e., at a frequency further from the band edge than the quadratic one. This is made evident in Fig 5.15(d), where the dependence of n_g with the distance to the band edge $\Delta\lambda$ is shown for different waveguides encountered before: the comb presented here [Fayard et al. 2022], the original half-W1 from [Zang et al. 2016] and the optimized half-W1 with a linear band from the former section [Bouscal et al. 2024]. The solid green curve is extracted from the green band in Fig. 5.15(c). It is parallel to the dashed green straight line with a slope of $-3/4$, confirming the quartic dispersion of the comb slow mode. For a given n_g, the corresponding $\Delta\lambda$ is larger than for the original half-W1. As most PCWs, both half-W1s show a quadratic dispersion up to around $\Delta\lambda = 0.5$ nm. At higher $\Delta\lambda$, the linear band optimization shows its strength as n_g stays almost constant, surpassing even the comb. As detailed in Chapter 4, a larger $\Delta\lambda$ means more robustness to both disorder and systematic errors in the fabrication. If we plan on working close to the band edge, the comb is more robust while offering a high n_g, which might be interesting for future work at $n_g > 50$. For $\Delta\lambda \gtrsim 0.5$ nm however, linear bands have the upper hand. Figure 5.15(e) displays the effective mass for the three structures and confirms these observations, as a high effective mass is also a witness of tolerance of a slow mode to fabrication imperfections [Faggiani et al. 2016; Zang et al. 2016].

We calculate in the following subsection that, despite the moderate slowdown of the light in the comb, we can achieve a strong atom-photon interaction.

5.3.2 A strong light-matter interaction

The spontaneous emission rate of an excited atom and the β factor introduced earlier is computed for atoms trapped around a comb waveguide. The 1D Purcell factor

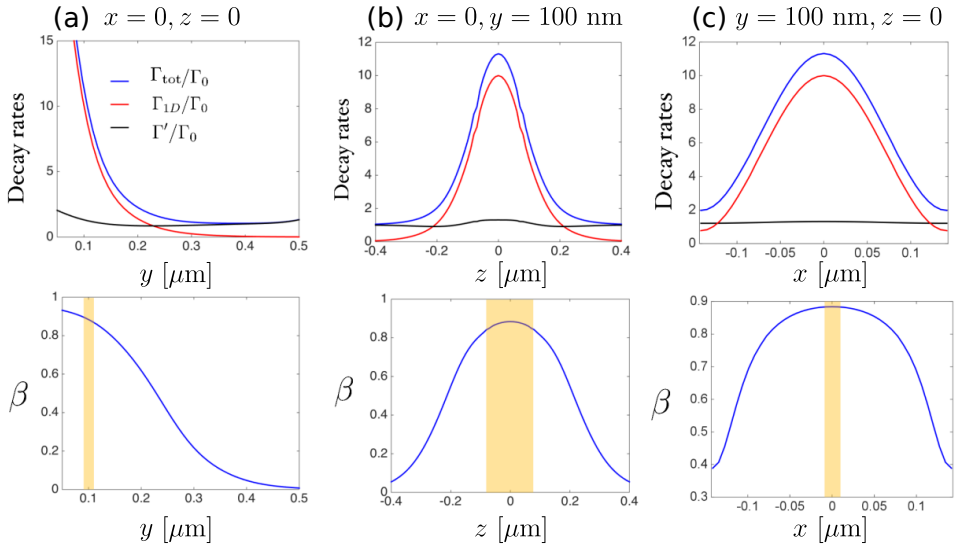

Figure 5.16: Decay rates of an atom near the 3D comb waveguide.
Top row: Decay rates Γ_{tot} (blue), Γ_{1D} (red) and Γ' (black) along three different axes. All decay rates are normalized to Γ_0.
Bottom row: Variation of the β factor $\beta = \Gamma_{1D}/\Gamma_{tot}$ along the same directions. The yellow areas represent the trap extension (defined as the volume for which $U_{tot} < U_{min} + k_B \times 50\,\mu K$). Reproduced from [Fayard et al. 2022].

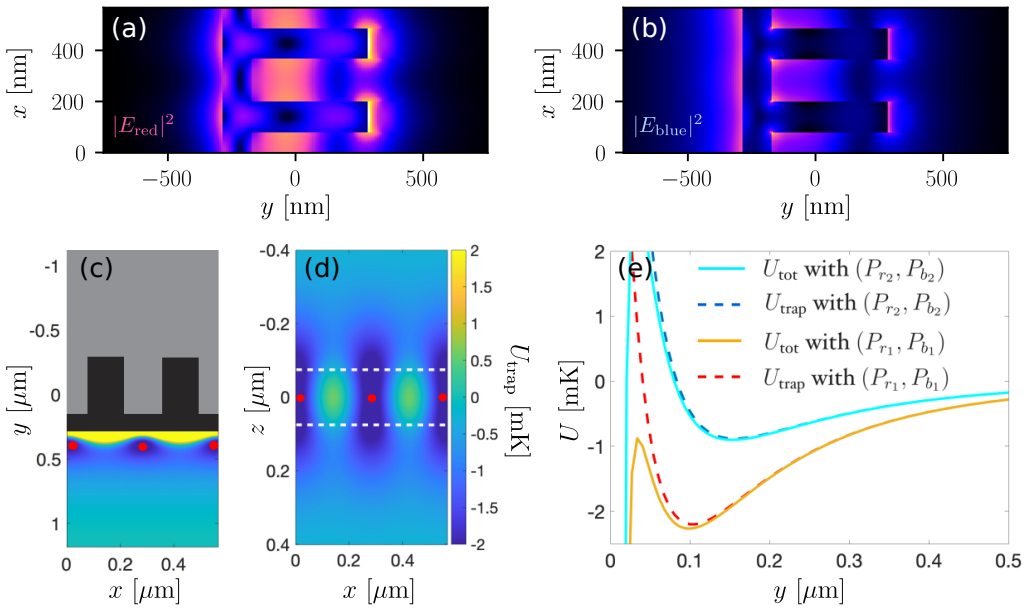

Figure 5.17: Two-color dipole trap around the comb waveguide. First row: Intensity profile of (a) the blue-detuned mode E_{blue} at $\lambda_{\mathrm{blue}} = 736\,\mathrm{nm}$. (b) and the red-detuned mode E_{red} at $\lambda_{\mathrm{red}} = 837\,\mathrm{nm}$. The intensity is represented in the (x, y) plane at $z = 0$ (cross-section through the center of the GaInP membrane). We can see that the maxima of intensity of the red and blue are shifted by $a/2$. Second row: (c) 2D trapping potential U_{tot} in the (x,y) plane (d) and in the (x,z) plane at d) 100 nm from the waveguide. We do not show the potential around the teeth (gray area); it is repulsive and does not exhibit trapping sites. The dashed lines in (b) remind the position of the GaInP membrane. (e) Potential along y for different values of the powers (see main text) with and without the CP potential.

$\Gamma_{1\mathrm{D}}/\Gamma_0$ is computed as before with Eq. (2.44), but in contrast to the previous section we model the atoms as a simpler two-level system with the D_2 line transition frequency and spontaneous decay in free space. The decay is computed for a linear dipole transition along y, as the electric field on the edge of the comb has a very dominant E_y component. In contrast with the nanoscale waveguides encountered before (nanofiber, nanobeam and half-W1), this feature makes the interaction here not chiral. The value of the 1D Purcell factor is given by the red curve in Figs. 5.16(a-c).

The decay rates Γ_{tot} and Γ' are computed like for the half-W1 and displayed in the first row of Fig. 5.16 and the β factor in the second row. Their variation as a function of the position of the atom along three different axes are plotted. The yellow areas represent the volume around the minimum of potential where atoms are most likely to be trapped.

For large distances, $d > 400$ nm, the emission rate $\Gamma_{1\mathrm{D}}$ into the slow mode is negligible compared to the emission rate Γ' into the radiation continuum and the β factor tends towards zero. As the distance d decreases, the atom enters the region where the field of the slow mode is intense and Fig. 5.16(a) shows a strong enhancement of $\Gamma_{1\mathrm{D}}$ that results in an increase of the β factor. For a trapping distance of $y = 100$ nm, $\Gamma_{1\mathrm{D}} = 10\,\Gamma_0, \Gamma' = 1.3\,\Gamma_0$, and $\beta = 0.88$. This number is significantly larger than the value of $\beta \approx 0.5$ that has been experimentally observed for the alligator waveguide [Goban et al. 2015; Hood et al. 2016] or theoretically predicted for the optimized half-W1 waveguide.

5.3.3 Guided trap around the comb waveguide

The last step needed for an atom-PCW platform is to support a stable evanescent trap. We show that the asymmetric comb allows to trap Rb atoms with a two-color evanescent dipole trap as close as 100 nm from the waveguide, where $\beta = 0.88$. For accessibility reasons and because of the spatial profile of modes at the comb teeth, it is not appropriate to create a trap on this side of the comb. Therefore, we aim at trapping atoms on the side opposite the teeth, as pictured in Fig. 5.14.

Once again, we design a two-color dipole trap with guided modes. We have chosen to work with $\lambda_{\text{red}} = 837$ nm for the red-detuned field and $\lambda_{\text{blue}} = 736$ nm for the blue-detuned field. These wavelengths are displayed in Fig. 5.15(c) with red and light blue dots. The electric field intensities of the corresponding guided modes are shown in Fig. 5.17(a-b). As expected from its proximity to the light line, the red mode shows little structure along x. The blue-detuned mode has a more pronounced periodic modulation, with intensity maxima in front of the comb teeth at $x = a/2$, the atoms will hence be attracted to the region in-between the comb teeth, while being repulsed from the teeth. This configuration is suited for trapping in the x direction. Along y, the decay lengths of both modes allow the creation a potential well with a minimum at $y = 100$ nm, by playing on the relative powers of the beams.

As before, we have computed the total trapping potential U_{tot} for Rb atoms with `nanotrappy`, taking into account the same CP potential for a slab of thickness t. Figures 5.17(c-e) display maps of the trapping potential U_{tot} in the (x, y) and (x, z) planes and along the y axis, for two different pairs of powers $(P_{r1}, P_{b1}) = (1.6, 1.3)$ mW and $(P_{r2}, P_{b2}) = (1, 1.3)$ mW. These configurations give a trap at a position of $d = 100$ nm (160 nm) from the surface and a depth of 2.2 mK (0.8 mK). We have hence demonstrated the possibility to trap cold Rb atoms at short distances from the comb waveguide where the electric field of the slow mode is linearly polarized, avoiding the need for vector shift cancellation. The weak trapping in the azimuthal direction has yet to be characterized in this situation. The optimized asymmetric comb waveguide fulfills all criteria introduced in Chapter 4 in order to achieve a realistic atom-PCW platform.

5.4 Fabrication and first optical characterization

The three promising waveguides designs have to be fabricated in order to be interfaced with cold atoms. All the fabrication discussed in the following section is done at the Centre de Nanosciences et de Nanotechnologies (C2N), by our partners Malik Kemiche and Sukanya Mahapatra under the supervision of Kamel Bencheikh and Ariel Levenson. We refer to the PhD Thesis of Sukanya Mahapatra (in preparation) for a thorough explanation of the fabrication and characterization processes. This section only aims at giving an understanding of the main challenges and show first promising results.

5.4.1 The challenge of fabricating suspended transparent waveguides

The fabrication of the designed waveguides is a challenge on several levels.

First, as we want waveguides guiding 780 nm light (instead of telecom, more common for these kinds of structures), all the geometrical features are reduced. For example, the radius of the holes in the half-W1 is of 63 nm, compared to 114 nm

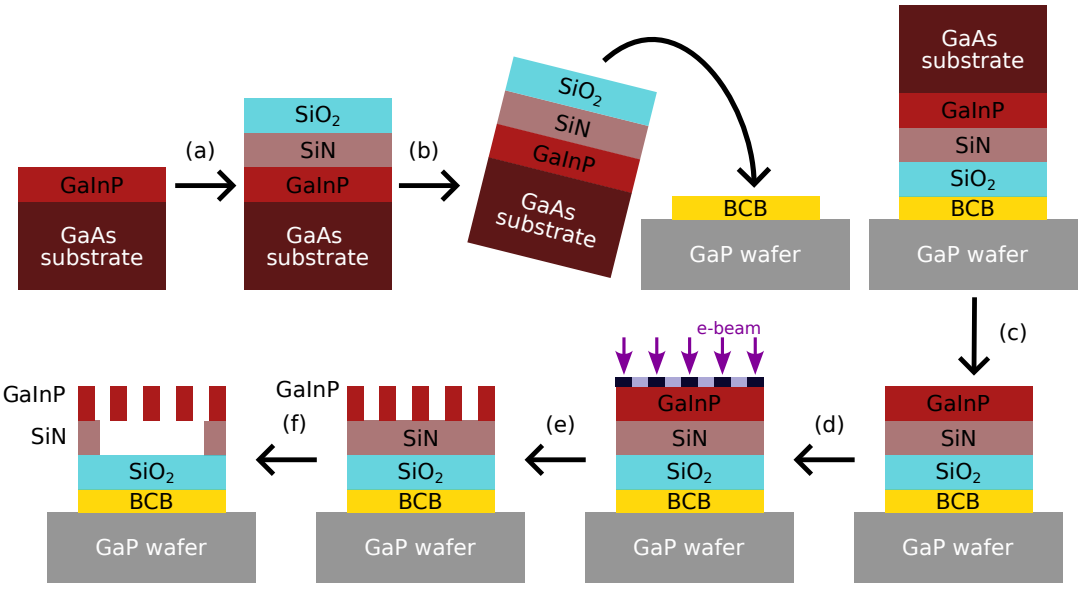

Figure 5.18: Summary of the fabrication process. (a) Deposition of SiN and SiO_2 on the GaInP heterostructure. SiO_2 layer is only 20 nm thick, while the SiN one is around 2 µm. (b) Bonding on a GaP (transparent) substrate thanks to benzocyclobutene (BCB, 500 nm thick). (c) Removal of the GaAs substrate via wet-etching. (d) Deposition of a hydrogen silsesquioxane (HSQ) negative resist, selective illumination with the electron beam of the resist following the chosen design. The illuminated resist will harden, protecting the underlying GaInP. (e) Dry-etching of GaInP with plasma and removing of the resist. (f) Dry-etching of underlying SiN with another plasma.

in [Li et al. 2008]. Extremely high accuracy and precision are hence needed in the fabrication.

As we will interface them in a cell where many lasers will be used for cooling down the atoms or trapping, it is preferable to have transparent structures at 780 nm, meaning the fabrication should only involve transparent layers (including the substrate).

Finally, all the structures have to be suspended for an increased optical access, to remove reflective interfaces, and avoid leakage of the mode into the substrate and adsorption of the atoms onto it.

A fabrication protocol tackling all these challenges had to be designed through months of trial and error. It is summarized in Figure 5.18. The GaInP layers used to fabricate the waveguides come as heterostructures, provided by Isabelle Sagnes and Grégoire Beaudoin from C2N. They consist of 150 nm thick GaInP layers grown on a 500 µm thick GaAs substrate, not transparent at 780 nm. The first three steps in Fig. 5.18 consists in transferring the GaInP layer onto a transparent GaP substrate. A negative resist is then deposited on the GaInP and patterned via electron beam lithography. Subsequent plasma etching removes the zones that were not exposed by the e-beam, revealing the waveguide structure. The SiN is then underetched for suspension of the guiding region. Finally, the substrate is sawn (or cleaved) at the edge to allow coupling into the waveguide with a focused free-space laser. A sawn substrate can be seen in Fig. 5.20(b).

More information on the creation of e-beam masks, optimization of the e-beam dose, field stitching errors and other hurdles in the development of the fabrication protocol can be found in Sukanya Mahapatra's thesis. Some scanning electron microscope (SEM) pictures of fabricated samples for the three different waveguides are shown in Fig. 5.19. All three structures have been fabricated with high resolution

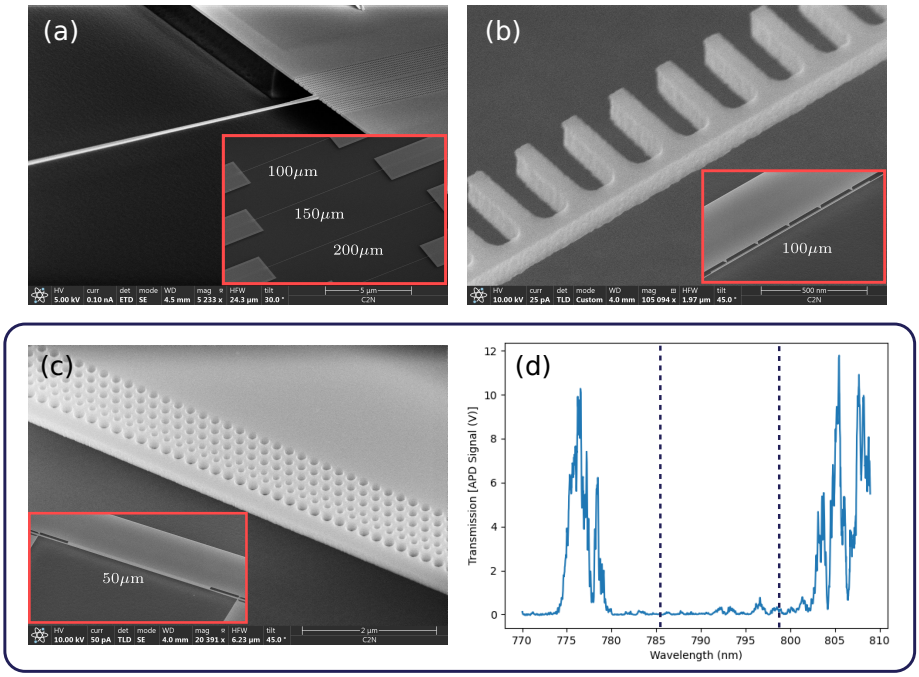

Figure 5.19: SEM pictures of some fabricated samples. (a) Nanobeam, (b) comb and (c) half-W1 waveguides. Insets show a wider scale of the structures with the associated lengths of the waveguide regions displayed. A single chip holds tens of different waveguides (up to 64) with different lengths and designs. Note the excellent quality of the fabrication with very sharp edges. We see that waveguides can be suspended over important lengths without deformation (with the help of tethers for the comb). (d) Transmission spectrum of a 100 µm long half-W1 waveguide. The dashed lines show the extent of the theoretical band gap between the two guided modes.

and for different lengths. They now have to be optically characterized to check if they match the predicted features.

5.4.2 Characterization of the samples

After fabrication, the transmission spectrum of the samples is characterized. The waveguide chip is mounted on a 3-axis micrometric translation stage and a high-NA microscope objective is used to couple light from free-space into the input coupler (see Fig. 5.20(a-b) for a picture of the fabricated couplers that terminate all the samples). Light propagates first inside a rigid W1 waveguide supporting a fast-guided mode at 780 nm, which can be seen in Fig. 5.20(b). It then goes through the designed suspended waveguided and is collected at the output with a similar microscope objective and sent to an avalanche photodiode. A tunable Littman/Metcalf diode laser (**Sacher Lasertechnik TEC-500-0780-030-M**), which can emit light from 770 to 810 nm, allows to probe the transmission of the selected waveguide over a wide range of wavelengths.

We observe in Fig. 5.19(d) such a transmission spectrum for a 100 µm long half-W1 waveguide. A photonic band gap is apparent (manifesting by vanishing transmission), although slightly shifted from the design value. As the e-beam dose was slightly too low for these fabricated samples (leading to etched holes wider than their nominal value), we expect the optimal samples to match the theoretical band gap more closely.

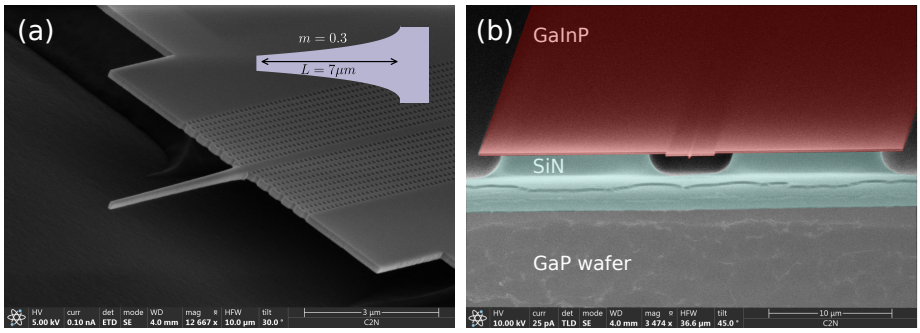

Figure 5.20: Fabricated coupler and suspended fast access W1 waveguide. (a) SEM picture of the trapezoidal coupler with the relevant parameters in inset and its connection to a suspended fast access W1. (b) Perpendicular view of a similar structure, where the substrate has been sawn close to the coupler. The different materials have been outlined. We see clearly the etched SiN layer. The SiO_2 and BCB layers are not visible on this image as they are only a few tens of nanometers thick.

Two localized transmission bands are present, likely corresponding to the two lowest gap-guided bands from Fig. 5.8(a).

The observed oscillations in the transmitted bands can give crucial information on the group velocity of the light inside the waveguide. Indeed, they are usually caused by reflections either on the output edges of the couplers or at the transition between the fast W1 and the suspended waveguide, creating a Fabry-Perot cavity with a limited finesse. The free spectral range of such a cavity is related to the group index via $\Delta\lambda_{\mathrm{FSR}} = \lambda^2/(n_{\mathrm{g}}L)$, where L the effective cavity length. Further improvements on the signal-to-noise ratio of these spectra and on the impedance matching between the fast-access waveguides and the slow-mode ones could allow to estimate n_{g} at the band position.

Conclusion

Many experimental and technological challenges have yet to be overcome to enable further neutral-atom waveguide-QED protocols. As such, experimental robustness of the targeted waveguide platforms is a critical requirement, as is evanescent trapping of atoms. In our work, we proposed and engineered three bona fide platforms for trapping cold Rubidium atoms close to nanofabricated waveguides based on high-index GaInP. Because of the strong mode confinement, atoms can be trapped down to $\approx 110\,\mathrm{nm}$ from the surface at input powers compatible with nanophotonic devices. For a simple nanobeam, the resonant mode couples to the atoms with a 1D Purcell factor of $0.1 - 0.2$, while this can reach values of 0.83 for the half-W1 or even 10 for the comb waveguide. In terms of β factors, these PCWs proposed platforms can outperform the Alligator waveguide (only existing atom-PCW platform, where up to 3 atoms where interfaced but never trapped in the evanescent field). The performances of these atom/PCW hybrid platforms keep getting closer to their solid-state counterparts, with the additional strength of a facilitated scale up in terms of atom numbers. This is summarized in Figure 5.21, which updates the findings of [Sheremet et al. 2023] with our proposals.

This study has been carried out for conservative parameters and a strong focus on robustness against fabrication imperfections has been done by engineering the band structure for a large bandwidth, facilitating first implementations. Our predictions do

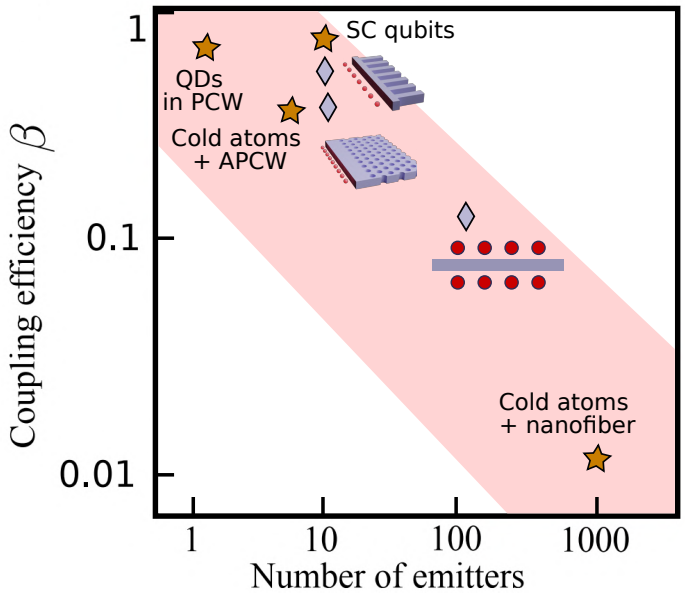

Figure 5.21: Comparison of coupling efficiency β and number of emitters N for different Waveguide QED platforms. The figure is adapted from [Sheremet et al. 2023] with the existing platforms displayed as stars and with addition of the proposals from this chapter as diamonds (comb, half-w1, nanobeam).

not take into account the coupling enhancement coming from the bad cavity formed by the output edges of the waveguides. Enhancements of 2 to 5 from the theoretical values have been reported [Goban et al. 2015].

In this challenging endeavor, a multi-step fabrication process has also been developed in order to fabricate such demanding transparent, suspended, high-index PCWs. First characterizations results are promising as they show the presence of photonic band gaps around the expected positions. Further measurements are needed in order to have a more precise characterization of the samples, including the actual group index of the guided bands.

Future generations of the PCWs should support higher group index, albeit with narrower bandwidths [Li et al. 2008]. This novel platform – tailor-designed for atom integration, chiral coupling, robustness, large optical access – offers unique advantages for studying coherent and dissipative dynamics in the Waveguide QED framework.

Part III:

Experimental realization of a cold atom platform

- To the secret lab! Pull the lever Kronk.
Wrong lever! *[Falls into the alligator pit]*
- Why do we even *have* that lever?
The Emperor's New Groove (2000)

CHAPTER 6

A VERSATILE COLD ATOM EXPERIMENT FOR INTERFACING PHOTONIC-CRYSTAL WAVEGUIDES AND RUBIDIUM ATOMS

Contents

To probe light-matter interaction in a waveguide-QED configuration, we have to interface the waveguides designed and fabricated in Chapter 5 with cold atoms. To this end, an experiment allowing cooling of Rubidium 87 atoms in a magneto-optical trap (MOT), transport and delivery to the structures as well as dipole trapping has to be built. This experiment was started from an empty room at the very end of 2019, before Covid lockdowns. Learning from the existing experiments interfacing nanophotonics and cold atoms we chose to realize a versatile, two-chamber system with cold atoms transport between a MOT chamber and a science chamber. This chapter delves into the details of the experimental apparatus. It covers both the building process of the optical and vacuum setup in order to get a Rubidium MOT as well as all the hardware and software experimental control implemented.

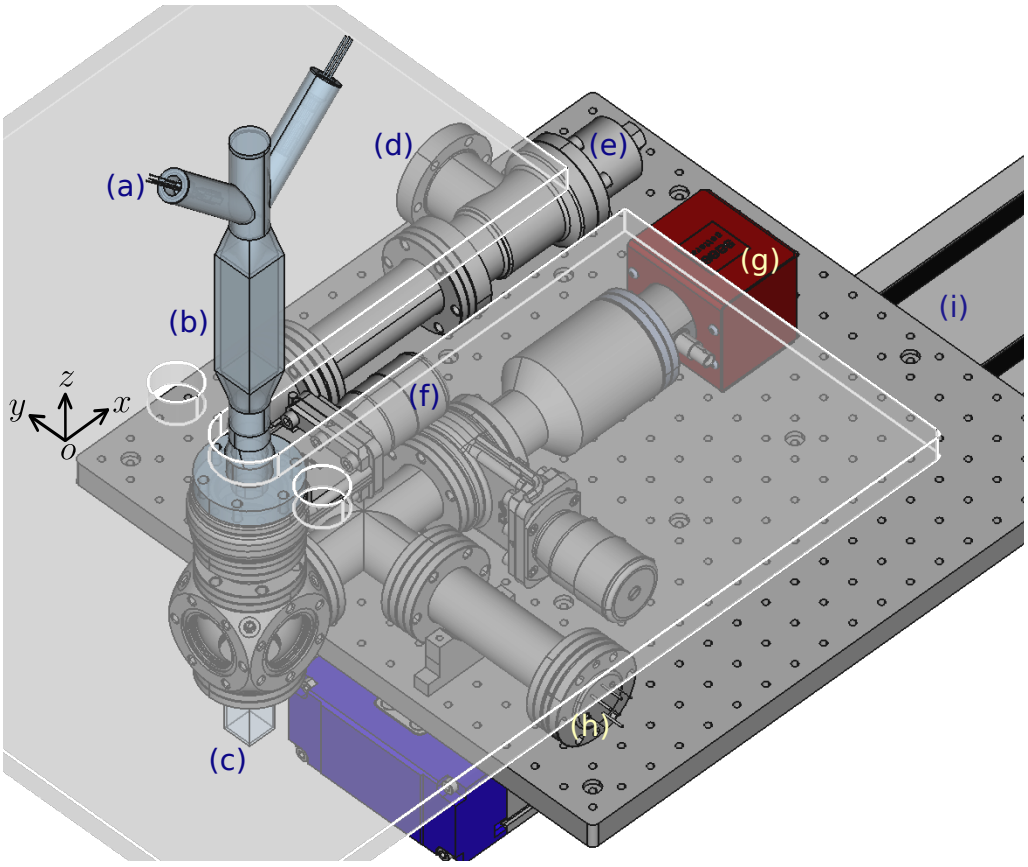

Figure 6.1: 3D rendering of the vacuum system showing the movable two-chamber setup. (a) Rubidium dispensers integrated in the glass cell, (b) MOT glass cell, (c) Science chamber, (d) To turbo pump, (e) Angle valve to seal from the turbopump or the air (f) Gate valve to keep the MOT chamber under vacuum when changing the science chamber, (g) Ion-NEG pump, (h) Ion gauge, (i) Precision translation stage. The upper breadboard supporting the MOT optics is displayed in transparent grey with white edges. The MOT chamber can slide through the slit cutout into the MOT breadboard when translating the lower breadboard. Design made on FreeCAD.

6.1 Presentation of the versatile two-chamber cold atom experiment: main considerations and design choices

Inspired by previous experiments interfacing photonic crystals and cold atoms (most notably in the groups of Jeff Kimble [Goban et al. 2014; Luan et al. 2020] and Mikhail Lukin [Thompson et al. 2013]), we designed a two-chamber experiment. The top chamber will be used to create a Rubidium 87 magneto-optical trap (MOT) at microkelvin temperatures. The cloud will then be moved to the lower cell glass called the science chamber. This chamber will hold the waveguide sample. In there, atoms will eventually be delivered from a secondary cold atomic cloud to the surface traps thanks to optical tweezers, which is the subject of Chapter 7. In the science chamber, light will be coupled from free space into the slow-mode waveguides thanks to high-NA objectives with long working distances, so that the guided mode can interact with trapped atoms close to the surface. The main reason to choose a two-chamber design instead of a single one is to decrease as much as possible the Rb gas pressure in the science chamber. Indeed, Rubidium is reactive and can deteriorate the waveguides by adsorption on the GaInP. This design was implemented in Kimble's group in the last

generation of the Alligator PCW experiment [Luan et al. 2020] with Cesium and it has helped increase by a lot the lifetime of the fabricated samples. Another reason is the difficulty to create a MOT directly around such large waveguide samples as they would perturb the MOT cooling beams via spurious reflections. The two-chamber vacuum system is depicted in Figure 6.1.

As we will need to change the waveguide chip from time to time, we have to design the experiment so that removing the science chamber is made as easy as possible. To this end, the whole vacuum system is placed on an industry-grade translation stage. Changing the science chamber boils down to only removing a coil and a mirror for the MOT optics breadboard and then translating the whole vacuum system to remove the chamber in a less crowded zone. The vacuum is made safer to break by the presence of gate valves that can isolate the MOT chamber and the ion pump.

6.2 Building of the vacuum and optical system

In order to set up a cold atom experiment, one has to operate in vacuum as collisions with background gas molecules will heat up the atoms which might escape from the trap. To achieve a low enough collision rate, we aim at ultra high vacuum (UHV), i.e. background gas pressure below 10^{-9} mbar. As such low pressures are more easily achievable for small volumes, we design a compact vacuum system making use of small chambers. As the sample will be coupled from free space lasers, both the MOT and the science chamber can be made out of glass. The vacuum system consists of the MOT chamber with in-built Rubidium getters, the science chamber, tubes and nipples to allow connections to a turbo pump, the ion/NEG pump and an ion gauge (see Fig. 6.1). The MOT cell and the ion/NEG pump can be isolated from the rest thanks to gate valves (**VAT 01032-CE01**, not UHV) and the whole system can be disconnected from the turbopump via an angle valve (**VAT 54132-GE02**, UHV grade).

6.2.1 Glass cell and Rubidium dispensers

We use for the MOT chamber a rectangular glass cell with integrated Rubidium dispensers manufactured by Precision Glassblowing. The rectangular part is 10 cm tall, 3 cm wide and made out of 2.5 mm thick (estimated) Pyrex glass, while the complete glass structure is 30 cm tall. It has external AR-coating for 780 nm light (but not internal). A common difficulty with glass cells is that they have to be connected to a metal vacuum system eventually. In this case, we choose to deal with this issue by using a cell that already has a glass-to-metal transition. The lower end of the cell is metallic and has a flange that can directly be carefully screwed onto the vacuum system.

Six SAES alkali metal dispensers for Rubidium are integrated in the chamber, with electrical feedthroughs into the air. They can release hot Rubidium atoms when heated via the Joule effect. At first use, the getters need to be activated, which happens at a given current threshold. We powered them with the turbopump on, increasing the current every 10 minutes, until the pressure in the chamber ceased to decreased a few minutes after changing the current setting, signaling that there is no protective layer on the getter to pump out. In our case this happened for $I = 5.2\,\mathrm{A}$. After activation, we lower the current to drive them at the lowest possible value that gives a sufficient gas pressure, $I = 3.8\,\mathrm{A}$ in our setup, in order to maximize their lifetime. We want the pressure to be as low as possible, as the hot Rb atoms fly directly to the center of the chamber, potentially reducing the lifetime of the trapped

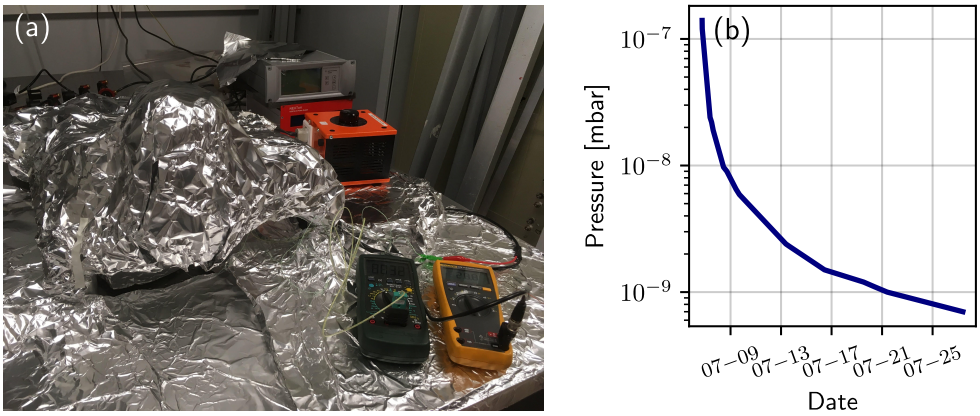

Figure 6.2: Baking to UHV. (a) Vacuum system wrapped in aluminium foil during the baking process. The temperature is monitored at sensitive positions of the chamber thanks to Ohmmeters. During the baking, the system is pumped by the turbopump only. (b) Evolution of the pressure after switching on the ion-NEG pump (post-baking). An important outgassing could explain the very slow decrease, but a pressure below 10^{-9} mbar was reached eventually.

cold atoms through collisions. The dispensers are powered with a programmable current source (**elc ALR3203**).

6.2.2 Reaching ultrahigh vacuum

Before pumping a chamber to ultrahigh vacuum, one has to inspect and clean its components very carefully. First, one has to look for any defect in the flanges or seals as they can lead to leaks that can prevent the system to reach UHV. Then, the parts are thoroughly cleaned to reduce the outgassing. Indeed, components exposed to high vacuum can continuously emit gas trapped on their surface. This can manifest as a leak (virtual leak) and slow down the pumping process. Cleaning all the components (tubes, flanges, screws and anything made of stainless steel) in consecutive ultrasound baths of acetone and ethanol can reduce this effect. Ethanol is used second as it leaves less residue than acetone.

The building stage is critical as the right amount of torque has to be set to the screws. We use silver-coated screws in order to avoid fusing at the threads, and deformable copper seals between the flanges. After building, we bake the vacuum system (without the glass chambers) in order to further drive out water, gases and other contaminants trapped in the different parts of the chamber. The baking artificially accelerates the outgassing process. We wrap the chamber with a heating tape and then isolate it with aluminium foil (see Fig. 6.2(a)). Thermocouples monitor the temperature at the position of the valves, which are the most sensitives parts as they can only go up to 250 °C. We increase the temperature up to 200 °C at a rate of about 40 °C per hour. This rate is very safe, as the chamber is made entirely of the same stainless steel, it expands altogether at the same rate. We bake the chamber for a few hours while pumping it with a turbo pump (**Pfeiffer Vacuum HiCube 80 Eco**).

After baking, we keep the turbopump on until we reach 5×10^{-7} mbar (which can take a day or two), and wait for the whole setup to cool down completely. We then turn on a second pump (**Saes Getters NEXTorr Z-100**) which is a combination of a passive non-evaporable getter (NEG) pump and an ion pump, and close the angle

valve. The NEXTorr has both an active ion pump which ionizes the gas passing through its getters and absorbing the produced ions, with a pumping speed of $15\,\mathrm{L\,s^{-1}}$, and a passive NEG pump which traps gas molecules on its surface by sorption on its metallic surface, at a rate up to $150\,\mathrm{L\,s^{-1}}$ for H_2. Figure 6.2(b) shows that pressures below 10^{-9} mbar are eventually reached after two weeks, probably because of further outgassing.

6.2.3 Building of the magnetic coils for the MOT

The end goal of the experiment is to deliver atoms into an evanescent dipole trap a few hundred of microkelvins deep, close to the waveguides. We then need to cool atoms to a few microkelvins, which can be done with a MOT. A MOT is an essential technique in atomic physics to create a cold atomic cloud by combining two effects. Hot atoms are slowed down thanks to the radiation pressure force of lasers sent in all 6 directions, detuned by a few MHz from the Rb D_2 line to address the fast, Doppler-shifted atoms. Besides that, a strong magnetic field gradient created inside the chamber, in combination with the lasers, acts as a restoring force, trapping the atoms at the zero of magnetic field. This confinement happens because of the differential dependence in the B-field of the different m_F magnetic sublevels of the ground state of Rubidium. These two processes, with a subsequent molasses phase can produce atomic clouds at temperatures down to $10\,\mu\mathrm{K}$ for Rubidium 87. The theory of the different physical mechanisms at play in magneto-optical traps can be found in many textbooks, and is nicely illustrated in [Berroir 2022]. As MOTs have been developed since the late 1980s [Chu et al. 1986], some technology leaps have made them more accessible than ever.

Two main ingredients are hence needed for a magneto-optical trap: near resonant lasers for slowing down the atoms and a magnetic field gradient for confinement. This magnetic field gradient is usually created by a pair of coils (referred to as MOT coils) in near anti-Helmholtz configuration. We design a pair of circular coils that easily produce magnetic field gradients over $20\,\mathrm{G\,cm^{-1}}$ with a current of 10 A, avoiding the need for water cooling. To be able to use the coils with a small electrical current, we aim at having the most compact coils possible, while preserving optical access for the MOT beams. We settle on coils with a mean radius of 35.3 mm, separated by 4 cm. Because the MOT chamber is 3 cm wide, the coils end up 5 mm away from the MOT chamber surface, as depicted in the CAD rendering from Fig. 6.3(a). This explains the x-asymmetry of the coil holders depicted in red. The coils are made with 1.6 mm diameter copper wire with 45 turns split into 6 staggered layers. Simulations with realistic coils show this configuration is sufficient to create a gradient of $25\,\mathrm{G\,cm^{-1}}$ along the x-axis with a current of 10 A (see Figure 6.3(c)), which is more than enough. On a daily basis, gradients from 8-15 $\mathrm{G\,cm^{-1}}$ are used to create a MOT (meaning currents in the 2.5-5 A range).

To avoid eddy currents as much as possible the coils holders are fabricated in a plastic polymer (Ertacetal®) instead of metal. The holder has an inner radius of 26 mm and is 5 mm thick. The copper wire is turned in the most homogeneous way possible thanks to a manual turn (see Fig. 6.3(b)). Epoxy glue is applied after each layer to make the coil rigid and improve thermal conduction. Each coil holder is supported by two custom-made metallic feet with adjustable height.

To check if the fabricated coils were producing the expected magnetic field, we measured it in a test setup mimicking the approximate separation of the coils in the real system with magnetic field sensors (**Texas Instruments DRV425EVM**). The sensor was put along x and moved with a translation stage along the x axis.

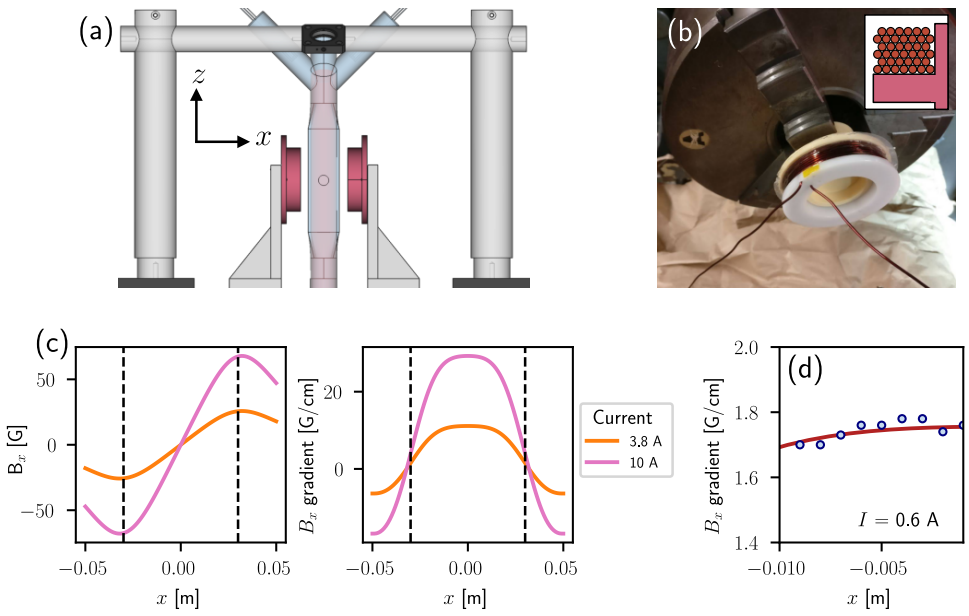

Figure 6.3: Design, fabrication and characterization of the MOT coils. (a) Scheme of the position of the MOT coils (coil holders in red) around the glass chamber. (b) Turning of a coil on their Ertacetal holder. Inset: cut of a coil to show the staggered arrangement of the 6 layers. (c) Simulated value of the **B** field and gradient along the x axis produced by the 2 coils in near anti-Helmholtz configuration for a typical current used in the experiment (3.8 A) and the maximal one (10 A). Simulations were done for realistic coils with staggered structure and actual wire diameter. (d) Simulated (red) and measured (blue) magnetic field gradient near the center of the pair. Measurement done at 0.6 A.

Figure 6.3(d) shows good agreement of this measurement with our design. As these sensors can only measure fields up to 5 G, this characterization was conducted at a low current (I = 0.6 A).

Dynamical control of the magnetic field

The current in the coils is produced by a controllable current source which can go up to 30 A (**Delta Elektronika SM 52-30**). The current can be controlled dynamically by sending the source an analog signal. As we are mostly interested in switching off the field very fast, we use an external electrical switch rather than the source capabilities, which has a response time of around 1 ms. The homemade switch is composed of an IGBT, a 50V transil diode which allows the passage of high currents which will dissipate in a 47 Ω resistor on switch off. The magnetic field can be turned off in about 50 µs with this switch. It is decoupled electronically from the control pseudoclock (discussed later in 6.3.1) by an optocoupler card which also converts the trigger signal in the 0-5 V range to a -15/+15 V TTL for optimal gating of the IGBT.

6.2.4 A translation stage for versatility

As discussed in the introduction, we want the setup to offer a simple way to change the waveguide chip in the science cell. A solution found was to put the whole vacuum chamber on a translation stage (depicted in Figure 6.4(b)). A wide slit has been cut out in the MOT breadboard (in white) to allow the vacuum chamber to be removed by a translation along the x axis. Only a coil and a few MOT optics have to be

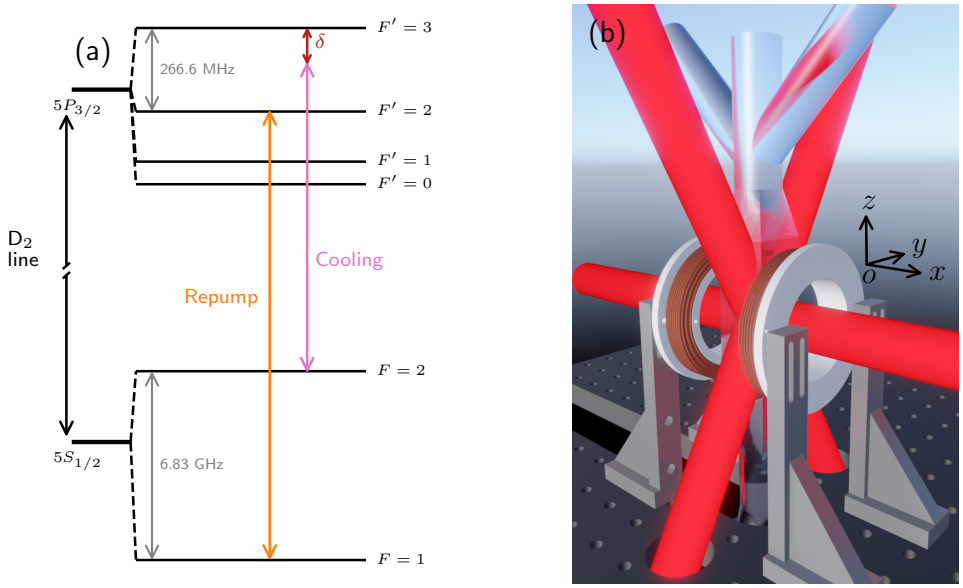

Figure 6.4: Optical cooling of ^{87}Rb. (a) Hyperfine structure of Rubidium 87 and laser frequencies used for the MOT. The trapping beam is on a closed transition, detuned by $\delta = -2\pi \times 9.5$ MHz, while the repump beam brings back the atoms that fell on the lower groundstate. The repump is a sideband on the cooling beam created with an EOM. (b) 3D view of the MOT cooling geometry. The beams coming on the vertical plane allow to keep an important optical access.

removed before proceeding. After closing the gate valves, the vacuum can be broken and the science cell replaced with a new sample. The translation stage (**Rollon H1420055N07992A**) has a useful stroke length of 500 mm and can resist up to 16 tons of load. It is actuated by hand, every turn moving the stage by 20 mm. It has a bidirectional repeatability of 45 µm. No wobble is detected at any position: as the movement is performed by two caged linear recirculating ball bearing guides and a preloaded ball screw, it is very stable.

6.2.5 Optical setup for a first MOT

We now look at the optical setup needed to cool down the Rubidium atoms. ^{87}Rb has been one of the earliest elements to be cooled down (even being the first one to be cooled to a Bose-Einstein condensate [Anderson et al. 1995]). As such, a strong technical knowledge has been developed regarding lasers at the ^{87}Rb transition wavelengths, based on frequency doubling of telecom ones, especially regarding their integration, miniaturization and stability. As an example, a gravimeter based on a cold Rubidium interferometer was successfully deployed on Mt. Etna. The whole setup was designed by Muquans and measured less than 900 L [Antoni-Micollier et al. 2022].

Optical cooling scheme

We cool the Rubidium 87 with the usual scheme depicted in Figure 6.4(a). All the lasers are on the Rubidium D_2 line. The two $5S_{1/2}$ states are long lived, while the excited states decay at a rate $\Gamma/2\pi = 6.07$ MHz. The atoms are Doppler cooled with

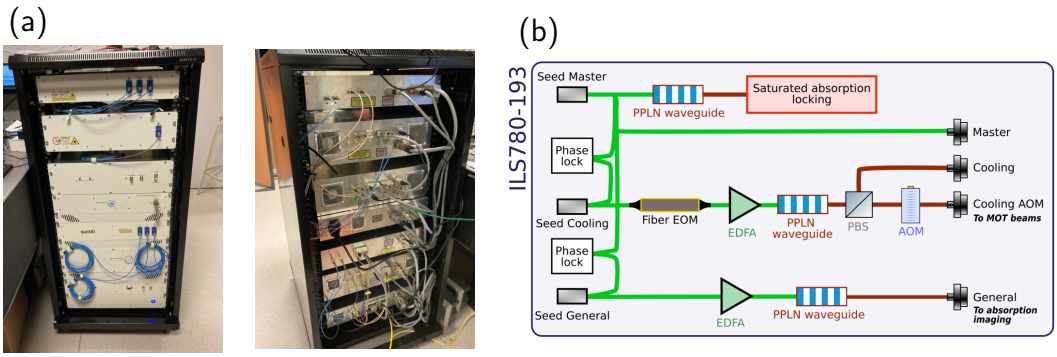

Figure 6.5: Integrated Muquans laser. (a) Front and back picture of the laser rack. The rack is 24U as both ILS780-193 and ILS780-214 laser systems have been combined into the same rack (see main text). (b) Simplified system for the ILS780-193. It has three 780 nm outputs with 500 mW of accessible power each.

laser beams detuned by $\delta = -2\pi \times 9.5$ MHz from the $|5S_{1/2}, F = 2\rangle \rightarrow |5P_{3/2}, F' = 3\rangle$ cyclic transition, a value that has been optimized.

Because the other excited hyperfine levels are not so far in frequency, it can happen that the cooling beams excite a detuned transition $|5S_{1/2}, F = 2\rangle \rightarrow |5P_{3/2}, F' = 2\rangle$. Because of selection rules ($\Delta F = 0, \pm 1$) the atoms can decay into the $F = 1$ ground state, which is dark for the cooling laser. We recycle the population in $F = 1$ to $F = 2$ via a repumping beam which is resonant on the $|5S_{1/2}, F = 1\rangle \rightarrow |5P_{3/2}, F' = 2\rangle$ transition. As the population being lost into the dark state is small[1], the repump beam does not need to be very strong.

An integrated laser system

All the cooling beams are generated thanks to an integrated turn-key laser based on a frequency-doubled telecom solution **Muquans ILS780 193**. The laser, packaged in a 12U rack (see Fig. 6.5), has a 1550 nm master seed that is locked automatically via Rb saturated absorption after doubling in frequency. Two other 1550 nm seed lasers are phase locked to the master, amplified via Erbium-doped fiber amplifiers (EDFA) and doubled in frequency with a temperature-controlled periodically-poled Lithium-Niobate (PPLN) waveguide, generating two 780 nm outputs that we call Cooling and General. We have access to the direct digital synthesizers (DDS) controlling the phase locks of the two seed lasers, allowing to effectively tune the 780 nm output frequency over a range of $\simeq 600$ MHz around the D_2 transition. The repump beam is generated with a fiber electro-optic modulator (EOM) integrated inside the laser before doubling, with a side band at 6.568 GHz. The Cooling path is split into two path inside the laser, one has an integrated fiber acousto-optic modulator (AOM) that we will use later as a switch. As we do not have access directly to the power of the repump beam, we optimize the power of the EOM in situ by maximizing the number of atoms in the MOT.

[1] We estimate with optical Bloch equations that the rate of pumping into $F = 1$ is more than 30 times lower than into $F = 2$, due to the large detuning of the cooling beam from the $F' = 2$ excited state

MOT configuration

We split the Cooling AOM output into three distinct paths that are then coupled into polarization-maintaining (PM) fibers. They go to collimators that output beams with a diameter $\approx 15\,\text{mm}$ in three directions shone into the atoms (see Figure 6.4(b) for the actual 3D geometry). The wide beams provide a large volume where the atoms are cooled, increasing the MOT loading rate R. Each beam is retro-reflected to have cooling in the 6 directions. We have in the end $\simeq 15\,\text{mW}$ in each free-space beam over which a fraction corresponds to the repump beam.

The homemade collimators use achromatic doublets with a focal length of 75 mm. They are mounted on a cage with an orientable quarter waveplate which is aligned as to generate a circular polarization on the atoms. This configuration allows for sub-Doppler polarization gradient cooling [Dalibard and Cohen-Tannoudji 1989], which is done in the molasses phase that follows the MOT loading.

By turning on both the lasers and magnetic field, we can obtain a continuous MOT. But we might want to make sequences in order to dynamically change parameters or just to accumulate a sufficient amount of measurements. To do so, we need hardware and software control of all the instruments involved in the experiment.

6.3 Building a full experimental control for high resolution sequences

A couple of cold atoms experiments already exist in our team, but they are running on old versions of Python or LabView. One of the goals of this new experiment is to implement a more up-to-date control system and then adapt it to the other setups. We decided to control the experiment with a master pseudoclock based on a programmable system on chip (PSoC) for the hardware, while software communication, monitoring and running will be done thanks to the Python-based `labscript` suite. A functional diagram of the experimental control is shown in Figure 6.6, detailing the communication between the software and hardware parts. This section is a summary of how each one of these two aspects of experimental control work.

6.3.1 On Hardware control: fabricating a centralized trigger source

A pseudoclock to rule them all

To perform our experiments we need to communicate with a given number of instruments and control them via analog or digital input control signals. We hence need a dedicated hardware to generate all those control signals and send them to the right instruments. `labscript` is designed to be used with a pseudoclock master device. A pseudoclock is a device which provides a variable frequency clocking signal, which is used to trigger other instruments (called children) when we want them to update their output state. A pseudoclock hence only changes value when one of its clocked devices needs to update an output rather than at a constant rate, eliminating unnecessary repetitive instructions stored by the instruments and sent by the clock. A comprehensive introduction on pseudoclocks can be found in [Starkey 2019].

A convenient hardware to make a pseudoclock are field-programmable gate arrays (FPGA) based controllers. Indeed, they are very fast, allowing operations up to the GHz level. A FPGA is physically modified by the code compilation which sets up the links between logical gates needed to realize the computation. This makes the computation fast and extremely versatile (up until compilation). Moreover, they have

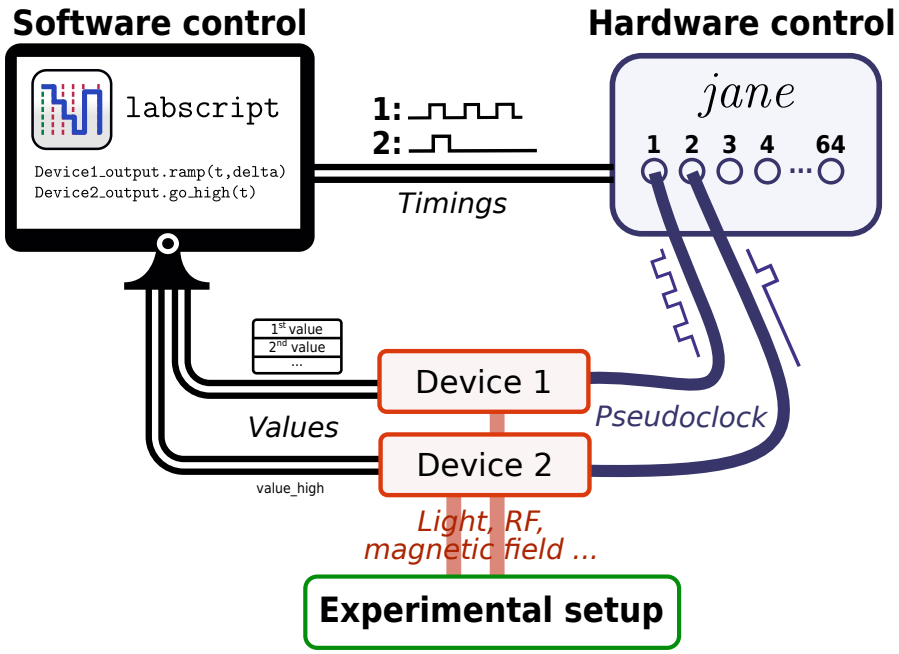

Figure 6.6: Functional diagram of the experimental control. A computer controls the whole experiment with `labscript`, a software written in Python 3. Instructions regarding the different changes are written in the experiment logic code in natural language. The instructions are sent through Ethernet connection to the devices in a device-specific formatting and the timing instructions to *jane*, the master pseudoclock. *jane* then sends the pseudoclocking signals to the connected devices through BNC cables. Section 6.3 will focus first on the master pseudoclock hardware and then introduce the `labscript` suite and its application to our experiment. A more detailed breakdown of the control system is shown in Figure 6.9.

a limited memory, which can be a hurdle when setting long lists of instructions to be sent by the pseudoclock.

FPGAs can be coupled to microprocessors to overcome some of their limitations, run Linux and allow easy communication with a control computer through Ethernet protocol. This is the concept of Red Pitayas (RP)[2], which are programmable systems on chip (FPGA + microprocessor on a single chip) with digital and analog inputs and outputs. Red Pitayas have a Linux-based operating system and pre-compiled FPGA Verilog code which allows to use them as oscilloscopes, lock-in + PID or spectrum analyzers very easily. We first tried to develop a pseudoclock out of a RP by modifying its Verilog code. It was possible to make it work as such but because of the complex RP overlay that includes many capabilities, the number of instructions (i.e changes of the pseudoclock state) that could be sent to a single digital output was limited to 16000. When trying to use various independent outputs, this decreased very fast, reaching only a few tens of instructions for 8 outputs.

jane: a pseudoclock combining the speed of an FPGA and the memory of a microprocessor

This was clearly not enough to use it as a pseudoclock for our experiment: a 10 ms long ramp already needs a million output updates if we want a maximum resolution. We use instead a more customizable platform based on the same PSoC idea. Starting from a bare PSoC is very hard as both the hardware and firmware have to be

[2]The board can be found at `https://redpitaya.com/stemlab-125-14/` and costs around 450€.

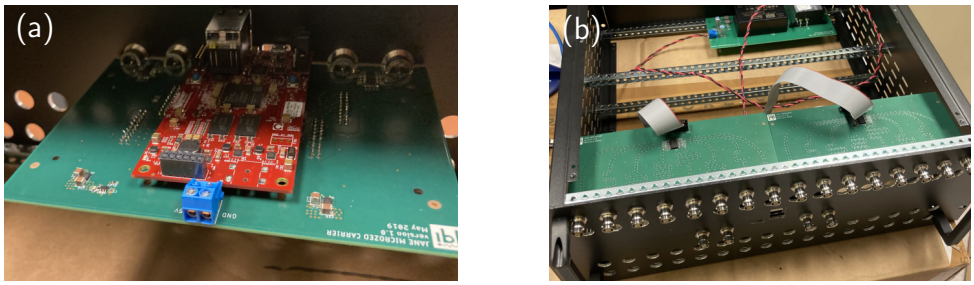

Figure 6.7: Construction of *jane* master pseudoclock. (a) Microzed evaluation board on its carrier board. (b) Final pseudoclock box being built with BNC outputs. Breakout boards are seen connected to the main carrier board with ribbon connector.

designed. We hence turned to a platform developed by the Joint Quantum Institute (JQI) in Maryland that had exactly the capabilities needed [Sitaram et al. 2021]. Their platform, called *jane*, is based on a Microzed evaluation board (**Avnet Microzed Zynq-7020**, more or less a RP without analog outputs, see Fig. 6.7(a)) and designed to work as a pseudoclock. A server initializes on startup, allowing communication through Ethernet port to a host PC. The communication is made simple via a specially designed API, which is integrated in a *jane* `labscript` driver (see subsection 6.3.2). The FPGA is configured to work as a pseudoclock with a custom Verilog code. Another feature of *jane* is that it comes with an easy-to-build hardware platform, designed around the Microzed chip, comprising a custom carrier board, eight breakout boards and a power supply. The mounted device is shown in Fig. 6.7(b). All the details concerning both the hardware platform and the firmware can be found in [Sitaram et al. 2021][3].

The pseudoclock instructions are designed in the experiment control PC (thanks to `labscript` as we will see later) which sends them to *jane* via the Ethernet connection. The list of instructions is fed to the FPGA which executes them. To overcome the memory limitation, *jane* uses the dynamic RAM (DRAM) of the microprocessor to store the following instructions while the previous ones are being processed. A so-called ping-pong memory partitions the FPGA memory in two, updating one half with the DRAM data while the other half is being read by the FPGA. The instructions are 128 bit words giving the status of each of the 64 digital outputs (1 bit for each), the delay before the next instruction in 32 more bits, the rest used to encore more specific instructions. The use of the DRAM increases the number of instructions sent from a few thousands (with FPGA alone) to over 8 million.

As the Microzed 7Z020 was not available, we used its lighter 7Z010 version. The main differences between the two are FPGA memory sizes, which is twice smaller for the latter. After a few adaptations on the Verilog code and *jane* API, it could be used as intended.

[3] All the original codes for configuring both the Microzed and the host PC, including the `labscript` drivers, as well as the technical designs for the carrier and breakout boards can be found at `https://github.com/JQIamo/jane/tree/main`.

6.3.2 A versatile software suite optimized for cold atom experiments: `labscript`

The `labscript` way of thinking

We want to implement into our experiment a control software that is written in Python 3 as it benefits from a strong knowledge basis and maintenance. Since we also want the experiment to be controllable by people who are not necessarily fluent in Python, we would like a control that makes use of graphical user interfaces (GUI).

For these reasons, we chose to use the `labscript` suite in our cold atoms setup [Starkey et al. 2013]. The suite is composed of Python-based softwares and is designed for shot-based experiments, where each shot has a distinct start and end point, is typically repeated many times but often not identically. For example, a single shot can mean the production and characterization of an atom cloud. The `labscript` softwares run a shot end to end, from its creation with the right parameters, to its execution by sending suitable instructions to the instruments involved in the sequence, to the post-processing of the results. Most of the following is derived from the very thorough PhD theses by P. Starkey [Starkey 2019] and C. Billington [Billington 2018], which contain all the information a reader interested in setting up the `labscript` suite in their own experiment needs. We provide a short summary of the main ideas behind `labscript` and highlight a few specificities of our experiment not trivial to include into this framework.

`labscript` assumes the whole experiment is controlled by a master pseudoclock. We use *jane* as introduced before. The main idea of `labscript` is to be able to write a simple code for the experimental control, called experiment logic, specifying how we want the actual outputs of the children devices to be modified throughout the shot: e.g. turning on the magnetic field, ramping the detuning of the lasers, switching the state of the AOMs...

Each instrument connected to the control computer needs a `labscript` driver, which mostly states how to convert an end-user instruction ("ramp up the detuning") into a language the instrument will understand (for example a dictionary with a sampled linear ramp with relevant detuning parameters sent via a HTTP request). Once the experiment logic is written, device-specific lists of instructions are created thanks to the drivers. A pseudoclock signal is also computed for each pseudoclocked instrument, indicating to them when they need to read their next instruction and update their outputs.

This of course is possible only if all the relevant `labscript` drivers are specified. Fortunately, some common devices are already implemented in the suite and need very little tuning[4]. This is the case of the National Instrument devices and Basler cameras. Some others had to be written from scratch.

End-to-end tracking of shots with `labscript` softwares

In practice, only the experiment logic has to be written as a custom Python file, all the rest of the `labscript` capabilities (i.e. creating and running shots end-to-end) is handled by a suite of GUI-based softwares (see Figure 6.8) that we detail in the following. This allows the end user to use the experiment without needing an extensive knowledge of Python.

[4]The labscript suite is open-source and available online. The supported drivers can be found at https://docs.labscriptsuite.org/projects/labscript-devices/en/latest/devices/.

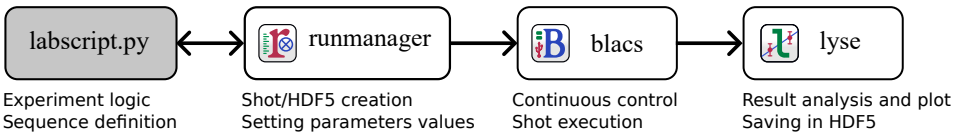

Figure 6.8: `labscript` workflow. A Python file describes the experiment logic in terms of the end user outputs. Global parameters can be defined in there. Their value for a given shot is specified in **runmanager** which creates a HDF5 file for each shot, i.e. for each set of parameters, which contains the corresponding hardware instructions to be sent to each instrument. This shot is executed via **blacs**, which also allows to continuously monitor the state of the instruments when no shots are run. The results are analyzed in **lyse**, either individually or by batches. Figure adapted from [Starkey et al. 2013], simplified.

- **runmanager** is for shot preparation. The global parameters defined in the experiment logic file can be set in a convenient way in **runmanager**. Once set, it outputs a HDF5 file, called shot file, with the values of all the parameters. This file will be updated throughout the whole process, eventually becoming a self-contained history of an entire shot from initial parameters to plot analysis. **runmanager** allows to define sweeps of parameters by just setting up a list for a given one. It will hence produce many shot files that will be run sequentially.

- **blacs** is for shot execution. It has two regimes of operation, continuous and sequential. The continuous mode allows to monitor the state of the instruments before and after the sequences. It can also be used to turn on and configure some devices before running the sequences. In our system, we use it to create a continuous MOT to check if the laser is working well. Custom **blacs** tabs have to be set up for every instrument that can be monitored and controlled in a continuous way. [Starkey 2019] gives an outline on how to write custom **blacs** drivers. The sequential mode takes the HDF5 shot file generated before and sends all the instructions to the relevant devices. It has many in-built capabilities like a queue that allows to send many shots at the same time (waits for one to finish before running the following one) or repeated checks that the connections to the devices are always up and running. Measurements taken during a sequence (like pictures) are saved into the HDF5 file.

- **lyse** is for analysis of the results. Any shot file can be uploaded and analyzed through custom Python files. It can analyze individual files or do multi-shot analysis in a very simple way (for example to get the temperature after a time-of-flight imaging).

`labscript` also includes **runviewer** to see the theoretical traces of the shots.

Logical diagram of the experiment

A logical diagram showing the connection between the different parts of the experiments is shown in Figure 6.9. We have a *jane* master pseudoclock with 64 digital outputs (only 5 displayed). The orange blocks represent physical devices. They are defined in the code by a `labscript` device type in bold. One has to define outputs for each device, shown as the black boxes. Several different outputs can act on a single physical channel, represented in green. We note that *jane* has three kinds of outputs:

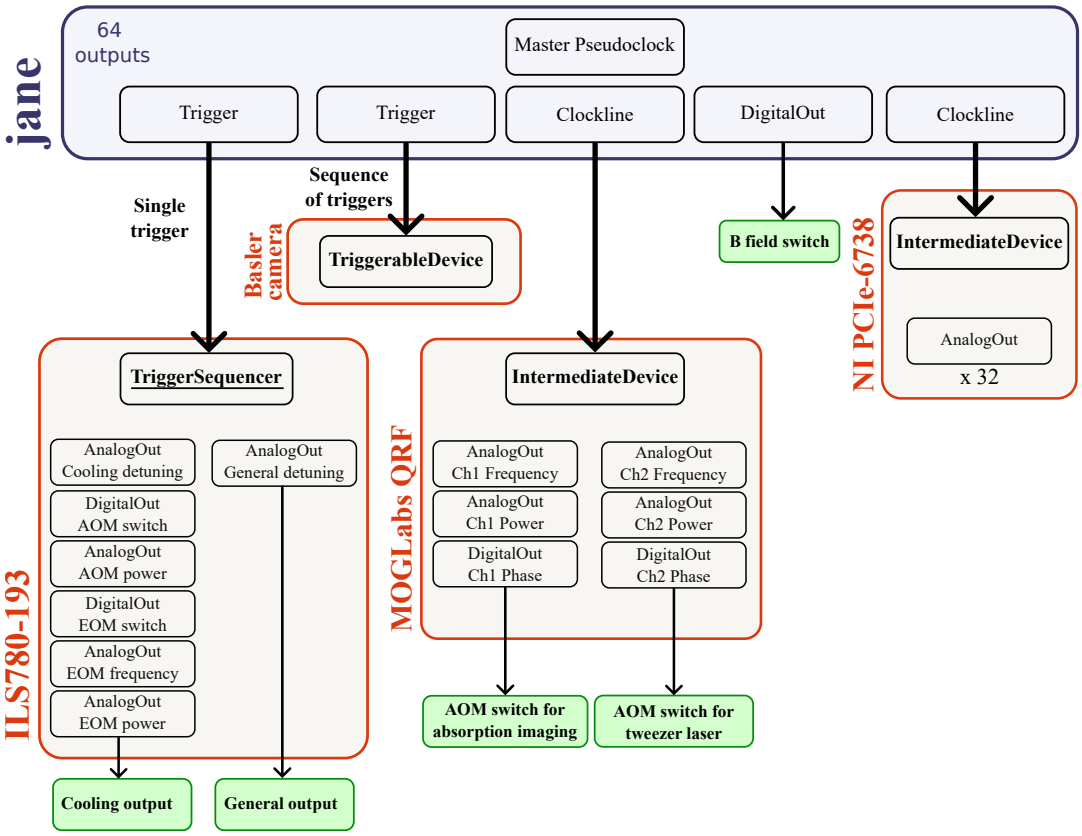

Figure 6.9: Experiment connection table. Structure from the `labscript` Python file defining the connection table. All are controlled from *jane* (in blue), either as a real pseudoclocked device or as a single triggered instrument. The boxes in orange represent physical devices which are represented as children device of jane in the experiment control. The ILS780-193 and MOGLabs QRF drivers were written for this experiment. The names in the black boxes are declared devices or outputs in the `labscript` experiment code. The first box of the orange devices (TriggerableDevice, IntermediateDevice, TriggerSequencer) give the main `labscript` class the child devices falls into, depending on its capabilities. TriggerSequencer is underlined as it is a custom class. Some boxes are grouped in the same column to show that in the end there are many parameters acting on the same physical channel (in green).

- Clockline refers to a pseudoclocking signal as described earlier. It has to be connected to an IntermediateDevice which accept lists of instructions read sequentially at each pseudoclock switch. Both the DDS (**MOGLabs QRF241, 4 channels**), which control the AOMs for switching the cooling beams, and the NI Card are concerned[5].

- Trigger is similar as it is produced when giving instructions to the daughter TriggerableDevice. The difference is that triggered devices can only do one action when receiving the trigger (typically turn on or off), they do not accept instruction lists. A single trigger with a given width is created by *jane* when needed. It takes into account the possible delays and compensates for them. It is the primary resource for cameras and our integrated lasers.

[5]The DDS can also be used as a TriggerableDevice with a *jane* Trigger. The trigger signal goes to a ON/OFF port of the DDS rather than to a configurable one. This allows to turn on and off the signal way faster but forbids to control its parameters dynamically (shaping the pulse for example).

- DigitalOut is an independent digital output that can be addressed directly in the `labscript` code. This is useful when the end channel is not a device we can communicate with, for example the MOT magnetic field switch.

More DigitalOut outputs are used for shutters, and more Triggers for cameras but are not displayed for clarity. The complete connection table and experiment logic for our experiment is reproduced in Appendix C.

Adding the integrated laser

From the previous discussion we understand that `labscript` is designed for an experiment running with two kinds of instruments: either instruments that can be clocked in real time updating their outputs at each change of the pseudoclock or devices that repeat the same task (usually take data) upon triggering. Unfortunately, this is not the case of our integrated Muquans laser. The ILS780 has an internal proprietary sequencer that can be triggered externally. Sequences are normally defined via the laser API, sent via HTTP requests and run internally, thanks to an internal 100 MHz clock. The laser updates its outputs at each beating of this internal signal. We were not able to bypass it in order to send directly a *jane* pseudoclock signal to clock the laser sequences in real time. This type of device, triggered once but able to run sequences does not fall naturally in the default `labscript` classes.

We write a new class `TriggerSequencer`, that enables the integration of the laser in the experiment logic. This class allows a device to be triggered only once, while permitting to define a sequence for its output channels (which will be translated and sent to the laser internal sequencer). This is achieved by the use of virtual pseudoclocks (called dummy pseudoclocks here). As *jane* can trigger children pseudoclocks, we trigger a dummy one, that "clocks" the ILS780. Thanks to this trick, `labscript` can keep track of the changes of the ILS780 parameters values during a sequence while sending physically only a single trigger pulse at $t = 0$ to trigger the dummy clock, which in reality goes to the laser sequencer. To avoid unsynchronization of the *jane* clock and the laser internal clock, the ILS780 can be fed with a reference signal at 100 MHz which we can choose to be created from *jane*. The complete code of the TriggerSequencer class is given in Appendix C.

We can now control all the needed instruments to create atomic clouds in timed sequences. We present our MOT experimental sequences and various characterizations of the cloud in the following.

6.4 Cooling down the atoms

6.4.1 MOT experimental sequence

A simple experimental sequence is shown in Figure 6.10. We see the three different stages of the experiment:

- First, the MOT phase is realized by switching on the magnetic gradient and while both the cooling and repumping beams (i.e. the EOM) are on. The length of this part can be widely tuned depending on the number of atoms we want to load (see Figure 6.12(b)).

- Then, the atoms are cooled further in a shorter molasses phase over which the power of the lasers is reduced with an exponential ramp and the detuning of the cooling beam increased to 100 MHz. The length of this step, fixed at 1.5 ms, has been optimized to produce a cloud at the lowest possible temperature.

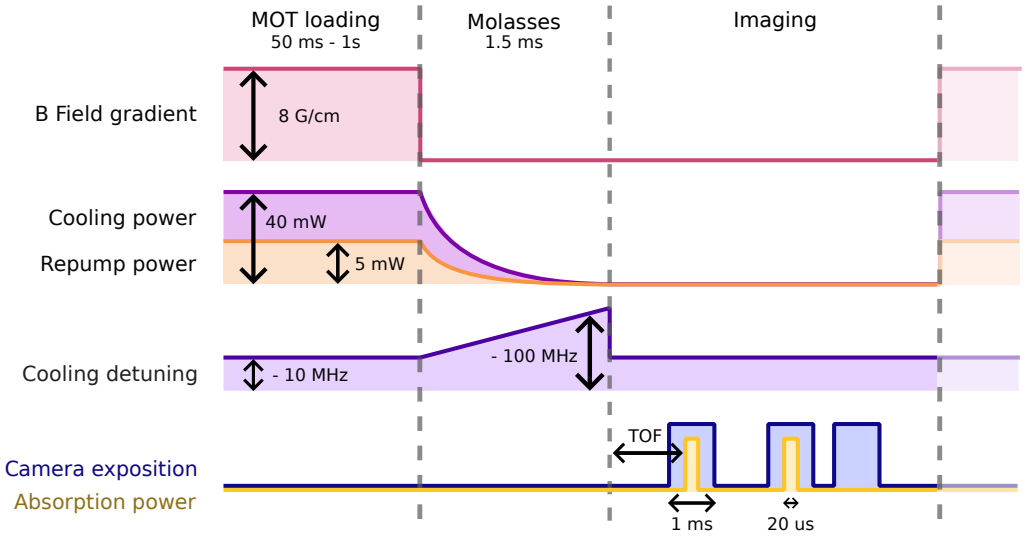

Figure 6.10: Typical experimental timing sequence. Depending on the number of atoms wanted, the MOT loading phase can be adjusted. The molasses phase for sub-Doppler cooling is achieved by turning off the B-field while putting an exponential ramp to the cooling and repump powers. The cooling detuning is also increased linearly. The time-of-flight (TOF) is counted from the end of the molasses phase. An example of measurement is shown here as the absorption imaging consisting of taking three pictures with the atoms, without and without any light. The TOF is varied sequence to sequence in order to get a temperature measurement.

- Finally, everything is turned off and the MOT is in free-falling expansion. We image the MOT with the absorption imaging setup during this phase. A picture is taken by turning on the absorption beam during 1 ms and exposing the camera for 20 µs. We take three pictures: one with the atoms (after a tunable time of flight), one with the absorption light on but after the atoms have fallen down completely (that we call the reference image) and a last one without any light to record the camera background (that we call the dark image), corresponding to the dark counts in each pixel.

The cycle can then restart with the same or another set of experimental parameters defined in the following HDF5 file. This is a simple experiment but allowed to establish the tools for future ones.

6.4.2 Absorption imaging for characterization of the system

We want to eventually load the MOT atoms into a optical conveyor belt to transport them to the science chamber. As such, it is important to have an appropriate absorption imaging setup to optimize and monitor relevant parameters the loading of the conveyor belt may depend on, e.g. the number of atoms and their temperature.

To this end, a resonant pulse (coming from the General output of the ILS780) is sent on the atoms and the shadow imaged on a CMOS camera (**Basler acA2440-35um**). The pulse length and emission is set by a single-pass, free-space, switching AOM (**AA Optoelectronic MT180-B30A1-IR**), controlled by a RF signal at 80 MHz and 30 dBm generated by a dedicated channel of the MOGLabs DDS. The beam is coupled into a PM fiber, which is then recollimated into a 1 inch beam and sent to the atoms. A 4f, 1:1 setup with two achromatic doublets of focal length 150 mm images the cloud into the camera. A typical free fall of the atoms over 20 ms will correspond to 2 mm, i.e. 570 pixels. The preparation of the beam and

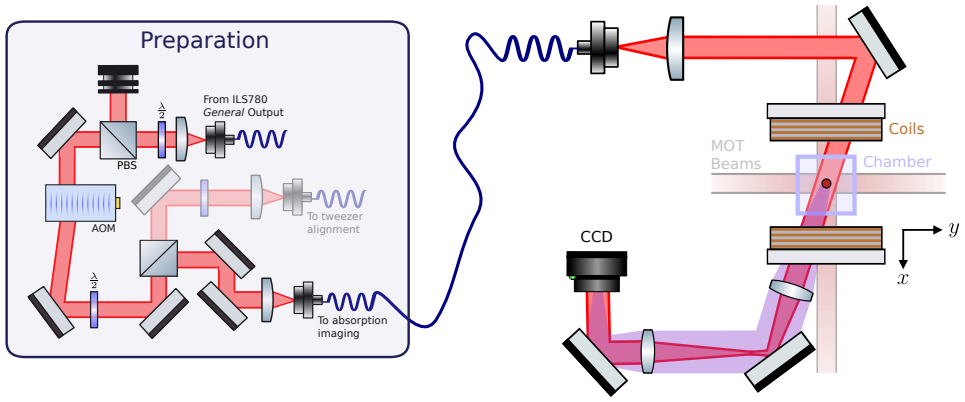

Figure 6.11: Optical setup for the absorption imaging in the horizontal plane. An AOM in the preparation part is used as a switch to be able to send short pulses through the absorption imaging setup. A 1:1 setup is obtained with 4f imaging. The lenses are achromatic doublets of focal length 150 mm. The angle on entry of the glass cell is to avoid clipping the horizontal MOT beam. The shadow of the atoms imaged on the camera is shown in purple. $\frac{\lambda}{2}$: half-wave plate, PBS: polarizing beamsplitter, AOM: acousto-optic modulator.

the geometry of the setup around the MOT cell is shown in Figure 6.11. A small angle has to be found on the entry of the glass cell so that the beam fits through the magnetic coil holders while not blocking the MOT cooling beam in the x-direction. A typical absorption image obtained with this setup is shown in Figure 6.12(a).

Optical depth

A central figure of merit when working with cold atom experiments is the optical depth (OD) of the sample. The OD measures the attenuation of the light that propagated through the cloud. By modelling the cloud as a dense vapour of atoms with a density n, each one acting as a particle with an absorption cross section $\sigma_{\text{sc}} = \frac{3\lambda^2}{2\pi}$, we can write the Beer-Lambert law which gives the attenuation of the intensity throughout the propagation along x:

$$\frac{dI}{dx} = -n(x)\sigma_{\text{sc}} I(x). \tag{6.1}$$

If the atomic density n is constant over x, we can integrate this expression as:

$$I_{\text{out}} = I_0 \mathrm{e}^{-n\sigma_{\text{sc}} L} = I_0 \mathrm{e}^{-\text{OD}} \tag{6.2}$$

where L is the extension of the cloud along x. This expression assumes the absorption cross section is independent of the intensity, which is valid for $I_0 \ll I_{\text{sat}}$, where $I_{\text{sat}} = \hbar\omega\frac{\Gamma}{2}$ is the saturation intensity of the cyclic transition. The power of the imaging probe beam is around 200 µW which yields an intensity around $I_0 \simeq 0.1 \times I_{\text{sat}}$, to stay in the constant σ_{sc} regime. Equation (6.2) also neglects multiple scatterings, considering the absorbed light is not re-emitted, and other complex processes [Veyron et al. 2022]. This is acceptable for the low densities and powers considered here, as this approximation typically leads to an underestimation of the atom number.

As we saw in Fig. 6.10, we take three pictures for the absorption imaging: one with atoms, one without after they fell, one without any probe light. From these pictures we extract the intensities I_{atoms}, $I_{\text{reference}}$ and I_{dark} respectively. The constant n approximation allows to write the OD as the logarithm of these measured intensities.

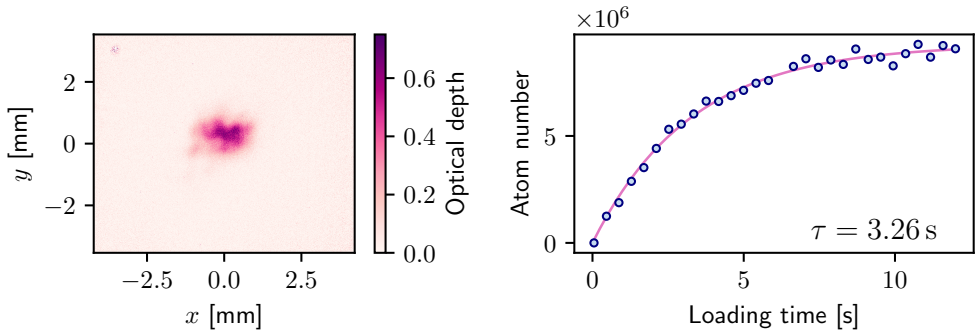

Figure 6.12: Loading of the MOT. (a) A typical absorption image of the cloud, $t = 2.9\,\text{ms}$ after the molasses phase. The peak OD is around 0.8. (b) Number of atoms loaded into the MOT with the loading time. An exponential fit (in pink) gives an estimate of the lifetime of the atoms in the MOT, $\tau = 3.3\,\text{s}$. The atom numbers are estimated with Eq. (6.4).

The OD is then expressed as:

$$\text{OD} = -\ln \frac{I_{\text{atoms}} - I_{\text{dark}}}{I_{\text{reference}} - I_{\text{dark}}}. \tag{6.3}$$

At then end of the molasses phase, our cloud has a typical peak OD close to 1 (see Fig. 6.12(a)), meaning 63% of the input light has been absorbed.

Atom number

The number of atoms in the cloud can be estimated from the OD. Indeed, from Eq. (6.2), we can write the OD simply as $\text{OD} = nL\sigma_{\text{sc}}$, with $nL = n_{\text{col}}$ being the column density i.e. the number of atoms in an infinitesimal thin column of length L. Integrating n_{col} over the transverse area of the cloud (i.e of the camera) gives the total number of atoms [Hinney 2019]:

$$N = \iint_{x,y} n_{\text{col}}(x,y)dxdy = \frac{1}{\sigma_{\text{sc}}} \iint_{x,y} \text{OD}(x,y)dxdy \simeq \frac{A_{\text{pixel}}}{\sigma_{\text{sc}}} \sum_{i,j} \text{OD}_{i,j} \tag{6.4}$$

where $\text{OD}_{i,j}$ is the OD for the pixel at position (i,j), and A_{pixel} the area of a pixel on the imaging camera ($A_{\text{pixel}} = 3.5\,\mu\text{m} \times 3.5\,\mu\text{m} = 11.9\,\mu\text{m}^2$). We can estimate the atom number with a single shot OD image. We can load up to 10 millions atoms in the MOT without changing the beam powers or the current in the getters.

MOT loading dynamics

The number N of atoms loaded in the MOT can be described by the following dynamic equation [Lindquist et al. 1992]:

$$\frac{dN}{dt} = R - \Gamma N - \beta \int_{\mathcal{V}} n_{\text{MOT}} d\mathcal{V} \tag{6.5}$$

where R is the loading rate. The next two terms describe loss of atoms from the MOT due to collisions with hot background gases (at a rate Γ) and due to two body intratrap collisions, characterized by a collision factor β and the density of atoms trapped n_{MOT}, respectively.

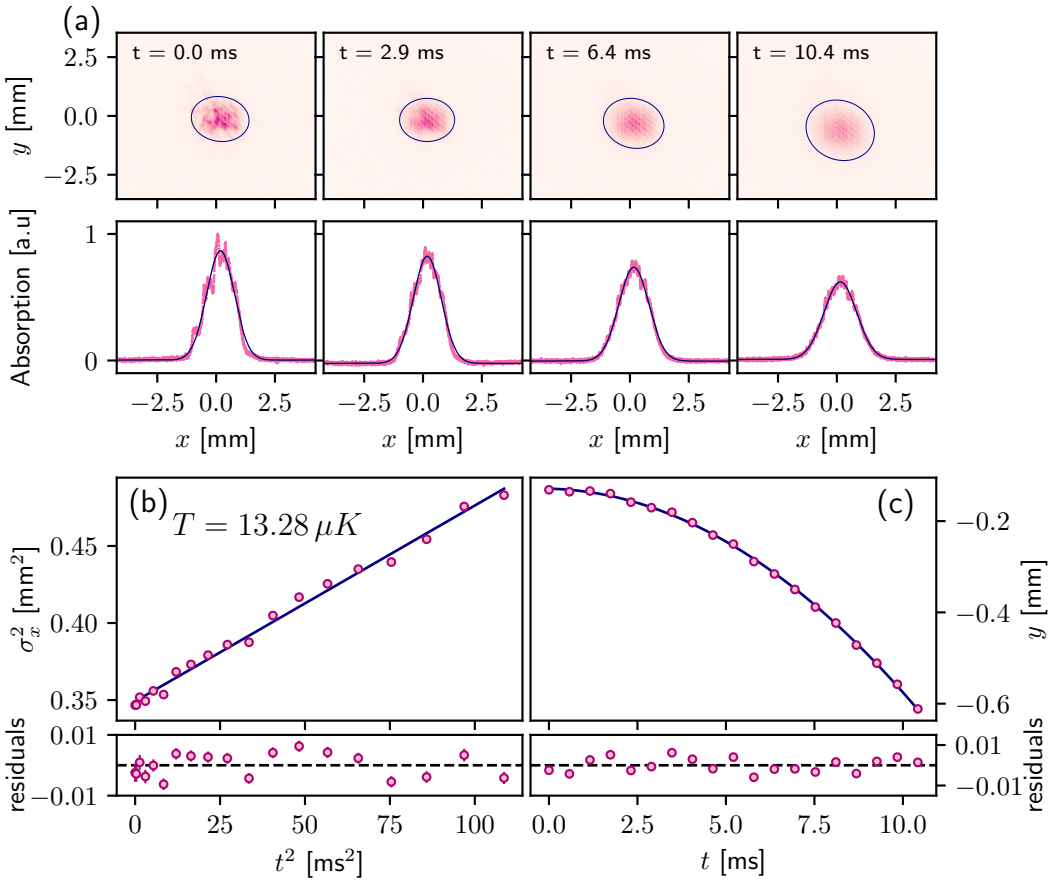

Figure 6.13: MOT temperature measurement. (a) Absorption images of the cold atomic cloud after different holding times. The clouds are fitted by a 2D Gaussian ellipse. The blue lines represent the fit contours at 2σ. The lower plots show the expansion on a 1D cut. (b) Estimation of the temperature by measurement of cloud expansion. The cloud width is extracted from the line plots in (a) and the fit done with Equation (6.6). In this case, it yields a cloud temperature of 13.3 µK. (c) Free fall of the center of mass. This is used to check the calibration of our imaging setup if the coefficient of the fitted 2$^{\text{nd}}$ order polynomial differs from $-1/2g$.

If we neglect the two-body collisions (which we can usually do for dilute gases, i.e. $n \lesssim 10^{12}$ cm^{-1}), the solution is an exponential loading curve of the form $N(t) = N_{\text{eq}}\left(1 - \mathrm{e}^{-\Gamma t}\right)$, where $N_{\text{eq}} = \frac{R}{\Gamma}$ is the number of trapped atoms at equilibrium. The loading rate R is proportional to the background atom density n_{bg}, to U_{trap}^2 but also to the beams diameters [Gibble et al. 1992]. It is simple to increase both of these parameters by either increasing the current of the getters, the intensity of the cooling beams or their diameter. Figure 6.12(b) shows such a loading curve in our setup, making possible to estimate the values of R and Γ to be respectively $2.8 \times 10^6\,\text{s}^{-1}$ and $0.3\ \text{s}^{-1}$ (i.e. 3.3 s lifetime). [Haw et al. 2012] report loading rates around $4.7 \times 10^6\,\text{s}^{-1}$ for similar intensities and detuning but higher vapor density.

Temperature

We perform time-of-flight imaging in order to get an estimate of the temperature of the atoms in the cloud. We let the cloud evolve freely after the molasses phase. The cloud will expand during its free fall. We image the cloud at different stages of

the expansion, over different shots, and at every step we fit the cloud by a Gaussian distribution in both the x and y axis. Let σ be the width of the Gaussian distribution fitted, then the evolution of the cloud size can be related to its temperature by:

$$\sigma(t) = \sqrt{\sigma_0^2 + \frac{k_B T}{M} t^2} \tag{6.6}$$

where σ_0 is the value of sigma at the first measurement (here at $t = 0$), M is the mass of a Rubidium atom. Figure 6.13(b) shows a plot of σ^2 with t^2, the slope of the fitted line is the 1D root mean square velocity $\frac{k_B T}{M}$. With this simple and compact setup, we can reach temperature around 10 µK. As expected his is well below the Doppler temperature for the Rubidium D_2 line $T_D = \frac{\hbar\Gamma}{2k_B} = 146\,\mu\text{K}$.

These temperatures should be low enough to load either an optical conveyor belt for transport or a single optical tweezer, as prepared in Chapter 7.

6.4.3 Next experimental steps: Bringing the atoms to the samples

After getting a cloud of cold atoms in the MOT chamber, we have to transfer them to the science chamber, 30 cm down in the -z direction. To do so, we plan on using an optical conveyor belt. It is creating by a red-detuned standing wave, that will act as a 1D lattice, trapping the atoms in the maxima of intensity. Then, the phase of one of the lasers is linearly shifted to accelerate the lattice down, transporting the atoms in the same direction [Cladé 2005]. This conveyor belt will be produced by another integrated laser (**Muquans ILS780 214**) which noticeably has two independent outputs at a frequency $f = f_{D_2} - 100$ GHz. This laser can be seen in Fig. 6.5, as it was integrated into the same rack, in the upper section.

Regarding the science chamber, we need to attach the fabricated waveguide chips characterized in 5.4 on its surface. This was done in [Luan et al. 2020] thanks to optical bonding with liquid glass. Light can then be coupled inside the waveguide from free-space with high-NA objectives, as was done during the characterization process.

Conclusion

Over this PhD work, a two-chamber experiment for cold Rubidium 87 atoms was constructed from scratch and the apparatus characterized in various aspects. A versatile, Python-based control system was implemented in the experiment, relying on a master pseudoclock made with a programmable system on chip and interfaced via the `labscript` suite. This work provided a reliable solution for experimental control to be transferred to the group. The measurements show that we can routinely produce a MOT of over 4 million atoms at temperatures $\simeq 10\,\mu\text{K}$. The atoms have now to be brought down to the science chamber where they will be interfaced with our custom waveguides.

CHAPTER 7

TRAPPING ATOMS IN OPTICAL TWEEZERS WITH HIGHER-ORDER MODES

Contents

The previous chapter detailed the cold atoms setup built in order to interface the fabricated photonic-crystal waveguides (PCW). PCWs are made of semiconductor material, and Rubidium is reactive, likely leading to significant adsorption or reaction at the surface, which would modify the structure dispersion properties [Yu 2017]. Even if this degradation is mitigated by the two-chamber design, we want to be able to deliver atoms to the waveguide surface one by one, reducing the background Rubidium pressure to a minimum. Precise delivery of atoms to nanostuctures is a daunting task as any dipole trap at the proximity of a surface will be reflected and show a complex intensity patterns which will impede efficient transport of the atoms. The presence of Casimir-Polder interactions and the nanometric scales of the designed structures contribute to make this task extremely challenging.

This chapter delves into the theory and the set up of specific tweezers made with Laguerre-Gaussian beams as they should allow for tighter traps and reduced reflections on the surfaces, easing the loading and transport of atoms to the structures, compared to their Gaussian counterparts.

7.1 Delivering atoms to structures with optical tweezers

7.1.1 The advent of optical tweezers

Since Arthur Ashkin's first demonstration of trapping of dielectric spheres thanks to radiation pressure in 1970 [Ashkin 1970], optical tweezers have come a long way. This groundbreaking work has laid the foundation for the optical manipulation of individual systems including nanoparticles [Aspelmeyer et al. 2014], biological material [Grier 2003] or cold atoms [Schlosser et al. 2001].

Optical tweezers are an ideal tool to trap and manipulate cold atoms. The strong intensity gradient and spatially-dependent light shift around the focal point allow for the creation of a very tight dipole trap. For a tight enough trap, loading multiple atoms ejects them from the trap in pairs. This mechanism, known as "collisional blockade" ensures all traps are either empty or with a single atom [Schlosser et al. 2002]. Used for investigating the scattering on a single atom [Masters et al. 2023] or to probe interactions between neighbours by using tweezers arrays [Chen et al. 2023], there is no doubt that optical tweezers offer an outstanding amount of control. Tweezer arrays with cold atoms are a very promising platform for simulating complex Hamiltonians, as is apparent from the number of experiments being built in laboratories around the world. They also offer many opportunities for quantum computing and metrology contributing to their popularity [Kaufman and Ni 2021].

7.1.2 The daunting task of delivering atoms to nanostructures

The flexibility of optical tweezers have made them strong candidates for helping with the daunting task of delivering cold atoms to the vicinity of dielectric structures. This step is crucial in order to load the evanescent dipole traps presented in Chapters 3 and 5. Outstanding control is required here, as simply sending atoms straight onto the structure will lead to adsorption, because of Casimir-Polder (CP) interactions and reactivity of the material, gradually modifying its dispersion properties.

However, optical tweezers can get reflected by the surface of the nanostructure and the reflected light will interfere with the incoming one creating a standing wave, with the closest bright spot at $z_1 \sim \lambda/4$ from the surface[1] and additional trapping sites farther away spaced in increments of $\lambda/2$, as shown in Fig. 7.1(b). This effect, a priori detrimental, can be used as it offers a z_1 trap very close to the surface. This standing wave can be loaded directly from a continuous MOT surrounding the structure but the presence of background gas can degrade quickly the PCW, as observed in the case of Cesium in [Goban et al. 2015]. It is safer to load the tweezer away from the structure and then approach it, but in this case the loading probability into the closest trap is small. [Béguin et al. 2020a] have estimated that with a tweezer perpendicular to the surface, less than 1% of atoms initially trapped in an optical tweezer far from the structure can be loaded into the z_1 trap, by varying the focus position longitudinally. This is because of the complex modulation of the intensity pattern during transport. The tweezer axis can otherwise be moved transversally towards the structure which increases slightly the delivery efficiency [Thompson et al. 2013].

Other protocols to increase control on the delivery of atoms include using a focused optical conveyor belt going through the transparent structure [Burgers et al. 2019;

[1] For an imperfect reflective surface, the position of z_1 actually depends on the width of the structure. For a width t and refractive index n, the position of the first trapping site z_1 is given by the smallest integer m such that $z_1 = \left(m + \frac{1}{2}\right)\frac{\lambda}{2} - n \times t \in [0, \lambda/2]$. For $t = 0$, $m = 0$ and we recover $z_1 = \frac{\lambda}{4}$.

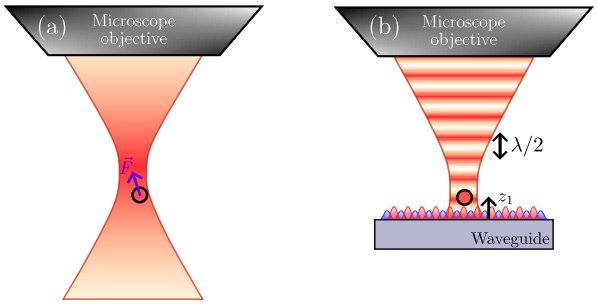

Figure 7.1: Optical tweezer and interference pattern produced by reflection on a surface. (a) The tweezer is usually created by a microscope objective with high numerical aperture. The strong intensity gradient close to the focal point restores the atom position. (b) When shone on a structure (here a PCW), interference fringes appear, tightening the trap, with the closest trap site at z_1. The two-color dipole trap used for trapping close to nanostructures is represented by the red and blue sines. Note that there is more that one trapping site around the tweezer waist

Kim et al. 2019] or to approach them via an optical guided beam, i.e. a focused beam diffracted by the structure itself [Zhou et al. 2023].

Here we focus on the situation depicted in Fig. 7.1(b) of a focus-tunable tweezer reflecting off a dielectric surface. It was proposed in [Béguin et al. 2020a] that using superpositions of Laguerre-Gaussian modes can reduce the number of fringes away from the surface. This should increase the loading efficiency into the z_1 trap site and also offer tighter traps in the longitudinal direction.

7.2 A better tweezer for nanostructures with Laguerre-Gaussian modes

An optical tweezer made by a sum of specific Laguerre-Gaussian (LG) modes has been proposed in [Béguin et al. 2020a], a theoretical study made in collaboration with our group. In the following we revisit this work to adapt it to our experimental setup parameters. We first introduce the LG modes and look at how this superposition can give tighter optical traps more suited for transport close to structures, in both paraxial and vectorial regimes.

7.2.1 Laguerre-Gaussian modes: Introduction

Electric field of a Laguerre-Gaussian beam

Laguerre-Gaussian modes are a family of monochromatic solutions of the electromagnetic wave equation in the paraxial approximation obtained from the Maxwell wave equation (2.7) assuming a slowly varying envelope:

$$\Delta_\perp \xi - 2ik\frac{\partial \xi}{\partial z} = 0 \tag{7.1}$$

where $\Delta_\perp$ is the Laplacian on the coordinates transverse to the propagation axis z and ξ is the electric field amplitude when writing the electric field $\mathbf{E}$ as $\mathbf{E} = \xi \mathrm{e}^{-i(kz-\omega t)}\hat{\mathbf{e}}_i$.

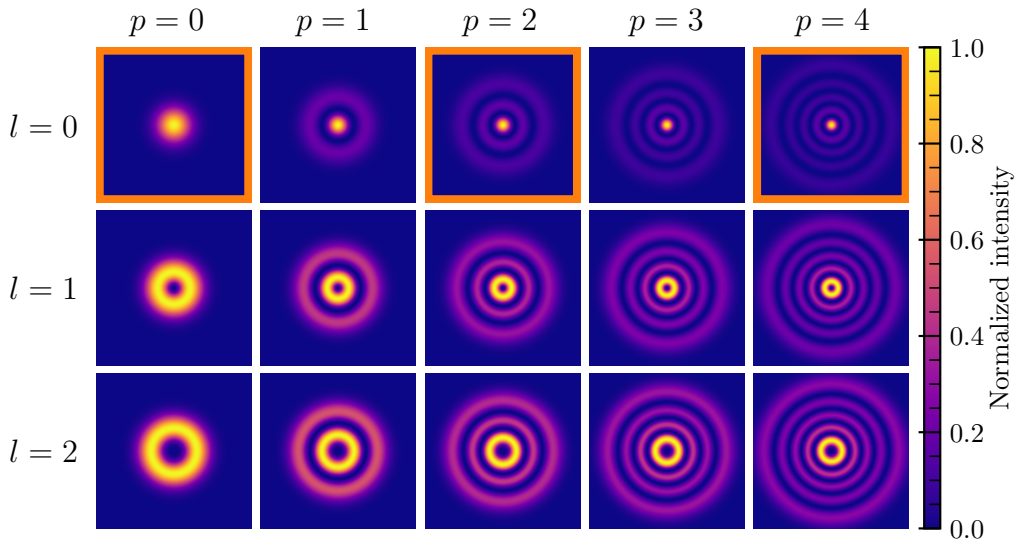

Figure 7.2: Normalized intensities of the first Laguerre-Gauss modes for varying p and l. The modes outlined in orange are the ones used in the coherent superposition E_Σ from [BÉGUIN et al. 2020a].

The total electric field for a Laguerre-Gaussian mode with order p and l is given by:

$$E_p^l(r,\theta,z) = A_p^l(r,z)\ \underbrace{\mathrm{e}^{-ik\frac{r^2}{2R(z)}}}_{\text{curvature}}\ \underbrace{\mathrm{e}^{-il\phi}}_{\text{polar}}\ \underbrace{\mathrm{e}^{i\psi(z)}}_{\text{Gouy}}\ \underbrace{\mathrm{e}^{i(kz-\omega t)}}_{\text{propagation}} \tag{7.2}$$

where we decomposed it into an amplitude term $A_p^l(r,z)$ and phase terms that we will describe in the following. The amplitude term can be expressed as:

$$A_p^l(r,z) = \sqrt{\frac{P_0}{w(z)^2}}\sqrt{\frac{2p!}{\pi(p+|l|)!}}\left(\frac{r\sqrt{2}}{w(z)}\right)^{|l|} \times L_p^{|l|}\left[\frac{2r^2}{w(z)^2}\right]\mathrm{e}^{\frac{-r^2}{w(z)^2}} \tag{7.3}$$

where $L_p^{|l|}\left[2r^2/w(z)^2\right]$ is the generalized Laguerre polynomial[2] of orders n and $|l|$ evaluated at $2r^2/w(z)^2$. As Eq. (7.3) only gives the scalar field amplitude, we can choose the polarization. We will consider in the following that it is well defined and linear along $\hat{\mathbf{e}}_x$, $\mathbf{E}_p^l = E_p^l\hat{\mathbf{e}}_x$. This expression is convenient as it is written in terms of the total beam power P_0.

Figure 7.2 shows 15 intensity profiles of LG modes with orders $p = 0-4$ and $l = 0-2$, and with the same input power P_0. We note that increasing p leads to more rings around the center and a narrower central spot. For $l \neq 0$, the center becomes dark (*donut beam*), with the dark region getting larger with l. For $p = 0$ and $l = 0$ (Fig. 7.2, top left), Eq. (7.2) reduces to the well known Gaussian beam expression ($L_0^0 = 1$). As such, the variation of the waist with the propagation $w(z)$ is the same

[2]Generalized Laguerre polynomials of order $n \in \mathbb{N}$ and $\alpha \in \mathbb{R}$ are defined as

$$L_n^{(\alpha)} = \frac{x^{-\alpha}\mathrm{e}^x}{n!}\frac{d^n}{dx^n}(\mathrm{e}^{-x}x^{n+a}) \tag{7.4}$$

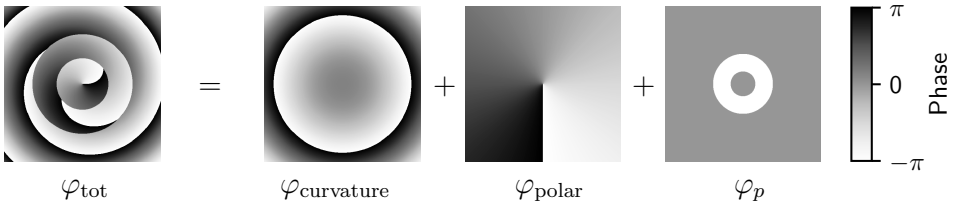

Figure 7.3: Phase of a E_2^1 mode at $z = z_r$. Total phase and its decomposition on the curvature and polar components. The phase jumps in φ_p correspond to a sign inversion of A_p^l due to a zero-crossing of $L_p^{|l|}$. It is not a phase term from Eq (7.2), but carries significant information. Both Gouy and propagation phases are uniform.

as for a Gaussian case and reads:

$$w(z) = w_0 \sqrt{1 + \left(\frac{z}{z_{\text{R}}}\right)^2} \tag{7.5}$$

where z_{R} is the Rayleigh range, $z_{\text{R}} = \frac{\pi w_0^2}{\lambda}$, with w_0 the waist at focus.

Discussion of the different phase terms

We will now discuss the different phase terms that appear and are underlined in Eq. (7.2). Some of these contributions are displayed in Fig. 7.3 for the E_2^1 mode, as an illustrative example.

- Curvature phase: Phase coming from the non-planarity of the wavefront. Adds a quadratic dependence in r with a curvature radius defined as $R(z) = z\left[1 + \left(\frac{z_{\text{R}}}{z}\right)^2\right]$. At the focal point, R goes to infinity and this contribution vanishes.
- Polar phase: This phase term only appears for non-zero $|l|$. It gives a forked phase profile as seen in Fig. 7.3 with a singularity in the center. This is characteristic of light carrying a non-zero orbital angular momentum, which can be a valuable resource in quantum information protocols [Nicolas et al. 2014]. In the following, we will only consider modes with $l = 0$, hence this phase will vanish.
- Gouy phase: Phase that a beam acquires gradually when crossing the focal region. For a Gaussian beam it varies from $-\pi/2$ to $\pi/2$. It is here modified with respect to the usual Gaussian beam:

  $$\psi(z) = (2p + |l| + 1)\arctan\left(\frac{z}{z_{\text{R}}}\right) \tag{7.6}$$

  Using higher order modes enhances this phase change, increasing the slope around $z = 0$ and the amplitude at infinity.
- Propagation phase: Usual phase of a propagating monochromatic plane wave along z.

7.2.2 A tighter trap with a coherent superposition of LG modes: paraxial case

Laguerre-Gauss beams are an interesting tool, already used for the manipulation of cold atoms, but usually only donut beams ($l \neq 0$) are considered as resources. Cold

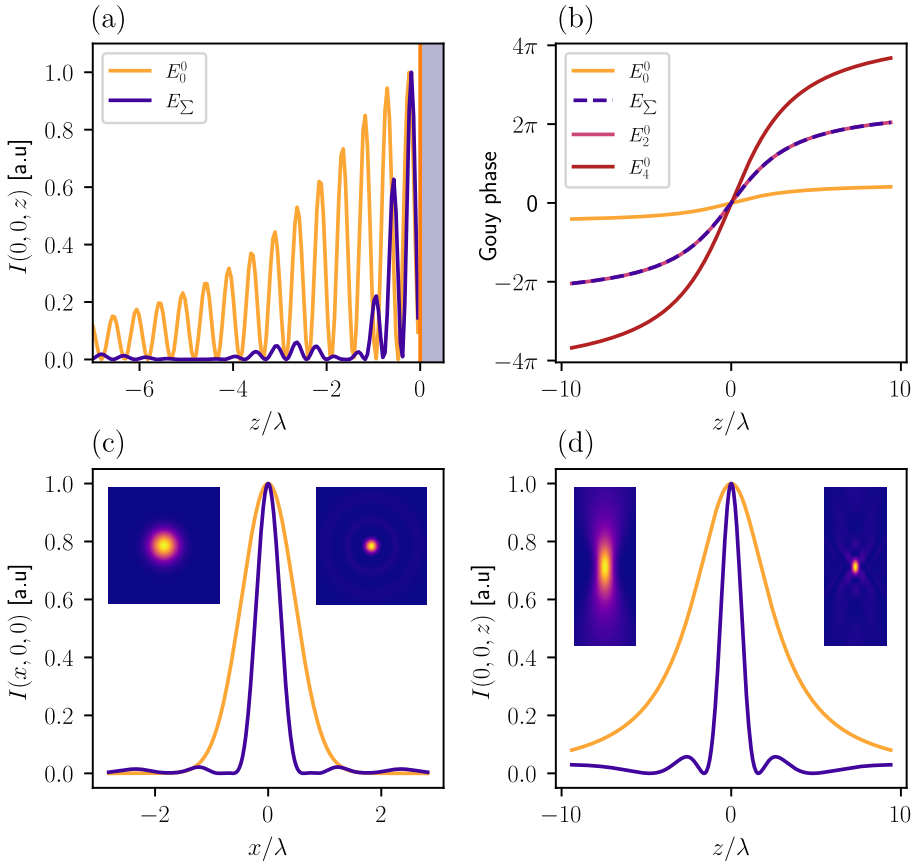

Figure 7.4: Reduced reflections and characteristic lengths in $\mathbf{E}_\Sigma$ compared to a Gaussian beam, in the paraxial regime. (a) Reflections on a perfectly reflecting surface (b) Gouy phase along the propagation axis. The Gouy phase for the superposition is equal to the one for the LG mode E_2^0[3]. (c) Reduced waist of the superposition in the transverse (x, y) plane. (d) Shorter longitudinal extension for $\mathbf{E}_\Sigma$.

atomic clouds have been channeled with such beams [Cabrera Gutiérrez 2014] and circular Rydberg atoms have been individually trapped thanks to dark optical tweezers based on $l > 0$ LG modes [Cortiñas et al. 2020]. However, bright optical tweezers based on higher p modes have yet to be demonstrated.

As seen in 7.1.2, the spurious reflections on the surface are an important hurdle impeding optical trapping close to structures. There are a few ideas to reduce these unwanted reflections [Zhou et al. 2023]. One such idea is to use modes whose intensity profile is limited in the propagation direction, leading to a smaller region where interferences can occur.

This can be achieved by combining modes of light which have very different phase dependence in the z direction. Combining them via coherent superposition can lead

[3] As we consider $l = 0$ and we only look on the optical axis ($r = 0$), all the phase terms vanish except for the Gouy phase $\propto 2p + 1$. We can express the sum simply

$$\begin{aligned}\mathbf{E}_\Sigma(0,0,z) &= \sqrt{\frac{2P_0}{\pi w(z)^2}}\left(\mathrm{e}^{-i\arctan\frac{z}{z_R}} + \mathrm{e}^{-i5\arctan\frac{z}{z_R}} + \mathrm{e}^{-i9\arctan\frac{z}{z_R}}\right)\\ &= \sqrt{\frac{2P_0}{\pi w(z)^2}}\left(2\cos\left(4\arctan\frac{z}{z_R}\right)+1\right)\mathrm{e}^{-i5\arctan\frac{z}{z_R}}\end{aligned}$$

by factoring by $\mathrm{e}^{-i5\arctan\frac{z}{z_R}}$. This leads to $\arg(\mathbf{E}_\Sigma) = 4\arctan\frac{z}{z_R} = \arg(\mathbf{E}_2)$.

to suppression of the strong intensity regions as they can be out of phase for $z > z_R$. This can be achieved by using a superposition of Laguerre-Gaussian modes with zero orbital angular momentum ($l = 0$) [Béguin et al. 2020a], as they have a p dependent Gouy phase. Indeed, as seen in Figure 7.4(b), the Gouy phase of such beams becomes steeper with higher p and saturates to higher values. Summing them also allows to cancel the outer intensity rings that would be detrimental when using a single $E^0_{p>0}$.

We denote by $\mathbf{E}_\Sigma$ the field resulting from a coherent superposition of modes with $p = 0, 2$ and 4:

$$\mathbf{E}_\Sigma = \mathbf{E}^0_0 + \mathbf{E}^0_2 + \mathbf{E}^0_4 \tag{7.7}$$

All the modes are computed with the same waist w_0 fed into Eq. (7.3) even though for $p \neq 0$, the characteristic size of the beam at focus is given by $w_{\mathrm{LG}} = w_0\sqrt{2p+1}$ and not by w_0.

We first study this superposition in the paraxial regime, where LG beams are a solution of the Maxwell's equations. We use, as in the experiment described in 7.3.2, a laser of wavelength 1064 nm, and suppose we can create a Gaussian tweezer with waist $w_0 = 1\,\mu\mathrm{m}$ and a 1 mK deep trap. All the fields will have a linear polarization along the x axis.

Figure 7.4(a) shows that making a dipole trap with such a superposition leads to reduced interference fringes close to the surface while Figs. 7.4(c-d) highlight the narrow intensity profiles obtained in both transverse and longitudinal directions. This leads to an increased confinement, especially along the propagation axis, when compared to a simple Gaussian tweezer. We define the trap volume V as the product of the full widths at half maxima in each directions, $V = \Delta x \Delta y \Delta z$. In the case represented in Fig. 7.4, $V_0 = 1.18 \times 1.18 \times 5.9\,\mu\mathrm{m}^3 = 8.2\,\mu\mathrm{m}^3$ and $V_\Sigma = 370 \times 10^{-3}\,\mu\mathrm{m}^3$, i.e a reduction of the trapping volume by a factor 22. In terms of trapping frequencies, we have $(\omega_x, \omega_y, \omega_z) = 2\pi \times (97, 97, 23)$ kHz for a Gaussian beam and $2\pi \times (207, 207, 71)$ kHz for the E_Σ superposition.

However, if the former expressions give a sense that a tighter trap is achievable with a superposition of LG modes, optical tweezers are by definition strongly focused beams usually made with objectives with a numerical aperture[4] NA ≥ 0.4, where the paraxial approximation breaks down. The calculations have then to be carried out taking into account the full vectorial properties of focused light, where the LG modes are no longer solutions of the Maxwell's equations. To do so, we introduce the Debye-Wolf (DW) formalism in the following and show that our superposition still provides a significant improvement.

7.2.3 LG superposition with tightly focused tweezers: vectorial case

The Debye Wolf formalism for tightly focused beams

When using optics with high numerical aperture, we cannot use the paraxial approximation anymore as the focused beams will have a strong angle with the optical axis. We need to use a diffraction theory that takes into account the vector nature of the electromagnetic fields. The Debye-Wolf (DW) theory provides a theoretical framework to express those focused beams [Wolf and Gabor 1959][5]. We follow [Novotny 2006] for introducing this framework.

[4] Defined as NA $= n \sin\theta_{\max}$, with $\theta_{\max}$ the half-angle of the maximum cone of light that can enter or exit the focusing object.

[5] The DW theory is valid for large Fresnel numbers $F := R^2/(f\lambda)$, where R is the lens radius and f its focal length. In our case $F \simeq 1500$.

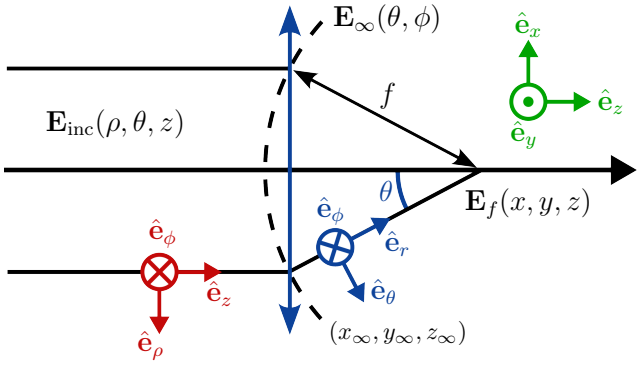

Figure 7.5: Systems of coordinates needed for the computation of the fields in the focal point with the Debye-Wolf integral. In red is the coordinate system for expressing the incoming field. The one in blue is used for expressing $\mathbf{E}_\infty$, the field on the sphere of radius of curvature f. Finally the beam at the focus is expressed in terms of the Cartesian coordinates (in green).

We consider a paraxial incoming beam $\mathbf{E}_{\text{inc}}$, impinging on a focusing object with focal length f, as depicted in Figure 7.5. An important concept of the DW theory is the reference sphere, represented in Fig. 7.5 as a dashed line. An incoming ray meets its conjugate that intersect the focal point on a sphere of radius f named the reference sphere. A point on this sphere is denoted by $(x_\infty, y_\infty, z_\infty)$ or in spherical coordinates (f, θ, ϕ) (blue coordinate system). The distance to the optical axis ρ of the incoming beam is simply equal to $\rho = f \sin\theta$. The maximum distance from the optical axis we can consider without clipping of the incoming field is equal to the radius of the lens R, hence $R = f \sin\theta_{\max} = f \times \text{NA}$, by definition of the NA. At the reference sphere the lens converts the incoming cylindrical beam to a spherical wave, justifying to switch from a cylindrical coordinate system (in red) to a spherical one (in blue).

Before the reference sphere, the incoming field $\mathbf{E}_{\text{inc}}$ can be decomposed into the red basis where the unit vectors are, in Cartesian coordinates,

$$\hat{\mathbf{e}}_\rho = \begin{pmatrix} \cos\phi \\ \sin\phi \\ 0 \end{pmatrix}, \ \hat{\mathbf{e}}_\phi = \begin{pmatrix} -\sin\phi \\ \cos\phi \\ 0 \end{pmatrix}, \ \hat{\mathbf{e}}_z = \begin{pmatrix} 0 \\ 0 \\ 1 \end{pmatrix}. \tag{7.8}$$

where ϕ is the azimuthal angle around the z-axis ($\phi = \pi$ in Fig. 7.5). As we assumed the incoming field to be in the paraxial regime, it only has non-zero components transverse to the propagation (i.e. along $\hat{\mathbf{e}}_\rho$ and $\hat{\mathbf{e}}_\phi$). After refraction, the unit vector $\hat{\mathbf{e}}_\phi$ is unchanged but $\hat{\mathbf{e}}_\rho$ is transformed into $\hat{\mathbf{e}}_\theta$ which can be written in cartesian coordinates as:

$$\hat{\mathbf{e}}_\theta = \begin{pmatrix} \cos\phi\cos\theta \\ \sin\phi\cos\theta \\ -\sin\theta \end{pmatrix}. \tag{7.9}$$

The total refracted electric field, on the reference sphere $\mathbf{E}_\infty$, is given in this new basis (in blue) by:

$$\mathbf{E}_\infty(\theta,\phi) = [t^s[\mathbf{E}_{\text{inc}} \cdot \hat{\mathbf{e}}_\phi]\hat{\mathbf{e}}_\phi + t^p[\mathbf{E}_{\text{inc}} \cdot \hat{\mathbf{e}}_\rho]\hat{\mathbf{e}}_\theta] \sqrt{\frac{n_1}{n_2}\cos\theta} \tag{7.10}$$

This mapping is obtained by projecting $\mathbf{E}_{\text{inc}}$ on the basis axes of the red cylindrical coordinate system $(\hat{\mathbf{e}}_\rho, \hat{\mathbf{e}}_\phi)$ and writing that refraction conserves these components in the new coordinate system $(\hat{\mathbf{e}}_\theta, \hat{\mathbf{e}}_\phi)$. The $\sqrt{n_1/n_2 \cos\theta}$ term comes from energy conservation, and more precisely from the fact that the power transported in a given area around a ray is conserved.

For an input polarization along the x axis, $\mathbf{E}_{\text{inc}} = E_{\text{inc}}\, \hat{\mathbf{e}}_x$, we can write:

$$\mathbf{E}_\infty(\theta,\phi) = E_{\text{inc}}(\theta,\phi)[\cos\phi\, \hat{\mathbf{e}}_\theta - \sin\phi\, \hat{\mathbf{e}}_\phi]\sqrt{\frac{n_1}{n_2}\cos\theta} \tag{7.11}$$

$$= \frac{1}{2}E_{\text{inc}}(\theta,\phi)\begin{bmatrix}(1+\cos\theta)-(1-\cos\theta)\cos 2\phi\\ -(1-\cos\theta)\sin 2\phi\\ -2\cos\theta\sin\phi\end{bmatrix}\sqrt{\frac{n_1}{n_2}\cos\theta} \tag{7.12}$$

Even though $\mathbf{E}_\infty(\theta,\phi)$ is given in terms of the spherical coordinates, it is written as a Cartesian vector.

In the Debye-Wolf formalism, the electric field $\mathbf{E}_f(x,y,z)$ in a region close to the focus is obtained by integrating propagating plane waves of amplitude $E_\infty(\theta,\phi)$ from the reference sphere to the position $\mathbf{r} = (x,y,z)$. We say that $E_\infty(\theta,\phi)$ is the plane wave spectrum of the focused field $\mathbf{E}_f(x,y,z)$,

$$\mathbf{E}_f(\mathbf{r}) = C\iint_{\mathcal{S}} \mathbf{E}_\infty(\theta,\phi)\mathrm{e}^{i\mathbf{k}\cdot\mathbf{r}}d\Omega \tag{7.13}$$

where $d\Omega = \sin\theta d\theta d\phi$ is the infinitesimal solid angle, $\mathcal{S}$ is the surface of the reference sphere on which the integration is carried out (i.e for $\phi \in \{0, 2\pi\}$ and $\theta \in \{0, \theta_{\max}\}$, because of the finite size of the lens) and $\mathbf{k}$ is the wave vector normal to $\mathcal{S}$ with components given by

$$k_x = k\sin\theta\cos\phi,\ k_y = k\sin\theta\sin\phi,\ k_z = k\cos\theta. \tag{7.14}$$

This approximation is valid when the point of interest is close enough to the focus ($\mathbf{r}_0 = \vec{0}$), as the wave vector $\mathbf{k}$ in the integration is close to the real one needed to reach $\mathbf{r}$. Rewriting Eq. (7.13) with θ and ϕ, and switching to spherical coordinates, we obtain:

$$\boxed{\mathbf{E}_f(\rho,\phi,z) = C\int_0^{\theta_{\max}}\int_0^{2\pi} \mathbf{E}_\infty(\theta,\phi)\ \mathrm{e}^{ikz\cos\theta}\mathrm{e}^{ik\rho\sin\theta\cos(\phi-\varphi)}\sin\theta d\theta d\phi} \tag{7.15}$$

As we will focus on Laguerre-Gaussian modes with $l = 0$, we have azimuthal symmetry. In that case, $\mathbf{E}_{\text{inc}}(\theta,\phi) = E_{\text{inc}}(\theta)\ \hat{\mathbf{e}}_x$ and we can plug Eq. (7.12) into Eq. (7.15) and carry out many simplifications. The total electric field near the focus for a paraxial and azimuthally symmetric incoming electric field is given by:

$$\mathbf{E}_f(\rho,\phi,z) = \frac{C}{2}\sqrt{n_1/n_2}\begin{bmatrix}I_{00}+I_{02}\cos 2\phi\\ I_{02}\sin 2\phi\\ -2iI_{01}\cos\phi\end{bmatrix} \tag{7.16}$$

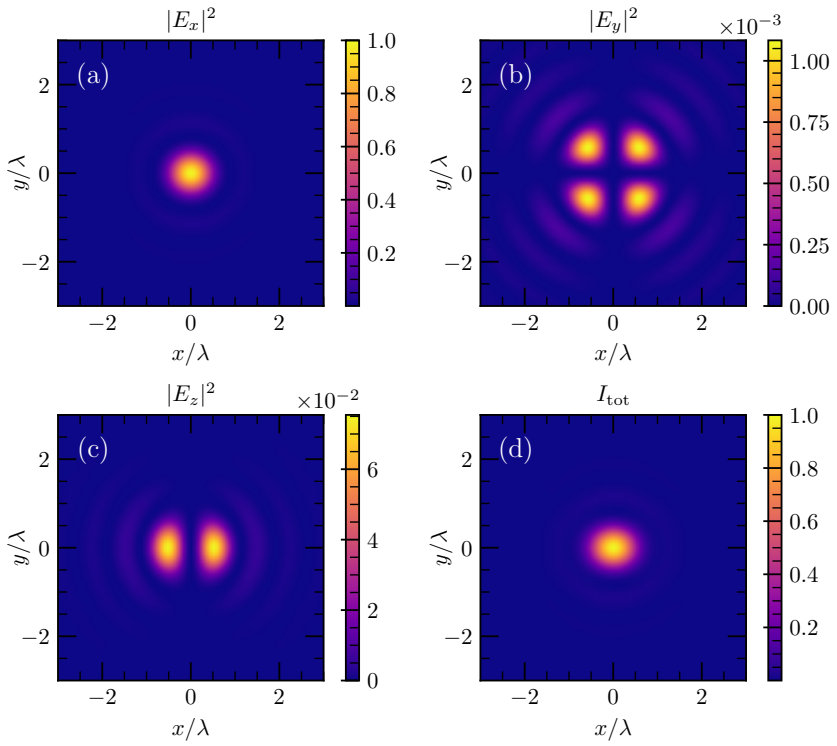

Figure 7.6: Focused Gaussian beam polarized along x focused by an objective of NA = 0.7 for an overfilled pupil. The (a) x, (b) y and (c) z components as well as (d) the total intensity are computed with the Debye-Wolf integral. The intensity is normalized to its maximum. We notice that in this range, an asymmetry of the focal point appear, as it is extended along the direction of polarization, even thought the x-component stays predominant.

where $\mathbf{E}_f$ is a Cartesian vector and

$$\begin{cases} I_{00} = \displaystyle\int_0^{\theta_{\max}} E_{\text{inc}}(\theta)\sqrt{\cos\theta}\,\sin\theta\,(1+\cos\theta)\,J_0(k\rho\sin\theta)\,\mathrm{e}^{ikz\cos\theta}d\theta \\ I_{02} = \displaystyle\int_0^{\theta_{\max}} E_{\text{inc}}(\theta)\sqrt{\cos\theta}\,\sin\theta\,(1-\cos\theta)\,J_2(k\rho\sin\theta)\,\mathrm{e}^{ikz\cos\theta}d\theta \\ I_{01} = \displaystyle\int_0^{\theta_{\max}} E_{\text{inc}}(\theta)\sqrt{\cos\theta}\,(\sin\theta)^2\,J_1(k\rho\sin\theta)\,\mathrm{e}^{ikz\cos\theta}d\theta \end{cases} \tag{7.17}$$

where the J_n are the Bessel functions of the first kind of order n[6].

For computing each point near the focal plane (x, y, z), we need to evaluate a 1D integral on θ. Figure 7.6 shows the intensity profile of a x-polarized Gaussian beam focused by an objective of NA = 0.7, for $z = 0$. We notice a non-zero electric field along z, characteristic of fields focused out of the paraxial approximation and

[6]The Bessel functions appear naturally in this expression as they can be written as integrals:

$$J_n(x) = \int_{-\pi}^{\pi} \mathrm{e}^{-i(n\tau - x\sin\tau)}d\tau \tag{7.18}$$

Using Bessel functions makes the calculations faster as it allows going from a 2D to a 1D integral and they are efficiently evaluated in `scipy`.

a breaking of the azimuthal asymmetry on the intensity at the focal point. The intensity profile is elongated along the direction of polarization of the incoming field.

Writing the Debye-Wolf integral as a Fourier transform for fast calculation

Computing the field at the focal point can be long as for every point in the grid we have to evaluate various integrals (2D integrals if the incoming field does not have azimuthal symmetry). In order to take advantage of the Python capabilities, we modify Eq. (7.15) to write it as a Fourier transform (FT) [Leutenegger et al. 2006; Cai et al. 2019]. This will allow us to use the Fast Fourier Transform (FFT) algorithm, which is well optimized for speed. We start from Eq. (7.13):

$$\mathbf{E}_f(\mathbf{r}) = C \iint_{\mathcal{S}} \mathbf{E}_\infty(\theta,\phi) e^{ik_z z} \mathrm{e}^{i(k_x x + k_y y)} \sin\theta d\theta d\phi \tag{7.19}$$

where we recall that the integral is carried along the reference sphere surface $\mathcal{S} = \{\phi \in [0, 2\pi],\ \theta \in [0, \theta_{\max}]\}$. In order to replace the spherical integration by a planar integration over k_x and k_y we use the relation $\frac{1}{k_z} dk_x dk_y = k \sin\theta d\theta d\phi$ [Leutenegger et al. 2006] which gives:

$$\mathbf{E}_f(\mathbf{r}) = \frac{C}{k} \iint_{\mathcal{D}} \mathrm{e}^{ik_z z} \mathbf{E}_\infty(\theta,\phi) \mathrm{e}^{i(k_x x + k_y y)} \frac{dk_x dk_y}{k_z} \tag{7.20}$$

The integration domain is now $\mathcal{D} = \left\{(k_x, k_y) : k_x^2 + k_y^2 \leq (k \sin\theta_{\max})^2\right\}$. This looks very much like a 2D Fourier transform, apart from the limited domain of integration (which should be $\mathbb{R}^2$ for a 2D FT). We extend the integral in Eq. (7.20) by setting $\mathbf{E}_\infty(\theta,\phi)$ to 0 outside of $\mathcal{D}$. The extended field is written $\overline{\mathbf{E}}_\infty(\theta,\phi)$. Eq. (7.20) can now be written as a 2D Fourier transform on k_x and $k_y$of the quantity $\mathrm{e}^{ik_z z}\overline{\mathbf{E}}_\infty(\theta,\phi)/k_z$:

$$\boxed{\mathbf{E}_f(x,y,z) = -\frac{if}{\lambda_0 k} \mathscr{F}(\mathrm{e}^{ik_z z}\overline{\mathbf{E}}_\infty(\theta,\phi)/k_z)} \tag{7.21}$$

where the constant C has been made explicit. For a low NA system, $k_z \simeq k$ and we recover the Fraunhofer integral for which $\mathbf{E}_f \propto \mathscr{F}(E_{\mathrm{inc}})$. The numerical implementation is done on Python with the FFT algorithm. As we want an equidistant sampling of the domain in k_x and k_y, Eqs. (7.14) gives us the discretization of $\theta^{n,m}$ and $\phi^{n,m}$ needed to compute the fields.

We then proceed as follows. The 2D array coordinates ($k_x^{n,m}$, $k_y^{n,m}$) are converted into ($\theta^{n,m}$,$\phi^{n,m}$) which are used to sample $\mathbf{E}_\infty(\theta^{n,m}, \phi^{n,m})$. We ensure the electric field is set to 0 for $\theta > \theta_{\max}$ where $\theta_{\max} = \max(\arcsin(\mathrm{NA}), \arcsin(\rho_{\max}/f))$. We then add an important zero-padding to increase the resolution of our simulation in the focal plane. This FFT-based method is at least 50 times faster than the former one evaluating the integrals subsequently for each point in the plane of interest. Indeed, a single Fourier transform gives the electric field in the transverse plane (x,y) at any given z. This technique can be generalized to compute the field in any given plane going through the focal point by a basis change [Cai et al. 2019].

The LG superposition in the tightly focused regime

Now that we have a theory to compute strongly focused fields with a reasonable approximation we use it to compare Gaussian and Laguerre-Gaussian superposition tweezers. Indeed, even if the LG modes are not solution of the Maxwell's equations

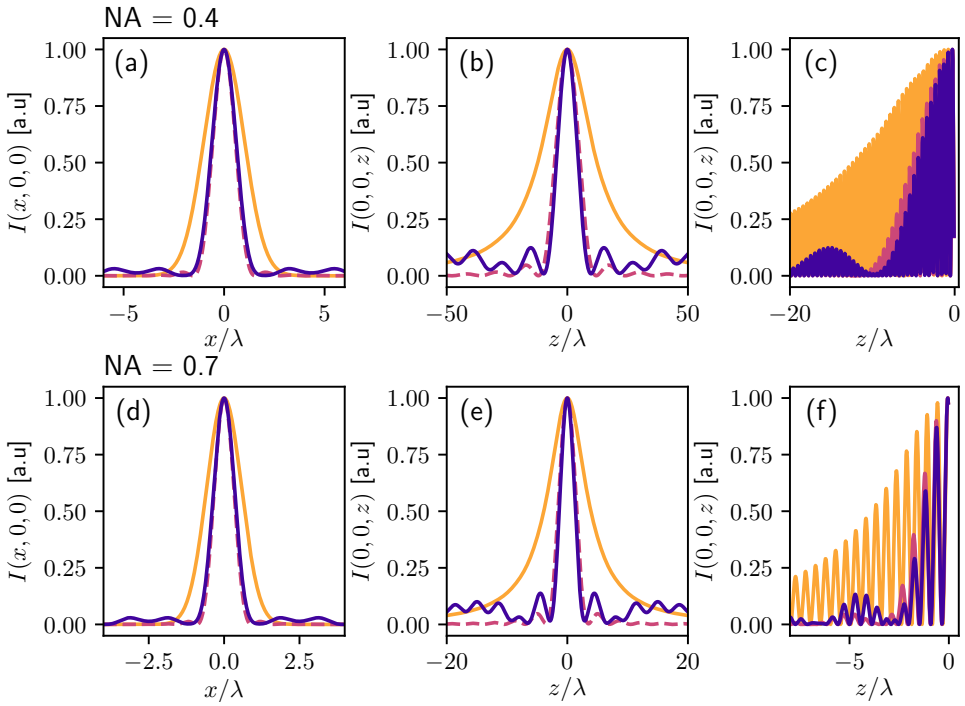

Figure 7.7: Reduced reflections and narrower traps for the LG superposition in the Debye-Wolf formalism. The top row corresponds to NA = 0.4 and the bottom one to NA = 0.7. Orange: Focused Gaussian beam $\mathbf{E}_0$ at $F_0 = 0.4$, Blue: Focused LG superposition $\mathbf{E}_\Sigma$ for $F_0 = 0.4$, Pink: Gaussian beam overfilling the objective pupil ($F_0 \gg 1$). Intensity cuts along (a)(d) the x transverse and (b)(e) z longitudinal axes. (c)(f) Compares the reflections patterns for a perfect mirror at the waist.

outside of the paraxial approximation, nothing prevents from sending the same superposition onto high-NA objectives and computing the predicted trap.

As seen in Equation (7.15), the integral is limited to a domain that depends on $\theta_{\max}$. This value is given by the geometrical constraint of the transverse size of the focusing lens. As such, the incoming beams have a finite size which appears in the calculations. To quantify the dependence of the focused field on the size of the incoming beam, we define the filling factor $F_0 = w_0/R$, where w_0 is the waist of the incoming beam and R the clear aperture radius of the lens. Different F_0 may produce very different beam shapes on the focal plane. For small NA[7], $R = f \times \mathrm{NA} = f \sin\theta_{\max}$.

Figure 7.7 compares $\mathbf{E}_0$ and $\mathbf{E}_\Sigma$ focused fields in the Debye-Wolf formalism for NA = 0.4 and NA = 0.7, both taken at $F_0 = 0.4$[8]. While only NA = 0.7 can produce focused beams with a waist w_0 on the order of 1 µm, NA = 0.4 can be sufficient to create Gaussian tweezers in the collisional blockade regime. This NA will be kept in the following as the objectives used in the first version of the experiment have NA = 0.4. Figs. 7.7(a,b,d,e) confirm the trap tightening along x and z compared to the Gaussian case with the same F_0. They show however that the gain is limited compared to a plane wave input (in pink, in this case $F_0 = 10$). In this overfilling case, the field at the focal plane is a diffraction-limited Airy spot. We try to avoid being in this case as overfilling the objective aperture sends substantial amount of

[7] $\mathrm{NA} = \sin\theta_{\max} = \sin[\arctan(R/f)] \simeq R/f$

[8] Value of $F_0 = 0.4$ chosen as it corresponds to the first local maximum in ω_z (see Fig. 7.8(b)). There is a higher ω_z achievable at $F_0 = 0.737$ but its intensity profile has important revival lobes along z.

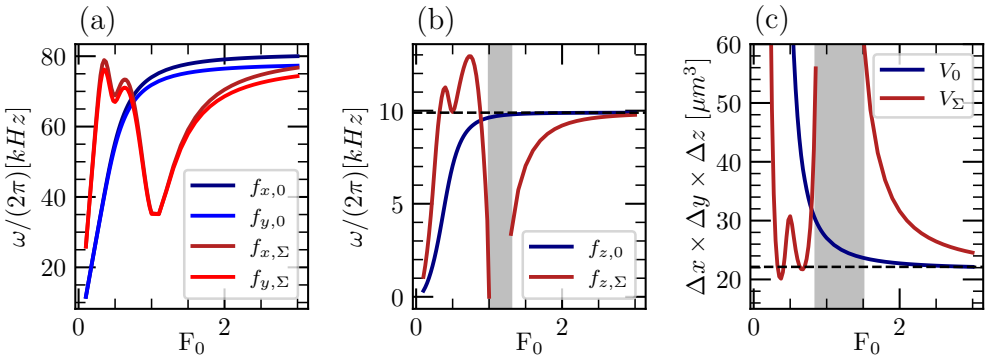

Figure 7.8: Trap frequencies f_i and volumes for a tightly focused $\mathbf{E}_0$ and $\mathbf{E}_\Sigma$ in the DW formalism. (a) f_x and f_y, (b) f_z, (c) and trap volumes V_0 and V_Σ dependence with F_0. The subscripts 0 and Σ refer to the Gaussian tweezer and the LG superposition (7.7) respectively. The calculations are done with NA = 0.4, and for a trap depth set to 1 mK. For some values of F_0 we can have a trap with a smaller volume and a larger trap frequency along z than with a Gaussian beam with any filling factor, as shown by the 2 dashed lines in (b) and (c).

power into the air and, more importantly, can introduce important aberrations at the focus, as discussed in the following.

Figure 7.8 is a more systematic study of these effects as it shows the variation of the trapping frequencies in all three directions and of the trapping volume of a Rubidium atom trapped by a 1064 nm laser with respect to the filling factor F_0. For each point the trap depth is set to 1 mK. Note that ω_x and ω_y are no longer equal as the polarization of the incoming field introduces an asymmetry in the focal plane.

It shows that increasing the filling factor for a Gaussian beam makes the trap tighter and with higher trap frequencies. In this regime ($F_0 \gtrsim 1$) the Gaussian beam is so large it illuminates the input lens uniformly and looks like a plane wave. This effect manifests in 7.8(a-c) as a saturation for high F_0 as increasing the filling factor more does not change much the incoming profile. We note that for our LG superposition, the longitudinal trap frequency ω_z is larger than this diffraction limited regime for $F_0 \in [0.32, 0.9]$. The mode volume is also decreased for values of F_0 around 0.37 and 0.67. The trapping frequency can be increased by 30% and the trapping volume reduced by 9% by using a LG tweezer with an adequate filling factor, compared to the best Gaussian case.

Tighter traps at lower filling factors

If the gains in terms of trap frequencies are substantial in the LG superposition case, they are only marginal in terms of trap volume (and in Δz, which determines the fringes profile, as seen in Figs. 7.7(b)(d)). This raises the question: why should one implement a more complex superposition if an overfilled Gaussian performs almost as well?

For a given setup, using a LG superposition allows to work at lower power and filling factor to produce traps of similar depths and narrower widths. This is true even compared to an overfilled Gaussian input. This appears in Fig. 7.9 which shows the power needed to create optical tweezers with an objective of NA = 0.4 for both a Gaussian or a LG superposition input (Fig. 7.9(a) and (b) respectively). In the Gaussian case, significant amounts of power are needed to produce traps in the millikelvin regime ($P \approx 20$ mW), because of the relatively low NA. The needed power

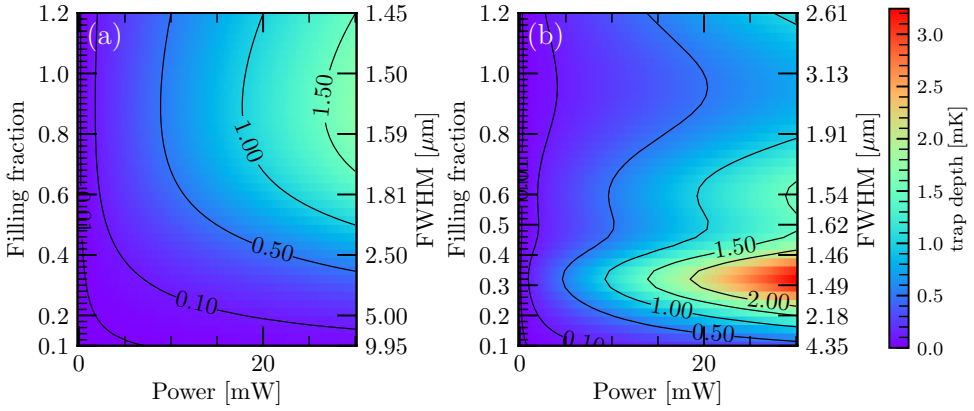

Figure 7.9: Tweezer trap depth with the injected power and microscope objective filling factor. (a) Simulations for a Gaussian tweezer in the vector regime, NA = 0.4, $f = 10\,\text{mm}$. We notice that for this objective with a relatively small NA, we need substantial power to create a 1 mK trap. At a given power, the trap becomes weaker when $F_0 > 0.8$ as we are clipping power out. The right axis gives the full-width half-maximum of the trap for the corresponding filling factor F_0. (b) For a E_Σ superposition, we have tighter traps hence less power is needed.

is reduced in the LG superposition case[9]. But most importantly, F_0 is also reduced for similar trap characteristics. As an example a FWHM of 1.5 µm is achieved in the LG superposition case for a filling factor ≈ 0.3, more than 3 times lower than in the Gaussian case. With NA = 0.4 one can hope to reach the collisional blockade regime with LG sums for $F_0 < 0.3$ and only a few mW of power.

Experimentally, working at low F_0 can help reduce aberrations that can be detrimental for such high-focused traps. Most experiments using high focusing lenses to produce single tweezers work with a limited filling factor, as it is difficult to obtain a perfect point spread function in the overfilled case. F_0 is taken around 0.2 in [Masters et al. 2023] for a NA = 0.55 aspheric lens, and [Bruno et al. 2019] includes a discussion of why they chose $F_0 = 0.35 - 0.55$ as a compromise between the reduction of the waist and the spherical aberrations introduced by their NA = 0.5 aspheric lens.

If the theoretical limits of the trap parameters are close in both cases, LG superpositions offer an additional experimental capability which gives more versatility in the possible traps generated by a given setup. Experiments will show if this strategy increases the loading rate even for NA = 0.4.

7.3 Generating the tweezers experimentally

With these promising simulations at hand, we now delve on how to produce such a superposition of Laguerre-Gaussian modes experimentally, and more generally, how to control the spatial profile of a given electric field thanks to spatial light modulators.

7.3.1 Optical holography for shaping the full light field

The immense versatility of spatial light modulators

Measuring and controlling the complex profile of light has been a critical question since the 1940s. Indeed, by detecting a beam on a camera one can only access its

[9]The power needed for these traps can be further decreased by using higher-NA objectives. As an example, for NA = 0.7, 0.5 mW are sufficient to produce a 1 µm wide Gaussian trap, 2 mK deep.

intensity. Since then, many techniques have been proposed to record both the phase and amplitude of the light field [Gabor 1948], creating the field known as holography. Subsequently, this knowledge was applied to engineer either the phase, amplitude or both properties of the light in order to create custom spatial distributions.

With the emergence of digital holography, this capability became more accessible. Spatial light modulators (SLM) are phase-only modulators based on liquid crystals, similar to the ones found in LCD screens. These highly birefringent components are arranged in an 2D array in SLMs, placed between electrodes. The axis of each liquid crystal (= 1 pixel) can be set independently by tuning the local applied voltage. An incoming light beam going through the SLM acquires position-dependent phase defined by the angle of the liquid crystal. The 2D phase shift can hence be engineered with a so-called phase mask, with a resolution close to that of the liquid crystal array.

This phase-only modulation can be converted into amplitude modulations on the Fourier plane of a lens, making SLMs suitable for creating complex intensity patterns. This versatility, combined with their speed and moderate cost, has made them essential tools in many fields from adaptive optics in astronomy, to microscopy in biological tissues, to optical communications, and they have become particularly instrumental in generating optical tweezer arrays for trapping and manipulating cold atoms [Pasienski and DeMarco 2008; Barredo et al. 2016; Endres et al. 2016].

Separating the modulated light with an imprinted blazed grating

As SLMs are usually interfaced with computers, these phase masks are displayed on the SLM with grey-scale images where the value of each pixel (from 0 to 255) encodes a given physical phase-shift. However, the electric response of the liquid crystals is not linear, and look-up tables (LUT) given by the manufacturer have to be used to allow to convert the applied voltage into a phase value.

The modulation efficiency of the SLM falls short of 100% and is dependent of the phase masks applied. To get rid of the unmodulated part, blazed gratings (BG) are usually added to the targeted phase mask. This mask imprints a linear phase

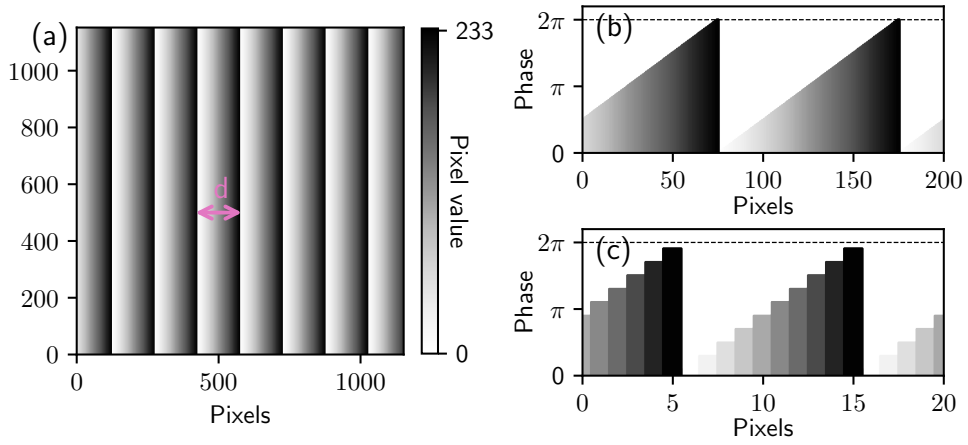

Figure 7.10: Blazed grating on a SLM and pixelation. (a) Blazed-grating displayed on the SLM with a pitch $d_{\mathrm{BG}} = 150$ pixels. (b) Discretized 1D cut of the phase pattern with a low spatial frequency ($d_{\mathrm{BG}} = 100$), (c) and for a high spatial frequency ($d_{\mathrm{BG}} = 10$). In this case, the pixelation is evident. As a result, the SLM shows a lower diffraction efficiency for high-frequency phase patterns.

$\varphi(x)$[10] on the beam, making it analogous to a prism (see Fig. 7.10(a)). Some part of the light is diffracted with an angle θ related to the slope of the linear phase while the unmodulated part is simply reflected. This allows to separate these two components. The diffraction efficiency decreases with the displayed spatial frequency of the blazed grating (see [Labuhn 2016] for a more thorough discussion), because a rapidly-varying phase can no longer be well approximated by the one imprinted of the pixelated SLM (see Fig.7.10(b-c)). A sweet spot has to be found as a high spatial frequency means a better separation of the spots on the Fourier plane. In our case, we use $d_{\mathrm{BG}} = 10$, needed for easy filtering of the 1$^{\mathrm{st}}$ diffraction order, with an efficiency around 70%.

In the following we use an electrically-addressed liquid crystal on silicon (LCOS) SLM (**Meadowlark Optics P1920-600-1300**) with 1952 pixels in the horizontal axis and 1152 on the vertical one, and a pixel pitch of 9.2 µm.

7.3.2 Optical setup for holography

The optical setup for the generation of optical tweezers with an SLM is shown in Fig. 7.11. The tweezers are generated with a 1064 nm fiber laser with external seeder (**Azurlight ALS-IR-1064-20-E**), sent through an acousto-optic modulator (AOM) (**AA Opto-electronic MT110-A1-1064**) for fast switching. It is coupled into a high power single-mode photonic-crystal fiber (**Alphanov LMA-PM-15 421**) before arriving on the 4f imaging setup presented here. The 1064 nm laser can output up to a few Watts of power, which can be useful if we want to increase the number of traps. The output beam of the fiber is collimated to a beam with 6.7 mm waist and reflected off the surface of the SLM. We make a 1:1 image of the SLM mask on the input pupil of the objective through a 4f setup. The beam is then focused into the atoms thanks to a microscope objective (**Mitutoyo M Plan Apo NIR B 20x**). Another one can be used to image the structured tweezers.

This 4f setup is convenient for a few reasons. It allows filtering of the unwanted diffraction orders in the Fourier plane after the first lens. Because it makes a 1:1 image of the SLM plane onto the objective input plane, looking at the phase mask sent gives a good idea of the field on the objective pupil. Moreover, 4f systems are less sensitive to misalignment in the propagation axis in comparison to 2f systems [Fitzpatrick et al. 2020]. It is realised in our setup by using 2 achromatic doublets of focal length 300mm (**Thorlabs AC254-300-C-ML**), and putting a diaphragm on the Fourier plane to filter out the 0$^{\mathrm{th}}$ order. A beam sampler (**Thorlabs BSF10-C**, asymmetric beam-splitter with $T = 90\% - R = 10\%$) picks-up some of the light in order to monitor the structured beam on a CMOS camera (lower one in Fig. 7.11).

A scientific CMOS camera (**Hamamatsu Orca Fusion C14440**) has been interfaced (and included in `labscript`) to collect the fluorescence of the trapped atoms. The light at 780 nm is separated from the trapping light by a dichroic mirror (**Thorlabs DMLP950**).

There are a few experimental points to keep in mind for the impinging light when setting up the SLM, in order to use it to its maximum capabilities:

- Shape: The input has to be a plane wave or a Gaussian beam. Either work as the phase mask can be compensated for the shape of the initial beam. This is done by using the output of the single mode fiber. Careful alignment of the

[10] $\varphi(x) = \frac{2\pi x}{d_{\mathrm{BG}} d_{\mathrm{pix}}} \mod[2\pi]$, with d_{BG} the pitch in pixels and d_{pix} the pixel width.

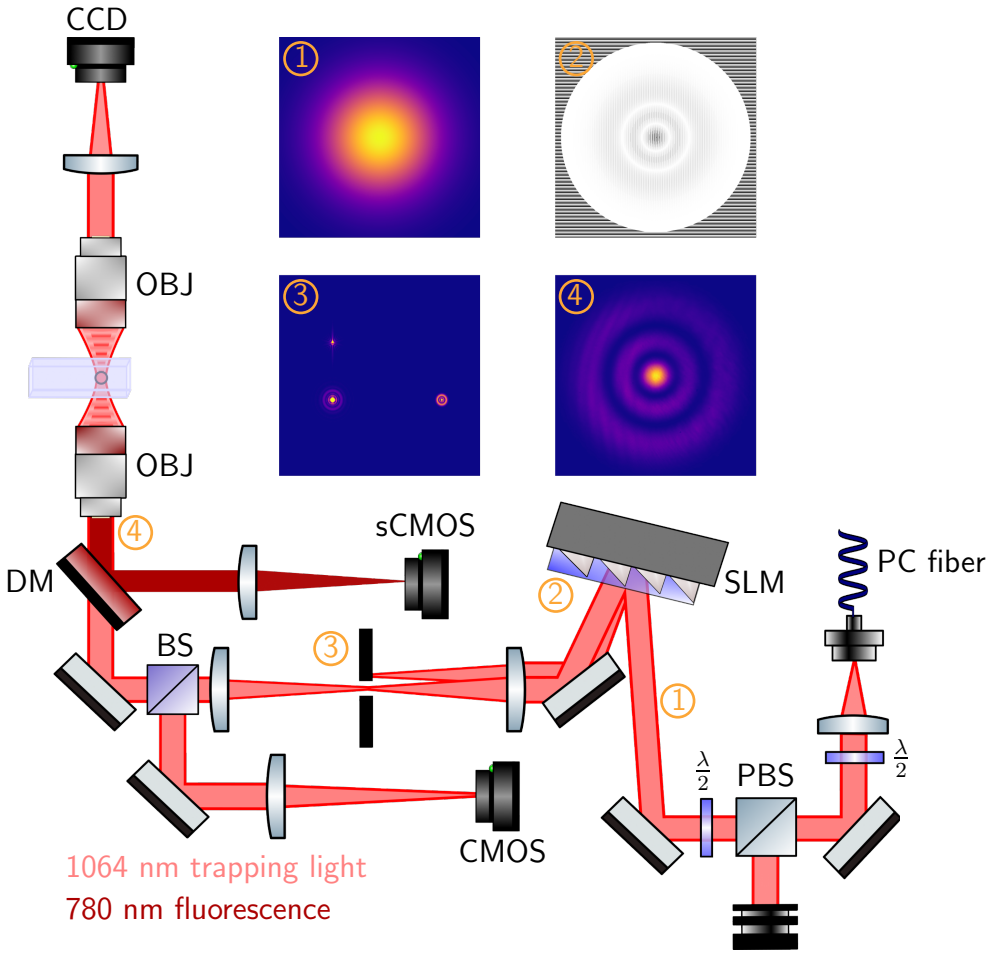

Figure 7.11: 4f setup for generating Gaussian or LG tweezers with a SLM. A Gaussian beam, coming from a high-power photonic-crystal single-mode fiber, is reflected off of the SLM, after cleaning of the polarization. A 4f setup allows for filtering in the Fourier plane, keeping only the 1st diffracted order. The distance between the SLM and the input plane of the objective is equal to 4 focal lengths of the achromatic doublets. The SLM mask is imaged with a scale 1:1 on the objective entrance pupil. DM: dichroic mirror, CMOS: CMOS camera for monitoring the tweezer shape, sCMOS: scientific CMOS camera for collecting fluorescence of trapped atoms, BS: beam sampler, PBS: polarizing beam splitting, OBJ: microscope objective. The insets show (1) the Gaussian intensity profile after the fiber output, (2) the phase mask sent to the SLM (with a pupil), (3) the simulated intensity on the Fourier plane, with the interesting order on the right, and (4) the measured intensity on the objective input plane. All of these images are made for a LG E_2^0 mode and with the mask generated with Method 2 described in section 7.3.3.

Gaussian beam on the center of the SLM has to be carried out with diaphragms for the compensation to be correct.

- Polarization: As SLMs are made with birefringent liquid crystals, polarization of the incoming light is critical. To work efficiently, it has to be linear along the slow (here vertical) axis of the SLM. A half-waveplate ($\lambda/2$) and 1 inch polarizing beam splitter (PBS) are placed after the fiber output to align and clean the polarization.

- Incidence: The incidence angle has to be as low as possible. Indeed, the phase accumulates throughout the propagation in the liquid crystal layer and a bigger angle means a longer layer crossed, which does not match the specifications given by the software. In our setup, we have an angle of around 5° between the incoming beam and the SLM normal vector.

- Wavelength: The wavelength of the input laser has to be adapted to the SLM. The phase shifts introduced by the crystals are wavelength-dependent, it is possible to calibrate the SLM with a Look-Up Table (LUT) in order to correct the values of voltage to apply for a given wavelength. A common figure of merit is the the pixel value to achieve a π phase shift compared to a pixel value of 0, $V_{2\pi}$. This value is strongly dependent on the wavelength of the incoming light. For our 1064 nm laser, $V_{2\pi} = 223$, as the SLM was calibrated at 780 nm. The phase of the output beam can be manipulated with a resolution of $2\pi/223$.

7.3.3 Obtaining high purity SLM masks: amplitude-encoding phase masks

It is possible to generate Laguerre-Gaussian beams by straight-forwardly imprinting the radial phase jumps φ_p (see Fig. 7.3) of the wanted LG beam on the SLM (**Method 1**). However this leads to modes with a purity that does not go over 80% as shown in [Arlt et al. 1998]. Instead we follow the proposals from [Arrizón et al. 2007] and [Bolduc et al. 2013] which show that an exact mapping exists between the phase-only modulation of the SLM and any complex electric field. It is then possible to find the phase mask to send to the SLM for a given target field. Note that the solution is not unique, hence the different proposals.

The idea of these phase masks is to take advantage of the blazed grating that is added for filtering the 1^{st} diffraction order and modulate its depth. Indeed, the closer the modulation is to a full $0 - 2\pi$ range, the more light the SLM can send to the 1^{st} diffraction order. With this modulation the intensity sent to the atoms [Davis et al. 1999] can be controlled locally, engineering the intensity distribution pixel by pixel. While this comes at the cost of more loss into the 0^{th} order, it is possible to obtain modes with higher purity [Clark et al. 2016].

Let us get a feeling of why this amplitude encoding can lead to higher purity. A linearly-polarized electric field on a plane transverse to the propagation axis z is described by both a scalar amplitude and a phase as follows:

$$E(x, y) = a(x, y)\mathrm{e}^{i\phi(x,y)}. \tag{7.22}$$

We will call E the target field. On the contrary, the phase mask applied to the SLM modulates only the phase of the incoming wave. If we assume that we found a phase modulation of the SLM that allows to reproduce our field E, the transmittance of

the SLM can be written as:

$$h(x,y) = \mathrm{e}^{i\psi(a(x,y),\phi(x,y))} \tag{7.23}$$

where $\psi(x,y)$ is the phase mask applied on the SLM. This function $\psi(a,\phi)$ depends on both the amplitude and phase of the target field. We expand the function $h(x,y)$ as a Fourier series in the domain of ϕ:

$$h(x,y) = \sum_{q=-\infty}^{+\infty} h_q(x,y) \text{ where } h_q(x,y) = c_q^a \, \mathrm{e}^{iq\phi} \tag{7.24}$$

and where the coefficients c_q^a are given by:

$$c_q^a = \frac{1}{2\pi} \int_{-\pi}^{\pi} \mathrm{e}^{i\psi(\phi,a)} \mathrm{e}^{-iq\phi} d\phi. \tag{7.25}$$

With this notation, the first order term h_1 in the expansion of h is equal to the target electric field E if c_1^a is proportional to a, $c_1^a = Aa$ is verified. If we want this condition to be verified, taking the real and imaginary parts of Eq. (7.25) lead to the following system:

$$\begin{cases} \displaystyle\int_{-\pi}^{\pi} \sin[\psi(\phi,a) - \phi] d\phi = 0, \\ \displaystyle\int_{-\pi}^{\pi} \cos[\psi(\phi,a) - \phi] d\phi = 2\pi A a(x,y). \end{cases} \tag{7.26}$$

We need to find a family of functions $\psi(\phi,a)$ that verify the above system of equations. [Arrizón et al. 2007] proposes to use:

$$\psi(a,\phi) = f(a) \sin\phi \tag{7.27}$$

where the function f has still to be determined. In this case we obtain $h(x,y) = \mathrm{e}^{if(a)\sin\phi}$. We use the Jacobi-Angler identity to write this complex exponential as as sum of Bessel functions:

$$\mathrm{e}^{if(a)\sin\phi} = \sum_{m=-\infty}^{+\infty} J_m[f(a)] \mathrm{e}^{im\phi} \tag{7.28}$$

where J_m is the Bessel function of the first kind of order m. By comparing this expression to Eq. (7.24) we obtain an expression of the c_q^a coefficients in term of the Bessel functions:

$$c_q^a = J_q[f(a)] \tag{7.29}$$

Remembering the condition so that $h_1 = E$, we find that the function f used to modulate the amplitude of the target field on the phase mask, has to verify the condition:

$$\boxed{J_1[f(a)] = Aa} \tag{7.30}$$

We need to invert this expression to obtain the function f. This is done numerically and gives a function defined in the range [0,1] with values in [0,1.84]. We find that this function f is linear for small values of a, which is consistent with the simpler mapping $\psi(a,\phi) = a\sin\phi$, proposed in [Davis et al. 1999]. We refer to this mapping as **Method 2**. Intuitively, this method implements amplitude modulation with the

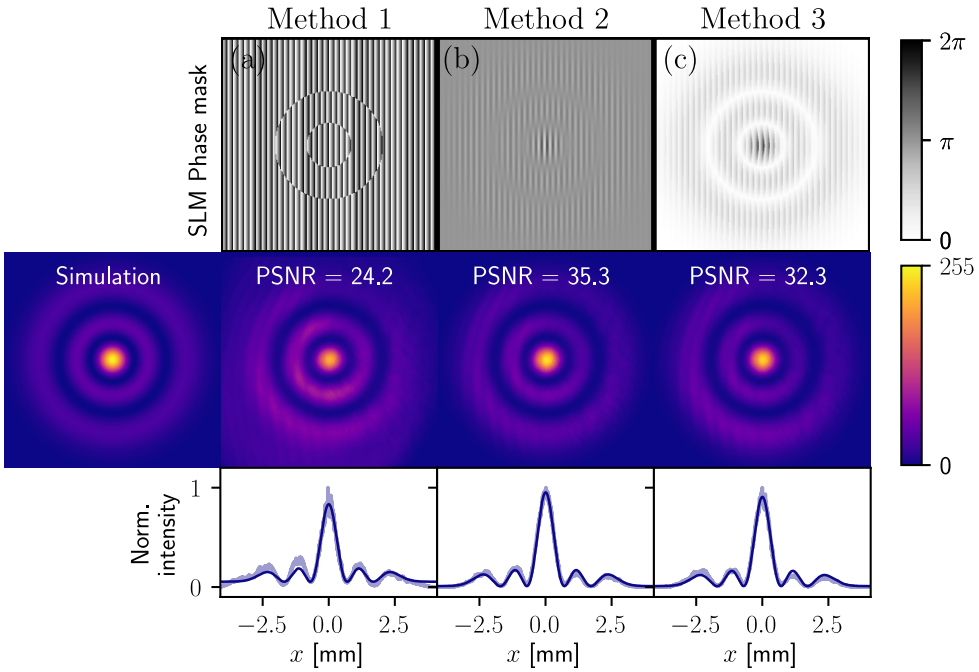

Figure 7.12: Comparison of the purity of the LG modes generated by the three different methods. Masks generated to produce a beam with waist $w_0 = 1.4\,\text{mm}$. The simulated intensity profile for the LG E_2^0 beam with the same w_0 is presented on the left. Each column shows mask, image at the objective input and 1D cut through the maximum. (a) Mask produced by only taking the phase of the LG beam and adding a BG (Method 1). It has no modulation of the amplitude of the BG. We see the mode decays too slowly after the 2nd ring. (b) Mask generated with Method 2 [Arrizón et al. 2007] gives the highest PSNR. (c) Method 3 from [Bolduc et al. 2013].

SLM by inverting the diffraction efficiency of the blazed grating.

A similar mapping between the phase-only hologram and the phase and intensity of the target field is derived in [Bolduc et al. 2013], which is based on the inversion of the expression $\sin(f(a))/f(a) = Aa$. We also use this method (referred to as **Method 3**) in the following.

Figure 7.12 shows the phase masks and profiles of a LG E_2^0 mode generated by three different methods. Method 1 corresponds to just applying the phase of the target LG beam on the SLM, Method 2 is the amplitude and phase encoding technique detailed in this subsection [Arrizón et al. 2007] and Method 3 is the similar one from [Bolduc et al. 2013]. The pictures are taken by a camera at the input plane of the objectives. There are different ways to measure the purity of the generated beams, relying on image analysis. We choose to use the Peak Signal to Noise Ratio (PSNR) defined in [Clark et al. 2016] as a figure of merit. We define as $I_{\text{sim}}^{i,j}$ the value of pixel (i,j) for the simulated date and $I_{\text{exp}}^{i,j}$ for the experimental image, the PSNR per decibel reads:

$$\text{PSNR} = 10\log_{10}\left(\frac{\max(I_{\text{exp}})^2}{\text{MSE}}\right). \tag{7.31}$$

where MSE is the mean square error between I_{sim} and I_{exp}, $\text{MSE} = \sum_{i,j}\left(I_{\text{sim}}^{i,j} - I_{\text{exp}}^{i,j}\right)^2$.

The higher the PSNR, the closer the image is to the theoretical one. [Clark et al.

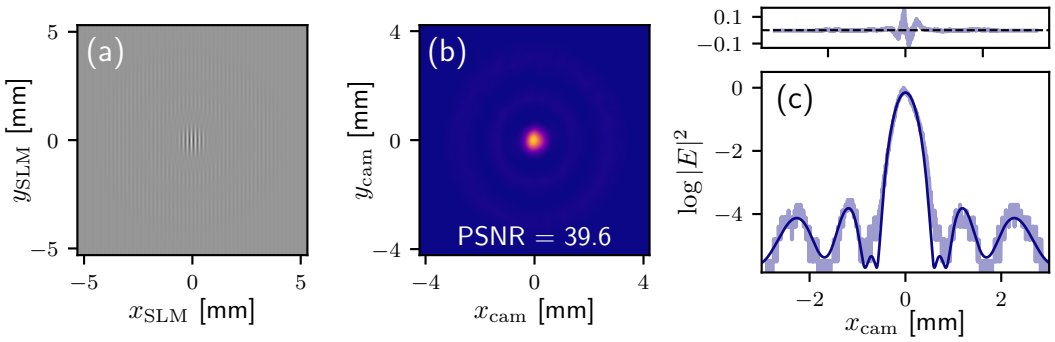

Figure 7.13: Mask and intensity profile of the E_Σ superposition on a paraxial setup. (a) Mask, computed with Method 2. (b) Normalized intensity profile recorded on the CMOS camera. The rings are barely visible. (c) 1D cut of the intensity profile at the center of the camera, in log scale to emphasize the oscillations around the central spot. The upper plot shows the residuals.

2016] reports values as high as 40. Before calculation of the PSNR, the experimental picture is centered, normalized, and has its background removed. The masks given by Methods 2 and 3 give PSNR = 35.3 and 32.3 respectively. It is clear that playing on the amplitude of the blazed grating increased the purity of the mode, compared to Method 1. The values are in reasonable agreement with the values reported in [Clark et al. 2016] for these methods, albeit slightly lower. We expect some better filtering of the observed vertical fringes might increase them.

Even if Method 2 has a worse diffraction efficiency, we choose to realize our superposition with it, as it gives better results. We show in Fig. 7.13 a result of such a superposition created with Method 2 mask. This is done for a nominal waist $w_0 = 1\,\mathrm{mm}$. The computed PSNR is very high, and the purity of the mode is confirmed by the 1D fit in Fig. 7.13(c). The data is shown on a log y-axis to highlight the oscillations around the central peak and their very precise fit with the theory. We can hence produce LG superposition in the paraxial regime with very high purity. From our calculations from Section 7.2.3, we should achieve tight LG-based tweezers with this experimental setup.

A word on optical aberrations and ongoing work

Since we are using objectives with high numerical apertures, the field in the focal plane is very sensitive to any aberration introduced by the optical setup. These aberrations are kept to a minimum by using achromatic doublets and infinitely-corrected microscope objectives. We discuss the aberrations that can be introduced in the different parts of the setup.

During propagation from the PC fiber to the input plane of the objective, aberrations can occur because of imperfect alignment into a lens or small deformation of a mirror. This can be reduced by using larger optics. Work is being carried out to implement a Gerchberg-Saxton algorithm [Gerchberg and Saxton 1972] in order to further compensate for them. This iterative algorithm uses the intensity profile of an input collimated beam and the measured profile of the beam at the focus of a lens and uses the Fraunhofer approximation to propagate the light fields back and forth with Fourier and inverse Fourier transforms. At each step, the computed amplitude is replaced by the experimental one, until it finds the right input phase to apply to the Gaussian input so that it transforms into the experimental spot on the Fourier plane. This gives the aberrated phase introduced through propagation up to the objective.

Subtracting this phase from the SLM phase mask helps correcting for these effects [Hering et al. 2016].

As discussed in Section 7.2.3, more aberrations (usually spherical) can be introduced when overfilling the entrance pupil of the objective and clipping of the input Gaussian beam. Indeed, we notice that going to a high filling factor seems to introduce aberrations, as the focal spot becomes asymmetric in the longitudinal direction, but this has to be characterized more precisely. For a Gaussian beam, we restrict for now to values of $F_0 < 0.6$, which increase the minimum width of trap achievable. This minimum waist can be decreased by using objectives with higher NA, or replacing the Gaussian input by a LG superposition (even with lower F_0).

The objectives themselves can be imperfect. They were characterized thanks to a Gerchberg-Saxton setup, implemented in Collège de France, in the team of Michel Brune and Clément Sayrin, and found to be very good. Their mask can also be subtracted from the SLM phase mask.

Conclusion

In this chapter, we have introduced theoretical and experimental tools to produce single-atom traps with optical tweezers. Following a proposal by [Béguin et al. 2020a], a strong emphasis has been put on the generation of optical tweezers with higher-order Laguerre-Gaussian modes, as it was showed theoretically they can provide tighter trapping potentials and easier atom loading close to nanostructures through reduced reflections. We proved that these results still hold for objectives with NA $= 0.4$. Moreover, we showed these improvements are possible in experimentally credible regimes (low F_0 and powers). Doing so, we introduced a theoretical framework and implemented fast algorithms based on FFTs to study the focusing of arbitrary light beams out of the paraxial approximation. Substantial work has been conducted to interface a spatial light modulator on the experiment, and on the creation of specific phase masks to generate high purity individual Laguerre-Gauss beams and LG superpositions. The methods introduced for generating the phase masks provide an immense versatility for future experiments.

Ongoing work should soon bear fruit and provide some results on trapping single Rubidium atoms in our setup. Trapping frequencies have then to be characterized with precision to compare the Gaussian and LG cases. Further efforts regarding correction of aberrations should be carried out in order to ensure the traps at the position of the atoms deviate as little as possible from their theoretical predictions. With this new experimental tools at hand, the next step is to apply them to loading atoms into the evanescent dipole traps of our nanofabricated photonic-crystal waveguides.

CONCLUSION

Summary

In this thesis, we have introduced numerous tools needed to build a versatile Waveguide QED platform coupling slow-mode photonic-crystal waveguides and cold atoms trapped close to their surface.

After motivating our work in the context of the exciting pathways opened by Waveguide QED, with an emphasis on the quantum optics and many-body physics applications, we introduced the theoretical basis of light-matter interaction close to nanostructures. The study of such interaction at resonance enabled us to define relevant figures of merit to quantify the coupling of atoms to a guided mode, such as the 1D Purcell factor. More importantly, it was then expressed for experimentally realistic multilevel atoms, in a practical, numerically computable way in terms of the 1D Green's function of the waveguide mode. This can help making more accurate predictions of what should be observed in experiments. We then introduced the light-matter interaction formalism out of resonance, for reviewing methods of dipole trapping around nanostructures, most of them based around the two-color evanescent dipole trap scheme. We subsequently presented `nanotrappy`, a Python package optimized for the simulation of optical dipole traps for multilevel atoms. Calculations carried out with `nanotrappy` allowed us to introduce a novel near-field trap around nanofibers based on vacuum forces and dressing of excited levels, allowing to trap atoms as close as 50 nm from the surface.

Chapter 4 provided an introduction to the field of photonic crystals and established the requirements photonic-crystals waveguides have to meet in order to be interfaced in a cold atom experiment. Precise designs of different waveguides were then presented in Chapter 5, with a strong emphasis on having a slow-mode at the Rubidium wavelength, having an two-color dipole trap scheme available and making them robust to fabrication imperfections. The half-W1 waveguide was optimized to get linear bands which offer a constant group index over a large bandwidth while the comb waveguide was designed to have a quartic dispersion at the band edge which allows to work at high group indices even for relatively large detunings from the band edge. Both strategies provide an increased robustness to fabrication imperfections. Even with such conservative constraints, the expected coupling of the trapped atoms to the guided mode is above 50% and even close to 90% for the comb waveguide. These predicted performances come close to state-of-the-art solid-state platforms.

The final two chapters provided a deep exploration of the experimental apparatus, detailing the design and construction of a versatile, two-chamber cold atom experiment tailored to integrate such waveguides. The experimental control was developed from Python-scipted open-source solutions and conceived to be fast, modular and user-friendly. Chapter 7 finally presented an additional experimental capability we want to develop, i.e. delivering atoms to the waveguide surface in a controlled way. This has been a challenging task in the community because of the perturbations introduced by the structures when approaching a focused beam. A recent proposal involving higher-order Laguerre-Gauss modes to reduce spurious reflections on the surfaces was studied in the context of our experiment and started being implemented.

Perspectives and outlooks

As the experiment is still in its development phase, several improvements are expected in order to make it a versatile Waveguide QED platform for cold atoms and photonic-crystal waveguides.

Single atom detection in a tweezer As important work has been carried out on the tweezer setup we hope very soon to detect a single atom trapped in our Gaussian tweezer. Precise characterization will then be needed to compare this trap with the one made with the higher-order Laguerre-Gaussian superposition. If successful, these tweezers with reduced reflections on surfaces could be a significant tool for efficiently delivering atoms to our waveguides, and for the community in general.

Interfacing of waveguides and transport First generation of optimized waveguides have been fabricated and are being characterized. They now have to be integrated in the science cell. One approach could be through the optical bonding of the substrate to glass holders with "liquid glass" (silicate bonding), which in turn would be bonded to the surface of the chamber, as demonstrated in [Luan et al. 2020]. In the meantime, transport to the science chamber has to be implemented thanks to an optical conveyor belt. Atoms might have to be cooled again or even retrapped in the science cell. As of now, the tweezer setup is made in the MOT chamber, it will eventually have to be moved to the science cell.

Single atom coupling to a waveguide With a nanophotonic chip immersed in a cold atomic cloud in the science cell, we expect to see some sign of the enhanced atom-light coupling close to a slow-mode photonic-crystal waveguide, with or without guided trap. From the efficient coupling of a single atom to the waveguide mode, which can lead to perfect reflection, our experiment may allow us to unlock the full potentialities of quantum non-linear optics protocols at the single photon level. These include implementing single-photon transistors [Chang et al. 2007], Fock state photon sorting [Yang et al. 2022] or deterministic generation of non-Gaussian states of light. This regime has been achieved in cavity-based experiments [Magro et al. 2023] and explored in quantum dots coupled to PCWs [Le Jeannic et al. 2022], but has yet to be demonstrated in Waveguide QED platforms with cold atoms.

From few- to many-body physics in the band gap The interest of atom-based platforms are their scalability, compared to their solid-state counterparts. In the longer run, one-by-one arrangement of 1D arrays trapped along the waveguide edge with Laguerre-Gaussian tweezers should allow our platform to provide a robust

interface between tens or hundreds of emitters and slow-mode waveguides. In the propagating regime, this setup can allow to witness collective dissipative dynamics like superradiance [Cardenas-Lopez et al. 2023] or engineer atomic spin squeezing [Qi et al. 2018].

With the fabrication process now refined, we can envision the design of PCWs to position atomic frequencies within the band gap. This shifting of the band gap could also be achieved via heating of the structure with an additional heating beam. This unique feature will distinguish our platform as a singular tool for probing atom-photon bound states or simulating exotic many-body states of matter emerging from nearest-neighbors-like Hamiltonians [Douglas et al. 2015] or spin models with topological long-range interactions [Bello et al. 2019], hard to treat classically.

Some further theoretical studies can also be carried out on the impact of the shape of the dispersion on the mediated spin-spin interaction and could unveil some new interesting physics, as it is usually assumed to be linear.

This thesis not only consolidates a robust framework for Waveguide QED but also ignites the spark for a continuum of research that could lead to groundbreaking advancements in quantum technologies.

APPENDIX A

CALCULATION OF CASIMIR-POLDER INTERACTIONS

Casimir-Polder (CP) interactions emerge from correlated fluctuations of the quantum vacuum between a polarizable particle (like an atom) and a surface. At very short distances this manifests as a strong attractive potential on the atoms, towards the surface. These interactions are usually very hard to compute as they depend on the exact response of the total structure over all frequencies (information contained in the scattering Green's tensor). Estimations of the CP potential is still possible by introducing drastic approximations on the geometries considered. We introduce in this appendix a more precise approximation that allows to deal with atoms close to dielectric slabs.

A.1 Casimir-Polder interactions close to a semi-infinite dielectric slab

Let us consider a semi-infinite dielectric structure, filling the full volume for $x < 0$. An atom for any given $x > 0$ into vacuum, at small enough x will feel a CP potential. This potential can be though of as the interaction between the atomic vacuum-induced fluctuating dipole with its own image by the surface. If the atom is close enough to the surface, we assume the interaction is instantaneous, and using classical electrodynamics, the CP potential takes the Lennard-Jones form [Lennard-Jones 1932]:

$$U_{\mathrm{CP}}^{\mathrm{plane}} = -\frac{C_3}{x^3} \tag{A.1}$$

where C_3 is a constant that depends on the atomic polarizability and dielectric permittivity of the material. At larger distances, we have to take into account retardation for the exchanged virtual photons. The interaction potential is modified to $U = -C_4/x^4$ as demonstrated in Casimir and Polder seminal paper [Casimir and Polder 1948].

The simple expression (A.1) is often used even for finite or non planar geometries (like nanofibers or microtoroids), as it gives an estimation of the value of the potential at close distances with the good order of magnitude, usually overestimated [Le Kien et al. 2004; Stern et al. 2011].

A.2 Computing the C_3 coefficient for ^{87}Rb close to GaInP

Even if we use Equation (A.1), it is necessary to compute the C_3 coefficient which depends both on the atom and the surface properties. [Derevianko et al. 1998; Johnson et al. 2004] gives the procedure to follow in the case of a perfectly conducting wall. For a Rubidium 87 atom in front of a perfectly conducting half-space, $C_3 = 3.53\,\text{au} = 2.28 \times 10^{-48}\text{J.m}^3$. For a dielectric wall, we expect this value to be smaller as the interaction with the dipole image must be reduced. In this case the formula for C_3 is adapted [Caride et al. 2005]:

$$C_3 \approx \frac{\hbar}{4\pi}\int_0^{+\infty} \alpha(i\xi)\frac{\epsilon(i\xi)-1}{\epsilon(i\xi)+1}d\xi \tag{A.2}$$

where α is the atomic scalar polarizability and ϵ the material dielectric function. Both functions are evaluated in this expression over the imaginary frequency axis.

A.2.1 Computing $\alpha(i\xi)$

We recall that in a varying electric field, an atom exhibits a Stark shift ΔE whose value is given by the polarizabilty tensor $\alpha_{\mu\nu}$:

$$\Delta E(F, m_F; \omega) = -Re(\alpha_{\mu\nu})E_\mu^{(-)}E_\nu^{(+)}. \tag{A.3}$$

$\alpha_{\mu\nu}$ can be decomposed into a scalar, vector and tensor part, as introduced thoroughly in Chapter 3. Taking into account only the scalar polarizability, ΔE reduces to $\Delta E = -\alpha^{(0)}(F;\omega)|E^{(+)}|^2$. The scalar polarizability $\alpha^{(0)}$ is written

$$\alpha^{(0)}(F;\omega) = \sum_{F'} \frac{2\omega_{FF'}\langle F||\mathbf{D}||F'\rangle^2}{3\hbar(\omega_{FF'}^2 - \omega^2)} \tag{A.4}$$

where $\langle F||\mathbf{D}||F'\rangle$ is the reduced matrix element from state $|F\rangle$ to $|F'\rangle$. In the Python code we used the reduced matrix elements (taken from ARC [Šibalić et al. 2017]) which verify $\langle F||\mathbf{D}||F'\rangle^2 = \langle F|\boldsymbol{d}|F'\rangle^2 g_F$ (where $g_F = 2F+1$ is the degeneracy of the ground state).

These matrix elements are given in ARC in units of $a_0 e$ where a_0 is the Bohr radius ($a_0 = 5.29 \times 10^{-11}$) and e the fundamental charge. To get α in atomic units, we still need to multiply everything by $1/4\pi\epsilon_0 a_0^3$ ($4\pi\epsilon_0 = 1$ in au). In our calculation of $\alpha^{(0)}$ we took into account the transitions $^5S_{1/2} \to {}^nP_{1/2}$ and $^5S_{1/2} \to {}^nP_{3/2}$ for n going from 5 to 20. Figure A.1(a) shows the obtained dependence of the scalar polarizability for Rubidium 87 with the wavelength. The sharp dispersive features are indicators of the presence of electronic transitions. The whole curve matches very well the one obtained in ARC via their `plotPolarizability` function.

To compute C_3 we can just put imaginary frequencies in our analytical expression, which yields:

$$\alpha^{(0)}(F;i\xi) = \sum_{F'} \frac{2\omega_{FF'}\langle F||\mathbf{D}||F'\rangle^2}{3\hbar(\omega_{FF'}^2 + \xi^2)} \tag{A.5}$$

The obtained scalar polarizability for Rubidium 87 over the imaginary axis has a very different shape from the one over the real axis, as shown in Figure A.1(b). We compare our results, with the calculations from [Derevianko et al. 2010] and find very good agreement.

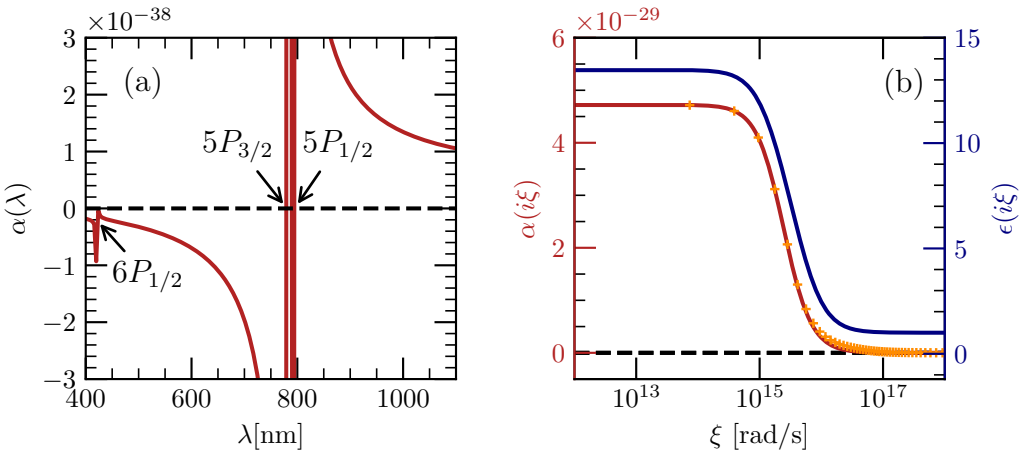

Figure A.1: Dispersive response functions for GaInP and Rubidium atoms. (a) Scalar polarizability of $5S_{1/2}$ ^{87}Rb. Arrows show the most important transitions from the ground state. (b) Scalar polarizability of $5S_{1/2}$ ^{87}Rb $\alpha(i\xi)$ and dielectric function of GaInP $\epsilon(i\xi)$ evaluated along the imaginary axis. Our calculations show good agreement with the data from [Derevianko et al. 2010], displayed as the orange crosses.

A.2.2 Computing $\epsilon(i\xi)$

Materials usually have a frequency-dependent response, leading to a total refractive index that varies with frequency. We usually write the complex refractive index as $n(\omega) = n'(\omega) + in''(\omega)$ where n' is the real refractive index and n'' the extinction coefficient. $n(\omega)$ can be evaluated through a range of real frequencies through experimental characterization. Data for GaInP in the $205 - 950$ nm range can be found in [Schubert et al. 1995].

The dielectric function can be deduced from the complex refractive index by squaring it: $\epsilon(\omega) = n^2(\omega) = \epsilon'(\omega) + i\epsilon''(\omega)$ where $\epsilon''(\omega) = 2n'(\omega)n''(\omega)$ and $\epsilon'(\omega) = n'(\omega)^2 - n''(\omega)^2$.

We now need to evaluate the dielectric function over the imaginary axis. As this function has no analytical form, we will use some results from complex analysis in order to get $\epsilon(i\xi)$. We first note that ϵ evaluated for imaginary frequencies is real. Indeed, by construction $\epsilon^*(\omega) = \epsilon(-\omega^*)$. For $\omega = i\xi$, $\epsilon^*(i\xi) = \epsilon(i\xi)$ hence $\epsilon(i\xi)$ must be real.

To get the expression of $\epsilon(i\xi)$, we use the modified Kramers-Kronig relations [Antezza et al. 2004] (which are applicable because ϵ is regular in the upper half plane). The common relations give, when integrating along the real axis ω,

$$\epsilon'(\omega) - 1 = \frac{1}{\pi} P \int_{-\infty}^{+\infty} \frac{\epsilon''(x)}{x - \omega} dx \tag{A.6}$$

where P is the Cauchy principal value of the integral. Using the fact that $\epsilon''(\omega)$ is odd, we can rewrite ϵ' as

$$\epsilon'(\omega) - 1 = \frac{1}{\pi} P \int_{0}^{+\infty} \frac{\epsilon''(x)}{x - \omega} dx + \frac{1}{\pi} P \int_{0}^{+\infty} \frac{\epsilon''(x)}{x + \omega} dx \tag{A.7}$$

$$= \frac{2}{\pi} P \int_{0}^{+\infty} \frac{x\epsilon''(x)}{x^2 - \omega^2} dx. \tag{A.8}$$

Taking $\omega = i\xi$ along the imaginary axis, the principal value is no longer critical, since there is no pole here (the integration over x is still on the real axis). Replacing ω by $i\xi$ we recover the equation from [Antezza et al. 2004]

$$\epsilon(i\xi) = 1 + \frac{2}{\pi}\int_0^{+\infty} \frac{x\epsilon''(\omega)}{x^2+\xi^2}dx \tag{A.9}$$

where x is still a real frequency over which the integration is performed. If n'' is close to 0 in a wide range of frequencies (for example for SiO2, SiN or GaInP), we can use the equivalent expression:

$$\epsilon(i\xi) = 1 + \frac{2}{\pi}\int_0^{+\infty} \frac{\omega[\epsilon'(\omega)-1]}{\omega^2+\xi^2}d\omega \tag{A.10}$$

The shape of the dielectric function evaluated along the imaginary axis for GaInP is shown in Fig. A.1(b) in blue. Its maximum at low frequencies is close to the square of the maximum refractive index of GaInP.

A.2.3 Numerical results

Now that we know the values of α and ϵ over the imaginary axis, we use Eq. (A.2) to compute the C_3 coefficient for a Rubidium atom close to a infinite dielectric. We first compare our results with values that already exist in literature. For a Rubidium atom close to a SiO2 plane, [Solano et al. 2019] give $C_3 = 4.94 \times 10^{-49}\,\mathrm{J\,m^3} = h \times 746\,\mathrm{Hz\,\mu m^3}$. Our calculation gives $C_3 = 4.85 \times 10^{-49}\,\mathrm{J\,m^3}$ when using the SiO2 values from [Philipp 1997], which is only a 2% difference.

To the best of our knowledge, there were no previous computations of the C_3 coefficient of the CP interactions between GaInP and Rubidium atoms. We obtain for this combination: $C_3 = 1.43\,\mathrm{au} = 9.25 \times 10^{-49}\mathrm{J\,m^3} = h \times 1.4 \times 10^3\,\mathrm{Hz\,\mu m^3}$ for an atom in the ground state $^5S_{1/2}$. We use this value in all the computations of traps around GaInP nanostructures (as it is the case throughout Chapter 5).

These values give an estimation of the C_3 coefficients and hence of the CP potential. One has to keep in mind the limitations of such an estimation:

- At the distances from the surface we are interested in $(100 - 300\,\mathrm{nm})$ we are in the transition regime from an interaction in C_3/z^3 to one in C_4/z^4 [Stern et al. 2011]. C_3 is not sufficient to describe the real shape of the CP potential, and will lead to an overestimation.
- At very low frequencies, the behaviour of the dielectric functions are usually not known as they become hard to measure. This can be a limitation in the accuracy of the computation of C_3 as $\alpha(i\xi)$ is important for low frequencies, making the value of $\epsilon(i\xi)$ crucial in the same range.
- Equation (A.2) is approximate and depends strongly on temperature.

The approximations introduced and the values of C_3 computed are usually enough to give an idea of the strength of the CP interaction at short range. But in some situations, the shape of the structure cannot be neglected anymore. We introduce in the following an approximate way of dealing with this situation.

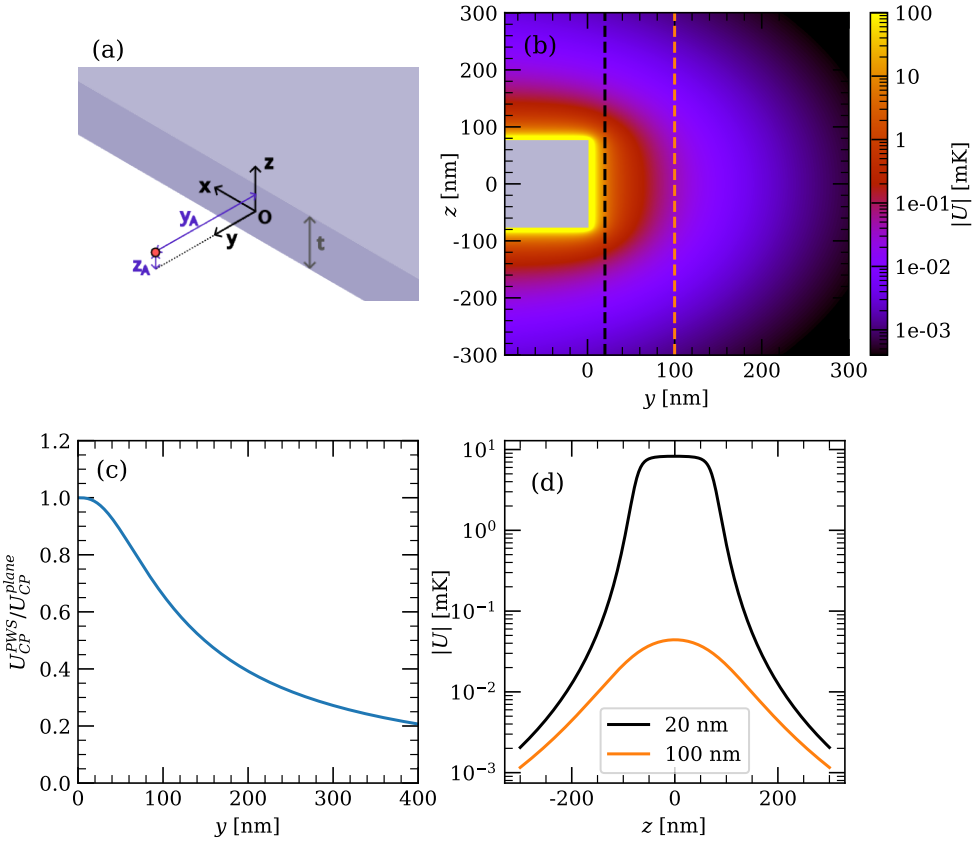

Figure A.2: Calculation of the Casimir-Polder interaction between the structure and the atom with PWS. (a) Coordinate system used with the simplified slab of thickness t (b) 2D log plot of the magnitude of the CP in the transverse plane of the crystal (c) Comparison between the PWS potential and the one for an semi-infinite dielectric plane at $z = 0$. As expected, they are comparable at small distances, as the solid angle under which the atom interacts with the surface becomes large. (d) Shape of the vertical dependence of the interactions at different distances from the surface. At close distances we have a plateau and fast decay on each side. At 100 nm the shape is very different with a slower decay.

A.3 Pair-wise summation approximation for a z-dependent potential

The optical traps around the PCW slabs proposed in Chapter 5 all have an important extension in the azimuthal directions. As discussed in the main text, this is due to the vertical decay of the guided evanescent fields which forbid to have a tight trapping in this direction, when using the same polarization. We cannot, in this regime, use the approximation that our atoms are in front of an infinite dielectric plane, as the atoms can travel over vertical distances on the order of the slab thickness. Assuming an infinite surface would create a fake barrier at $y = 0$ and $z > t/2$ whereas using the formula but limiting it to the range $-t/2 < z < t/2$ would create a discontinuity at these lines.

A formula based on scattering theory can be used for computing these CP interactions for these more complex geometries [Lambrecht et al. 2006]. While analytical

solutions have only been found for simple geometries [Antezza et al. 2004], it is possible to write it in terms of the scattering Green's tensor and use an electromagnetic solver to compute the latter [Rodriguez et al. 2009]. As this comes at the expense of very intensive computations, we turn to an approximated and simpler derivation of these interactions from first principles. We sum the van der Waals (vdW) interaction between the trapped atom and all the "atoms" (i.e. elements of volume with the material's polarizability) constituting the structure. This method, referred to as pairwise summation (PWS), assumes the vdW potentials to be additive, neglecting collective effects in the material. The magnitude of these collective effects can be significant, yet it has been shown that the results are within 30% of the exact calculation [Sparnaay 1959; Bitbol et al. 2013] which is sufficient for our purposes.

Hence, we write:

$$U_{\mathrm{CP}}^{\mathrm{PWS}} = \int_{\mathcal{V}} U_{\mathrm{vdW}} \tag{A.11}$$

where we will consider U_{vdW} as A/r^6, the approximation for short range interactions. A is a constant term that depends on the polarizabilities of the atoms involved in the integral [Bitbol et al. 2013]. The value of A is not critical here as it will be determined afterwards by comparing our result to the known one for an infinite plane. The integral spans the whole volume $\mathcal{V}$ of the structure. For simplicity we assume the waveguide to be a semi-infinite slab of thickness t (see Figure A.2(a)). This is reasonable as the structures considered correspond to this approximation for $\gtrsim$ 200 nm. This allows us to write $r = \sqrt{x^2 + (y' - y_a)^2 + (z' - z_a)^2}$, where (y_a,z_a) denote the position of the atom. x_a is irrelevant because the structure is infinite in this direction.

$$U_{\mathrm{CP}}^{\mathrm{PWS}} = A \int_0^{-\infty} dy \int_{-t/2}^{t/2} dz \int_{-\infty}^{+\infty} dx \frac{1}{(x^2 + (y - y_a)^2 + (z - z_a)^2)^3} \tag{A.12}$$

The integral can be calculated analytically and we obtain

$$\begin{aligned} U_{\mathrm{CP}}^{\mathrm{PWS}}(y_a, z_a) = -\frac{A\pi}{8} \Bigg[& \frac{2y_a^3 - \sqrt{1/(y_a^2 + (t - z_a)^2}(2y_a^4 + y_a^2(t - z_a)^2 + 2(t - z_a)^4}{3y^3(t - z_a)^3} \\ & + \frac{2y_a^3 - \sqrt{1/(y_a^2 + (t + z_a)^2}(2y_a^4 + y_a^2(t + z_a)^2 + 2(t + z_a)^4}{3y_a^3(t + z_a)^3} \Bigg] \end{aligned} \tag{A.13}$$

We note that when $t \to +\infty$, equation (A.13) reduces to $U_{\mathrm{CP}}^{\mathrm{PWS}} = \frac{A\pi}{6y_a^3}$, and we recover the usual dependence for an atom in front of a dielectric half-space. Comparing this to $U_{\mathrm{CP}}^{\mathrm{plane}}$ (A.2) we find $A = \frac{6C_3}{\pi}$. We take for C_3 the values computed in the previous subsection.

The obtained spatial dependence of the CP interactions is shown in Figure A.2(b). Figure A.2(c) shows that with this expression we depart significantly from the infinite plane formula after only 100 nm as the finite thickness of the slab cannot be neglected. Finally, Figure A.2(d) shows how the transverse shape of the potential changes with distance, an important feature for our trapping scheme, which is not encapsulated in $U_{\mathrm{CP}}^{\mathrm{plane}}$.

This more complex, and more realistic, shape of the CP potential allows to have a better understanding of the behavior of the atoms trapped in the vicinity of our proposed PCW and to avoid numerical divergences when simulating such traps.

APPENDIX B

SIMULATION METHOD FOR PHOTONIC CRYSTALS

Maxwell's equations are not approximations: they are exact for classical fields. However, only very few analytical solutions of these equations exist, either in free space (plane waves, Laguerre-Gaussian beams, Hermite-Gauss beams...) or in uniform waveguides. To obtain solutions in more complex media, one has to rely on numerical simulations. We introduce a few of them used throughout this manuscript.

B.1 Rigorous coupled-wave analysis (RCWA)

Rigorous coupled-wave analysis (RCWA) is a method usually employed for simulating gratings, for example for computing the energy going into every diffraction order. It consists in writing the field inside the grating as coupled propagating plane waves. The grating is discretized into layers in the propagation direction, and the electric and magnetic fields in each layer are expanded into a set of plane waves. The boundary conditions are then used to relate the fields in one layer to the fields in the next layer. The problem becomes an eigenvalue problem for a given frequency.

With a few tweaks, it can be applied to guided optics problems [Silberstein et al. 2001]. The idea is to replicate many times the waveguide of interest in space, creating an artificial periodicity in the transverse direction. The obtained periodic structure can then be treated as a grating. Because the waveguides should not be coupled, absorptive layers have to be inserted between them.

This approach is the one which has been developed in Institut d'Optique over the last years [Lecamp et al. 2007] and used in the comb waveguide proposal [Fayard et al. 2022].

B.2 Transfer matrix formalism

This approach is widely used to analyze the propagation of light through a stratified 1D medium. It applies to any 1D photonic crystal, as it can be used to model the scattering off any defect in a material (for example a hole or a pillar). We define the transmission matrix M of any layer as:

$$\begin{pmatrix} E_{\text{in}}^{+} \\ E_{\text{in}}^{-} \end{pmatrix} = M \cdot \begin{pmatrix} E_{\text{out}}^{+} \\ E_{\text{out}}^{-} \end{pmatrix} \tag{B.1}$$

Where the $\pm$ superscript denotes respectively forward and backward propagating fields. For a 1D Bragg mirror shown in the main text, that is constituted of homogeneous layers of dielectric material, the transfer matrix for a single layer is given by [Yeh 2005]:

$$M = \begin{pmatrix} \cos(n_j k d_j) & \frac{i}{n_j}\sin(n_j k d_j) \\ i n_j \sin(n_j k d_j) & \cos(n_j k d_j) \end{pmatrix} \tag{B.2}$$

where n_j is the refractive index and d_j the width of layer j.

We consider a 1D Bragg mirror which only has 2 kinds of layers with parameters (n_1, d_1) and (n_2, d_2). The total transfer matrix is given by multiplying for each layer

$$M_{\text{tot}} = \underbrace{M_2 M_1 ... M_2 M_1}_{\text{N layers}} \tag{B.3}$$

The reflection and transmission coefficients are obtained directly as

$$\begin{cases} r = \dfrac{M_{\text{tot}}^{11} + M_{\text{tot}}^{12} - M_{\text{tot}}^{21} - M_{\text{tot}}^{22}}{M_{\text{tot}}^{11} + M_{\text{tot}}^{12} + M_{\text{tot}}^{21} + M_{\text{tot}}^{22}} \\ t = \dfrac{2}{M_{\text{tot}}^{11} + M_{\text{tot}}^{12} + M_{\text{tot}}^{21} + M_{\text{tot}}^{22}} \end{cases} \tag{B.4}$$

The energy reflection coefficient $|r|^2$ in Figure 4.1(b) is computed with this method.

B.3 Eigenmode expansion methods for solving Maxwell's equations

As the eigenvalue equation defined in Chapter 4 (4.2) is linear, it is possible to solve for $\mathbf{H}$ by expanding it on a basis of orthonormal modes. This basis can be chosen to be the set of plane waves or a set of guided modes of a uniform slab.

B.3.1 Plane Wave Expansion method (PWE)

Plane wave expansion was introduced by Steven Johnson and John Joannopoulos in their seminal paper [Johnson and Joannopoulos 2001]. The idea is the following: as solutions of the eigenvalue equation (4.2) are Bloch modes, we can write the periodic Bloch envelope as a Fourier series, i.e. an infinite sum of plane waves. This gives:

$$\mathbf{H}_{n,\mathbf{k}}(\mathbf{r}) = \mathbf{u}_{n,\mathbf{k}}(\mathbf{r}) e^{i\mathbf{k}\cdot\mathbf{r}} = \sum_j \mathbf{c}_{n,\mathbf{k},j} e^{i(\mathbf{k}+\mathbf{g}_j)\cdot\mathbf{r}} \tag{B.5}$$

where the $\mathbf{g}_j$ are reciprocal lattice vectors (not restricted to the 1BZ).

A similar decomposition is done for the dielectric function and both expansions are plugged into Eq. (4.2). After some algebra and a Fourier transform, the problem of finding the coefficients of the Fourier series (B.5) reduces to a matrix diagonalization problem. As the Fourier series has an infinite number of coefficients $\mathbf{c}_{n,\mathbf{k},j}$, the 2D matrix to diagonalize has also infinite dimensions. In order to perform the diagonalization, we have to set a maximum number of harmonics N_{harm} to be considered in the expansion. This is equivalent to setting a maximum length of the reciprocal lattice vectors included.

The eigenvalues converge pretty fast with the number of harmonics considered. But if we try to reconstruct the field from this truncated decomposition, this is

not so much the case. Indeed, truncating the Fourier series gives rise to the Gibbs phenomenon, as we are dropping long reciprocal lattice vectors (i.e. short range features in real space). This phenomenon can be very detrimental in case of strong index contrast. This method is hence not suited for computing the fields at the edge of waveguides (at the edge of the comb or Half-W1 waveguides or on top of a W1).

Because of the decomposition in Fourier series PWE assumes Bloch periodic conditions in all dimensions. It cannot be employed for a 2D PC slab which has no periodicity on the z direction. This complexity can be approximated by replacing the refractive index of the material by an effective refractive index seen by the fundamental mode propagating in the slab. This allows to have frequencies closer to the real values.

B.3.2 Guided Mode Expansion method (GME)

Guided mode expansion is an attempt at a more accurate PWE, by taking into account the finite width of photonic-crystal slabs. It is reasonable to describe photonic modes in these systems starting from slab waveguide modes and introducing the effect of a dielectric modulation in the core and cladding layers [Andreani and Gerace 2006]. This is the central idea of the guided-mode expansion method, in which PCW modes are expanded in the basis of guided modes of an effective homogeneous waveguide. This approach is suited as guided modes of a uniform slab can be written as a basis of orthonormal modes[1] The solutions of Eq. (B.5) can be written as

$$\mathbf{H}_{\mathbf{k}}(\mathbf{r}) = \sum_{j,\alpha} \mathbf{c}_{\alpha,\mathbf{k},j} \mathbf{H}^{\text{guided}}_{\text{k+g}_j,\alpha} \tag{B.6}$$

where the $\mathbf{H}^{\text{guided}}_{\text{k+g}_j,\alpha}$ are guided modes for a uniform slab of same thickness and with a constant dielectric function $\bar{\epsilon} = \frac{1}{\mathcal{V}_{\text{layer}}} \int_{\mathcal{V}_{\text{layer}}} \epsilon(\mathbf{r}) d\mathbf{r}$, defined as the averaged ϵ over the whole photonic crystal layer. The α subscript denotes both the order of the mode and its polarization (TE-like or TM-like). These modes have an analytical expression involving simple trigonometric functions inside the slab and exponential decay outside of it. As for the PWE method, the dielectric constant is written as a Fourier series.

The GME method is fundamentally approximate, as the leaky modes of the effective slab are not included on the expansion. The basis over which the decomposition is made is hence not complete. Leaky modes can however be used to compute the loss of a given mode into the upper and lower claddings. Another limitation, shared with PWE, is the impossibility to handle dispersive materials. Indeed, we solve an eigenvalue equation where the eigenvalue is $\propto \omega$, the frequency of the mode. It is hence not possible to include a dependence in ω in the left hand side of Eq. (4.2) and keep the same method.

PWE and GME simulations carried out in Chapter 4 and 5 use the open-source *legume* package [Minkov et al. 2020]. In this software, we have to set a maximum reciprocal lattice wave-vector length in units of $2\pi/a$ referred to as *gmax* (for a PCW, $N_{\text{harm}} = 2gmax + 1$ as we only consider propagation in 1D). As for PWE, GME simulations assume periodicity in 2 directions. This can add spurious modes, especially for asymmetric waveguides. A way of getting rid of them (at the cost of a bigger simulation domain) is to symmetrize the structures as can be seen in Figure B.1(a).

[1] Modes of a waveguide satisfy the orthogonality relation $\int_{\mathcal{V}} \mathbf{H}_i^*(\mathbf{r}) \mathbf{H}_j(\mathbf{r}) = \delta_{ij}$ [Snyder and Love 2012].

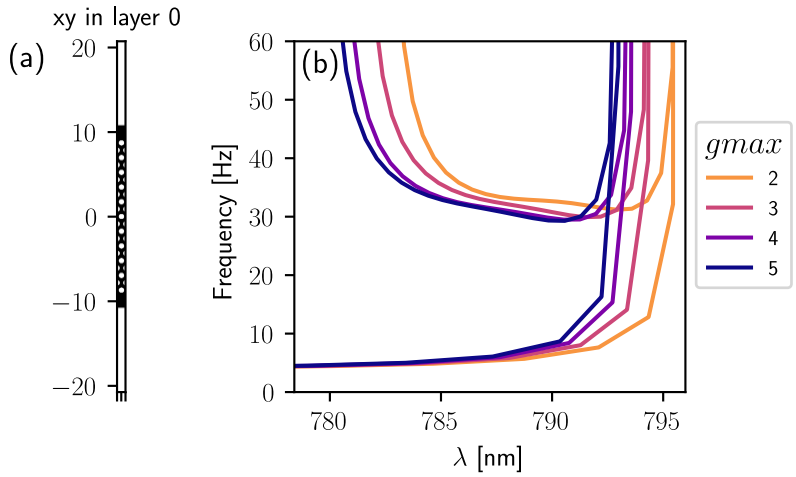

Figure B.1: GME simulation zone and convergence. (a) Actual simulation domain in *legume* showing the symmetrization. Two waveguides are actually simulated at $y = 10$ and $y = -10$ (in units of a). Boundary conditions in the 2 directions. (b) While the value of n_g does not change much with increasing $gmax$, there is a substantial shift in wavelength above $gmax = 2$, which is the value used for optimization.

B.3.3 Convergence of expansion methods

Truncating the Fourier decomposition to a relatively small number of harmonics N_{harm} can still give an accurate result. Indeed, Figure B.1 shows the convergence of the GME algorithm with $gmax$. The plot shows the group index of the slow-mode of the optimized Half-W1 waveguide from Section 5.2 for different values of $gmax$.

If $gmax = 4$ has already very well converged, the time needed for the computation is drastically increased from the $gmax = 2$ case, as seen in Table B.1. We also notice that the main error between these two settings is a shift in frequency, the shape of the curve and the group index value being very close. For this reason, the systematic optimizations of the waveguides are made with $gmax = 2$, as going from GME to FDTD already comes with a shift in frequency.

gmax	2	3	4	5	6
PWE	0.09	0.89	5.24	20.41	52.1
GME	0.84	4.0	13.8	38.8	92.3

Table B.1: Simulation time (in seconds) for each point. Average over a 40 point band structure for different values of the maximum harmonics considered in the PWE and GME methods

B.3.4 Simulation parameters

The simulation parameters used for most of the Half-W1 simulations are displayed in Table B.2.

Parameters	Half-W1
Dielectric constant	11.2 for GME, 7.88 for PWE
Number of rows	10 (for each)
Simulation size	$a \times 40a$
Boundary conditions	Bloch × Bloch
gmax	2 for optimization, 4 for plotting

Table B.2: GME Simulation parameters.

B.4 Finite Difference Time Domain

B.4.1 The FDTD method

Finite Difference Time Domain (FDTD) simulations are based on the direct resolution of Maxwell's equations in time domain and allows to get the full evolution of **E** and **H** in time and space. The equations are solved on a discrete grid in both space and time. Derivative are approximated by taking the difference between neighbouring sites on the grid. The mesh is necessarily rectangular. The **E** and **H** components are staggered in space, and **E** and **H** are never computed at the same point in time.

$$\mathbf{E}(x,t) \rightarrow \mathbf{E}\left(\left(i+\frac{1}{2}\right)\Delta x, \left(n+\frac{1}{2}\right)\Delta t\right) = \mathbf{E}_{i+\frac{1}{2}}^{n+\frac{1}{2}} \tag{B.7}$$

$$\mathbf{H}(x,t) \rightarrow \mathbf{H}\left(i\Delta x, n\Delta t\right) = \mathbf{H}_{i}^{n} \tag{B.8}$$

Discretizations work as follows

$$\frac{\partial \mathbf{E}^n}{\partial t} = \frac{\mathbf{E}^{n+\frac{1}{2}} - \mathbf{E}^{n-\frac{1}{2}}}{\Delta t} + O(t^2) \tag{B.9}$$

And the same applies for the space derivatives, and **H**. This method is very general (no assumption on the medium nor sources), versatile and accurate (second order error), but computationally very intensive. This is especially true when going 3D. Other advantages of FDTD include the fact that it is possible to have a broadband response in a single simulation and that it is possible to include dispersive materials.

FDTD simulations throughout this thesis have been realized with the Ansys Lumerical software. Note that other softwares have been tested during this thesis, including BandSolve (from RSoft) and the open-source Meep (from MIT).

The following provides a more in-depth introduction to the FDTD software, emphasizing the main points to keep in mind when simulating PCWs in dispersive materials.

In FDTD simulations, band diagrams are obtained by randomly distributing a given number of dipoles inside the structure that will excite it over a range of discretized frequencies. Monitors are placed in the same area to record the response. A strong response at a given frequency denotes the presence of a band. Field monitors can be added to record the spatial profile of the field. A specificity of this method is that it gives a 2D response map where the bands have to be retrieved through some post-processing.

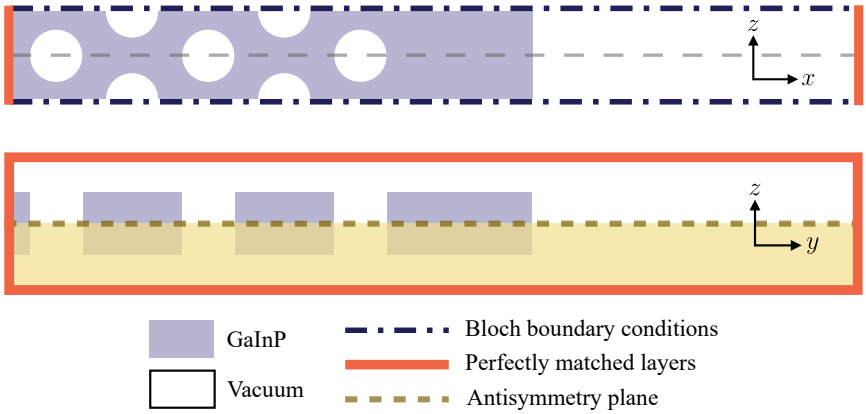

Figure B.2: 3D FDTD simulation cell for a Half-W1 waveguide (a) xy plane (b) yz plane.

B.4.2 Boundary conditions

As FDTD calculations can be very time consuming, we restrict as much as possible the simulation domain.

Bloch boundary conditions

We first restrict the simulation to one unit cell of the waveguide. In order to mimic an infinite length waveguide, we have to implement Bloch boundary conditions on the x boundaries. They impose:

$$E(x=0) = E(x=a)\mathrm{e}^{i\Delta\varphi} \tag{B.10}$$

Specifying the value of $\Delta\varphi$ allows choosing the component along x of the $\mathbf{k}$ we simulate[2]. By performing a sweep over $\Delta\phi$ we can construct the bandstructure of the waveguide for k_x ranging from 0 to $\pi/2$.

Symmetry conditions for different polarizations

Another way of reducing the simulation domain is to exploit the symmetries of the modes sought. In most of the manuscript we look for TE-like modes (symmetry of the electric field by the xy plane, see Fig. 4.5(a)). We can impose this condition on the FDTD solver, *de facto* reducing the simulating region by a factor of 2 (see Fig. B.2) as it will only simulate the half space $z > 0$. As the dipoles exciting the modes are magnetic dipoles, this corresponds to imposing an antisymmetric boundary condition in the FDTD solver on the xy plane.

Perfectly matched layers

For the 3 remaining boundaries, we use perfectly matched layers (PML). They are artificial absorbing layers that allow the field to disappear without having to extend the simulation cell to infinity. They allow to truncate the simulation zone, while mimicking an open system.

As incident $\mathbf{k}$ vectors with very small angles may cause divergence, we use stabilized PML which avoid these issues at the cost of added computational complexity.

[2] In this sense they are most general than the periodic boundary conditions that are realized only for $\Delta\varphi = 0$, i.e. they only compute modes for $k_x = 0$.

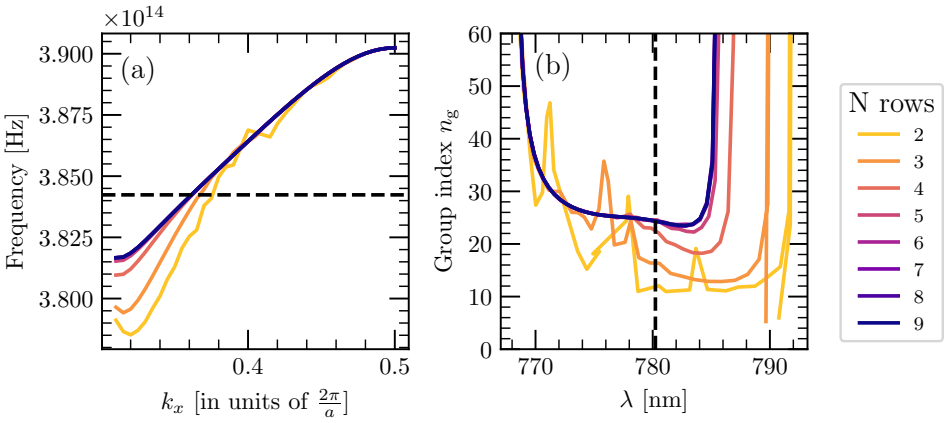

Figure B.3: Dependence of the slow mode with the number of rows in 3D FDTD simulation for a Half-W1 waveguide (a) Dispersion diagram (b) Group index variation n_g with the wavelength.

Moreover, one has to be careful that no sharp interfaces cross the PMLs as this can easily lead to divergence in the simulation.

B.4.3 How many rows are enough?

A final way to reduce the complexity of the simulation, is to limit the transverse size of the actual waveguide. Indeed, as seen in Figure 4.1, the photonic band gap appears after only a few layers. We can look here after how many rows of holes in the Half-W1, the dispersion curve of the slow mode is not affected anymore by the addition of new rows.

Figure B.3 show 3D FDTD simulations of the slow band dispersion and group index for waveguides with different number of rows of holes (the simulation width is kept constant). It shows that after 6 rows, the light dispersion is basically not affected by new rows. We choose to settle on 7 rows in both simulation and fabrication.

This is important for limiting the complexity of the meshing with can improve speed in the simulation. Moreover, as explained in Chapter 5, for the fabrication masks have to be generated before the e-beam lithography and because a lot of details have to be drawn over long distances and many waveguides, these can take a substantial amount of computation time. Making them simpler limits the RAM bottleneck of this step.

B.4.4 Simulation parameters

Table B.3 summarizes the most relevant parameters for the 3D FDTD simulations in Lumerical.

Parameters	Half-W1
Number of rows	7
FDTD simulation size	$a \times 2t \times N_{\text{rows}}\sqrt{\frac{3}{2}}a$
Boundary conditions	Bloch × PML × PML
PML profiles	stabilized
Mesh step size	6 nm × 3 nm × 3 nm
Simulation time	3 ps
Sources	Magnetic dipoles
Size of region with dipoles	$a \times 100$ nm × 20 nm
Number of dipoles	10
Number of monitors	10

Table B.3: 3D FDTD Simulation parameters in Lumerical.

APPENDIX C

EXPERIMENT SOFTWARE DETAILS

C.1 `Labscript` experiment logic

Example of the `labscript` experiment logic file for our absorption imaging sequence. We first have to import all the relevant drivers, define the devices and their connections to *jane* and then write the sequence in the main function.

```
#Import of all the relevant labscript devices
from labscript import *
from labscript_devices.DummyIntermediateDevice import DummyIntermediateDevice
from labscript_devices.Jane import Jane
from labscript_devices.SLMframe import SLMframe
from labscript_devices.ILS780.labscript_devices import ILS780
from labscript_devices.DummyPseudoclock.labscript_devices import DummyPseudoclock
from labscript_devices.PylonCamera.labscript_devices import PylonCamera
from labscript_devices.MOGLabsQRF_noTable import MOGLabsQRF_noTable
from labscript_devices.MOGLabsQRF import MOGLabsQRF

'''Definition of the experiment connection table'''

#Definition of the output lines from "jane"
Jane(name='jane_0', board_number=0, time_based_stop_workaround = True,
    ↪time_based_stop_workaround_extra_time=0.5)
Trigger('ILS780_trigger', parent_device = jane_0.direct_outputs, connection = 'flag 1')
Trigger('camera_trigger', parent_device = jane_0.direct_outputs, connection = 'flag 2')
Trigger('camera2_trigger', parent_device = jane_0.direct_outputs, connection = 'flag 12')
DigitalOut('B_switch', parent_device = jane_0.direct_outputs, connection = 'flag 3')
ClockLine(name='jane_0_clockline_2', pseudoclock=jane_0.pseudoclock, connection='flag
    ↪4')
ClockLine(name='jane_0_clockline_3', pseudoclock=jane_0.pseudoclock, connection='flag
    ↪5')
ClockLine(name='jane_0_clockline', pseudoclock=jane_0.pseudoclock, connection='flag 9')
DigitalOut('MOT_shutter', parent_device = jane_0.direct_outputs, connection = 'flag 10')
DigitalOut('imaging_shutter', parent_device = jane_0.direct_outputs, connection = 'flag
    ↪11')
DigitalOut('DDS1_out', parent_device = jane_0.direct_outputs, connection = 'flag 13')
DigitalOut('DDS2_out', parent_device = jane_0.direct_outputs, connection = 'flag 14')

#jane triggers what it thinks is an independent pseudoclock that is supposed to create a
    ↪pseudoclocking signal for the laser.
#Instead, the trigger goes to the laser, and the dummy_clock does not generate any signal.
DummyPseudoclock(name='dummy_clock', trigger_device=ILS780_trigger,
    ↪trigger_connection ="trigger")
```

```
ILS780(name = "ILS780_193", parent_device=ILS780_trigger, pseudoclock =
    ↪dummy_clock.clockline, BLACS_connection = '10.80.2.101:222')

#Cooler path, can change detuning with phase lock
AnalogOut(name = "cool_detuning", parent_device=ILS780_193, connection =
    ↪'cool_detuning', default_value = -10000000 )
AnalogOut(name = "gen_detuning", parent_device=ILS780_193, connection =
    ↪'gen_detuning', default_value = 80000000)

#3 parameters to set EOM in cooling path
DigitalOut(name ='cool_EOM_switch', parent_device=ILS780_193,
    ↪connection='cool_EOM_switch', default_value = True)
AnalogOut(name = 'cool_EOM_power', parent_device=ILS780_193, connection =
    ↪'cool_EOM_power' , default_value = 0.26)
AnalogOut(name = 'cool_EOM_freq', parent_device=ILS780_193, connection =
    ↪'cool_EOM_freq', default_value= 6568000000)

#2 parameters to turn on cooling_AOM path and regulate its power
DigitalOut(name ='cool_AOM_switch', parent_device=ILS780_193,
    ↪connection='cool_AOM_switch', default_value = True)
AnalogOut(name = 'cool_AOM_power', parent_device=ILS780_193, connection =
    ↪'cool_AOM_power', default_value = 5 )

#Signal sent by the laser for troubleshooting
DigitalOut(name = "ext_trigger_0", parent_device=ILS780_193,
    ↪connection='ext_trigger_0')

#Configuration of DDS for switching the absorption laser and the tweezer
MOGLabsQRF_noTable(name="QRF421",
   parent_device=jane_0_clockline,
   addr = '10.80.2.103')
DDS(name="dds1",parent_device=QRF421,connection="channel 0", default_freq = 80,
    ↪default_amp = 30)
DDS(name="dds2",parent_device=QRF421,connection="channel 1", default_freq = 110,
    ↪default_amp = 33)

# 24147755 Setting up absorption camera
#Attributes are defined for the sequence mode of blacs, manual_mode_camera_attributes
    ↪are for its continuous mode. Exposure time in microseconds.
#Binning used and pixel encoding downgraded in continuous mode to increase frame rate
PylonCamera('cam1',camera_trigger,'trigger',24147755,
          minimum_recovery_time = 27e-3,
          camera_attributes={
              "PixelFormat" : 'Mono12p', 'GainAuto':'Off', 'AcquisitionMode' : 'Continuous',
    ↪'TriggerSelector' : 'FrameStart', 'TriggerMode':'On', 'TriggerSource':'Line1',
    ↪'TriggerActivation':'RisingEdge', 'TriggerDelay': 0, 'ExposureMode':'Timed',
    ↪'ExposureTime': 100, 'ExposureAuto':'Off', 'BinningHorizontal' : 1, 'BinningVertical'
    ↪: 1},
          manual_mode_camera_attributes={
              'PixelFormat' : 'Mono8', 'AcquisitionMode' : 'Continuous', 'TriggerMode':'Off',
    ↪'ExposureMode':'Timed', 'ExposureTime': 100, 'BinningHorizontal' : 4,
    ↪'BinningVertical' : 4}
          )

''' Experiment logic starts here'''
#Before the start of the experiment sequence, the cooling laser is on by default
if __name__ == '__main__':
```

```
    start()
    t = 100e-6
    #Switch on the magnetic field and hold for the MOT loading time
    B_switch.go_high(t)
    t += MOT_loading

    if molasses :
    # if molasses phase on, detune the cooling and shut it off with exponential ramp
        B_switch.go_low(t)
        cool_detuning.ramp(t=t-laser_delay, duration=t_molasses,initial=cooling_detuning,
                final= det_post_molasses, samplerate = 5000)
        cool_AOM_power.exp_ramp(t=t-laser_delay, duration=t_molasses,initial =
      ↪AOM_power,
                final = AOM_power_post_molasses, samplerate = 50)
        ext_trigger_0.go_low(t-laser_delay)
        t += t_molasses + t_hold
        cool_AOM_switch.go_low(t-laser_delay)
    else :
        cool_AOM_switch.go_low(t-laser_delay)
        ext_trigger_0.go_low(t-laser_delay)
        B_switch.go_low(t)
        cool_detuning.ramp(t=t, duration=0.5e-3, initial=cooling_detuning,
                final=-100000000, samplerate= 10)

    t+= t_flight

    '''Take absorption image after waiting t_flight'''
    DDS1_out.go_high(t) #turns on absorption beam
    cam1.expose(t-cam_delay, 'absorption', trigger_duration = 1e-3)
    t += pulse_dur
    DDS1_out.go_low(t)

    t+= 50e-3
    '''Take reference image'''
    imaging_shutter.go_low(t)
    DDS1_out.go_high(t)
    cam1.expose(t-cam_delay, 'reference', trigger_duration = 1e-3)
    t += pulse_dur
    DDS1_out.go_low(t)

    t+= 50e-3
    '''Take dark image'''
    imaging_shutter.go_low(t)
    cam1.expose(t-cam_delay, 'dark', trigger_duration = 1e-3)
    stop(t+50e-3) #end of sequence
```

C.2 The `TriggerSequencer` class

Adapted from the TriggerableDevice class from `labscript`

```
class TriggerSequencer(Device):
    trigger_edge_type = 'rising'
    minimum_recovery_time = 0

    @set_passed_properties(property_names = {})
    def __init__(self, name, parent_device, pseudoclock, **kwargs):
        if isinstance(parent_device, Trigger):
```

```
8           if self.trigger_edge_type != parent_device.trigger_edge_type:
9               raise LabscriptError(
10              'Trigger edge type for %s is \'%s\',' %(name, self.trigger_edge_type)+
11              'but existing Trigger object %s ' % parent_device.name +
12              'has edge type \'%s\'' % parent_device.trigger_edge_type)
13          self.trigger_device = parent_device
14      elif parent_device is not None:
15          # Instantiate a trigger object to be our parent:
16          self.trigger_device = Trigger(name + '_trigger',
17          parent_device, self.trigger_edge_type)
18          parent_device = self.trigger_device
19
20      self._TriggerableDevice__triggers = []
21      self.initial_trigger_time = 0
22      Device.__init__(self, name, pseudoclock, 'internal', **kwargs)
23      self.connection = "trigger"
24      self.trigger_device.add_device(self)
25
26  def set_initial_trigger_time(self, t):
27      t = round(t,10)
28      self.initial_trigger_time = t
29
30  def trigger(self, t, duration):
31      """Request parent trigger device to produce a trigger
32      at time t with given duration.
33      Only ask for a trigger if one has not already been requested
34      by another device attached to the same trigger:"""
35      if type(t) in [str, bytes] and t == 'initial':
36          t = self.initial_trigger_time
37      t = round(t,10)
38      already_requested = False
39      for other_device in self.trigger_device.child_devices:
40          print("sweeping other devices", other_device)
41          if other_device is not self:
42              for other_t, other_duration
43                  in other_device._TriggerableDevice__triggers:
44                  if t == other_t and duration == other_duration:
45                      already_requested = True
46      if not already_requested:
47          print("trigger sent !")
48          self.trigger_device.trigger(t, duration)
49      # Check for triggers too close together (check for overlapping
50      # triggers already performed in Trigger.trigger()):
51      start = t
52      end = t + duration
53      for other_t, other_duration in self._TriggerableDevice__triggers:
54          other_start = other_t
55          other_end = other_t + other_duration
56          if (
57              abs(other_start - end) < self.minimum_recovery_time
58              or abs(other_end - start) < self.minimum_recovery_time
59          ):
60              msg = """%s %s has two triggers closer together than
61              the minimum recovery time: one at t = %fs for %fs, and another
62              at t = %fs for %fs. The minimum recovery time is %fs."""
63              msg = msg % (
64                  self.description, self.name, t,
```

```
65                  duration, start, duration, self.minimum_recovery_time,
66              )
67              raise ValueError(dedent(msg))
68
69      self._TriggerableDevice___triggers.append([t, duration])
70
71  def do_checks(self):
72      for device in self.trigger_device.child_devices:
73          if device is not self:
74              for trigger in self._TriggerableDevice___triggers:
75                  if trigger not in device._TriggerableDevice___triggers:
76                      start, duration = trigger
77                      raise LabscriptError(
78                      'TriggerableDevices %s and %s share a trigger.'
79                      %(self.name, device.name) +
80                      '%s has a trigger at %fs for %fs,'
81                      %(self.name, start, duration) +
82                      'but there is no matching trigger for %s.'
83                      %device.name +
84                      'Devices sharing a trigger must have identical
85                      trigger times and durations.')
86
87  def generate_code(self, hdf5_file):
88  #Checks if triggers are well defined and transforms the sequence into
89  #code understandable by the device
90      self.do_checks()
91      Device.generate_code(self, hdf5_file)
```

BIBLIOGRAPHY

Albrecht, B., Meng, Y., Clausen, C., Dareau, A., Schneeweiss, P., and Rauschenbeutel, A. (2016). "Fictitious magnetic-field gradients in optical microtraps as an experimental tool for interrogating and manipulating cold atoms". *Phys. Rev. A* **94**, p. 061401 (cit. on pp. 33, 36).

Almeida, V. R., Panepucci, R. R., and Lipson, M. (2003). "Nanotaper for compact mode conversion". *Opt. Lett.* **28**, pp. 1302–1304. doi: 10.1364/OL.28.001302 (cit. on p. 73).

Alton, D. J., Stern, N. P., Aoki, T., Lee, H., Ostby, E., Vahala, K. J., and Kimble, H. J. (2011). "Strong interactions of single atoms and photons near a dielectric boundary". *Nat. Phys.* **7**, pp. 159–165. doi: 10.1038/nphys1837 (cit. on p. 46).

Alton, D. J. (2013). "Interacting single atoms with nanophotonics for chip-integrated quantum networks". PhD thesis. California Institute of Technology (cit. on pp. 39, 46, 47).

Anderson, M. H., Ensher, J. R., Matthews, M. R., Wieman, C. E., and Cornell, E. A. (1995). "Observation of Bose-Einstein Condensation in a Dilute Atomic Vapor". *Science* **269**, pp. 198–201. doi: 10.1126/science.269.5221.198 (cit. on pp. 28, 109).

Andreani, L. C. and Gerace, D. (2006). "Photonic-crystal slabs with a triangular lattice of triangular holes investigated using a guided-mode expansion method". *Phys. Rev. B* **73**, p. 235114. doi: 10.1103/PhysRevB.73.235114 (cit. on pp. 65, 81, 156).

Antezza, M., Pitaevskii, L. P., and Stringari, S. (2004). "Effect of the Casimir-Polder force on the collective oscillations of a trapped Bose-Einstein condensate". *Phys. Rev. A* **70**, p. 053619. doi: 10.1103/PhysRevA.70.053619 (cit. on pp. 150, 151, 153).

Antoni-Micollier, L. et al. (2022). "Detecting Volcano-Related Underground Mass Changes With a Quantum Gravimeter". *Geophys. Res. Lett.* **49**, e2022GL097814. doi: https://doi.org/10.1029/2022GL097814 (cit. on p. 109).

Aoki, T., Dayan, B., Wilcut, E., Bowen, W. P., Parkins, A. S., Kippenberg, T. J., Vahala, K. J., and Kimble, H. J. (2006a). "Observation of strong coupling between one atom and a monolithic microresonator". *Nature* **443**, pp. 671–674. doi: 10.1038/nature05147 (cit. on p. 9).

— (2006b). "Observation of strong coupling between one atom and a monolithic microresonator". *Nature* **443**, pp. 671–674 (cit. on p. 46).

Arcari, M. et al. (2014). "Near-Unity Coupling Efficiency of a Quantum Emitter to a Photonic Crystal Waveguide". *Phys. Rev. Lett.* **113**, p. 093603. DOI: 10.1103/PhysRevLett.113.093603 (cit. on pp. 14, 18, 58, 64).

Arlt, J., Dholakia, K., Allen, L., and Padgett, M. J. (1998). "The production of multiringed Laguerre–Gaussian modes by computer-generated holograms". *J. Mod. Opt.* **45**, pp. 1231–1237. DOI: 10.1080/09500349808230913 (cit. on p. 140).

Arrizón, V., Ruiz, U., Carrada, R., and González, L. A. (2007). "Pixelated phase computer holograms for the accurate encoding of scalar complex fields". *J. Opt. Soc. Am. A* **24**, p. 3500. DOI: 10.1364/josaa.24.003500 (cit. on pp. 140, 141, 142).

Artoni, M., La Rocca, G., and Bassani, F. (2005). "Resonantly absorbing one-dimensional photonic crystals". *Phys. Rev. E* **72**, p. 046604. DOI: 10.1103/PhysRevE.72.046604 (cit. on p. 12).

Asano, T., Song, B.-S., and Noda, S. (2006). "Analysis of the experimental Q factors ~1 million) of photonic crystal nanocavities". *Opt. Express* **14**, p. 1996. DOI: 10.1364/oe.14.001996 (cit. on p. 67).

Asenjo-Garcia, A., Moreno-Cardoner, M., Albrecht, A., Kimble, H. J., and Chang, D. E. (2017a). "Exponential improvement in photon storage fidelities using subradiance & "selective radiance" in atomic arrays". *Phys. Rev. X* **7**, p. 031024. DOI: 10.1103/PhysRevX.7.031024 (cit. on p. 18).

Asenjo-Garcia, A., Hood, J. D., Chang, D. E., and Kimble, H. J. (2017b). "Atom-light interactions in quasi-one-dimensional nanostructures: A Green's function perspective". *Phys. Rev. A* **95**, p. 033818. DOI: 10.1103/PhysRevA.95.033818 (cit. on p. 12).

Ashkin, A. (1970). "Acceleration and Trapping of Particles by Radiation Pressure". *Phys. Rev. Lett.* **24**, pp. 156–159. DOI: 10.1103/PhysRevLett.24.156 (cit. on p. 124).

Aspelmeyer, M., Kippenberg, T. J., and Marquardt, F. (2014). "Cavity optomechanics". *Rev. Mod. Phys.* **86**, pp. 1391–1452. DOI: 10.1103/RevModPhys.86.1391 (cit. on pp. 9, 124).

Bajcsy, M., Hofferberth, S., Peyronel, T., Balic, V., Liang, Q., Zibrov, A. S., Vuletic, V., and Lukin, M. D. (2011). "Laser-cooled atoms inside a hollow-core photonic-crystal fiber". *Phys. Rev. A* **83**, p. 063830. DOI: 10.1103/PhysRevA.83.063830 (cit. on p. 10).

Balykin, V. I., Hakuta, K., Le Kien, F., Liang, J. Q., and Morinaga, M. (2004). "Atom trapping and guiding with a subwavelength-diameter optical fiber". *Phys. Rev. A* **70**, pp. 2–5. DOI: 10.1103/PhysRevA.70.011401 (cit. on pp. 10, 38).

Barredo, D., Léséleuc, S. de, Lienhard, V., Lahaye, T., and Browaeys, A. (2016). "An atom-by-atom assembler of defect-free arbitrary two-dimensional atomic arrays". *Science* **354**, pp. 1021–1023. DOI: 10.1126/science.aah3778 (cit. on p. 137).

Béguin, J. B., Laurat, J., Luan, X., Burgers, A. P., Qin, Z., and Kimble, H. J. (2020a). "Reduced volume and reflection for bright optical tweezers with radial Laguerre – Gauss beams". *Proc. Natl. Acad. Sci. U.S.A* **117**, pp. 26109–26117. DOI: 10.1073/pnas.2014017117 (cit. on pp. 124, 125, 126, 129, 144).

Béguin, J.-B., Qin, Z., Luan, X., and Kimble, H. J. (2020b). "Coupling of light and mechanics in a photonic crystal waveguide". *Proc. Natl. Acad. Sci. U.S.A* **117**, pp. 29422–29430. DOI: 10.1073/pnas.2014851117 (cit. on p. 79).

Bello, M., Platero, G., Cirac, J. I., and González-Tudela, A. (2019). "Unconventional quantum optics in topological waveguide QED". *Sci. Adv.* **5**, eaaw0297. doi: 10.1126/sciadv.aaw0297 (cit. on pp. 13, 147).

Bellouvet, M. (2018). "Condensation de Bose-Einstein et simulation d'une méthode de piégeage d'atomes froids dans des potentiels sublongueur d'onde en champ proche d'une surface nanostructurée". PhD thesis. Université de Bordeaux (cit. on p. 47).

Bellouvet, M., Busquet, C., Zhang, J., Lalanne, P., Bouyer, P., and Bernon, S. (2018). "Doubly dressed states for near-field trapping and subwavelength lattice structuring". *Phys. Rev. A* **98**, p. 023429. doi: 10.1103/PhysRevA.98.023429 (cit. on pp. 47, 49).

Bennett, A. J. et al. (2016). "Cavity-enhanced coherent light scattering from a quantum dot". *Sci. Adv.* **2**, e1501256. doi: 10.1126/sciadv.1501256 (cit. on p. 23).

Berroir, J. (2022). "Atomic arrays trapped around a nanofiber: collective non-linear quantum optics". PhD thesis. Sorbonne Université (cit. on pp. 13, 15, 107).

Berroir, J., Bouscal, A., Urvoy, A., Ray, T., and Laurat, J. (2022). "Nanotrappy: An open-source versatile package for cold-atom trapping close to nanostructures". *Phys. Rev. Res.* **4**, p. 013079. doi: 10.1103/PhysRevResearch.4.013079 (cit. on pp. 4, 33, 36, 77).

Billington, C. J. (2018). "State-dependent forces in cold quantum gases". PhD thesis. Monash University. doi: 10.26180/5bd68acaf0696 (cit. on p. 114).

Bitbol, A. F., Canaguier-Durand, A., Lambrecht, A., and Reynaud, S. (2013). "Pairwise summation approximation for Casimir potentials and its limitations". *Phys. Rev. B* **87**, p. 045413. doi: 10.1103/PhysRevB.87.045413 (cit. on pp. 87, 153).

Bolduc, E., Bent, N., Santamato, E., Karimi, E., and Boyd, R. W. (2013). "Exact solution to simultaneous intensity and phase encryption with a single phase-only hologram". *Opt. Lett.* **38**, p. 3546. doi: 10.1364/ol.38.003546 (cit. on pp. 140, 142).

Bopp, J. M., Plock, M., Turan, T., Pieplow, G., Burger, S., and Schröder, T. (2022). "'Sawfish' Photonic Crystal Cavity for Near-Unity Emitter-to-Fiber Interfacing in Quantum Network Applications". arXiv: 2210.04702 [quant-ph] (cit. on pp. 60, 67).

Born, M. and Wolf, E. (1999). *Principles of Optics*. 7th ed. Cambridge University Press (cit. on p. 7).

Bouscal, A. and D'Ascoli, S. (2022). *Voyage au Coeur de l'Atome : la physique quantique en dix innovations spectaculaires*. First Editions (cit. on p. 1).

Bouscal, A. et al. (2024). "Systematic design of a robust half-W1 photonic crystal waveguide for interfacing slow light and trapped cold atoms". *New J. Phys.* **26**, p. 023026. doi: 10.1088/1367-2630/ad23a4 (cit. on pp. 4, 31, 38, 45, 59, 69, 74, 75, 93, 95).

Boustimi, M., Baudon, J., Candori, P., and Robert, J. (2002). "Van der Waals interaction between an atom and a metallic nanowire". *Phys. Rev. B* **65**, p. 155402. doi: 10.1103/PhysRevB.65.155402 (cit. on p. 33).

Brehm, J. D., Gebauer, R., Stehli, A., Poddubny, A. N., Sander, O., Rotzinger, H., and Ustinov, A. V. (2022). "Slowing down light in a qubit metamaterial". *Appl. Phys. Lett.* **121**, p. 204001. doi: 10.1063/5.0122003 (cit. on pp. 14, 15).

Bruno, N., Bianchet, L. C., Prakash, V., Li, N., Alves, N., and Mitchell, M. W. (2019). "Maltese cross coupling to individual cold atoms in free space". *Opt. Express* **27**, pp. 31042–31052. doi: 10.1364/OE.27.031042 (cit. on p. 136).

Buonaiuto, G., Jones, R., Olmos, B., and Lesanovsky, I. (2019). "Dynamical creation and detection of entangled many-body states in a chiral atom chain". *New J. Phys.* **21**, p. 113021. DOI: 10.1088/1367-2630/ab4f50 (cit. on p. 85).

Burgers, A. P., Peng, L. S., Muniz, J. A., McClung, A. C., Martin, M. J., and Kimble, H. J. (2019). "Clocked atom delivery to a photonic crystal waveguide". *Proc. Natl. Acad. Sci. U.S.A* **116**, pp. 456–465. DOI: 10.1073/pnas.1817249115 (cit. on pp. 3, 44, 124).

Cabrera Gutiérrez, N. C. (2014). "Modes de Laguerre-Gauss et canalisation d'atomes froids". PhD thesis. Université Paris Sud (cit. on p. 128).

Cai, Y., Wang, Z., Liang, Y., Ren, F., Yao, B., Lei, M., and Yan, S. (2019). "Direct calculation of tightly focused field in an arbitrary plane". *Opt. Commun.* **450**, pp. 329–334. DOI: https://doi.org/10.1016/j.optcom.2019.06.022 (cit. on p. 133).

Cao, M., Hoffet, F., Qiu, S., Sheremet, A. S., and Laurat, J. (2020). "Efficient reversible entanglement transfer between light and quantum memories". *Optica* **7**, pp. 1440–1444. DOI: 10.1364/optica.400695 (cit. on p. 8).

Cardenas-Lopez, S., Masson, S. J., Zager, Z., and Asenjo-Garcia, A. (2023). "Many-Body Superradiance and Dynamical Mirror Symmetry Breaking in Waveguide QED". *Phys. Rev. Lett.* **131**, p. 033605. DOI: 10.1103/PhysRevLett.131.033605 (cit. on pp. 12, 147).

Caride, A. O., Klimchitskaya, G. L., Mostepanenko, V. M., and Zanette, S. I. (2005). "Dependences of the van der Waals atom-wall interaction on atomic and material properties". *Phys. Rev. A* **71**, p. 042901. DOI: 10.1103/PhysRevA.71.042901 (cit. on p. 149).

Carminati, R., Cazé, A., Cao, D., Peragut, F., Krachmalnicoff, V., Pierrat, R., and De Wilde, Y. (2015). "Electromagnetic density of states in complex plasmonic systems". *Surf. Sci. Rep.* **70**, pp. 1–41. DOI: https://doi.org/10.1016/j.surfrep.2014.11.001 (cit. on p. 21).

Casimir, H. B. and Polder, D. (1948). "The influence of retardation on the London-van der Waals forces". *Phys. Rev.* **73**, p. 360. DOI: 10.1103/PhysRev.73.360 (cit. on pp. 37, 87, 148).

Chang, D. E., Sinha, K., Taylor, J. M., and Kimble, H. J. (2014a). "Trapping atoms using nanoscale quantum vacuum forces". *Nat. Commun.* **5**, p. 4343. DOI: https://doi.org/10.1038/ncomms5343 (cit. on p. 47).

Chang, D. E., Sørensen, A. S., Demler, E. A., and Lukin, M. D. (2007). "A single-photon transistor using nanoscale surface plasmons". *Nat. Phys.* **3**, pp. 807–812. DOI: 10.1038/nphys708 (cit. on pp. 11, 146).

Chang, D. E., Vuletić, V., and Lukin, M. D. (2014b). "Quantum nonlinear optics - Photon by photon". *Nat. Photon.* **8**, pp. 685–694. DOI: 10.1038/nphoton.2014.192 (cit. on p. 7).

Chang, D. E., Douglas, J. S., González-Tudela, A., and Kimble, H. J. (2018). "Colloquium: Quantum matter built from nanoscopic lattices of atoms and photons". *Rev. Mod. Phys.* **90**, p. 031002. DOI: 10.1103/RevModPhys.90.031002 (cit. on p. 9).

Chen, C. et al. (2023). "Continuous symmetry breaking in a two-dimensional Rydberg array". *Nature* **616**, pp. 691–695. DOI: 10.1038/s41586-023-05859-2 (cit. on p. 124).

Chin, Y. S., Steiner, M., and Kurtsiefer, C. (2017). "Nonlinear photon-atom coupling with 4Pi microscopy". *Nat. Commun.* **8**, p. 1200. DOI: 10.1038/s41467-017-01495-3 (cit. on pp. 7, 32).

Chopin, A., Ghorbel, I., Combrié, S., Marty, G., Raineri, F., and De Rossi, A. (2022). "Time-correlated photons from an $In_{0.5}Ga_{0.5}P$ photonic crystal cavity on a silicon chip". *Phys. Rev. Res.* **4**, p. 043132. DOI: 10.1103/PhysRevResearch.4.043132 (cit. on pp. 52, 71).

Chu, S., Bjorkholm, J. E., Ashkin, A., and Cable, A. (1986). "Experimental Observation of Optically Trapped Atoms". *Phys. Rev. Lett.* **57**, pp. 314–317. DOI: 10.1103/PhysRevLett.57.314 (cit. on pp. 38, 107).

Cladé, P. (2005). "Oscillations de Bloch d'atomes ultrafroids et mesure de la constante de structure fine". PhD thesis. Université Pierre et Marie Curie (cit. on p. 122).

Clark, T. W., Offer, R. F., Franke-Arnold, S., Arnold, A. S., and Radwell, N. (2016). "Comparison of beam generation techniques using a phase only spatial light modulator". *Opt. Express* **24**, pp. 6249–6264. DOI: 10.1364/OE.24.006249 (cit. on pp. 140, 142, 143).

Cohen-Tannoudji, C. and Dupont-Roc, J. (1972). "Experimental Study of Zeeman Light Shifts in Weak Magnetic Fields". *Phys. Rev. A* **5**, p. 968. DOI: 10.1103/PhysRevA.5.968 (cit. on p. 90).

Colman, P., Combrié, S., Lehoucq, G., and Rossi, A. D. (2012). "Control of dispersion in photonic crystal waveguides using group symmetry theory". *Advanced Photonics Congress*. Optica Publishing Group, IM3B.4. DOI: 10.1364/IPRSN.2012.IM3B.4 (cit. on p. 69).

Combrié, S., Tran, Q. V., De Rossi, A., Husko, C., and Colman, P. (2009). "High quality GaInP nonlinear photonic crystals with minimized nonlinear absorption". *Appl. Phys. Lett.* **95**, p. 221108. DOI: 10.1063/1.3269998 (cit. on pp. 71, 89).

Cortiñas, R. G., Favier, M., Ravon, B., Méhaignerie, P., Machu, Y., Raimond, J. M., Sayrin, C., and Brune, M. (2020). "Laser Trapping of Circular Rydberg Atoms". *Phys. Rev. Lett.* **124**, p. 123201. DOI: 10.1103/PhysRevLett.124.123201 (cit. on p. 128).

Corzo, N. V., Gouraud, B., Chandra, A., Goban, A., Sheremet, A. S., Kupriyanov, D. V., and Laurat, J. (2016). "Large Bragg Reflection from One-Dimensional Chains of Trapped Atoms Near a Nanoscale Waveguide". *Phys. Rev. Lett.* **117**, p. 133603. DOI: 10.1103/PhysRevLett.117.133603 (cit. on p. 78).

Corzo, N. V., Raskop, J., Chandra, A., Sheremet, A. S., Gouraud, B., and Laurat, J. (2019). "Waveguide-coupled single collective excitation of atomic arrays". *Nature* **566**, pp. 359–362. DOI: 10.1038/s41586-019-0902-3 (cit. on pp. 13, 14, 15, 33, 36, 86).

Cox, S. J. and Dobson, D. C. (1999). "Maximizing Band Gaps in Two-Dimensional Photonic Crystals". *SIAM J. Appl. Math.* **59**, pp. 2108–2120. DOI: https://www.jstor.org/stable/118418 (cit. on p. 69).

Crosnier, G., Sanchez, D., Bouchoule, S., Monnier, P., Beaudoin, G., Sagnes, I., Raj, R., and Raineri, F. (2017). "Hybrid indium phosphide-on-silicon nanolaser diode". *Nat. Photon.* **11**, pp. 297–300. DOI: 10.1038/nphoton.2017.56 (cit. on p. 52).

Dalibard, J. and Cohen-Tannoudji, C. (1989). "Laser cooling below the Doppler limit by polarization gradients: simple theoretical models". *J. Opt. Soc. Am. B* **6**, pp. 2023–2045. DOI: 10.1364/JOSAB.6.002023 (cit. on p. 111).

Darquié, B. et al. (2005). "Controlled Single-Photon Emission from a Single Trapped Two-Level Atom". *Science* **309**, pp. 454–456. DOI: 10.1126/science.1113394 (cit. on p. 7).

Davis, J. A., Cottrell, D. M., Campos, J., Yzuel, M. J., and Moreno, I. (1999). "Encoding amplitude information onto phase-only filters". *Appl. Opt.* **38**, p. 5004. doi: 10.1364/ao.38.005004 (cit. on pp. 140, 141).

Dayan, B., Parkins, A. S., Aoki, T., Ostby, E. P., Vahala, K. J., and Kimble, H. J. (2008). "A Photon Turnstile Dynamically Regulated by One Atom". *Science* **319**, pp. 1062–1065. doi: 10.1126/science.115226 (cit. on p. 46).

Derevianko, A., Johnson, W. R., and Fritzsche, S. (1998). "Many-body calculations of the static atom-wall interaction potential for alkali-metal atoms". *Phys. Rev. A* **57**, pp. 2629–2634. doi: 10.1103/PhysRevA.57.2629 (cit. on p. 149).

Derevianko, A., Porsev, S. G., and Babb, J. F. (2010). "Electric dipole polarizabilities at imaginary frequencies for hydrogen, the alkali – metal, alkaline – earth, and noble gas atoms". *At. Data Nucl. Data Tables* **96**, pp. 323–331. doi: 10.1016/j.adt.2009.12.002 (cit. on pp. 149, 150).

Dicke, R. H. (1954). "Coherence in Spontaneous Radiation Processes". *Phys. Rev.* **93**, pp. 99–110. doi: 10.1103/PhysRev.93.99 (cit. on p. 8).

Douglas, J. S., Habibian, H., Hung, C.-L., Gorshkov, A. V., Kimble, H. J., and Chang, D. E. (2015). "Quantum many-body models with cold atoms coupled to photonic crystals". *Nat. Photon.* **9**, pp. 326–331. doi: 10.1038/nphoton.2015.57 (cit. on pp. 13, 147).

Drexhage, K. H., Kuhn, H., and Schäfer, F. P. (1968). "Variation of the Fluorescence Decay Time of a Molecule in Front of a Mirror". *Bunsenges. Phys. Chem.* **72**, pp. 329–329. doi: 10.1002/bbpc.19680720261 (cit. on pp. 17, 22).

Dubois, F. (2018). "Étude des propriétés spectro-spatiales des cristaux photoniques membranaires à symétrie brisée". PhD thesis. École Centrale de Lyon (cit. on pp. 72, 94).

Endres, M. et al. (2016). "Atom-by-atom assembly of defect-free one-dimensional cold atom arrays". *Science* **354**, pp. 1024–1027. doi: 10.1126/science.aah3752 (cit. on p. 137).

Engelen, R. J. P., Mori, D., Baba, T., and Kuipers, L. (2009). "Subwavelength Structure of the Evanescent Field of an Optical Bloch Wave". *Phys. Rev. Lett.* **102**, p. 023902. doi: 10.1103/PhysRevLett.102.023902 (cit. on p. 47).

Faggiani, R. et al. (2016). "Lower bound for the spatial extent of localized modes in photonic-crystal waveguides with small random imperfections". *Sci. Rep.* **6**, p. 27037. doi: 10.1038/srep27037 (cit. on pp. 67, 95).

Fayard, N. et al. (2022). "Asymmetric comb waveguide for strong interactions between atoms and light". *Opt. Express* **30**, pp. 45093–45109. doi: 10.1364/oe.475162 (cit. on pp. 4, 38, 45, 47, 60, 64, 69, 72, 74, 75, 86, 92, 95, 154).

Fedorovich, G., Kornovan, D., Poddubny, A., and Petrov, M. (2022). "Chirality-driven delocalization in disordered waveguide-coupled quantum arrays". *Phys. Rev. A* **106**, p. 043723. doi: 10.1103/PhysRevA.106.043723 (cit. on p. 85).

Ferioli, G., Glicenstein, A., Robicheaux, F., Sutherland, R. T., Browaeys, A., and Ferrier-Barbut, I. (2021). "Laser-Driven Superradiant Ensembles of Two-Level Atoms near Dicke Regime". *Phys. Rev. Lett.* **127**, p. 243602. doi: 10.1103/PhysRevLett.127.243602 (cit. on p. 8).

Ferioli, G., Glicenstein, A., Ferrier-Barbut, I., and Browaeys, A. (2023). "A non-equilibrium superradiant phase transition in free space". *Nat. Phys.* **19**, pp. 1345–1349. doi: 10.1038/s41567-023-02064-w (cit. on p. 8).

Fitzpatrick, C., Wilson, A., Sawyer, T., Christopher, P. J., Wilkinson, T. D., Bondhiek, S., and Gordon, G. (2020). "Robustness to misalignment of low-cost,

compact quantitative phase imaging architectures". *OSA Contin.* **3**, pp. 2660–2679. DOI: 10.1364/OSAC.395498 (cit. on p. 138).

Frandsen, L. H., Lavrinenko, A., Fage-Pedersen, J., and Borel, P. I. (2006). "Photonic crystal waveguides with semi-slow light and tailored dispersion properties". *Opt. Express* **14**, pp. 2440–2445. DOI: 10.1364/acp.2011.83081x (cit. on pp. 69, 81, 82).

Frisch, U. (1968). "Wave propagation in random media". *Probabilistic Methods in Applied Mathematics.* **1**, pp. 75–198 (cit. on p. 22).

Gabor, D. (1948). "A new microscopic principle". *Nature* **161**, pp. 777–778. DOI: 10.1038/161777a0 (cit. on p. 137).

García, P. D., Kiršanskė, G., Javadi, A., Stobbe, S., and Lodahl, P. (2017). "Two mechanisms of disorder-induced localization in photonic-crystal waveguides". *Phys. Rev. B* **96**, p. 144201. DOI: 10.1103/PhysRevB.96.144201 (cit. on p. 67).

Gerchberg, R. W. and Saxton, W. O. (1972). "A practical algorithm for the determination of phase from image and diffraction plane pictures". *Optik* **35**, pp. 237–246 (cit. on p. 143).

Gibble, K. E., Kasapi, S., and Chu, S. (1992). "Improved magneto-optic trapping in a vapor cell". *Opt. Lett.* **17**, pp. 526–528. DOI: 10.1364/OL.17.000526 (cit. on p. 121).

Gleyzes, S. et al. (2007). "Quantum jumps of light recording the birth and death of a photon in a cavity". *Nature* **446**, pp. 297–300. DOI: 10.1038/nature05589 (cit. on p. 9).

Goban, A. et al. (2014). "Atom–light interactions in photonic crystals". *Nat. Commun.* **5**, p. 3808. DOI: 10.1038/ncomms4808 (cit. on pp. 3, 15, 33, 60, 64, 104).

Goban, A. et al. (2012). "Demonstration of a state-insensitive, compensated nanofiber trap". *Phys. Rev. Lett.* **109**, p. 033603. DOI: 10.1103/PhysRevLett.109.033603 (cit. on pp. 13, 32, 33, 36, 38, 42, 47, 87, 90).

Goban, A., Hung, C.-L., Hood, J. D., Yu, S.-P., Muniz, J. A., Painter, O., and Kimble, H. J. (2015). "Superradiance for Atoms Trapped along a Photonic Crystal Waveguide". *Phys. Rev. Lett.* **115**, p. 063601. DOI: 10.1103/PhysRevLett.115.063601 (cit. on pp. 14, 15, 18, 45, 86, 96, 101, 124).

Goban, A. (2015). "Strong atom-light interactions along nanostructures: Transition from free-space to nanophotonic interfaces". PhD thesis. California Institute of Technology (cit. on p. 42).

González-Tudela, A., Hung, C.-L., Chang, D. E., Cirac, J. I., and Kimble, H. J. (2015). "Subwavelength vacuum lattices and atom-atom interactions in two-dimensional photonic crystals". *Nat. Photon.* **9**, pp. 320–325. DOI: 10.1038/nphoton.2015.54 (cit. on p. 47).

Gouraud, B., Maxein, D., Nicolas, A., Morin, O., and Laurat, J. (2015). "Demonstration of a Memory for Tightly Guided Light in an Optical Nanofiber". *Phys. Rev. Lett.* **114**, p. 180503. DOI: 10.1103/PhysRevLett.114.180503 (cit. on pp. 13, 15).

Gouraud, B. (2016). "Optical nanofibers interfacing cold atoms. A tool for quantum optics." PhD thesis. Université Pierre et Marie Curie (cit. on pp. 13, 34, 39).

Goy, P., Raimond, J.-M., Gross, M., and Haroche, S. (1983). "Observation of Cavity-Enhanced Single-Atom Spontaneous Emission". *Phys. Rev. Lett.* **50**, pp. 1903–1906. DOI: 10.1103/PhysRevLett.50.1903 (cit. on pp. 10, 17, 23).

Grier, D. G. (2003). "A revolution in optical manipulation". *Nature* **424**, pp. 810–816. DOI: 10.1038/nature01935 (cit. on p. 124).

Grimm, R., Weidemüller, M., and Ovchinnikov, Y. B. (2000). "Optical Dipole Traps for Neutral Atoms". *Adv. At. Mol. Opt. Phys.* Vol. 42. Academic Press, pp. 95–170 (cit. on p. 33).

Hammerer, K., Sørensen, A. S., and Polzik, E. S. (2010). "Quantum interface between light and atomic ensembles". *Rev. Mod. Phys.* **82**, pp. 1041–1093. DOI: 10.1103/RevModPhys.82.1041 (cit. on p. 7).

Haroche, S. and Raimond, J.-M. (2006). *Exploring the Quantum: Atoms, Cavities, and Photons*. Oxford University Press (cit. on p. 17).

Haw, M., Evetts, N., Gunton, W., Dongen, J. V., Booth, J. L., and Madison, K. W. (2012). "Magneto-optical trap loading rate dependence on trap depth and vapor density". *J. Opt. Soc. Am. B* **29**, pp. 475–483. DOI: 10.1364/JOSAB.29.000475 (cit. on p. 121).

Hering, J., Waller, E. H., and Freymann, G. V. (2016). "Automated aberration correction of arbitrary laser modes in high numerical aperture systems". *Opt. Express* **24**, pp. 28500–28508. DOI: 10.1364/OE.24.028500 (cit. on p. 144).

Hinney, J. (2019). "Generation of squeezed light with nanofiber-trapped atoms". PhD thesis. TU Wien (cit. on p. 120).

Hood, J. D., Goban, A., Asenjo-Garcia, A., Lu, M., Yu, S.-P., Chang, D. E., and Kimble, H. J. (2016). "Atom-atom interactions around the band edge of a photonic crystal waveguide". *Proc. Natl. Acad. Sci. U.S.A* **113**, pp. 10507–10512. DOI: 10.1073/pnas.1603788113 (cit. on pp. 3, 15, 39, 96).

Hood, J. D. (2017). "Atom-light interactions in a photonic crystal waveguide". PhD thesis. California Institute of Technology (cit. on pp. 24, 25).

Huisman, S. R. et al. (2012). "Measurement of a band-edge tail in the density of states of a photonic-crystal waveguide". *Phys. Rev. B* **86**, p. 155154. DOI: 10.1103/PhysRevB.86.155154 (cit. on p. 67).

Hung, C. L., Meenehan, S. M., Chang, D. E., Painter, O., and Kimble, H. J. (2013). "Trapped atoms in one-dimensional photonic crystals". *New J. Phys.* **15**, p. 83026. DOI: 10.1088/1367-2630/15/8/083026 (cit. on pp. 44, 86).

Joannopoulos, J. D., Johnson, S. G., Winn, J. N., and Meade, R. D. (2008). *Photonic Crystals: Molding the flow of light*. 2nd ed. Princeton University Press (cit. on pp. 54, 55, 80).

John, S. (1987). "Strong localization of photons in certain disordered dielectric superlattices". *Phys. Rev. Lett.* **58**, pp. 2486–2489. DOI: 10.1103/PhysRevLett.58.2486 (cit. on p. 52).

Johnson, S. G., Fan, S., Villeneuve, P. R., Joannopoulos, J. D., and Kolodziejski, L. A. (1999). "Guided modes in photonic crystal slabs". *Phys. Rev. B* **60**, pp. 5751–5758. DOI: 10.1103/PhysRevB.60.5751 (cit. on p. 57).

Johnson, S. G. and Joannopoulos, J. D. (2001). "Block-iterative frequency-domain methods for Maxwell's equations in a planewave basis". *Opt. Express* **8**, pp. 173–190. DOI: 10.1364/OE.8.000173 (cit. on pp. 64, 155).

Johnson, W., Dzuba, V., Safronova, U., and Safronova, M. (2004). "Finite-field evaluation of the Lennard-Jones atom-wall interaction constant C_3 for alkali-metal atoms". *Phys. Rev. A* **69**, p. 022508. DOI: 10.1103/PhysRevA.69.022508 (cit. on pp. 37, 87, 149).

Kaufman, A. M. and Ni, K.-K. (2021). "Quantum science with optical tweezer arrays of ultracold atoms and molecules". *Nat. Phys.* **17**, pp. 1324–1333. DOI: 10.1038/s41567-021-01357-2 (cit. on p. 124).

Kim, M. E., Chang, T.-H., Fields, B. M., Chen, C.-A., and Hung, C.-L. (2019). "Trapping single atoms on a nanophotonic circuit with configurable tweezer lattices". *Nat. Commun.* **10**, p. 1647. DOI: 10.1038/s41467-019-09635-7 (cit. on p. 124).

Kimble, H. J. (2008). "The quantum internet". *Nature* **453**, pp. 1023–1030. DOI: 10.1038/nature07127 (cit. on p. 7).

Kleinbeck, K., Busche, H., Stiesdal, N., Hofferberth, S., Mølmer, K., and Büchler, H. P. (2023). "Creation of nonclassical states of light in a chiral waveguide". *Phys. Rev. A* **107**, p. 013717. DOI: 10.1103/PhysRevA.107.013717 (cit. on p. 85).

Kleppner, D. (1981). "Inhibited Spontaneous Emission". *Phys. Rev. Lett.* **47**, pp. 233–236. DOI: 10.1103/PhysRevLett.47.233 (cit. on p. 17).

Krauss, T. F., De La Rue, R. M., and Brand, S. (1996). "Two-dimensional photonic-bandgap structures operating at near-infrared wavelengths". *Nature* **383**, pp. 699–702. DOI: 10.1038/383699a0 (cit. on pp. 52, 58).

Krinner, L., Stewart, M., Pazmiño, A., Kwon, J., and Schneble, D. (2018). "Spontaneous emission of matter waves from a tunable open quantum system". *Nature* **559**, pp. 589–592. DOI: 10.1038/s41586-018-0348-z (cit. on pp. 14, 15).

Krutyanskiy, V. et al. (2023). "Entanglement of Trapped-Ion Qubits Separated by 230 Meters". *Phys. Rev. Lett.* **130**, p. 050803. DOI: 10.1103/PhysRevLett.130.050803 (cit. on p. 9).

Kurizki, G. (1990). "Two-atom resonant radiative coupling in photonic band structures". *Phys. Rev. A* **42**, pp. 2915–2924. DOI: 10.1103/PhysRevA.42.2915 (cit. on p. 13).

Kusmierek, K. J. et al. (2023). "Higher-order mean-field theory of chiral waveguide QED". *SciPost Phys. Core* **6**, p. 041. DOI: 10.21468/SciPostPhysCore.6.2.041 (cit. on p. 11).

Labuhn, H. (2016). "Rydberg excitation dynamics and correlations in arbitrary 2D arrays of single atoms". PhD thesis. Université Paris-Saclay (cit. on p. 138).

Lacroûte, C., Choi, K. S., Goban, A., Alton, D. J., Ding, D., Stern, N. P., and Kimble, H. J. (2012). "A state-insensitive, compensated nanofiber trap". *New J. Phys.* **14**, p. 023056. DOI: 10.1088/1367-2630/14/2/023056 (cit. on pp. 32, 36, 42, 43).

Lambrecht, A., Maia Neto, P. A., and Reynaud, S. (2006). "The Casimir effect within scattering theory". *New J. Phys.* **8**, p. 243. DOI: 10.1088/1367-2630/8/10/243 (cit. on p. 152).

Le Jeannic, H. et al. (2022). "Dynamical photon–photon interaction mediated by a quantum emitter". *Nat. Phys.* **18**, pp. 1191–1195. DOI: 10.1038/s41567-022-01720-x (cit. on pp. 11, 14, 146).

Le Kien, F., Balykin, V. I., and Hakuta, K. (2004). "Atom trap and waveguide using a two-color evanescent light field around a subwavelength-diameter optical fiber". *Phys. Rev. A* **70**, p. 063403. DOI: 10.1103/PhysRevA.70.063403 (cit. on pp. 32, 33, 37, 38, 87, 148).

Le Kien, F., Balykin, V. I., and Hakuta, K. (2005). "State-Insensitive Trapping and Guiding of Cesium Atoms Using a Two-Color Evanescent Field around a Subwavelength-Diameter Fiber". *J. Phys. Soc. Jap.* **74**, pp. 910–917. DOI: 10.1143/JPSJ.74.910 (cit. on pp. 36, 42).

Le Kien, F., Schneeweiss, P., and Rauschenbeutel, A. (2013a). "Dynamical polarizability of atoms in arbitrary light fields: General theory and application to

cesium". *Eur. Phys. J. D* **67**, p. 92. DOI: 10.1140/epjd/e2013-30729-x (cit. on pp. 30, 34).

Le Kien, F., Schneeweiss, P., and Rauschenbeutel, A. (2013b). "State-dependent potentials in a nanofiber-based two-color trap for cold atoms". *Phys. Rev. A* **88**, p. 033840. DOI: 10.1103/PhysRevA.88.033840 (cit. on p. 36).

Lecamp, G., Hugonin, J. P., and Lalanne, P. (2007). "Theoretical and computational concepts for periodic optical waveguides". *Opt. Express* **15**, pp. 11042–11060. DOI: 10.1364/OE.15.011042 (cit. on pp. 86, 154).

Lennard-Jones, J. (1932). "Processes of adsorption and diffusion on solid surfaces". *Trans. Faraday Soc.* **28**, pp. 333–359. DOI: 10.1039/TF9322800333 (cit. on p. 148).

Leutenegger, M., Rao, R., Leitgeb, R. A., and Lasser, T. (2006). "Fast focus field calculations". *Opt. Express* **14**, pp. 11277–11291. DOI: 10.1364/OE.14.011277 (cit. on p. 133).

Li, J., White, T. P., O'Faolain, L., Gomez-iglesias, A., and Krauss, T. F. (2008). "Systematic design of flat band slow light in photonic crystal waveguides". *Opt. Express* **16**, pp. 2621–2626. DOI: 10.1364/OE.16.006227 (cit. on pp. 69, 81, 82, 84, 98, 101).

Li, T., Miranowicz, A., Hu, X., Xia, K., and Nori, F. (2018). "Quantum memory and gates using a Λ-type quantum emitter coupled to a chiral waveguide". *Phys. Rev. A* **97**, p. 062318. DOI: 10.1103/PhysRevA.97.062318 (cit. on p. 85).

Liang, J., Ren, L. Y., Yun, M. J., Han, X., and Wang, X. J. (2011). "Wideband ultraflat slow light with large group index in a W1 photonic crystal waveguide". *J. Appl. Phys.* **110**, p. 063103. DOI: 10.1063/1.3634074 (cit. on p. 69).

Liedl, C., Pucher, S., Tebbenjohanns, F., Schneeweiss, P., and Rauschenbeutel, A. (2023). "Collective Radiation of a Cascaded Quantum System: From Timed Dicke States to Inverted Ensembles". *Phys. Rev. Lett.* **130**, p. 163602. DOI: 10.1103/PhysRevLett.130.163602 (cit. on pp. 13, 15).

Lindquist, K., Stephens, M., and Wieman, C. (1992). "Experimental and theoretical study of the vapor-cell Zeeman optical trap". *Phys. Rev. A* **46**, pp. 4082–4090. DOI: 10.1103/PhysRevA.46.4082 (cit. on p. 120).

Lodahl, P., Mahmoodian, S., Stobbe, S., Rauschenbeutel, A., Schneeweiss, P., Volz, J., Pichler, H., and Zoller, P. (2017). "Chiral quantum optics". *Nature* **541**, pp. 473–480. DOI: 10.1038/nature21037 (cit. on p. 85).

Lü, S., Zhao, J., and Zhang, D. (2010). "Flat band slow light in asymmetric photonic crystal waveguide based on microfluidic infiltration". *Appl. Opt.* **49**, pp. 3930–3934. DOI: 10.1364/AO.49.003930 (cit. on p. 72).

Luan, X., Béguin, J.-B., Burgers, A. P., Qin, Z., Yu, S.-P., and Kimble, H. J. (2020). "The Integration of Photonic Crystal Waveguides with Atom Arrays in Optical Tweezers". *Adv. Quantum Technol.* **3**, p. 2000008. DOI: https://doi.org/10.1002/qute.202000008 (cit. on pp. 73, 104, 105, 122, 146).

Luan, X. (2020). "Towards atom assembly on nanophotonic structures with optical tweezers". PhD thesis. California Institute of Technology (cit. on pp. 44, 45).

Mabuchi, H. and Kimble, H. J. (1994). "Atom galleries for whispering atoms: binding atoms in stable orbits around an optical resonator". *Opt. Lett.* **19**, pp. 749–751. DOI: 10.1364/OL.19.000749 (cit. on p. 45).

Magro, V., Vaneecloo, J., Garcia, S., and Ourjoumstev, A. (2023). "Deterministic freely propagating photonic qubits with negative Wigner functions". *Nat. Photon.* **17**, pp. 688–693. DOI: 10.1038/s41566-023-01196-y (cit. on p. 146).

Mahmoodian, S., Čepulkovskis, M., Das, S., Lodahl, P., Hammerer, K., and Sørensen, A. S. (2018). "Strongly Correlated Photon Transport in Waveguide Quantum Electrodynamics with Weakly Coupled Emitters". *Phys. Rev. Lett.* **121**, p. 143601. doi: 10.1103/PhysRevLett.121.143601 (cit. on p. 11).

Mahmoodian, S., Calajó, G., Chang, D. E., Hammerer, K., and Sørensen, A. S. (2020). "Dynamics of Many-Body Photon Bound States in Chiral Waveguide QED". *Phys. Rev. X* **10**, p. 031011. doi: 10.1103/PhysRevX.10.031011 (cit. on p. 85).

Masters, L., Hu, X.-X., Cordier, M., Maron, G., Pache, L., Rauschenbeutel, A., Schemmer, M., and Volz, J. (2023). "On the simultaneous scattering of two photons by a single two-level atom". *Nat. Photon.* **17**, pp. 972–976. doi: 10.1038/s41566-023-01260-7 (cit. on pp. 124, 136).

Mazoyer, S., Lalanne, P., Rodier, J. C., Hugonin, J. P., Spasenovi, M., Kuipers, L., Beggs, D. M., and Krauss, T. F. (2010). "Statistical fluctuations of transmission in slow light photonic-crystal waveguides". *Opt. Express* **18**, pp. 14654–14663. doi: 10.1364/OE.18.014654 (cit. on pp. 83, 94).

McKeever, J., Buck, J. R., Boozer, A. D., Kuzmich, A., Nägerl, H.-C., Stamper-Kurn, D. M., and Kimble, H. J. (2003). "State-Insensitive Cooling and Trapping of Single Atoms in an Optical Cavity". *Phys. Rev. Lett.* **90**, p. 133602. doi: 10.1103/PhysRevLett.90.133602 (cit. on p. 36).

Minkov, M., Williamson, I. A., Andreani, L. C., Gerace, D., Lou, B., Song, A. Y., Hughes, T. W., and Fan, S. (2020). "Inverse Design of Photonic Crystals through Automatic Differentiation". *ACS Photonics* **7**, pp. 1729–1741. doi: 10.1021/acsphotonics.0c00327 (cit. on pp. 70, 81, 156).

Molesky, S., Lin, Z., Piggott, A. Y., Jin, W., Vuckovic, J., and Rodriguez, A. W. (2018). "Inverse design in nanophotonics". *Nat. Photon.* **12**, pp. 659–670. doi: 10.1038/s41566-018-0246-9 (cit. on p. 70).

Monat, C. et al. (2014). "Integrated optical auto-correlator based on third-harmonic generation in a silicon photonic crystal waveguide". *Nat. Commun.* **5**, p. 3246. doi: 10.1038/ncomms4246 (cit. on p. 52).

Mori, D. and Baba, T. (2005). "Wideband and low dispersion slow light by chirped photonic crystal coupled waveguide". *Opt. Express* **13**, p. 9398. doi: 10.1364/OPEX.13.009398 (cit. on p. 69).

Mou, Y., Yang, X., Gallas, B., and Mivelle, M. (2023). "A Reversed Inverse Faraday Effect". *Adv. Mater. Technol.* **n/a**, p. 2300770. doi: https://doi.org/10.1002/admt.202300770 (cit. on p. 70).

Nayak, K. P., Melentiev, P. N., Morinaga, M., Le Kien, F., Balykin, V. I., and Hakuta, K. (2007). "Optical nanofiber as an efficient tool for manipulating and probing atomic fluorescence". *Opt. Express* **15**, pp. 5431–5438. doi: 10.1364/OE.15.005431 (cit. on p. 42).

Nayak, K. P., Le Kien, F., Morinaga, M., and Hakuta, K. (2009). "Antibunching and bunching of photons in resonance fluorescence from a few atoms into guided modes of an optical nanofiber". *Phys. Rev. A* **79**, p. 021801. doi: 10.1103/PhysRevA.79.021801 (cit. on p. 42).

Nguyen, H. S. et al. (2018). "Symmetry Breaking in Photonic Crystals: On-Demand Dispersion from Flatband to Dirac Cones". *Phys. Rev. Lett.* **120**, p. 66102. doi: 10.1103/PhysRevLett.120.066102 (cit. on pp. 69, 72, 92, 94).

Nicolas, A., Veissier, L., Giner, L., Giacobino, E., Maxein, D., and Laurat, L. (2014). "A quantum memory for orbital angular momentum photonic qubits". *Nat. Photon.* **8**, pp. 234–238 (cit. on p. 127).

Nieddu, T., Gokhroo, V., and Nic Chormaic, S. (2016). "Optical nanofibres and neutral atoms". *J. Opt.* **18**, p. 053001. DOI: 10.1088/2040-8978/18/5/053001 (cit. on p. 10).
Novotny, L. (2006). *Principles of Nano-optics*. Cambridge University Press (cit. on pp. 18, 129).

Ol'Shanii, M., Ovchinnikov, Y., and Letokhov, V. (1993). "Laser guiding of atoms in a hollow optical fiber". *Opt. Commun.* **98**, pp. 77–79. DOI: 10.1016/0030-4018(93)90761-S (cit. on p. 10).
Ovchinnikov, Y. B., Shul'ga, S. V., and Balykin, V. I. (1991). "An atomic trap based on evanescent light waves". *J. Phys. B* **24**, pp. 3173–3178. DOI: 10.1088/0953-4075/24/14/009 (cit. on p. 33).

Panuski, C. L. et al. (2022). "A full degree-of-freedom spatiotemporal light modulator". *Nat. Photon.* **16**, pp. 834–842. DOI: 10.1038/s41566-022-01086-9 (cit. on p. 13).
Pasienski, M. and DeMarco, B. (2008). "A high-accuracy algorithm for designing arbitrary holographic atom traps". *Opt. Express* **16**, pp. 2176–2190. DOI: 10.1364/OE.16.002176 (cit. on p. 137).
Patterson, M. (2009). "Classical and Quantum Optical Properties of Slow Light Photonic Crystal Waveguides". MA thesis. Queen's University (cit. on p. 25).
Peng, Z. et al. (2023). "Slow-light-enhanced on-chip 1D and 2D photonic crystal waveguide gas sensing in near-IR with an ultrahigh interaction factor". *Photon. Res.* **11**, pp. 1647–1656. DOI: 10.1364/PRJ.494762 (cit. on pp. 52, 64).
Petrov, A. Y. and Eich, M. (2004). "Zero dispersion at small group velocities in photonic crystal waveguides". *Appl. Phys. Lett.* **85**, pp. 4866–4868. DOI: 10.1063/1.1815066 (cit. on p. 69).
Philipp, H. (1997). "Silicon Dioxide (SiO2) (Glass)". *Handbook of Optical Constants of Solids*. Ed. by E. D. Palik. Academic Press, pp. 749–763 (cit. on p. 151).
Prasad, A. S. et al. (2020). "Correlating photons using the collective nonlinear response of atoms weakly coupled to an optical mode". *Nat. Photon.* **14**, pp. 719–722. DOI: 10.1038/s41566-020-0692-z (cit. on p. 13).
Pucher, S., Liedl, C., Jin, S., Rauschenbeutel, A., and Schneeweiss, P. (2022). "Atomic spin-controlled non-reciprocal Raman amplification of fibre-guided light". *Nat. Photon.* **16**, pp. 380–383. DOI: 10.1038/s41566-022-00987-z (cit. on p. 31).
Purcell, E. M., Torrey, H. C., and Pound, R. V. (1946). "Resonance Absorption by Nuclear Magnetic Moments in a Solid". *Phys. Rev.* **69**, pp. 37–38. DOI: 10.1103/PhysRev.69.37 (cit. on p. 17).

Qi, X., Jau, Y.-Y., and Deutsch, I. H. (2018). "Enhanced cooperativity for quantum-nondemolition-measurement–induced spin squeezing of atoms coupled to a nanophotonic waveguide". *Phys. Rev. A* **97**, p. 033829. DOI: 10.1103/PhysRevA.97.033829 (cit. on pp. 12, 76, 147).

Rayleigh, L. (1887). "XVII. On the maintenance of vibrations by forces of double frequency, and on the propagation of waves through a medium endowed with a periodic structure". *Lond. Edinb. Dubl. Phil. Mag.* **24**, pp. 145–159. DOI: 10.1080/14786448708628074 (cit. on p. 52).
Reiserer, A. and Rempe, G. (2015). "Cavity-based quantum networks with single atoms and optical photons". *Rev. Mod. Phys.* **87**, pp. 1379–1418. DOI: 10.1103/RevModPhys.87.1379 (cit. on p. 9).

Rephaeli, E. and Fan, S. (2012). "Stimulated Emission from a Single Excited Atom in a Waveguide". *Phys. Rev. Lett.* **108**, p. 143602. doi: 10.1103/PhysRevLett.108.143602 (cit. on p. 11).

Ritter, R., Gruhler, N., Pernice, W., Kübler, H., Pfau, T., and Löw, R. (2015). "Atomic vapor spectroscopy in integrated photonic structures". *Appl. Phys. Lett.* **107**, p. 041101. doi: 10.1063/1.4927172 (cit. on p. 76).

Robertson, E. J., Šibalić, N., Potvliege, R. M., and Jones, M. P. (2021). "ARC 3.0: An expanded Python toolbox for atomic physics calculations". *Comput. Phys. Commun.* **261**, p. 107814. doi: 10.1016/j.cpc.2020.107814 (cit. on p. 42).

Rodriguez, A. W., Mccauley, A. P., Joannopoulos, J. D., and Johnson, S. G. (2009). "Casimir forces in the time domain : Theory". *Phys. Rev. A* **80**, p. 012115. doi: 10.1103/PhysRevA.80.012115 (cit. on p. 153).

Rui, J., Wei, D., Rubio-Abadal, A., Hollerith, S., Zeiher, J., Stamper-Kurn, D. M., Gross, C., and Bloch, I. (2020). "A subradiant optical mirror formed by a single structured atomic layer". *Nature* **583**, pp. 369–374. doi: 10.1038/s41586-020-2463-x (cit. on p. 15).

Sagué, G., Vetsch, E., Alt, W., Meschede, D., and Rauschenbeutel, A. (2007). "Cold-atom physics using ultrathin optical fibers: Light-induced dipole forces and surface interactions". *Phys. Rev. Lett.* **99**, p. 163602. doi: 10.1103/PhysRevLett.99.163602 (cit. on p. 10).

Saranathan, V., Narayanan, S., Sandy, A., Dufresne E, E. R., and Prum, R. O. (2021). "Evolution of single gyroid photonic crystals in bird feathers". *Proc. Natl. Acad. Sci. U.S.A* **118**, p. 2101357118. doi: 10.1073/pnas.2101357118/-/DCSupplemental (cit. on p. 52).

Savona, V. (2011). "Electromagnetic modes of a disordered photonic crystal". *Phys. Rev. B* **83**, p. 085301. doi: 10.1103/PhysRevB.83.085301 (cit. on p. 67).

Schlosser, N., Reymond, G., Protsenko, I., and Grangier, P. (2001). "Sub-poissonian loading of single atoms in a microscopic dipole trap". *Nature* **411**, pp. 1024–1027. doi: 10.1038/35082512 (cit. on pp. 38, 124).

Schlosser, N., Reymond, G., and Grangier, P. (2002). "Collisional blockade in microscopic optical dipole traps". *Phys. Rev. Lett.* **89**, p. 023005. doi: 10.1103/PhysRevLett.89.023005 (cit. on p. 124).

Schubert, M., Gottschalch, V., Herzinger, C. M., Yao, H., Snyder, P. G., and Woollam, J. A. (1995). "Optical constants of GaxIn1-xP lattice matched to GaAs". *J. Appl. Phys.* **77**, pp. 3416–3419. doi: 10.1063/1.358632 (cit. on pp. 71, 150).

Schulz, S. A., O'Faolain, L., Beggs, D. M., White, T. P., Melloni, A., and Krauss, T. F. (2010). "Dispersion engineered slow light in photonic crystals: a comparison". *J. Opt.* **12**, p. 104004. doi: 10.1088/2040-8978/12/10/104004 (cit. on pp. 69, 81).

Shen, J.-T. and Fan, S. (2007). "Strongly Correlated Two-Photon Transport in a One-Dimensional Waveguide Coupled to a Two-Level System". *Phys. Rev. Lett.* **98**, p. 153003. doi: 10.1103/PhysRevLett.98.153003 (cit. on p. 11).

Sheremet, A. S., Petrov, M. I., Iorsh, I. V., Poshakinskiy, A. V., and Poddubny, A. N. (2023). "Waveguide quantum electrodynamics: Collective radiance and photon-photon correlations". *Rev. Mod. Phys.* **95**. doi: 10.1103/revmodphys.95.015002 (cit. on pp. 9, 100, 101).

Šibalić, N., Pritchard, J., Adams, C., and Weatherill, K. (2017). "ARC: An open-source library for calculating properties of alkali Rydberg atoms". *Comput.*

Phys. Commun. **220**, pp. 319–331. DOI: https://doi.org/10.1016/j.cpc.2017.06.015 (cit. on pp. 30, 39, 149).

Silberstein, E., Lalanne, P., Hugonin, J.-P., and Cao, Q. (2001). "Use of grating theories in integrated optics". *J. Opt. Soc. Am. A* **18**, pp. 2865–2875. DOI: 10.1364/JOSAA.18.002865 (cit. on p. 154).

Sitaram, A., Campbell, G. K., and Restelli, A. (2021). "Programmable system on chip for controlling an atomic physics experiment". *Rev. Sci. Instrum.* **92**, p. 055107. DOI: 10.1063/5.0047535 (cit. on p. 113).

Snyder, A. W. and Love, J. (2012). *Optical waveguide theory*. Springer Science & Business Media (cit. on pp. 24, 26, 27, 42, 65, 156).

Solano, P., Grover, J. A., Xu, Y., Barberis-Blostein, P., Munday, J. N., Orozco, L. A., Phillips, W. D., and Rolston, S. L. (2019). "Alignment-dependent decay rate of an atomic dipole near an optical nanofiber". *Phys. Rev. A* **99**, p. 013822. DOI: 10.1103/PhysRevA.99.013822 (cit. on p. 151).

Soljačić, M. and Joannopoulos, J. (2004). "Enhancement of nonlinear effects using photonic crystals". *Nat. Mater.* **3**, pp. 211–219. DOI: 10.1038/nmat1097 (cit. on p. 67).

Sparnaay, M. J. (1959). "On the additivity of London-van der Waals forces : an extension of London's oscillator model". *Physica* **25**, pp. 1959–217. DOI: 10.1016/S0031-8914(59)92714-4 (cit. on p. 153).

Spillane, S. M., Kippenberg, T. J., Vahala, K. J., Goh, K. W., Wilcut, E., and Kimble, H. J. (2005). "Ultrahigh-Q toroidal microresonators for cavity quantum electrodynamics". *Phys. Rev. A* **71**, p. 013817. DOI: 10.1103/PhysRevA.71.013817 (cit. on pp. 45, 46).

Starkey, P. T., Billington, C. J., Johnstone, S. P., Jasperse, M., Helmerson, K., Turner, L. D., and Anderson, R. P. (2013). "A scripted control system for autonomous hardware-timed experiments". *Rev. Sci. Instrum.* **84**, p. 085111. DOI: 10.1063/1.4817213 (cit. on pp. 114, 115).

Starkey, P. T. (2019). "A software framework for control and automation of precisely timed experiments". PhD thesis. Monash University. DOI: 10.26180/5d1db8ffe29ef (cit. on pp. 111, 114, 115).

Steck, D. A. (2001). *Rubidium 87 D Line Data*. Tech. rep. (cit. on pp. 28, 29, 35).

— (2019). *Quantum and Atom Optics*. available online at http://steck.us/teaching (cit. on pp. 21, 29, 30, 34, 35, 48).

Stern, L., Desiatov, B., Mazurski, N., and Levy, U. (2017). "Strong coupling and high-contrast all-optical modulation in atomic cladding waveguides". *Nat. Commun.* **8**, p. 14461. DOI: 10.1038/ncomms14461 (cit. on p. 76).

Stern, N. P., Alton, D. J., and Kimble, H. J. (2011). "Simulations of atomic trajectories near a dielectric surface". *New J. Phys.* **13**, p. 085004. DOI: 10.1088/1367-2630/13/8/085004 (cit. on pp. 46, 148, 151).

Stiesdal, N., Busche, H., Kleinbeck, K., Kumlin, J., Hansen, M. G., Büchler, H. P., and Hofferberth, S. (2021). "Controlled multi-photon subtraction with cascaded Rydberg superatoms as single-photon absorbers". *Nat. Commun.* **12**, p. 4328. DOI: 10.1038/s41467-021-24522-w (cit. on p. 15).

Stute, A., Casabone, B., Schindler, P., Monz, T., Schmidt, P. O., Brandstätter, B., Northup, T. E., and Blatt, R. (2012). "Tunable ion-photon entanglement in an optical cavity". *Nature* **485**, pp. 482–485. DOI: 10.1038/nature11120 (cit. on p. 9).

Su, Y., Chang, P., Lin, C., and Helmy, A. S. (2019). "Record Purcell factors in ultracompact hybrid plasmonic ring resonators". *Sci. Adv.* **5**, eaav1790. DOI: 10.1126/sciadv.aav1790 (cit. on p. 18).

Tabares, C., Muñoz de las Heras, A., Tagliacozzo, L., Porras, D., and González-Tudela, A. (2023). "Variational Quantum Simulators Based on Waveguide QED". *Phys. Rev. Lett.* **131**, p. 073602. DOI: 10.1103/PhysRevLett.131.073602 (cit. on pp. 13, 32).

Tey, M. K., Chen, Z., Aljunid, S. A., Chng, B., Huber, F., Maslennikov, G., and Kurtsiefer, C. (2008). "Strong interaction between light and a single trapped atom without the need for a cavity". *Nat. Phys.* **4**, pp. 924–927. DOI: 10.1038/nphys1096 (cit. on p. 7).

Teyssier, J., Saenko, S. V., Van Der Marel, D., and Milinkovitch, M. C. (2015). "Photonic crystals cause active colour change in chameleons". *Nat. Commun.* **6**, p. 6368. DOI: 10.1038/ncomms7368 (cit. on p. 52).

Therisod, R., Tardif, M., Villa, N., Marcoux, P. R., Picard, E., Hadji, E., Peyrade, D., and Houdré, R. (2022). "Bacterial Gram-Type Differentiation Accomplished with Hollow Photonic Crystal Cavities". *Light-Matter Interactions Towards the Nanoscale*. Springer Netherlands, pp. 357–359 (cit. on p. 52).

Thompson, J. D. et al. (2013). "Coupling a Single Trapped Atom to a Nanoscale Optical Cavity". *Science* **340**, pp. 1202–1205. DOI: 10.1126/science.1237125 (cit. on pp. 9, 33, 38, 39, 104, 124).

Thompson, R. J., Rempe, G., and Kimble, H. J. (1992). "Observation of normal-mode splitting for an atom in an optical cavity". *Phys. Rev. Lett.* **68**, pp. 1132–1135. DOI: 10.1103/PhysRevLett.68.1132 (cit. on p. 9).

Tiranov, A. et al. (2023). "Collective super- and subradiant dynamics between distant optical quantum emitters". *Science* **379**, pp. 389–393. DOI: 10.1126/science.ade9324 (cit. on pp. 14, 15, 64).

Tong, L., Gattass, R. R., Ashcom, J. B., He, S., Lou, J., Shen, M., Maxwell, I., and Mazur, E. (2003). "Subwavelength-diameter silica wires for low-loss optical wave guiding". *Nature* **426**, pp. 816–819. DOI: 10.1038/nature02193 (cit. on p. 42).

Tong, L., Lou, J., and Mazur, E. (2004). "Single-mode guiding properties of subwavelength diameter silica and silicon wire waveguides". *Opt. Express* **12**, pp. 1025–1035. DOI: 10.1364/OPEX.12.001025 (cit. on p. 62).

Türschmann, P., Le Jeannic, H., Simonsen, S. F., and Haakh, H. R. (2019). "Coherent nonlinear optics of quantum emitters in nanophotonic waveguides". *Nanophotonics* **8**, pp. 1641–1657. DOI: 10.1515/nanoph-2019-0126 (cit. on p. 9).

van Loo, A. F., Fedorov, A., Lalumière, K., Sanders, B. C., Blais, A., and Wallraff, A. (2013). "Photon-Mediated Interactions Between Distant Artificial Atoms". *Science* **342**, pp. 1494–1496. DOI: 10.1126/science.1244324 (cit. on pp. 14, 15).

Van Mechelen, T. and Jacob, Z. (2016). "Universal spin-momentum locking of evanescent waves". *Optica* **3**, pp. 118–126. DOI: doi.org/10.1364/OPTICA.3.000118 (cit. on p. 36).

Vaneecloo, J., Garcia, S., and Ourjoumtsev, A. (2022). "Intracavity Rydberg Superatom for Optical Quantum Engineering: Coherent Control, Single-Shot Detection, and Optical π Phase Shift". *Phys. Rev. X* **12**, p. 021034. DOI: 10.1103/PhysRevX.12.021034 (cit. on p. 9).

Vercruysse, D., Sapra, N. V., Yang, K. Y., and Vučković, J. (2021). "Inverse-Designed Photonic Crystal Circuits for Optical Beam Steering". *ACS Photonics* **8**, pp. 3085–3093. DOI: 10.1021/acsphotonics.1c01119 (cit. on p. 70).

Vernaz-Gris, P., Huang, K., Cao, M., Sheremet, A. S., and Laurat, J. (2018). "Highly-efficient quantum memory for polarization qubits in a spatially-multiplexed cold atomic ensemble". *Nat. Commun.* **9**, p. 363. DOI: 10.1038/s41467-017-02775-8 (cit. on p. 8).

Vernooy, D. W., Furusawa, A., Georgiades, N. P., Ilchenko, V. S., and Kimble, H. J. (1998a). "Cavity QED with high-Q whispering gallery modes". *Phys. Rev. A* **57**, R2293–R2296. DOI: 10.1103/PhysRevA.57.R2293 (cit. on p. 45).

Vernooy, D. W., Ilchenko, V. S., Mabuchi, H., Streed, E. W., and Kimble, H. J. (1998b). "High-Q measurements of fused-silica microspheres in the near infrared". *Opt. Lett.* **23**, pp. 247–249. DOI: 10.1364/OL.23.000247 (cit. on p. 45).

Vernooy, D. and Kimble, H. (1997). "Quantum structure and dynamics for atom galleries". *Phys. Rev. A* **55**, p. 1239. DOI: 10.1103/PhysRevA.55.1239 (cit. on p. 47).

Vetsch, E., Reitz, D., Sagué, G., Schmidt, R., Dawkins, S. T., and Rauschenbeutel, A. (2010). "Optical Interface Created by Laser-Cooled Atoms Trapped in the Evanescent Field Surrounding an Optical Nanofiber". *Phys. Rev. Lett.* **104**, p. 203603. DOI: 10.1103/PhysRevLett.104.203603 (cit. on pp. 13, 32, 33, 38, 42, 43, 87).

Vetsch, E. (2010). "Optical Interface Based on a Nanofiber Atom-Trap". PhD thesis. Johannes Gutenberg Universität (cit. on p. 42).

Veyron, R., Mancois, V., Gerent, J.-B., Baclet, G., Bouyer, P., and Bernon, S. (2022). "Quantitative absorption imaging: The role of incoherent multiple scattering in the saturating regime". *Phys. Rev. Res.* **4**, p. 033033. DOI: 10.1103/PhysRevResearch.4.033033 (cit. on p. 119).

Vlk, M., Datta, A., Alberti, S., Yallew, H. D., Murugan, G. S., and Jágerská, J. (2021). "Extraordinary evanescent field confinement waveguide sensor for mid-infrared trace gas spectroscopy". *Light Sci. Appl.* **10**, p. 26. DOI: 10.1038/s41377-021-00470-4 (cit. on pp. 52, 58).

Vorrath, S., Möller, S. A., Windpassinger, P., Bongs, K., and Sengstock, K. (2010). "Efficient guiding of cold atoms through a photonic band gap fiber". *New J. Phys.* **12**, p. 123015. DOI: 10.1088/1367-2630/12/12/123015 (cit. on p. 10).

Vyas, K., Cheriton, R., Liu, D., Ahmed, H., Schulz, S., and Dolgaleva, K. (2022). "Simulation and fabrication of slow light suspended air-bridge AlGaAs photonic crystal waveguide". *Integrated Optics: Devices, Materials, and Technologies XXVI*. Vol. 12004. SPIE, 120040N. DOI: 10.1117/12.2609253 (cit. on p. 69).

Wallraff, A. et al. (2004). "Strong coupling of a single photon to a superconducting qubit using circuit quantum electrodynamics". *Nature* **431**, pp. 162–167. DOI: 10.1038/nature02851 (cit. on p. 9).

Weiss, L., Gritsch, A., Merkel, B., and Reiserer, A. (2021). "Erbium dopants in nanophotonic silicon waveguides". *Optica* **8**, pp. 40–41. DOI: 10.1364/OPTICA.413330 (cit. on p. 64).

Welte, S., Hacker, B., Daiss, S., Ritter, S., and Rempe, G. (2018). "Photon-Mediated Quantum Gate between Two Neutral Atoms in an Optical Cavity". *Phys. Rev. X* **8**, p. 011018. DOI: 10.1103/PhysRevX.8.011018 (cit. on p. 9).

Will, E., Masters, L., Rauschenbeutel, A., Scheucher, M., and Volz, J. (2021). "Coupling a Single Trapped Atom to a Whispering-Gallery-Mode Microresonator". *Phys. Rev. Lett.* **126**, p. 233602. DOI: 10.1103/PhysRevLett.126.233602 (cit. on p. 33).

Wintersperger, K., Braun, C., Unal, F. N., Eckardt, A., Liberto, M. D., Goldman, N., Bloch, I., and Aidelsburger, M. (2020). "Realization of an anomalous Floquet topological system with ultracold atoms". *Nat. Phys.* **16**, pp. 1058–1063. DOI: 10.1038/s41567-020-0949-y (cit. on pp. 38, 47).

Wolf, E. and Gabor, D. (1959). "Electromagnetic diffraction in optical systems - I. An integral representation of the image field". *Proc. R. Soc. A* **253**, pp. 349–357. DOI: 10.1098/rspa.1959.0199 (cit. on p. 129).

Wu, J., Li, Y., Peng, C., and Wang, Z. (2010). "Wideband and low dispersion slow light in slotted photonic crystal waveguide". *Opt. Commun.* **283**, pp. 2815–2819. DOI: 10.1016/j.optcom.2010.03.037 (cit. on pp. 69, 81).

Wylie, J. M. and Sipe, J. E. (1984). "Quantum electrodynamics near an interface". *Phys. Rev. A* **30**, pp. 1185–1193. DOI: 10.1103/PhysRevA.30.1185 (cit. on p. 21).

Xiong, C. et al. (2011). "Slow-light enhanced correlated photon pair generation in a silicon photonic crystal waveguide". *Opt. Lett.* **36**, pp. 3413–3415. DOI: 10.1364/OL.36.003413 (cit. on p. 58).

Yablonovitch, E. (1987). "Inhibited Spontaneous Emission in Solid-State Physics and Electronics". *Phys. Rev. Lett.* **58**, pp. 2059–2062. DOI: 10.1103/PhysRevLett.58.2059 (cit. on p. 52).

Yang, F., Lund, M. M., Pohl, T., Lodahl, P., and Mølmer, K. (2022). "Deterministic Photon Sorting in Waveguide QED Systems". *Phys. Rev. Lett.* **128**, p. 213603. DOI: 10.1103/PhysRevLett.128.213603 (cit. on pp. 11, 146).

Ye, J., Kimble, H. J., and Katori, H. (2008). "Quantum state engineering and precision metrology using state-insensitive light traps". *Science* **320**, pp. 1734–1738. DOI: 10.1126/science.1148259 (cit. on p. 36).

Yeh, P. (2005). *Optical Waves in Layered Media*. 2nd ed. Wiley (cit. on p. 155).

Yoshioka, S. and Kinoshita, S. (2001). "Effect of Macroscopic Structure in Iridescent Color of the Peacock Feathers". *Forma* **17**, pp. 169–181 (cit. on p. 52).

Yu, S.-P. (2017). "Nano-Photonic Platform for Atom-Light Interaction". PhD thesis. California Institute of Technology (cit. on p. 123).

Yu, S. P. et al. (2014). "Nanowire photonic crystal waveguides for single-atom trapping and strong light-matter interactions". *Appl. Phys. Lett.* **104**, p. 111103. DOI: 10.1063/1.4868975 (cit. on pp. 3, 15, 38, 44).

Zang, X. et al. (2016). "Interaction between Atoms and Slow Light: A Study in Waveguide Design". *Phys. Rev. Appl.* **5**, p. 024003. DOI: 10.1103/PhysRevApplied.5.024003 (cit. on pp. 67, 78, 79, 86, 93, 95).

Zhou, X., Tamura, H., Chang, T.-H., and Hung, C.-L. (2023). "Coupling Single Atoms to a Nanophotonic Whispering-Gallery-Mode Resonator via Optical Guiding". *Phys. Rev. Lett.* **130**, p. 103601. DOI: 10.1103/PhysRevLett.130.103601 (cit. on pp. 125, 128).

Adrien Bouscal 15 Décembre 2023

Sujet : Guides d'ondes à modes lents et atomes froids : Vers une plateforme polyvalente d'électrodynamique quantique en guide d'onde

Résumé : Les récentes plateformes expérimentales qui combinent atomes froids et guides d'ondes nanométriques offrent une approche prometteuse pour atteindre un régime de couplage fort entre lumière et atomes en simple passage. Cette thèse porte sur la conception, la fabrication et la mise en œuvre d'une telle plateforme hybride permettant d'interfacer la lumière lente de guides d'ondes à cristaux photoniques avec des atomes de Rubidium froids piégés à proximité de leur surface. Les modes lents de ces guides doivent permettre une interaction lumière-matière renforcée par rapport aux systèmes existants en espace libre ou avec une nanofibre, ce qui rend cette nouvelle plateforme propice à la mise en place de protocoles d'électrodynamique quantique en guide d'onde. En portant une attention particulière à la robustesse des structures face aux imperfections de fabrication, nous proposons trois designs innovants de guides d'ondes à fort indice de réfraction permettant une interaction lumière-matière efficace ainsi que la mise en place de pièges dipolaires évanescents pour maintenir les atomes proches de leur surface. Nous décrivons ensuite le dispositif expérimental construit pour produire un nuage d'atomes froids, conçu pour intégrer de tels guides nanofabriqués et en approcher les atomes à l'aide de pinces optiques réalisées avec des modes optiques d'ordres supérieurs. Ce travail ouvre la voie à de futures plateformes d'électrodynamique quantique en guide d'onde avec des atomes froids qui pourraient constituer des ressources précieuses pour des protocoles d'optique quantique non-linéaire, la simulation quantique ou le calcul quantique variationnel.

Mots clés : Atomes froids, Nanophotonique, Optique quantique, Interaction lumière-matière, Cristaux photoniques, Electrodynamique quantique en guide d'onde

Subject: Slow-mode nanophotonics and cold atoms: Towards a versatile Waveguide QED platform

Abstract: Novel platforms interfacing trapped cold atoms and guided light in nanoscale waveguides are a promising route to achieve a regime of strong coupling between light and atoms in single pass, with applications to quantum non-linear optics and quantum simulation. This thesis focuses on the design, fabrication and implementation of such a hybrid experimental platform interfacing slow light from photonic-crystal waveguides with cold Rubidium atoms trapped in their vicinity. The slow guided modes from the waveguides should enhance the interaction between light and matter compared to free space or nanofiber-based existing platforms, making it conducive for Waveguide quantum electrodynamics (QED) protocols. Emphasizing the need for resilience against fabrication imperfections, we design three different high-index waveguides that allow for efficient light-matter interaction and evanescent dipole trapping of atoms close to their surface. Subsequently, we then detail our versatile cold atom experimental setup, specifically built for integrating these structures and delivering atoms to their surfaces using higher-order tweezers, and report initial experimental results. This work paves the way for hybrid Waveguide QED platforms with cold atoms which could serve as valuable resources for simulating Ising-like Hamiltonians or variational quantum computing.

Keywords: Cold atoms, Nanophotonics, Quantum optics, Photonic crystals, Light-matter interaction, Waveguide QED